NANOSTRUCTURED MATERIALS FOR ENERGY APPLICATION

ASHISH GAUR

A thesis submitted for the partial fulfillment of

the degree of Doctor of Philosophy

Institute of Nano Science and Technology

Knowledge City, Sector 81, SAS Nagar, Manauli PO, Mohali 140306, Punjab, India

Indian Institute of Science Education and Research

Knowledge city, Sector 81, SAS Nagar, Manauli PO, Mohali 140306, Punjab, India

May 2023

Dedicated to my Grand Mother

The one who inspired it but will not read it

DECLARATION

The work presented in this thesis has been carried out by me under the guidance of Dr. Vivek Bagchiat the Institute of Nano Science and Technology Mohali. This work has not been submitted in part or in full for a degree, a diploma, or a fellowship to any other university or institute. Whenever contributions of others are involved, every effort is made to indicate this clearly, with due acknowledgement of collaborative research and discussions. This thesis is a bonafide record of original work done by me and all sources listed within have been detailed in the bibliography.

ASHISH GAUR

In my capacity as the supervisor of the candidate's thesis work, I certify that the above statements by the candidate are true to the best of my knowledge.

Dr. VIVEK BAGCHI

ACKNOWLEDGEMENTS

I would like to begin by giving glory and thanks to God, the Almighty, who has bestowed upon me innumerable blessings, insights, and opportunities that have allowed me to complete my thesis.

I owe a great debt of appreciation to **Dr. Vivek Bagchi**, my mentor at INST Mohali, who provided me with countless hours of invaluable advice and support while we developed the ideas presented in this thesis.His great scientific knowledge and enthusiasm have always been a source of inspiration for me in my pursuit of understanding the many facets of material science. I'd want to express my gratitude to **Mrs. Monika Singh Bagchi** for their kindness and generosity. It was a pleasure to be in the company of such lovely individuals.

I wish to express my heartfelt gratitude to the director of INST **Prof. Amitava Patra**, and **Prof. H. N Ghosh** who gave me the opportunity to be a part of this prestigious institute and then for all the motivation, support and facilities he provided during my PhD time. I'd also like to give props to **Dr. Chandan Bera** and his student **Ms. Parrydeep Kaur,** one of our INST collaborator who did some theoretical delving into our findings.I also want to thank our collaborator **Dr. S. N. Jha** (BL-9, RRCAT) who helped me a lot in characterization and during the stay in RRCAT Indore.

I appreciate the time and effort put in by the members of my PhD Review Committee, who provided me with insightful comments and helpful feedback during the course of my thesis.

I also express my sincere thanks to myseniors Dr. Rajinder Kumar, Dr. Ritu Rai, Dr. Zubair Ahmed and Dr. Srinivasan. The time and energy they put into instructing me in synthesis, instrument handling and data analysis is priceless.A very special thank you to Dr. Rajinder for all of those inspiring and enlightening talks that took place during tea time.I also want to thank my juniors Mr. Vikas, Mr. Krishnkant, Ms. Rajdeep Kaur, Ms. Aashi and Ms. Rekha. who helped me a lot in the lab during my work. My extended

thanks to our interns Ms. Ekta, Ms. Manali, Mr. Joel Mathew John, Mr. Subhojit, Mr. Subhodip and Mr. Jatin. I would also like to extend my deepest gratitude to the **Late Mrs. Shilpa**. Her assistance during our research was of enormous value.

There's a lot I owe to my wonderful grandparents, **Late Shri Gangaprasad Gaur**, **Late Shri Barman and Tiwari**, **Late Shrimati Damayanti Devi Gaur** and **Late Shrimati Anandi Devi.** Their selflessness and blessings have made it possible for us to have a prosperous future.My special thanks goes to my grandmother **Late Shrimati Damayanti Devi gaur,** i learned from her the value of commitment, self-control, sacrifice, tolerance, and perseverance.I never would have considered pursuing a doctoral degree without her support.

I owe hugely to my dear parents**, Mr. Rajendra Kumar gaur** and **Mrs. Anshu Devi Gaur.** Their permanent love and confidence in me have encouraged me to go ahead in my study and career. You've both inspired me to aim high and go after my goals, so I'm eternally grateful. I'd also like to express my deepest love to my sisters **Tanu Gaur**, **Hemlata Gaur** and younger brother **Rochan Gaur**.

I wish to express my gratitude to my uncles **Mr. Vedprakash Gaur**, **Mr. Bharat Mohan Gaur** and **Mr. Sanjeev Gaur**. They educate me to keep my feet firmly planted on the ground while simultaneously reaching for the stars with all of the love and encouragement that I can get from them.During the course of my Ph.D., their lengthy phone calls on the weekends served as a stress reliever.My sincere gratitude goes out to my aunts **Mrs. Rajkumari Gaur** and **Mrs. Yashoda Gaur** for the generosity and compassion they have shown us on each of our visits to their homes.

I want to say thanks to my teachers, **Shri Sateesh Dabral, Shri Deendayal Jakhmola, Shri Vidhyadatt Joshi, Shri Chandramohan Singh Negi, Late Shree Jayanand Gaur, Shree Manvarlal Bharti, Shri Dinesh Rana, Late Shri Rajendra Kumar Yadav, Shri. Deepak Gusain, Shri Ashok Joshi, ShriChakradhar Singh Rana, Sri Padmendra Rana, Shri Somprakash Kandwal, Shri Dharampal Bisht, Shri Shashibhoosan Amoli, Sri Roshan Balooni and Mr.Pradeep Bisht** Thank you for

everything you've done for me over my years of education.You saw something in me that I didn’t see in myself.

I would also like to express my gratitude to **Arti Joshi** for all of her support since the beginning of my Ph.D. She has been there for me through all of my successes and failures. I also want to thank **Deepika Rani**, **Parul, Ritu** and **Sobhna** for providing help during the period of my work. I would like to express my thanks in particular to **Gagandeep Kaur, Bandana,** and **Mahima** for providing emotional support and help in reducing the stress. It was a nice time when all of us travelled to different places throughout our PhD studies and assisted one another in their challenging times.I would also like to thank **Dr. Rohit Varshney, Dr. Ravi Kumar Kunchala, Dr. Ashmeet Singh and Dr. Rejaul Karim** for teaching me many skill required for the research.I express my warm feelings of gratitude to my M.Sc. friends at Gurukula Kangri Vishwavidhayala Haridwar specially **Love Pratap** who has always been there for me whenever I have needed him.I would like to express my thanks in particular to **Hemant Gaur, Ashu, Deeksha, Renu, Jyoti, Shubham, Priyanshu, Hemlata** for helping me in various things which helps me in completing my work on time.

For infrastructural facility, I would like to thank the “Institute of Nanoscience and Technology” and “Indian Institute of Science Education and Research, Mohali and DST for financial supportI also want to thank all Administrative staff, Technical, Non-teaching staff and Security staff of INST Mohali for their valuable contribution tothe completion of my PhD.. Special thank to **Butta Singh Ji** and **Vikram Singh** who serves tea in our cabins during the initial days of our PhD.

ASHISH GAUR

Table of Contents

List of Figures

List of tables

Abbreviations and Nomenclature

IAHE	International Association of Hydrogen Energy
XANES	X-ray absorption near-edge structures
EXAFS	Extended X-ray absorption fine structure
NEXAFS	Near Edge X-ray absorption fine structure
DCM	Double Crystal Monochromator
PCS	Photon Correlation Spectroscopy
HER	Hydrogen Evolution reaction
HMT	Hexamethylenetetramine
TEM	Transmission Electron Microscopy
HRTEM	High-resolution Transmission Electron Microscopy
XPS	X-ray Photoelectron Spectroscopy
RHE	Reversible Hydrogen Electrode
EIS	Electrochemical Impedance Spectroscopy
GCE	Glassy Carbon Electrode
LSV	Linear Sweep Voltammetry
PXRD	Powder X-ray Diffraction
SEM	Scanning Electron Microscopy
CPE	Constant Phase Element
Pt	Platinum
TEOS	Tetraethyl orthosilicate
g-C_3N_4	Graphitic carbon nitride
NH3	Ammonia
FT-EXAFS	Fourier Transform Extended X-ray absorption fine structure
VASP	Vienna ab-initio Simulation Package
GGA	Generalized Gradient Approximation

PAW	Projector Augmented Plane Wave
GO	Graphene Oxide
EDX	Energy Dispersive X-ray
CN	Coordination Number
DFT	Density Functional Theory
HCl	Hydrochloric
MOFs	Metal-Organic Framework
TMBs	Transition Metal Borides
TMSs	Transition Metal Sulphide
TMOs	Transition Metal Oxide
TMCs	Transition Metal Carbide
TMNs	Transition Metal Nitrides
TMSes	Transition Metal Selenides
TMPs	Transition Metal phosphides
mV	Milli Volt
Hz	Hertz
σ^2	Disorder (Debye-Waller) factors
η	Overpotential
mg	Milligram
mA	Milli Ampere
F	Faraday Constant
K_β	Boltzmann Constant
R	Gas Constant
λ	Wavelength
q	Charge
$Å$	Angstrom

μ	Absorbance Coefficient
ϕ	Work Function
μL	Micro litre
g	Gram
°C	Degree Centigrade

Abstract

Recently, a new climate prediction was issued by World Meteorological Organization (WMO), stating that, "There is a ~20% chance that one of the next 5 years will be at least 1.5°C warmer than pre-industrial levels, but the chance is increasing with time." The heat stress due to high surface temperature in the coming days would reach extreme affecting human health, productivity, and mortality in many places on Earth Rising levels of CO_2 in the ocean causing huge proliferation of toxic algae, which is a potential threat to marine life, coastal communities, aquaculture and fisheries and of course human health. The ocean absorbs CO_2 at a rate of 22 million tons per day as revealed by the National Oceanic and Atmospheric Administration. Increased acidity of the ocean's surface water resulting in the dissolution of shells and skeletons causing the extinction of numerous species. An effort to obtain sustainable and clean energy, using electrocatalytic hydrogen generation reactions and oxygen evolution reactions could be potential solutions towards environmental degradation. In this regard the present thesis is focused on the formation of transition metal based heterostructures of metal phosphide, nitride, sulphide, oxide, single-atom catalyst (SACs), Metal-organic organic framework (MOF) and MOF-derived materials for hydrogen evolution reaction (HER), oxygen evolution reaction (OER) and oxygen reduction reaction (ORR). The first heterostructure we worked on is Co@NC@MoS_2 for oxygen evolution reaction (OER) in which the synergistic effect between Co@NC nanoparticles and MoS_2 nanosheets enhances the catalytic activity. The catalyst exhibit the overpotential of 297 mV at 10 mA cm^{-2} of current density. Moving forward we worked on transition metal oxide heterostructures and we developed CuO-NiO, Co_3O_4-NiO heterostructure for OER with overpotential of 231 mV and 311 mV and $NiWO_4$-NiO heterostructure for HER with overpotential of 71 mV. Further, taking the advantage of high electronegativity of metal fluorides we fabricated the metal fluoride and metal nitride heterostructure (Co-Ni_3N/CeF_3). This heterostructure exhibit the overpotential of 180 mV at 10 mA cm^{-2} of current density. This ultralow overpotential was obtained due to the interfacial charge transfer from Co-Ni_3N to CeF_3 results in the augmentation of valence state of Ni and Co which enhances the adsorption of intermediates on the catalyst surface. Further we move on to explore the pristine MOF for oxygen evolution reaction. the bimetallic Co, Ni based ultrathin metal-organic framework

nanoribbons (NiCo-NR) for oxygen evolution reaction. The slender NiCo-NR was formed by using ultrathin metal hydroxide ($NiCo(OH)_2$) mediated strategy. The NiCo-NR shows overpotential of 244 mV at a current density of 10 mA cm^{-2} current density. We suggest that in the ultrathin MOF nanoribbons surface atoms (Co,Ni) are coordinatively unsaturated. Due to the ultrathin nanostructuring of MOF sheets the inter-atomic electron transfer within the MOF makes more active adsorption sites on the surface. Our findings show that coordinatively unsaturated metal atoms are the dominant active centers, and the electrocatalytic activity is tuned by the coupling effect between Ni and Co metals. Moving forward we formed the heterostructure of Ni_3N-$MnCo_2O_4$ and Co-Ni_3N/$MnCo_2O_4$ and we explained the effect of Jahn-Teller distortion in these heterostructures. The suppression of Jahn-Teller distortion can enhance the oxygen adsorption on the catalyst surface by optimizing the adsorption energy.

Chapter 1

Introduction

1. Introduction

1.1. The Current Energy Crisis and the Role of Renewable Energy

In nature, materials tend to circulate in closed cycles whereby supply may be maintained via a number of chemical transformations. Then, at some point, it tapers off to the initial product, ensuring a holistic view of the materials' energy reserves. The oxygen, carbon, and nitrogen cycles, among others, provide many examples in nature that support this theory.[1,2] In many instances, humanity violates this fundamental principle in the modern day. Since the beginnings of industrialization and urbanisation, an unprecedented number of resources have been extracted without remorse.[3]As a result, humanity must master a variety of challenges. Energy and the environment are two of the most concerning ever-increasing preoccupations of modern human society, owing to dramatically expanding demand as well as the deteriorating environment caused by the consumption of fossil fuels.[4]It's true that as this modern period has progressed, our reliance on and propensity to use fossil fuels has grown, contributing considerably to an increase in the average global temperature as well as atmospheric carbon dioxide levels.[5]Newly increased production of fossil-based fuels such as coal, oil, or gas has been meeting the exponential growth in energy demand with the expansion of the global economy and population, but these resources are expected to be depleted within the next century at the latest.Since the beginning of the industrial period, the world's primary energy source has been fossil fuels like oil and coal. Seventy percent of the world's energy needs are met by these sources at the present time. The intense form of free energy offered by fossil fuels is an endearing quality. It took these complicated molecules millions of years to evolve into their current state by biological methods. In addition, it has the benefit that energy extraction through burning of these fuels is rather simple. The release of greenhouse gases from these nonrenewable energy sources, however, causes serious difficulties for the environment.[6,7]Global energy consumption was 5.79×10^{20} J in 2012, and it is projected to rise to 8.60×10^{20} J by 2040. The International Energy Agency also predicted that by 2040, global energy demand would have increased by 30%, while emissions of greenhouse gases like carbon dioxide would have risen to about 35.7 Gt annually.[8,9]This

critical issue is now a global one, and the development of carbon-neutral energy sources that can be produced sustainably is motivating scientists to develop innovative solutions. Although many nations are working hard to meet energy needs and reduce carbon emissions, they still won't be able to reach the specified objective by the deadline. These worries have pushed scientists and the general public to seek for alternative conversion technologies that are both environmentally benign and capable of meeting basic human requirements.[10-14]The current state of technology has already made it possible for us to make use of nonconventional forms of energy such as wind, turbines, solar cells, biomass plants, and many more.[15-18]The significant investment that has been made in the exploration and production of energy from renewable sources has led to a rise in the proportion of overall power generation that comes from these sources. There are a great number of obstacles that need to be overcome in order to achieve the goal of increasing the amount of renewable energy that is used in homes and corporations on a daily basis.The generation of energy from unconventional sources like the sun and wind is limited by the laws of nature rather than being endowed with an endless supply of energy. The economics, the ecology, and human health must all be taken into account while using renewable energy sources.[19]This growing importance is reflected in the formation of many policy initiatives to promote technology, most recently the hydrogen strategy for a climate-neutral Europe and the German hydrogen strategy. To utilise hydrogen technology on a wide scale, however, new infrastructure and extensive adjustments to the present system are required. Mostly all hydrogen gas has come from a non renewable source, most notably steam reforming methane (SRM).[20,21] Creating environmentally acceptable energy regulations that can be replaced with renewable energy resources to create hydrogen energy has gained a lot of focus recently. There is evidence that electrochemical water splitting is a viable method for producing hydrogen energy. Producing chemical energy, such as chemical fuel and hydrogen energy, from electrical energy generated by solar, marine, and wind sources. We will further discuss in details how hydrogen can be produced via electrochemical water splitting and about the functioning of hydrogen economy.

1.2.Hydrogen: Sustainable and Eco-Friendly Energy Option

1.2.1 Hydrogen

If we are successful in finding solutions to our energy problems, one of the most significant achievements will be the creation of chemical fuels from renewable sources. In the 21st century, one of the primary types of important scientific difficulties is the creation of hydrogen by the splitting of water. Hydrogen, a freely accessible molecule that exists in gas and liquid form in our surroundings. Hydrogen having the lowest energy content by volume but greatest by weight and owing to its greater energy content is utilised as a future energy carrier. Hydrogen delivers three times greater heating value compared to petroleum with zero hazardous emission. Due to the fact that it is a manufactured stimulant, it is subject to a rigorous production process that results in costs that are higher than those associated with petroleum refining.[22]

1.2.2. Hydrogen Economy and Obstacles

The phrase "hydrogen economy" was coined by J. B. S. Haldane and Professor John Bockris. The economy relied heavily on the idea of potential fuel, which may be found in the form of hydrogen. Hydrogen is generally regarded as one of the most secure and environmentally friendly energy carriers out of all the many types of energy sources. Molecular hydrogen, however, is not abundantly accessible, and in order to produce it one must mix other sources of hydrogen with it in a variety of ways. This is the case even if these characteristics seem encouraging. The economy is still in the process of developing; possibly it will be one of the significant infrastructure projects that will be undertaken in the near future. In general, it relates to hydrogen reservoirs, as well as the transportation of hydrogen and the many uses for hydrogen.[23-26]Hydrogen is an appealing energy carrier due to the fact that it does not produce any carbon-based by-products, which positions it as a candidate for inclusion among the sources of clean energy.[27] Consequently, the development of what is now commonly known as the hydrogen economy is required in order to investigate the cleanest and most secure carbon-free energy source.[28]There is no shadow of a doubt that in the not-too-distant future, the transition of technology based on traditional forms of energy into technology based on hydrogen will solve a significant number of the energy and climate-related challenges

that face the whole world.[29] The production, transportation, and use of hydrogen as an alternative to the use of fossil fuels were the primary focuses of the hydrogen economy.[30]Hydrogen storage, on the other hand, is a whole new notionthat has not received nearly as much attention as the storage of electrical energy. Hydrogen is heavily reliant on the chemical industry because it has no natural supplies. One of the most important events that led to the development of alternative energy sources was the oil crisis of 1973.

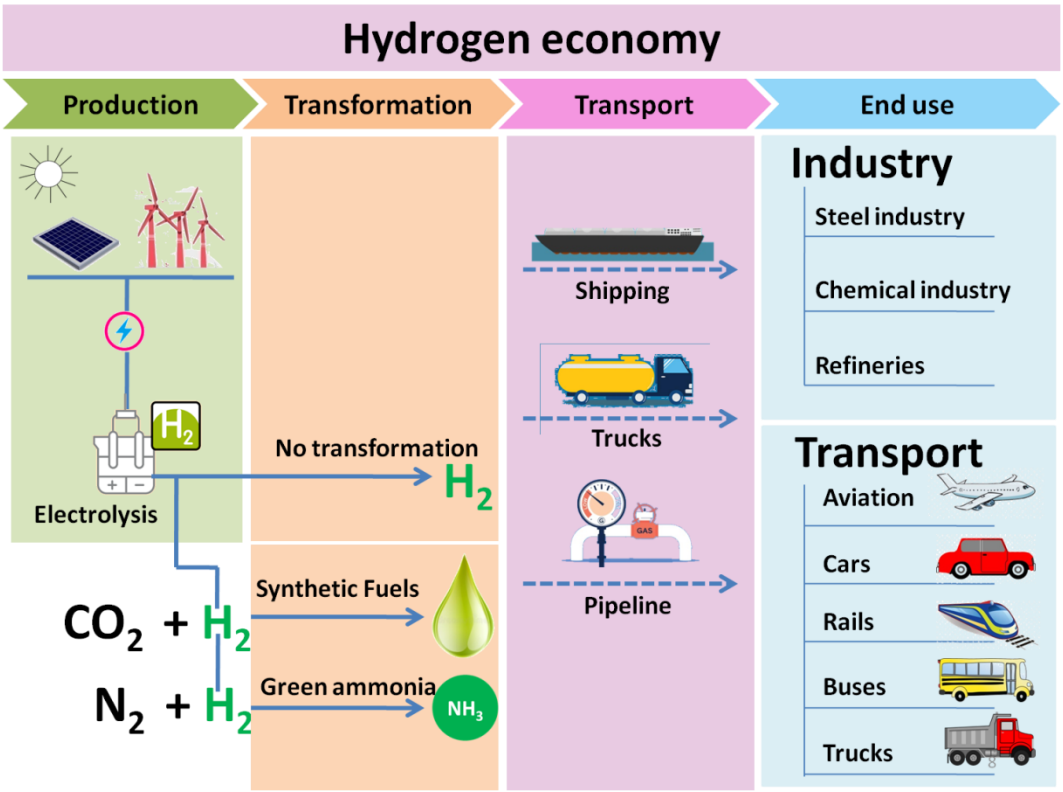

Figure 1.1.*Schematic showing the hydrogen economy in the society*

The idea of hydrogen energy was initially introduced during this period. The first conference focused on hydrogen generation, utilisation, and marketing was held in 1974, and an organisation called the "International association from hydrogen energy" was established. The organization's primary goal is to use and promote hydrogen as an energy carrier in the energy industry and businesses that are related to energy.The application of hydrogen as a unique material in several industries has enhanced the scalability of this carbon-free energy source.[31]The optimization of the hydrogen-based industries has

progressed as of late. It is extremely difficult to determine whether industrialisation is even possible given the restrictions on the conversion of all energy sources into hydrogen-based technologies.[32,33] The hydrogen economy in the modern society works in four different phases as shown in scheme1. Production includes the large scale electrolysis of water in which the electricity for this process should also come from renewable energy source with zero CO_2 emission. The hydrogen produced via electrolysis can be used further directly and transported or we can transform it into some synthetic fuels and green NH_3. After this we can transport it using pipelines, ships and trucks and it will reach to end users. This green hydrogen can be utilized in industry (steel industry, chemical industry and refineries) or in transportation (car, bus, train, trucks and aviation sector).

1.2.3. Infrastructure and contemporary conditions

In 2018, Rio de Janeiro serves as the gateway to the World Hydrogen Energy Conference, which took place between June 17 and June 22. Professor T. Nejat Veziroglud, the founding president of the International Association of Hydrogen Energy, was one of the keynote speakers at the event (IAHE). In his talk, he makes the assertion and expresses the expectation that the whole transition of the economy to hydrogen energy would be completed by the end of this century.Approximately 44 years ago, he was a part of a group called "Hydrogen Romantics." Along with 10 other people, he organised and presided over a conference called "Hydrogen Economy Miami Energy (THEME) Conference." In addition to that, the majority of people are concerned about the environment and the future of energy, making it imperative that attention be paid to these problems.[34,35] In the present circumstance, the most important thing that needs to be done is to identify the primary barrier to overcoming energy crises and the procedures that need to be taken for the hydrogen operation.It is necessary that all of the non-economic challenges be overcome, and the appropriate exploitation of hydrogen must be integrated in general decarbonisation strategy in order to draw notice from research engineering, reserves, and society. Hydrogen was formerly thought of as a potential energy carrier two centuries ago; however, the energy crisis of the 1970s motivated researchers to make technical advancements so that other energy sources might be

examined. This was done in an effort to prevent future energy crises. It is predicted that existing stocks of fossil fuel have a lifespan of up to forty years at most, particularly for petroleum, which is primarily used as a source of the energy supplier for industry and transportation.The economy based on hydrogen in the modern world is so intriguing that several organisations and nations are moving in the direction of an approach based on hydrogen energy and investing significantly to set up a common hydrogen energy infrastructure that conforms to international standards. It is anticipated that hydrogen will be able to fulfil around 18% of the demands for energy and will be able to cut approximately 6 Gt of greenhouse emissions, particularly CO2, on a yearly basis. In addition to that, the development of infrastructures for hydrogen might result in the creation of around 3 million new employments by the year 2050. It is projected that hydrogen could power around 400 million automobiles, which is a very big quantity and has the potential to make a significant contribution toward reducing emissions of greenhouse gases. An estimate of 15 to 20 million trucks that are now being utilised in transportation and around 5 million buses from private to government organisations in 2050 might operate on hydrogen economy, which looks to be approximately 20% to 25% of the transportation sector overall.[36-38]According to the current scenario, the production of hydrogen on a worldwide scale reaches around 45–65 metric tonnes per year as feedstock in a variety of sectors, which is comparable to 5.4–7.8 EJ. This quantity represents less than one percent of the total energy consumption in the planet at this moment in time. Internationally, exponential increase in hydrogen-based manufacturing and rise in hydrogen stations functioning worldwide as of 2018 will be a favourable move toward carbon-free energy sources. In many places, even hydrogen automobiles are commercially accessible, and it was projected that till date 225000 fuel cell heating systems for household usage have been utilised. This shift is a representation of a step that was taken just five years ago, and it is a positive feedback towards the hydrogen economy. The generation of hydrogen as well as its distribution are important causes for concern, and in order to effectively build a huge hydrogen economy on a global scale, a major increase is required. Therefore, in order to resolve the technological challenges and make changes in industries while increasing the interdisciplinary market, a variety of initiatives and organisations have been established all over the world.[39-41]The European

Commission High-Level group tasked with advancing and exploring hydrogen and fuel cell technology has already set a goal of 35% for zero-carbon hydrogen-based vehicle by 2040 and a huge hydrogen economy by 2050. European H_2 Mobility initiatives have already begun producing hydrogen and building filling stations in convenient areas. They proposed establishing a network of 65 refuelling stations by 2020 as part of the United Kingdom's hydrogen fuel cell initiative; this would kick off a market that is predicted to expand to include 1,150 stations by 2030, enough to nearly cover the whole country.[42]On the other hand, the U.S. Department of Energy set a goal for the year 2020 for how many conventional energy-based offices should switch to hydrogen-powered fuel cell technology. California could be considered the world leader in developing hydrogen infrastructure. It has 39 open retail stations and about 6,000 fuel cell cars on the road.[43,44]Japan is a major example for the rest of the world, and it has cut off its supply from a foreign country in a strong way. In 2014, compared to other countries, it was about 6% self-sufficient. They have made a policy to cut greenhouse gas emissions by 25.4% by 2030, compared to 2005 levels. In this situation, "Japan Hydrogen Mobility" has set a goal to build at least 80 stations by 2021, working with car companies and dealers to make this happen. As of 2018, there are probably already about 330 hydrogen filling stations around the world, with about half of them in Japan and the United States.[45,46]In Germany, the "National Organization of Hydrogen and Fuel Cell Technology" (NOW) has been trying to set up a 50-station programme for hydrogen energy. They have also started a lot of other strategic plans for the hydrogen economy. The main goal of these plans is to make hydrogen a decent choice to conventional energy sources.There were other nations, both established and developing, that have taken the initiative to switch their industries to a hybrid fuel system based on the hydrogen economy. It is predicted that in the not-too-distant future, hydrogen energy systems would be very effective, offering not only financial but also environmental benefits. It is not simple to tackle all challenges associated to the hydrogen economy since the appropriate administration and transport infrastructure of hydrogen-based companies is still in the process of development.To produce hydrogen, most rely on traditional methods, with fossil fuels being the primary contributor. About 48% of the world's hydrogen production comes from steam reforming of natural gases, while the other 30%

comes from the partial oxidation of crude oil. Together, these two processes account for the production of millions of metric tonnes of hydrogen annually. The coal gasification/pyrolysis and water electrolysis have 18% and 4% respectively. All of these methods have their own benefits but when comes to the clean and carbon-neutral process, water splitting recognised as one of the greatest approach for hydrogen creation.

1.3.Water splitting and electrocatalysis

1.3.1. Historical background

Electric discharge has been used for a long time in the process of water splitting, which has resulted in the formation of various gases. Jan Rudolph Deiman and Adriaan Paets van Troostwijk were the first people to record an electric discharge that occurred between two gold electrodes in an electrostatic machine in the year 1789 in Haarlem, The Netherlands. The experiment was conducted by Jan Rudolph Deiman. They did this by discharging the electric potential that was created between the two gold electrodes by using the Leyden jar, which was filled with water. It was discovered that a distinct form of gas was produced at each electrode, despite the fact that the gold electrode had the opposite charge. In later years, it was determined that the gas that had developed included hydrogen and oxygen, and a gradually future application was identified. Later, in the year 1800, Alessandro Volta invented the voltaic column, and William Nicholson and Anthony Carlisle were the ones who utilised it to electrolyze water.[47,48]Nearly two centuries have passed since the concept of water splitting being explored as a viable solution to concerns with energy. Because of the consistent work and improvement that was put into water electrolysis up until the year 1869, it has become an efficient and cost-effective method for the creation of hydrogen in the scientific community. At the same time, Zénobe Gramme in 1869 created the Gramme machine for hydrogen synthesis. Later, Dmitry Lachinov in 1888 discovered a system for industrial-scale hydrogen and oxygen generation. Large numbers of electrolyzed and power plants with around 100 megawatts of capacity were developed up to 1930. These plants not only generate hydrogen, but they also become a source of energy that is completely free of carbon emissions.[49-50]However, because hydrocarbons and other forms of energy, such as hydroelectricity, are so readily available and cheap to get, this method is rendered

obsolete, at least to some degree, by the ammonia fertiliser business. In the 1970s, when the world was facing an energy crisis, water electrolysis regained its prominence and established special attention as a potential solution to both the energy crisis and concerns with sustainable supplies. It becomes the easiest hydrogen generating process which seemsto give sustainable energy by decomposing water into hydrogen and oxygen.

1.3.2. Thermodynamics of water splitting

Molecule of hydrogen and oxygen combine to form the fundamental building blocks ofwater molecules. In any scenario, the dissociation of water into its component parts results in the production of hydrogen and oxygen. Due to their high gravimetric energy density at ambient temperature, hydrogen and oxygen can be combined using the right equipment to produce a tonne of usable energy and, as a bonus, some water. An explosion is a distinct possibility whenever there is a significant amount of energy involved, as in the scenario described above. But the reply is not artlessly realistic and hence does not lead to such adversity. If we turn this idea on its head and consider how it could be used to generate hydrogen and oxygen from water using an additional supply of energy, we might be able to alleviate our current energy crisis to a significant degree. The simulations of splitting water into hydrogen and oxygen at each of an electrolyser's multiple electrodes are primarily concerned with the water-splitting process.[51,52] In a device known as an electrolyser, an electrical charge transfer reaction leads to electrocatalytic water splitting. As a result, at the electrode-electrolyte contact, the electric supply initiates the water decomposition, which then transforms into chemical energy. Energy input for theelectrolysis of water may come from thermal, electrical, or solar sources. These catalytic processes are referred to as photocatalytic water splitting, electrocatalytic water splitting, or photoelectrochemical water splitting etc.[53-55] Because distilled water does not have a very high conductivity, a trace amount of electrolytes like salt or acid has been added to the water. These electrolytes are responsible for the increased conductivity of the water. The salt conducts electricity via electrically dissociated charged particles, and when extra electrical energy is supplied via metal or any other conductive material employed as electrodes, the charged particles begin to

collect on the electrode that has the opposite polarity.[56-57]The total reaction that occurs during the process of water splitting can be summarised as follows:

Overall water splitting $2H_2O \rightarrow 2H_2 + O_2$ (1.1)

At Cathode (HER) $2H_2O + 2e^- \rightarrow 2OH^- + H_2$ (1.2)

At Anode (OER) $2OH^- \rightarrow H_2O + {}^1/_2\, O_2 + 2e^-$ (1.3)

Open circuit voltage, also known as equilibrium potential, exists between two electrodes since current can flow in any direction and there is no external supply between them.[58,59]

Overall electrode potential $E^\circ = E_a^\circ - E_c^\circ$ (1.4)

Where E_a° and E_c° represent the electrode potentials of the anode and cathode of a half cell. Applying the following equation, we can determine how much energy is needed to produce a certain voltage in a typical cell.

Gibbs free energy $\Delta G^\circ = nFE^\circ$ (1.5)

The Gibbs free energy for splitting water is $\Delta G° = 237$ kJ mol^{-1}, while the total enthalpy is $\Delta H° = 286$ kJ mol^{-1}. In this equation, n represents the number of electrons, F the Faraday constant and E° the voltage at the standard cell.According to equation (1.5), which takes into account both the Gibbs free energy and the enthalpy, the reversible voltage, which is the total voltage that is needed in this reaction for overall water splitting, is 1.23 eV. Without taking into account the reaction enthalpy, it is not realistically possible to estimate the entire amount of energy that is required for this operation. The efficiency of the water splitting process is defined by this term, and it cannot be determined without it. Including the enthalpy term $\Delta H°$ in the equation allows for the calculation of the actual energy (1.5). The thermo neutral voltage, which has a value of 1.48 eV, was used as the basis for the overall voltage that was implemented.

When the process is evaluated between 1.22 and 1.48 eV, it is practically anticipated that the maximum amount of water that may be divided with the least amount of energy has occurred. The low and high scorching values for water splitting correspond to these theoretical and practically applied energies or voltages.[60-61]The terms "hydrogen evolution reaction" and "oxygen evolution reaction" are used to refer to the two reactions that occur in a half cell and are shown in equations (1.2) and (1.3), respectively. In most cases, these half-cell reactions involve oxidation and reduction, and they can be streamlined into a single term of equilibrium potential, as shown in the following example:

$$E_{eq} = E^{\circ} + {RT}/{nF}\, ln\, {a_0}/{a_r} \qquad (1.6)$$

at a standard condition of 25 degrees Celsius and one atmosphere pressure, where E_{eq} is the equilibrium potential, E° is the standard electrode potential, and ${a_0}/{a_r}$is the activity ratio that corresponds to the species in the chemical reaction; R and T are the gas constant and absolutetemperature; n and F have the meanings that are typically assigned to them. When the Nernst equation is applied to the reduction half-reaction, the result is equation 1.7, and when it is applied in the same way to the oxidation half-reaction, the result is equation 1.8. In light of this, the electrode potential for the half-cell reaction in relation to the standard hydrogen electrode can be computed as follows:

HER $$E_{eq} = -0.591 * pH \qquad (1.7)$$

OER $$E_{eq} = -0.591 * pH + 1.23 \qquad (1.8)$$

If the calculation is done based on hydronium ions in a reversible hydrogen electrode, then the same scale can be made independent of pH. This can be seen by looking at equations (1.7) and (1.8), which show that the overall equilibrium potential for HER and OER varies with the pH of the solution. Additionally, this can be seen by looking at equation (1.7). Such supporting ions change the activity to some degree, but the

thermodynamics of water splitting practically remains the same. The potential value for HER and OER will be 0 and 1.23 V with respect to a reversible hydrogen electrode at any pH scale. The previous discussion makes it abundantly clear that the total potential that is necessary to split the water is 1.23 volts, also referred to as the reversible electrode potential, and that the Gibbs free energy change and the enthalpy for the reaction require the energy equivalent to 237 kilojoules per mole and 286 kilojoules per mole, respectively.[62,63]Because it is not possible to obtain this value of free energy at ambient temperature, the water-splitting reaction is thermodynamically impossible and can only take place if an adequate amount of energy is supplied.Overpotential refers to the additional energy used to break through the activation barrier and initiate the usually slow electrochemical reaction. Higher potential is needed because of charge migration, bubble formation, and potential drop caused by voltage supply. Although we can't disregard the impact of such a barrier, we can reduce the overall kinetic barriers by facilitating the transition to a less energetically demanding intermediate state for the reaction. By contributing necessary intermediates, these redox-active species boost the process's overall effectiveness. This could only have occurred if the electrode material favours one side of the process over the other, hence increasing reaction kinetics while reducing energy costs. This reaction intermediate platform facilitates the rapid and low-voltage exchange of electrical and chemical potential energy.

1.3.3. Electrocatalyst

Since the dawn of civilization, when early humans first began making alcohol through fermentation, the value of catalysis has been widely recognised. This period of catalysis consisted only of personal interpretations that were sporadically acknowledged without any effort being made to shed light on the happenings that took place during this time. J. J. Berzelius, a Swedish chemist working at the Stockholm Academy in 1835, was the first person to detect an increase in reaction kinetics brought about by the involvement of a specific material.

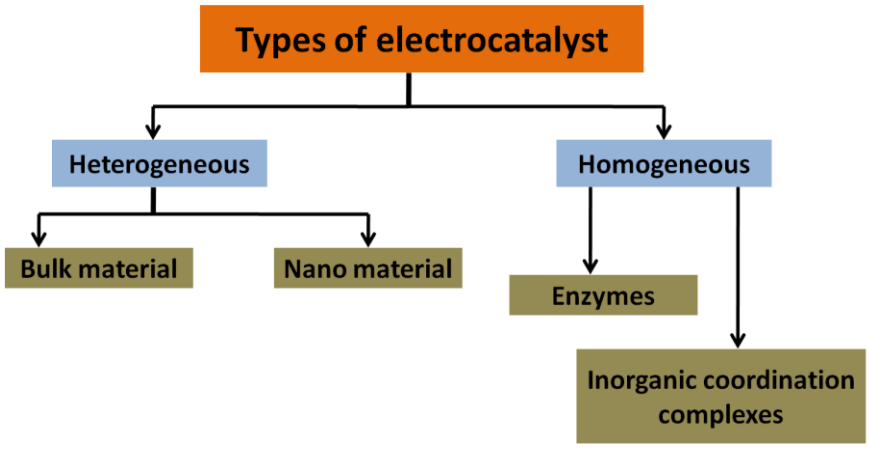

Figure.1.2. types of electrocatalyst as homogeneous and heterogeneous catalyst

He explains and makes statements about the forces that are responsible for this augmentation, naming those forces catalytic forces and coining the term "catalysis" to describe such materials. This is likely the earliest example of catalysis being recognised as a naturally occurring process that is widespread. Wilhelm Ostwald would later write that "it is probably not possible to conceive of a chemical reaction that cannot be altered by a catalyst." He detailed the working principle and described how the presence of the catalyst speeds up the reaction kinetics without disrupting the thermodynamic equilibrium of the chemical process.[64,65]At this point, it became evident that using a catalyst in a chemical process can result in industrial or financial gains, in addition to resolving time-consuming perspectives. As a result, the activation energy for the reaction can be lowered, making the process simpler. Recent years have seen a rise in the strategic importance and widespread application of studies involving this category of materials' perception. Carbon-neutral processes for transporting and storing energy have gained popularity due to rising concerns about climate change and environmental degradation. To efficiently drive a reaction toward a desired product while suppressing undesired by-products, a catalyst needs to be both active toward the reactant species and selective for one of the products. The selectivity and stability of a catalyst are of primary importance since its performance is sensitive to changes in pH, temperature, and an extremely oxidising or reducing environment. Important in the realm of electrocatalysis, these

catalysts are classified as either homogeneous or heterogeneous.[66-68]The homogeneous catalyst primarily exists as the same phase as the reactant in the chemical reaction, which makes the process of separating each substance difficult. The heterogeneous catalyst, on the other hand, despite being in a different phase than the reactant, is exceptional in its suitability for the catalytic action.[69]In electrochemical reactions, the catalytic activity of the material at the electrode surface is the focus of the electrocatalyst as well as the process known as electrocatalysis. In 1928, Bowden and Rideal were the first pioneers to give the concept of electrolysis and study the electrode reaction. They did this work. But if you ask scientists like Bockris and Khan, they will tell you that T. Grubb coined the word electrocatalysis in 1936 while he was working on fuel cells. This information comes from their research. The process that relies on the movement of electrons for oxidation or reduction at the surface of the substance that makes up the electrode or at the electrode itself. It alters the reaction kinetics and lowers the activation energy by providing an intermediate state in the reaction process. The electrocatalysis procedure studies the material properties of a solution and finds a relationship with reaction kinetics. The material utilised in the chemical process as an electrocatalyst must have a different activation energy than the other components of the reaction, which in turn must have different bonding between the reactant, product, and intermediates.[70]Due to altered thermodynamics caused by the electrode material, the surface catalytic reaction takes place along multiple reaction paths. As a result, any alteration of the material or a material property alters the kinetic process. This describes a material's potential to improve an electrochemical reaction while the conditions are the same.The kinetics varies depending upon the resilience of chemical bonds among electrode and electrolyteAn electrolyzer's efficiency could be multiplied by a good choice of electrode material. The hunt for such materials to increase electrode stability and the effort to lower investment and operating costs are ongoing.A compromise between various considerations of the material was required to determine the catalyst's practical usefulness. The relative strength of the catalyst in aspects of catalytic performance, better durability and the primary issue of its production cost are always the determining factors. By streamlining the synthesis process or creating a composite material with built-in synergy, the material's activity may be increased. So, replacing the noble material with a non-noble one could

also help you reach your goal. Non-noble materials are less likely to be used in electrocatalytic processes. One of the processes solely dependent on the characteristics of the electrodes is water splitting.

1.4. Hydrogen Evolution reaction (HER)

One of the best-known and extensively studied reactions in the domain of electrochemistry is the hydrogen evolution reaction (HER) on various metals in acidic or alkaline conditions. It is believed that hydrogen (H_2), which has the largest gravimetric energy density across all chemical fuels (142 MJ kg^{-1}) is the quintessential clean energy carrier, which might substantially ameliorate the environmental issues due to the fact that it would not emit any carbonaceous species.[71,72] The splitting of water into hydrogen and oxygen by photoelectrocatalysis and electrocatalysis are both potential pathways to the realisation of solar-to-hydrogen transformation. To produce the same quantity of gas per unit of time as electrochemical water splitting systems, photo-electrochemical water splitting devices require a significantly bigger electrode surface. This limits the selection of feasible catalysts and viable construction locations.[73,74] In addition, photoelectrochemical pathways logically preclude alternative renewable energy. Therefore, electrochemical water splitting is more appealing due to its greater flexibility and application despite having poorer solar-to-hydrogen efficiency than the direct photoelectrochemical technique. Integrating grid-scale renewable energy collecting networks with electrochemical water splitting technologies can effectively transform the irregular power generated from renewable energies into more valued H_2 and so improve the variety of renewable energy consumption. In addition, electrochemical water splitting generates H_2 of such high purity that it may be utilised both as an industrial supply and as a fuel gas in homes. Hydrogen is also a possible contender for electric car power systems since it is the ideal fuel for proton-exchange membrane fuel cells, a highly efficient energy conversion technology. In order to build a future energy infrastructure that is both clean and sustainable, it is essential to improve water electrolysis devices that can produce non-polluting H_2.[75,76]

1.4.1. Mechanism for the electrochemical hydrogen evolution reaction

Redox interactions between the electrode and electrolyte are at the core of the electrochemical process that constitutes electrocatalytic HER. H_2 can be produced by the reduction of either proton (H^+) or H_2O, which together entail a sequence of simple steps depending on the pH levels of the electrolyte.

1.4.2. HER in acidic media

It is popularly referred that two separate stages take place in acidic media during the HER at the surface of different catalysts. For HER to get started, an H^+ must first adsorb on the catalyst surface, where it will become an adsorbed hydrogen atom (H*), with * standing for an active site. A Volmer step, sometimes known as a discharge step, describes this procedure (Equation 1.9). The next process, called the Heyrovsky step or the electrochemical desorption step, involves a H* combining with an H^+ and an electron (e^-) to generate an H_2 molecule (Equation 2.0). The Tafel step, sometimes called the chemical desorption step, involves the conjunction of two H* on the catalyst surface (Equation 2.1), resulting in the formation of H_2. HER's total reaction may be described by (Equation 2.2), where E° is the standard electrode potential used to compare the potentials of different electrochemical processes.[77-80]

$$H^+ + e^- \rightarrow H^* \qquad (1.9)$$

$$H^* + H^+ + e^- \rightarrow H_2 \qquad (2.0)$$

$$2H^* \rightarrow H_2 \qquad (2.1)$$

$$2H^+ + 2e^- \rightarrow H_2 \qquad (2.2)$$

1.4.3. HER in alkaline media

Considering the HER in alkaline environments, the notation $\Delta G_H°$ may still be used to describe the adsorption behaviour of hydrogen on the surface of catalysts. It is noteworthy to observe that the volcano plot in alkaline medium only shifts up and down, rather than left and right, as it does in acidic solution. This is in contrast to how it shifts left and right in acidic solution. To be more exact, the exchange current densities of HER

on many metal catalysts in alkaline solutions are between two and three orders of magnitude lower than they are in acidic electrolytes. The fact that the alkaline HER follows a different route than the one that is used in acidic solutions is one of the primary explanations for the lower level of catalytic activity observed in alkaline solutions. As a result of the absence of H^+, the HER in alkaline media begins with the dissociation of H_2O molecules in order to provide protons. This process occurs in both the Volmer step (Equation (2.3)) and the Heyrovsky step (Equation (2.4)) of the alkaline HER, whereas the Tafel step continues to be the same as it is in acid solutions. The complete mechanism of the reaction is shown in Equation (2.5), and the E_o of this reaction when measured in relation to the standard hydrogen electrode (SHE) is -0.826

$$H_2O + e^- \rightarrow H^* + OH^- \quad (2.3)$$

$$H^* + H_2O + e^- \rightarrow OH^- + H_2 \quad (2.4)$$

$$2H_2O + 2e^- \rightarrow 2OH^- + H_2 \quad (2.5)$$

Because alkaline environments demand greater energy to produce protons, the HER kinetics of most catalysts are slower when operating in alkaline electrolytes. This is because alkaline environments are more basic. It has been observed that the activity of alkaline HER is managed by maintaining a careful equilibrium between $\Delta G_H°$ and the amount of energy needed to dissociate H_2O. However, the use of a number of HER catalysts, such as MoS_2 and Co_2P, is not recommended for the water dissociation process. As a result, one effective tactic for the development of efficient catalysts for alkaline HER is to encourage the process of water dissociation while maintaining a reasonable hydrogen adsorption energy.[81-84]

1.5. Oxygen evolution reaction (OER)

To improve the economic viability of various processes, such as biomass upgrading, electrochemical water splitting, carbon dioxide reuse, ammonia synthesisand others, significant amounts of effort have been devoted by both industry and academia to the development of energy storage technologies. These technologies are related to improving the efficiency of the processes in conundrum or producing value-added products.These

devices often rely on the oxygen evolution reaction for their anodes (OER).[85,86]In the OER, molecular oxygen is generated by the utilisation of a number of proton–electron–coupled processes. The reaction is very sensitive to changes in pH[87]To generate the potential difference of 1.23 V versus the normal hydrogen electrode (NHE) and hence drive the oxygen evolution reaction (OER) when pH is equal to zero, an additional current is needed.[88]According to the Nernst equation, this results in a change in the reaction potential, which is denoted by a value of 59 mV for each unit of pH. However, in order to prevent the pH from having an effect on the potential that is being applied and to maintain a working voltage of around 1.23 volts for OER, reversible hydrogen electrodes, also known as RHEs, are typically utilised as reference electrodes.The transfer of four electrons is necessary for the creation of one oxygen molecule, and the kinetically favourable OER process takes place as a series of multi-step reactions, with every step including the exchange of a single electron. Therefore, the accumulation of energy at each stage makes the kinetics of OER exceedingly slow, which results in a significant overpotential. Because of this, it is extremely desired to have an electrocatalyst that has a significant activity in order to go through the energy barrier. In an ideal world, the OER catalyst would have a low overpotential and good stability, in addition to having a significant earth-abundance and being readily available at a reasonable cost for its adaptability at industrial level.[89-92]However, the pricing and unavailability of noble metal-based materials are the key hurdles in practical uses. This is because noble metal-based materials are put at the top of the list when it comes to their durability in all pH levels, despite having fair activity toward OER. The quest for alternate sources that offer higher OER activity has received a significant amount of research and development work. Currently large amount of electrocatalyst have already been constructed, including noble-metal based, carbon-based , alloys, oxides and oxyhydroxide of copious metals (e.g. Mn, Co, Ni, and Fe, etc.)[93-100]

1.5.1. Mechanism for oxygen evolution reaction

Oxygen evolution reaction is the half cell reaction of overall water splitting. It has been observed that the reactions that take place at the cathode and anode sections of the water-splitting reaction are distinct depending on whether the circumstances are acidic or

alkaline. There have been several research groups that have suggested possible mechanisms for the oxygen evolution reaction that takes place at the anode electrode either for acidic or alkaline circumstances. These hypothesised mechanisms have both some differences and some commonalities with one another. The majority of the hypothesised pathways use the similar intermediates, such as MOH and MO, whereas the primary distinction likely centres on the reaction that produces oxygen. It should be emphasised that the formation of oxygen from a MO intermediate might occur via two distinct processes. The first one is the environmentally friendly approach, which is shown in through the direct combination of 2MO to produce O_2, while the second one is the one that includes the production of the MOOH intermediate, which then decomposes to produce O_2.[101-104]The proposed mechanism for acidic and alkaline condition is discussed below

In acidic condition:

$$M + H_2O + e^- \rightarrow MOH + H^+ + e^- \quad (2.6)$$

$$MOH + OH^- \rightarrow MO + H_2O + e^- \quad (2.7)$$

$$2MO \rightarrow 2M + O_2 \quad (2.8)$$

$$MO + H_2O \rightarrow MOOH + H^+ + e^- \quad (2.9)$$

$$MOOH + H_2O \rightarrow M + O_2 + H^+ + e^- \quad (3.0)$$

In basic condition:

$$M + OH^- \rightarrow MOH \quad (3.1)$$

$$MOH + OH^- \rightarrow MO + H_2O \quad (3.2)$$

$$2MO \rightarrow 2M + O_2 \quad (3.3)$$

$$MO + OH^- \rightarrow MOOH + e^- \quad (3.4)$$

$$MOOH + OH^- \rightarrow M + O_2 + H_2O \quad (3.5)$$

1.6. Factors impacting the dynamics of the HER & OER

In an electrochemical process, the materials that make up the electrodes are, by a substantial margin, the most crucial components. The catalytic activity changes along with the size, stoichiometry, and structural characteristics of the nanoparticles, all of which can be customised via nanostructuring, doping, interfacial structuring, and amplifying the synergy among both phases by in-situ grown nanoparticles. The catalytic activity changes along with these features. Therefore, rational design and the delicate manipulation of interfacial structure can improve the active sites by exposing the active sites on supports and increasing inherent activity via regulation of electronic structure. Because the electrocatalytic reaction takes place at the surface of the catalyst, the active site is the most important feature that decides the catalytic activity of the material.[105,106]. The catalytic characteristics of the material can be significantly improved by adjusting the geometry of the catalyst in order to improve it and reveal its active regions. In addition to this, the catalyst support contributes to the material's increased stability in its electrocatalytic state. The increment in the active site of the material, the provision of synergistic effects to the material, the tailoring of the structural and electronic arrangements, and the assistance of electron transport through a conducting material are the factors that are generally agreed upon to be responsible for an increase in the catalytic activity of the material. The many aspects that enhance and modify these factors can result from construction of designed surface and junction generated interfaces while the improvement in reaction-diffusion can be established by a porous network. The following is a brief discretionary summary of the aspects that we investigate and analyse in the work that we do for our thesis that are involved in the process of increasing the catalytic activity.

(i) Nanostructuring

In the past few decades, the electrocatalysis process has undergone amazing advancements, in part due to improvements in catalyst construction at the nanoscale. These developments have been significant in bringing prominence to alternative energy technologies that are reliant on electrochemical reactions and updating such technologies.

The interatomic spacing, crystalline structure, and crystallite size all play a role in determining the material's catalytic performance, and any change in any of these factors can result in a different kind of activity. The catalyst design is manipulated and optimised by the process of nanostructuring, and the coordination and binding connection at the surface of the material is also modified as a result.It's believed that the size of the nanoparticles is the most important factor in controlling the number of low-coordinated sites on the surface of the catalyst, which in turn alters and influences the reactant binding capacity. The active site and surface configuration have been modified in such a way that a high surface-to-volume ratio may be achieved.[107,108] This has resulted in a higher density of surface active sites. The interfacial atoms that are found on the surface of nanostructured materials result in a large volume fraction of atoms, which provides an amazing potential for plotting the exterior chemistry and the defects concentration. It is possible to investigate the possibility of perfecting the ability to regulate and manufacture such nanostructured material with a certain shape, size, and morphology in order to account for the material's high activity. In terms of their selectivity, such catalysts are able to satisfy the parameters set as special needs. Alterations to the crystallite size as well as the crystallite phase can be used to manipulate the surface property. The selectivity towards a certain plane and structure may also be a factor in boosting electrocatalytic activity. The chemistry that exists between surface and the nanostructuring has resulted in a number of fascinating new advances and has the potential to completely transform the chemical manufacturing industry. Nevertheless, the catalyst selectivity and the related performance of materials call for numerous upgrades, a comprehension of structure attributes, and well-defined size, shape, and composition of the materials.[109,111]

(ii) Heteroatom doping

The catalytic activity of the host material can be further enhanced through the use of heteroatom doping. The introduction of new elements changes the host material's optical, catalytic and electrical characteristics due to the redistribution of charges. These alterations to the material improve active sites and reduce the amount of energy expended

during intermediate production. The synergetic connection of the host and doped metals substantially promotes the catalytic characteristics of the material. Some examples of heteroatom with a distinct electronegativity than the host materials in heterostructure are B,C,N,P and S. Many people attempt to dope two or more heteroatoms during the investigation process of doping heteroatoms. Non-metal doping, in addition to metal doping, is used to increase the catalytic activity of nanomaterials.In comparison to pure MoS_2, Li et al. developed catalysts doped with N in MoS_2, with just an overpotential as minimal as 168 mV. The rise in HER activity is caused by the charge density of the S atom reaching its maximum following N doping.[111]

(iii) By forming heterostructure

Heterostructure is a term borrowed from the study of semiconductors. Heterostructures are structures formed of semiconductors in which the composition varies depending on how you are forming the structure. As per the definition, heterostructures are made up of an abundance of heterojunctions, which are the interfaces in between various components. The idea of heterostructure has expanded outside the realm of semiconductor physics as a result of the crossing over and merging of different knowledge networks. In a broader sense, heterostructures can be seen as composite structures that are made up of interfaces produced by various solid-state materials, such as conductors, insulators, and semiconductors, amongst others. This definition applies to heterostructures in their whole.Therefore, a heterostructured catalyst is made up of two or more distinct kinds of materials that are frequently bound together by either physical or chemical means. It is possible for the components that make up a heterostructure to either be active or nonactive, depending on how they contribute to the OER and HER catalytic performance of the catalysts. In spite of this, the majority of heterostructured catalysts, which include both active/active and active/nonactive types of heterostructures, show, increased electrocatalytic performance than their single counterparts. This is because heterostructured catalysts have a number of benefits that their single counterparts do not.To begin, the production of heterostructured OER and HER catalysts is a productive method that is capable of boosting the total number of active sites. The vast majority of

these heterostructured electrocatalysts have precise nanostructures that have extensively exposed edges. These edges provide adequate active sites for the adsorption of intermediates responsible for OER & HER[112-115]. Second, including substantial substrates like carbon cloth (CC) and nickel foam (NF), into nanostructured materials can permit fast mass diffusion, which is crucial to lowering overpotential and boosting the number of active sites[116-118]. Third, the activity and stability of the catalysts can be increased by developing certain uniform nanostructures in order to enhance the efficiency of the catalysts. Using a core–shell structure as an illustration, the species that are productivebut vulnerable can be preserved by a thin layer of species that are stable, which permits HER activity to last over a long period of time. Fourth, the disparity in the electronegativity of the various components that make up the heterostructured catalysts may drive electron transfer across the various components. This is something that is typically seen by a shift in the binding energy in the XPS spectra.[119-122]Some heterostructures' enhanced HER activity is a direct result of the way their electrons are redistributed, which controls the electronic structures or band structures of the components. The so-called synergistic effect also makes a sizeable contribution to the improved HER kinetics of the heterostructures.For alkaline OER &HER, transition metal hydroxides and oxides have been the most thoroughly investigated as water adsorption/dissociation promoters via heterostructured catalyst design.

1.7.Metal organic framework (MOF) and MOF derived materials for HER & OER

Metal-organic frameworks stand out as one of the most potentially useful precursors for the electrocatalysis process (MOFs). These materials take on fascinating morphologies such as core-cell and hollow architectures, all of which are advantageous for the carrier transport and mass transfer towards or away from the electrode.[123-126] For a variety of catalytic applications, including the hydrogen evolution reaction (HER), the transformation of carbon dioxide (CO_2), oxygen and nitrogen reduction reactions, MOFs that have been synthesized from metal cations and chemical molecules have been chosen. This is due to the fact that MOFs offer interesting properties, such as metal sites with available valency, significant surface area, high porosity, simple manipulation, and adjustable shape, all of which have the potential to have a positive impact on the catalytic

process.[127-130] The pore size of MOFs is determined by the length of the organic linker because MOFs are built from metal ions or clusters and organic linkers. Several investigations have been conducted on the subject of how changing the linkers affect the size of the pores. For example, Meng and his colleagues adjusted the pore size of Co-based MOF in the region of 22-26Å by introducing a benzene ring to the original ligands.[131]This caused the pore diameters to become larger. Thus, MOFs have been demonstrated as suitable materials for generating desirable architectures. MOFs can be generated by numerous ways such as microwaves, microwave, solvothermal, and electrochemical processes. The preparation method is dependent on the various applications that can be made with MOFs. For instance, the microwave method is favoured over other approaches because it can rapidly produce MOF crystals. Altering the frequency of the microwave equipment is all that is required for this operation, which allows for the morphological structure and size to be tailored to the user's specifications. The production of MOFs has seen significant success with the application of the solvothermal technique. However, because it takes a long time for the reaction to finish, it is only suitable for use in low-volume production, whereas the electrochemical process is well-suited for use in large-scale manufacturing. The utilisation of MOFs for the OER has been documented in a significant number of researches, with a variety of techniques being utilised for their synthesis. For OER applications, pristine MOFs may be utilised in their natural state without undergoing any modifications. The low conductivity of individual MOFs, on the other hand, makes it difficult to use these materials in electrochemical processes that produce oxygen.[132-135]As a result, numerous techniques have been published in order to transform MOFs into various alternative electrode materials for the OER. MOFs are capable of being pyrolyzed directly, which results in the production of metal and metal oxide catalysts. In addition, MOFs have the potential to be selenized or sulfurized, resulting in the formation of ultrastable catalysts for the OER in the form of metal selenides or metal sulphides. Additionally, ternary or binary metallic electrocatalysts that exhibit great performance for the OER can be produced by mixing various metal ions in the synthesis method to form MOFs.[136-138]

1.8.Transition metal sulfide for electrocatalysis

The configurations of the TMS can be divided into two different classes: the layeredMS_2 (M equals Mo and W) as well as the nonlayered M_xS_y (M equals transition metals). A typical layered MS_2 has the shape of a sandwich and is composed of three layers: first layer of metal, second and third layer of sulphur. The relatively mild pressures exerted by van der Waals allow each MS_2 unit cell to stack vertically, which makes it possible to exfoliate MS_2 into single layers. Depending on the configurations and bonding of MS_2, they can be broken down into a few different sorts of phases, which include 1T, 2H, and 3R phases. The H and T phases are the ones that appear the most frequently in MS_2, which has the transition metal atom centred in trigonal octahedral and prismatic an configurations. In addition, the production of 2H and 3R phases occurs as a consequence of the stacking of monolayer H phases in different orders.[139-142]The several phases of MS_2 each have their own unique electrical properties, as well as applications for those features.[143-144] In addition, the surface orientation of MS_2 molecules affects their electrochemical characteristics in a significant way. It has been observed that a single SMS trilayer can have two different kinds of surface sites: the basal plane and the edge. Both of these surface sites display anisotropic features. MS2's basal plane is inert compared to its active edge states. In addition, the electrical conductivity of MS_2 in the plane of the material is approximately 2200 times higher than the electrical conductivity of the interlayers. In 2005, Hinnemann and colleagues discovered that the (1010) Mo-edge structure of MoS_2 shares some similar properties with the nitrogenase, which is an enzyme that produces hydrogen.[145] According to calculations based on density functional theory (DFT), the edge of MoS_2 may serve as an active region for the hydrogen evolution reaction (HER).

1.9.Transition metal oxides for HER & OER

The heterojunctions construction is the primary method by which interface engineering is carried out. The production of heterostructures by merging different materials, such as metal–oxide, has been the subject of a significant amount of research. Through such technique, the intrinsic catalytic capabilities of individual parts can dramatically modified, which brings electrocatalysts with distinct physicochemical features toward HER & OER. As a result of a mismatch in the lattice at the interface within the various

components, the heterostructures entail disorder, defects, and many phases. These characteristics offer abundant sites that are catalytically highly active. More interfaces contribute to the construction of more tunnels for the carrier transfer, and create good connection between the catalyst and electrolyte. Additionally, the contact surfaces between the various part offer improved electronic conductivity as well as increased mechanical stability.[146-148]The adsorption energies of intermediates may be further adjusted by adjusting the electron density at the interface. This will allow for additional improvements. Depending on the benefits, the transition metal based heterostructures offer great potential for allowing superior electrocatalytic activity and importantscientific advancs in energy conversion devices. Even though progress has been achieved in the innovation of heterostructures, the interface engineering of transition metal-based oxides for oxygen electrocatalysis has yet to be appropriately summarised. This is despite the fact that there has been significant progress made in this area.[149,150] When it comes to defining the activity and durability of catalysts, the interfaces that exist between the various active components are of critical relevance. This results in the production of adequate accessible catalytic centres and improved contact in between electrocatalyst and electrolyte. The primary purpose of interface engineering is to maximise a material's activity by controlling the electronic structure of the material. This can be accomplished by regulating the material's electronic structure. For instance, Co_3O_4 is a promising OER electrocatalyst; however, it has weak conductivity and a narrow size distribution, which severely restricts the applications for which it may be used.[151,152] The enhancement of OER performance is significantly impacted by the roles that rational morphological regulation and electronic control play. Nanowire made of Co_3O_4/$Fe_{0.33}Co_{0.66}$ P was used in OER applications.[153] Such heterostructure with wire architecture shows better OER performance with overpotential of 291 mV at 800 mA cm^{-2}, which is relatively lesser than that of RuO_2 which is 446 mV. Calculations based on DFT were carried out so that the subtleties of the mechanism could be understood. According to the findings of the study, the active Co and O locations in the contact region not only reduce the overall electrochemical catalytic constraint for every phase of the OER, but they also provide an electron–hole-rich area that contributes to the high OER current density. This is because the high e_g filling of the Ni^{2+} has a poor ability to bond with oxygen. A microwave-

assisted hydrothermal approach was used by Chen et al. to develop the $NiO/NiCo_2O_4$ heterostructure, which was then used to remedy the problem. Corresponding physical characterizations reveal the formation of numerous Ni^{3+} ions on the $NiO/NiCo_2O_4$ interface, which can serve as the very active sites for OER. According to the results of subsequent DFT simulations, the interfaces between NiO and $NiCo_2O_4$ have favourable conditions for the absorption of OH^-. As a consequence of this, $NiO/NiCo_2O_4$ has superior OER properties, as evidenced by overpotential of 264 mV at 10 mA cm^{-2} hence; it outperforms the RuO_2 catalyst (281 mV).[154]The above reports demonstrates that by the formation heterostructure between different metal oxides enhances the electrocatalytic performance for HER and OER.

1.10Transition metal nitrides for HER & OER

Recent studies have shown that transition metal nitrides have the potential to be extremely efficient OER catalysts. These catalysts also have a steady electrocatalytic activity over a longer period of time.When nitrogen atoms are added to transition metals, the result is an increase in the d-electron density. Additionally, the contraction of the d-band causes the electronic structure of TMNs to resemble, up to the Fermi level, that of noble metals such as platinum and palladium. TMNs, in addition to having a metallic conductivity, have a strong corrosion resistance, which bodes well for their use in electrocatalytic water splitting in both acidic and alkaline mediums.Numerous TMNs, such as binary nitrides and single-phase nitrides, have been explored as catalysts in both HER and OER, and they demonstrate good activity and durability in a broad pH range.[155-158]Single-phase transition metal nitrides (TMNs) such as molybdenum nitride (MoN), vanadium nitride (VN), tungsten nitride (WN), titanium nitride (TiN) and nickel nitride (Ni_3N) have been investigated in electrochemical water splitting and show potential catalytic performance.[159-162].

1.10. Aim and objectives

The end objective of this thesis is to produce a number of transition metal-based heterostructures that can be used in a variety of electrocatalytic applications.In this regard the present thesis is focused on the formation of transition metal based heterostructures of

metal phosphide, nitride, sulphide, oxide, single-atom catalyst (SACs), Metal-organic organic framework (MOF) and MOF-derived materials for hydrogen evolution reaction (HER), oxygen evolution reaction (OER) and oxygen reduction reaction (ORR). The first heterostructure we worked on is Co@NC@MoS_2 for oxygen evolution reaction (OER) in which the synergistic effect between Co@NC nanoparticles and MoS_2 nanosheets enhances the catalytic activity. The catalyst exhibit the overpotential of 297 mV at 10 mA cm^{-2} of current density. Moving forward we worked on transition metal oxide heterostructures and we developed CuO-NiO, Co_3O_4-NiO heterostructure for OER with overpotential of 231 mV and 311 mV and $NiWO_4$-NiO heterostructure for HER with overpotential of 71 mV. Further, taking the advantage of high electronegativity of metal fluorides we fabricated the metal fluoride and metal nitride heterostructure (Co-Ni_3N/CeF_3). This heterostructure exhibit the overpotential of 180 mV at 10 mA cm^{-2} of current density. This ultralow overpotential was obtained due to the interfacial charge transfer from Co-Ni_3N to CeF_3 results in the augmentation of valence state of Ni and Co which enhances the adsorption of intermediates on the catalyst surface. Further we move on to explore the pristine MOF for oxygen evolution reaction. the bimetallic Co, Ni based ultrathin metal-organic framework nanoribbons (NiCo-NR) for oxygen evolution reaction. The slender NiCo-NR was formed by using ultrathin metal hydroxide ($NiCo(OH)_2$) mediated strategy. The NiCo-NR shows overpotential of 244 mV at a current density of 10 mA cm^{-2} current density. We suggest that in the ultrathin MOF nanoribbons surface atoms (Co,Ni) are coordinatively unsaturated. Due to the ultrathin nanostructuring of MOF sheets the inter-atomic electron transfer within the MOF makes more active adsorption sites on the surface. Our findings show that coordinatively unsaturated metal atoms are the dominant active centers, and the electrocatalytic activity is tuned by the coupling effect between Ni and Co metals. Moving forward we formed the heterostructure of Ni_3N-$MnCo_2O_4$ and Co-Ni_3N/$MnCo_2O_4$ and we explained the effect of Jahn-Teller distortion in these heterostructures.

References

1. Billatos, S., Green technology and design for the environment. CRC Press: 1997.

2. Jaccard, M., Sustainable fossil fuels: the unusual suspect in the quest for clean and enduring energy. Cambridge University Press: 2006.
3. Sheng, P., He, Y. and Guo, X., 2017. The impact of urbanization on energy consumption and efficiency. *Energy & Environment*, *28*(7), pp.673-686.
4. Shafiee, S. and Topal, E., 2008. An econometrics view of worldwide fossil fuel consumption and the role of US. *Energy policy*, *36*(2), pp.775-786.
5. Barbir, F., Veziroğlu, T.N. and Plass Jr, H.J., 1990. Environmental damage due to fossil fuels use. *International journal of hydrogen energy*, *15*(10), pp.739-749.
6. Smith, K.R., Khalil, M.A.K., Rasmussen, R.A., Thorneloe, S.A., Manegdeg, F. and Apte, M., 1993. Greenhouse gases from biomass and fossil fuel stoves in developing countries: A Manila pilot study. *Chemosphere*, *26*(1-4), pp.479-505.
7. Rodhe, H., 1990. A comparison of the contribution of various gases to the greenhouse effect. *Science*, *248*(4960), pp.1217-1219.
8. Chen, Z.; Chen, G., An overview of energy consumption of the globalized world economy. Energy Policy 2011, 39 (10), 5920-5928
9. Moriarty, P.; Honnery, D., Global renewable energy resources and use in 2050. In Managing Global Warming, Elsevier: 2019; pp 221-235
10. Iddrisu, I. and Bhattacharyya, S.C., 2015. Sustainable Energy Development Index: A multi-dimensional indicator for measuring sustainable energy development. *Renewable and Sustainable Energy Reviews*, *50*, pp.513-530.
11. Arnette, A. and Zobel, C.W., 2012. An optimization model for regional renewable energy development. *Renewable and Sustainable Energy Reviews*, *16*(7), pp.4606-4615.
12. Chu, S. and Majumdar, A., 2012. Opportunities and challenges for a sustainable energy future. *nature*, *488*(7411), pp.294-303.
13. Chu, S., Cui, Y. and Liu, N., 2017. The path towards sustainable energy. *Nature materials*, *16*(1), pp.16-22.
14. Bazmi, A.A. and Zahedi, G., 2011. Sustainable energy systems: Role of optimization modeling techniques in power generation and supply—A review. *Renewable and sustainable energy reviews*, *15*(8), pp.3480-3500.
15. McKenna, R., Pfenninger, S., Heinrichs, H., Schmidt, J., Staffell, I., Bauer, C., Gruber, K., Hahmann, A.N., Jansen, M., Klingler, M. and Landwehr, N., 2022. High-resolution large-scale onshore wind energy assessments: A review of potential definitions, methodologies and future research needs. *Renewable Energy*, *182*, pp.659-684.

16. Mishra, S., Ghosh, S. and Singh, T., 2021. Progress in materials development for flexible perovskite solar cells and future prospects. *ChemSusChem*, *14*(2), pp.512-538.
17. Briones-Hidrovo, A., Copa, J., Tarelho, L.A., Gonçalves, C., da Costa, T.P. and Dias, A.C., 2021. Environmental and energy performance of residual forest biomass for electricity generation: Gasification vs. combustion. *Journal of Cleaner Production*, *289*, p.125680.
18. Micallef, D. and Rezaeiha, A., 2021. Floating offshore wind turbine aerodynamics: Trends and future challenges. *Renewable and Sustainable Energy Reviews*, *152*, p.111696.
19. Beswick, R.R., Oliveira, A.M. and Yan, Y., 2021. Does the green hydrogen economy have a water problem?. *ACS Energy Letters*, *6*(9), pp.3167-3169.
20. Cho, H.H., Strezov, V. and Evans, T.J., 2022. Environmental impact assessment of hydrogen production via steam methane reforming based on emissions data. *Energy Reports*, *8*, pp.13585-13595.
21. Soltani, S.M., Lahiri, A., Bahzad, H., Clough, P., Gorbounov, M. and Yan, Y., 2021. Sorption-enhanced steam methane reforming for combined CO2 capture and hydrogen production: A state-of-the-art review. *Carbon Capture Science & Technology*, *1*, p.100003.
22. Abdalla, A. M.; Hossain, S.; Nisfindy, O. B.; Azad, A. T.; Dawood, M.; Azad, A. K., Hydrogen production, storage, transportation and key challenges with applications: a review. Energy conversion and management 2018, 165, 602-627
23. Falcone, P.M., Hiete, M. and Sapio, A., 2021. Hydrogen economy and sustainable development goals: Review and policy insights. *Current Opinion in Green and Sustainable Chemistry*, *31*, p.100506.
24. Oliveira, A.M., Beswick, R.R. and Yan, Y., 2021. A green hydrogen economy for a renewable energy society. *Current Opinion in Chemical Engineering*, *33*, p.100701.
25. Beswick, R.R., Oliveira, A.M. and Yan, Y., 2021. Does the green hydrogen economy have a water problem?. *ACS Energy Letters*, *6*(9), pp.3167-3169.
26. van der Spek, M., Banet, C., Bauer, C., Gabrielli, P., Goldthorpe, W., Mazzotti, M., Munkejord, S.T., Røkke, N.A., Shah, N., Sunny, N. and Sutter, D., 2022. Perspective on the hydrogen economy as a pathway to reach net-zero CO_2 emissions in Europe. *Energy & Environmental Science*, *15*(3), pp.1034-1077.

27. Ishaq, H., Dincer, I. and Crawford, C., 2022. A review on hydrogen production and utilization: Challenges and opportunities. *International Journal of Hydrogen Energy*, *47*(62), pp.26238-26264.
28. Zhu, J., Hu, L., Zhao, P., Lee, L.Y.S. and Wong, K.Y., 2019. Recent advances in electrocatalytic hydrogen evolution using nanoparticles. *Chemical reviews*, *120*(2), pp.851-918.
29. Weng, C.C., Ren, J.T. and Yuan, Z.Y., 2020. Transition metal phosphide-based materials for efficient electrochemical hydrogen evolution: a critical review. *ChemSusChem*, *13*(13), pp.3357-3375.
30. Zhao, G., Rui, K., Dou, S.X. and Sun, W., 2018. Heterostructures for electrochemical hydrogen evolution reaction: a review. *Advanced Functional Materials*, *28*(43), p.1803291.
31. Kannah, R.Y., Kavitha, S., Karthikeyan, O.P., Kumar, G., Dai-Viet, N.V. and Banu, J.R., 2021. Techno-economic assessment of various hydrogen production methods–A review. *Bioresource technology*, *319*, p.124175.
32. Dawood, F., Anda, M. and Shafiullah, G.M., 2020. Hydrogen production for energy: An overview. *International Journal of Hydrogen Energy*, *45*(7), pp.3847-3869.
33. Ji, M. and Wang, J., 2021. Review and comparison of various hydrogen production methods based on costs and life cycle impact assessment indicators. *International Journal of Hydrogen Energy*, *46*(78), pp.38612-38635.
34. El-Emam, R. S.; Özcan, H., Comprehensive review on the techno-economics of sustainable large-scale clean hydrogen production. Journal of Cleaner Production 2019, 220, 593-609.
35. Sheffield, J. W., The Extraordinary Hydrogen Romantic-The Story of Dr. T. Nejat Veziroglu. Международный научный журнал Альтернативная энергетика и экология 2019, (4-6), 12-13.
36. Garland, N. L.; Papageorgopoulos, D. C.; Stanford, J. M., Hydrogen and fuel cell technology: Progress, challenges, and future directions. Energy Procedia 2012, 28, 2-11.
37. Staffell, I.; Scamman, D.; Abad, A. V.; Balcombe, P.; Dodds, P. E.; Ekins, P.; Shah, N.; Ward, K. R., The role of hydrogen and fuel cells in the global energy system. Energy & Environmental Science 2019, 12 (2), 463-491
38. Romm, J. J., The hype about hydrogen: fact and fiction in the race to save the climate. Island Press: 2004.

39. Greene, D.L., Duleep, K.G. and Upreti, G., 2011. Status and outlook for the US non-automotive fuel cell industry: impacts of government policies and assessment of future opportunities. *Oak Ridge National Laboratory, Oakridge, TN. ORNL/TM-2011/101. Retrieved December*, *28*, p.2011.
40. Löbberding, L. and Madlener, R., 2019. Techno-economic analysis of micro fuel cell cogeneration and storage in Germany. *Applied energy*, *235*, pp.1603-1613.
41. Boait, P.J. and Greenough, R., 2019. Can fuel cell micro-CHP justify the hydrogen gas grid? Operating experience from a UK domestic retrofit. *Energy and Buildings*, *194*, pp.75-84.
42. Hacking, N.; Pearson, P.; Eames, M., Mapping innovation and diffusion of hydrogen fuel cell technologies: Evidence from the UK's hydrogen fuel cell technological innovation system, 1954–2012. International Journal of Hydrogen Energy 2019, 44 (57), 29805-29848.
43. Garland, N.L., Papageorgopoulos, D.C. and Stanford, J.M., 2012. Hydrogen and fuel cell technology: Progress, challenges, and future directions. *Energy Procedia*, *28*, pp.2-11.
44. Miller, E.L., Papageorgopoulos, D., Stetson, N., Randolph, K., Peterson, D., Cierpik-Gold, K., Wilson, A., Trejos, V., Gomez, J.C., Rustagi, N. and Satyapal, S., 2016. US Department of energy hydrogen and fuel cells program: progress, challenges and future directions. *MRS Advances*, *1*(42), pp.2839-2855.
45. Pingkuo, L. and Xue, H., 2022. Comparative analysis on similarities and differences of hydrogen energy development in the World's top 4 largest economies: A novel framework. *International Journal of Hydrogen Energy*, *47*(16), pp.9485-9503.
46. Zhang, Qian, Kai Chen, Xingchen Lai, and Jun Yu. "Construction of hydrogenation station based on electrolytic water hydrogen production technology and design specification of hydrogen-electricity complementary smart energy system." In *7th International Symposium on Advances in Electrical, Electronics, and Computer Engineering*, vol. 12294, pp. 202-206. SPIE, 2022.
47. Smolinka, T., Bergmann, H., Garche, J. and Kusnezoff, M., 2022. The history of water electrolysis from its beginnings to the present. In *Electrochemical Power Sources: Fundamentals, Systems, and Applications* (pp. 83-164). Elsevier.
48. Chisholm, G., Zhao, T. and Cronin, L., 2022. Hydrogen from water electrolysis. In *Storing Energy* (pp. 559-591). Elsevier.
49. Mostafaeipour, A.; Khayyami, M.; Sedaghat, A.; Mohammadi, K.; Shamshirband, S.; Sehati, M.-A.; Gorakifard, E., Evaluating the wind energy potential for hydrogen

production: a case study. International Journal of Hydrogen Energy 2016, 41 (15), 6200-6210

50. Santos, D. M.; Sequeira, C. A.; Figueiredo, J. L., Hydrogen production by alkaline water electrolysis. Química Nova 2013, 36 (8), 1176-1193.
51. Parkinson, B.; Turner, J.; Peter, L.; Lewis, N.; Sivula, K.; Domen, K.; Bard, A. J.; Fiechter, S.; Collazo, R.; Hannappel, T., Photoelectrochemical water splitting: materials, processes and architectures. Royal Society of Chemistry: 2013.
52. Wei, C. and Xu, Z.J., 2018. The comprehensive understanding of as an evaluation parameter for electrochemical water splitting. *Small Methods*, *2*(11), p.1800168.
53. Li, X., Hao, X., Abudula, A. and Guan, G., 2016. Nanostructured catalysts for electrochemical water splitting: current state and prospects. *Journal of Materials Chemistry A*, *4*(31), pp.11973-12000.
54. Khan, S.U., Al-Shahry, M. and Ingler Jr, W.B., 2002. Efficient photochemical water splitting by a chemically modified n-TiO2. *science*, *297*(5590), pp.2243-2245.
55. Wang, G., Wang, H., Ling, Y., Tang, Y., Yang, X., Fitzmorris, R.C., Wang, C., Zhang, J.Z. and Li, Y., 2011. Hydrogen-treated TiO2 nanowire arrays for photoelectrochemical water splitting. *Nano letters*, *11*(7), pp.3026-3033.
56. Anantharaj, S. and Noda, S., 2020. Amorphous catalysts and electrochemical water splitting: an untold story of harmony. *Small*, *16*(2), p.1905779.
57. Ghobadi, T.G.U., Ghobadi, A., Ozbay, E. and Karadas, F., 2018. Strategies for plasmonic hot-electron-driven photoelectrochemical water splitting. *ChemPhotoChem*, *2*(3), pp.161-182.
58. Godula-Jopek, A., Hydrogen production: by electrolysis. John Wiley & Sons: 2015.
59. Guo, Z.; Chen, Y.; Lu, N. L., Multifunctional nanocomposites for energy and environmental applications. John Wiley & Sons: 2018.
60. Yan, Y., Xia, B.Y., Zhao, B. and Wang, X., 2016. A review on noble-metal-free bifunctional heterogeneous catalysts for overall electrochemical water splitting. *Journal of Materials Chemistry A*, *4*(45), pp.17587-17603.
61. Pu, Z., Luo, Y., Asiri, A.M. and Sun, X., 2016. Efficient electrochemical water splitting catalyzed by electrodeposited nickel diselenide nanoparticles based film. *ACS applied materials & interfaces*, *8*(7), pp.4718-4723.
62. Shinagawa, T.; Takanabe, K., Towards versatile and sustainable hydrogen production through electrocatalytic water splitting: electrolyte engineering. *ChemSusChem* **2017,***10* (7), 1318-1336.

63. Giordano, L.; Han, B.; Risch, M.; Hong, W. T.; Rao, R. R.; Stoerzinger, K. A.; Shao-Horn, Y., pH dependence of OER activity of oxides: current and future perspectives. *Catalysis Today* **2016,***262*, 2-10.
64. Lindström, B.; Pettersson, L. J., A brief history of catalysis. *Cattech* **2003,***7* (4), 130-138
65. Jorpes, J. E., *Jac. Berzelius: his life and work*. Univ of California Press: 1970; Vol. 7
66. Ranade, V.V. and Joshi, S.S., 2016. Catalysis and Catalytic Processes. In *Industrial Catalytic Processes for Fine and Specialty Chemicals* (pp. 1-14). Elsevier.
67. Rothenberg, G., 2000. Catalysis. *Kirk-Othmer Encyclopedia of Chemical Technology*, pp.1-43.
68. Bronsted, J.N., 1928. Acid and Basic Catalysis. *Chemical Reviews*, *5*(3), pp.231-338.
69. Hattori, H., 1995. Heterogeneous basic catalysis. *Chemical reviews*, *95*(3), pp.537-558.
70. Trasatti, S., Electrocatalysis: understanding the success of DSA®. *Electrochimica Acta* **2000,***45* (15-16), 2377-2385
71. Eberle, U., Arnold, G. and Von Helmolt, R., 2006. Hydrogen storage in metal–hydrogen systems and their derivatives. *Journal of Power Sources*, *154*(2), pp.456-460.
72. Züttel, A., Remhof, A., Borgschulte, A. and Friedrichs, O., 2010. Hydrogen: the future energy carrier. *Philosophical Transactions of the Royal Society A: Mathematical, Physical and Engineering Sciences*, *368*(1923), pp.3329-3342.
73. Yang, W., Prabhakar, R.R., Tan, J., Tilley, S.D. and Moon, J., 2019. Strategies for enhancing the photocurrent, photovoltage, and stability of photoelectrodes for photoelectrochemical water splitting. *Chemical Society Reviews*, *48*(19), pp.4979-5015.
74. Li, X., Hao, X., Abudula, A. and Guan, G., 2016. Nanostructured catalysts for electrochemical water splitting: current state and prospects. *Journal of Materials Chemistry A*, *4*(31), pp.11973-12000.
75. Wang, Y., Pang, Y., Xu, H., Martinez, A. and Chen, K.S., 2022. PEM Fuel Cell and Electrolysis Cell Technologies and Hydrogen Infrastructure Development: A Review. *Energy & Environmental Science*.
76. Fragiacomo, P. and Genovese, M., 2020. Numerical simulations of the energy performance of a PEM water electrolysis based high-pressure hydrogen refueling station. *International Journal of Hydrogen Energy*, *45*(51), pp.27457-27470.
77. Strmcnik, D., Lopes, P.P., Genorio, B., Stamenkovic, V.R. and Markovic, N.M., 2016. Design principles for hydrogen evolution reaction catalyst materials. *Nano Energy*, *29*, pp.29-36.

78. Zheng, Y., Jiao, Y., Vasileff, A. and Qiao, S.Z., 2018. The hydrogen evolution reaction in alkaline solution: from theory, single crystal models, to practical electrocatalysts. *Angewandte Chemie International Edition*, *57*(26), pp.7568-7579.
79. Gao, D., Guo, J., He, H., Xiao, P. and Zhang, Y., 2022. Geometric and electronic modulation of fcc NiCo alloy by Group-VI B metal doping to accelerate hydrogen evolution reaction in acidic and alkaline media. *Chemical Engineering Journal*, *430*, p.133110.
80. Sun, L., Gao, M., Jing, Z., Cheng, Z., Zheng, D., Xu, H., Zhou, Q. and Lin, J., 2022. 1 T-Phase Enriched P doped WS2 nanosphere for highly efficient electrochemical hydrogen evolution reaction. *Chemical Engineering Journal*, *429*, p.132187.
81. Dong, S., Li, Y., Zhao, Z., Li, R., He, J., Yin, J., Yan, B. and Zhang, X., 2022. A Review of the Application of Heterostructure Catalysts in Hydrogen Evolution Reaction. *ChemistrySelect*, *7*(14), p.e202104041.
82. Zhang, H.M., Wang, J.J., Meng, Y. and Sun, J., 2022. Recent advances in amorphous metal phosphide electrocatalysts for hydrogen evolution reaction. *International Journal of Hydrogen Energy*.
83. Chen, M., Liu, J., Kitiphatpiboon, N., Li, X., Wang, J., Hao, X., Abudula, A., Ma, Y. and Guan, G., 2022. Zn-VOx-Co nanosheets with amorphous/crystalline heterostructure for highly efficient hydrogen evolution reaction. *Chemical Engineering Journal*, *432*, p.134329.
84. Li, M., Wang, L., Qian, Y. and Du, J., 2022. Facile synthesis of MoS2/CuS nanoflakes as high performance electrocatalysts for hydrogen evolution reaction. *International Journal of Hydrogen Energy*, *47*(8), pp.5319-5325.
85. Seh, Z.W., Kibsgaard, J., Dickens, C.F., Chorkendorff, I.B., Nørskov, J.K. and Jaramillo, T.F., 2017. Combining theory and experiment in electrocatalysis: Insights into materials design. *Science*, *355*(6321), p.eaad4998.
86. Chen, D., Chen, C., Baiyee, Z.M., Shao, Z. and Ciucci, F., 2015. Nonstoichiometric oxides as low-cost and highly-efficient oxygen reduction/evolution catalysts for low-temperature electrochemical devices. *Chemical reviews*, *115*(18), pp.9869-9921.
87. Tahir, M., Pan, L., Idrees, F., Zhang, X., Wang, L., Zou, J.J. and Wang, Z.L., 2017. Electrocatalytic oxygen evolution reaction for energy conversion and storage: a comprehensive review. *Nano Energy*, *37*, pp.136-157.
88. Gong, M. and Dai, H., 2015. A mini review of NiFe-based materials as highly active oxygen evolution reaction electrocatalysts. *Nano Research*, *8*(1), pp.23-39.

89. Wang, X., Zhong, H., Xi, S., Lee, W.S.V. and Xue, J., 2022. Understanding of oxygen redox in oxygen evolution reaction. *Advanced Materials*, p.2107956.
90. Zheng, X., Yang, J., Xu, Z., Wang, Q., Wu, J., Zhang, E., Dou, S., Sun, W., Wang, D. and Li, Y., 2022. Ru–Co Pair Sites Catalyst Boosts the Energetics for the Oxygen Evolution Reaction. *Angewandte Chemie International Edition*, *61*(32), p.e202205946.
91. Haase, F.T., Rabe, A., Schmidt, F.P., Herzog, A., Jeon, H.S., Frandsen, W., Narangoda, P.V., Spanos, I., Friedel Ortega, K., Timoshenko, J. and Lunkenbein, T., 2022. Role of Nanoscale inhomogeneities in Co2FeO4 catalysts during the oxygen evolution reaction. *Journal of the American Chemical Society*, *144*(27), pp.12007-12019.
92. Tian, L., Chen, H., Lu, X., Liu, D., Cheng, W., Liu, Y., Li, J. and Li, Z., 2022. Local photothermal and photoelectric effect synergistically boost hollow CeO2/CoS2 heterostructure electrocatalytic oxygen evolution reaction. *Journal of Colloid and Interface Science*, *628*, pp.663-672.
93. Wang, Z., Huang, J., Wang, L., Liu, Y., Liu, W., Zhao, S. and Liu, Z.Q., 2022. Cation-Tuning Induced d-Band Center Modulation on Co-Based Spinel Oxide for Oxygen Reduction/Evolution Reaction. *Angewandte Chemie International Edition*, *61*(16), p.e202114696.
94. Haase, F.T., Bergmann, A., Jones, T.E., Timoshenko, J., Herzog, A., Jeon, H.S., Rettenmaier, C. and Cuenya, B.R., 2022. Size effects and active state formation of cobalt oxide nanoparticles during the oxygen evolution reaction. *Nature Energy*, *7*(8), pp.765-773.
95. Ruan, Q.D., Liu, L.L., Wu, D.H., Feng, J.J., Zhang, L. and Wang, A.J., 2022. Cobalt phosphide nanoparticles encapsulated in manganese, nitrogen co-doped porous carbon nanosheets with rich nanoholes for high-efficiency oxygen reduction reaction. *Journal of Colloid and Interface Science*, *627*, pp.630-639.
96. Bai, X., Wang, L., Nan, B., Tang, T., Niu, X. and Guan, J., 2022. Atomic manganese coordinated to nitrogen and sulfur for oxygen evolution. *Nano Research*, pp.1-7.
97. Zhang, Y., Guo, P., Li, S., Sun, J., Wang, W., Song, B., Yang, X., Wang, X., Jiang, Z., Wu, G. and Xu, P., 2022. Magnetic field assisted electrocatalytic oxygen evolution reaction of nickel-based materials. *Journal of Materials Chemistry A*, *10*(4), pp.1760-1767.
98. Zhang, N., Hu, Y., An, L., Li, Q., Yin, J., Li, J., Yang, R., Lu, M., Zhang, S., Xi, P. and Yan, C.H., 2022. Surface Activation and Ni-S Stabilization in NiO/NiS2 for Efficient

Oxygen Evolution Reaction. *Angewandte Chemie International Edition*, *61*(35), p.e202207217.

99. Ahmad, I., Ahmed, J., Batool, S., Zafar, M.N., Hanif, A., Nazar, M.F., Ul-Hamid, A., Jabeen, U., Dahshan, A., Idrees, M. and Shehzadi, S.A., 2022. Design and fabrication of Fe2O3/FeP heterostructure for oxygen evolution reaction electrocatalysis. *Journal of Alloys and Compounds*, *894*, p.162409.
100. Sari, F.N.I., Chen, H.S., kumar Anbalagan, A., Huang, Y.J., Haw, S.C., Chen, J.M., Lee, C.H., Su, Y.H. and Ting, J.M., 2022. V-doped, divacancy-containing β-FeOOH electrocatalyst for high performance oxygen evolution reaction. *Chemical Engineering Journal*, *438*, p.135515.
101. Fabbri, E., Habereder, A., Waltar, K., Kötz, R. and Schmidt, T.J., 2014. Developments and perspectives of oxide-based catalysts for the oxygen evolution reaction. *Catalysis Science & Technology*, *4*(11), pp.3800-3821.
102. McCrory, C.C., Jung, S., Peters, J.C. and Jaramillo, T.F., 2013. Benchmarking heterogeneous electrocatalysts for the oxygen evolution reaction. *Journal of the American Chemical Society*, *135*(45), pp.16977-16987.
103. Gao, L., Cui, X., Sewell, C.D., Li, J. and Lin, Z., 2021. Recent advances in activating surface reconstruction for the high-efficiency oxygen evolution reaction. *Chemical Society Reviews*.
104. Du, J., Li, F. and Sun, L., 2021. Metal–organic frameworks and their derivatives as electrocatalysts for the oxygen evolution reaction. *Chemical Society Reviews*, *50*(4), pp.2663-2695.
105. Tang, Y.J., You, L. and Zhou, K., 2020. Enhanced Oxygen Evolution Reaction Activity of a Co2P@ NC–Fe2P Composite Boosted by Interfaces Between a N-Doped Carbon Matrix and Fe2P Microspheres. *ACS applied materials & interfaces*, *12*(23), pp.25884-25894.
106. Huang, J., Sun, Y., Du, X., Zhang, Y., Wu, C., Yan, C., Yan, Y., Zou, G., Wu, W., Lu, R. and Li, Y., 2018. Cytomembrane-structure-inspired active Ni–N–O interface for enhanced oxygen evolution reaction. *Advanced Materials*, *30*(39), p.1803367.
107. Yan, X., Zhao, Y., Biemolt, J., Zhao, K., Laan, P.C., Cao, X. and Yan, N., 2020. "Nano-garden cultivation" for electrocatalysis: controlled synthesis of Nature-inspired hierarchical nanostructures. *Journal of materials chemistry A*, *8*(16), pp.7626-7632.
108. Popczun, E.J., McKone, J.R., Read, C.G., Biacchi, A.J., Wiltrout, A.M., Lewis, N.S. and Schaak, R.E., 2013. Nanostructured nickel phosphide as an electrocatalyst for the

hydrogen evolution reaction. *Journal of the American Chemical Society*, *135*(25), pp.9267-9270.

109. Cai, Z., Li, A., Zhang, W., Zhang, Y., Cui, L. and Liu, J., 2021. Hierarchical Cu@ Co-decorated CuO@ Co3O4 nanostructure on Cu foam as efficient self-supported catalyst for hydrogen evolution reaction. *Journal of Alloys and Compounds*, *882*, p.160749.
110. Ganci, F., Cusumano, V., Livreri, P., Aiello, G., Sunseri, C. and Inguanta, R., 2021. Nanostructured Ni–Co alloy electrodes for both hydrogen and oxygen evolution reaction in alkaline electrolyzer. *International Journal of Hydrogen Energy*, *46*(16), pp.10082-10092.
111. Li, R., Yang, L., Xiong, T., Wu, Y., Cao, L., Yuan, D. and Zhou, W., 2017. Nitrogen doped MoS2 nanosheets synthesized via a low-temperature process as electrocatalysts with enhanced activity for hydrogen evolution reaction. *Journal of Power Sources*, *356*, pp.133-139.
112. Chu, K., Liu, Y.P., Li, Y.B., Guo, Y.L. and Tian, Y., 2020. Two-dimensional (2D)/2D interface engineering of a MoS2/C3N4 heterostructure for promoted electrocatalytic nitrogen fixation. *ACS Applied Materials & Interfaces*, *12*(6), pp.7081-7090.
113. Yu, X., Zhao, G., Gong, S., Liu, C., Wu, C., Lyu, P., Maurin, G. and Zhang, N., 2020. Design of MoS2/graphene van der Waals heterostructure as highly efficient and stable electrocatalyst for hydrogen evolution in acidic and alkaline media. *ACS applied materials & interfaces*, *12*(22), pp.24777-24785.
114. Lu, Y., Guo, X., Yang, L., Yang, W., Sun, W., Tuo, Y., Zhou, Y., Wang, S., Pan, Y., Yan, W. and Sun, D., 2020. Highly efficient CoMoS heterostructure derived from vertically anchored Co5Mo10 polyoxometalate for electrocatalytic overall water splitting. *Chemical Engineering Journal*, *394*, p.124849.
115. Liu, Y., Chen, Y., Tian, Y., Sakthivel, T., Liu, H., Guo, S., Zeng, H. and Dai, Z., 2022. Synergizing hydrogen spillover and deprotonation by the internal polarization field in a MoS2/NiPS3 vertical heterostructure for boosted water electrolysis. *Advanced Materials*, *34*(37), p.2203615.
116. Ren, C., Chen, Y., Du, L., Wang, Q., Li, L. and Tian, G., 2021. Hierarchical CuCo2S4 Nanoflake Arrays Grown on Carbon Cloth: A Remarkable Bifunctional Electrocatalyst for Overall Water Splitting. *ChemElectroChem*, *8*(6), pp.1134-1140.
117. Kahnamouei, M.H. and Shahrokhian, S., 2021. Ultrafast two-step synthesis of S-doped Fe/Ni (Oxy) Hydroxide/Ni nanocone arrays on carbon cloth and stainless-steel

substrates for water-splitting applications. *ACS Applied Energy Materials*, *4*(10), pp.10627-10638.

118. Chaudhari, N.K., Jin, H., Kim, B. and Lee, K., 2017. Nanostructured materials on 3D nickel foam as electrocatalysts for water splitting. *Nanoscale*, *9*(34), pp.12231-12247.
119. Gawande, M.B., Goswami, A., Asefa, T., Guo, H., Biradar, A.V., Peng, D.L., Zboril, R. and Varma, R.S., 2015. Core–shell nanoparticles: synthesis and applications in catalysis and electrocatalysis. *Chemical Society Reviews*, *44*(21), pp.7540-7590.
120. Yin, X., Yang, L. and Gao, Q., 2020. Core–shell nanostructured electrocatalysts for water splitting. *Nanoscale*, *12*(30), pp.15944-15969.
121. Lyu, X., Jia, Y., Mao, X., Li, D., Li, G., Zhuang, L., Wang, X., Yang, D., Wang, Q., Du, A. and Yao, X., 2020. Gradient-Concentration Design of Stable Core–Shell Nanostructure for Acidic Oxygen Reduction Electrocatalysis. *Advanced Materials*, *32*(32), p.2003493.
122. Liu, Z., Hu, J.E., Wang, Q., Gaskell, K., Frenkel, A.I., Jackson, G.S. and Eichhorn, B., 2009. PtMo alloy and MoO x@ Pt Core− shell nanoparticles as highly CO-tolerant electrocatalysts. *Journal of the American Chemical Society*, *131*(20), pp.6924-6925.
123. Feng, J., Zhou, H., Wang, J., Bian, T., Shao, J. and Yuan, A., 2018. MoS2 supported on MOF-derived carbon with core-shell structure as efficient electrocatalysts for hydrogen evolution reaction. *International Journal of Hydrogen Energy*, *43*(45), pp.20538-20545.
124. Zhang, S., Xia, W., Yang, Q., Kaneti, Y.V., Xu, X., Alshehri, S.M., Ahamad, T., Hossain, M.S.A., Na, J., Tang, J. and Yamauchi, Y., 2020. Core-shell motif construction: Highly graphitic nitrogen-doped porous carbon electrocatalysts using MOF-derived carbon@ COF heterostructures as sacrificial templates. *Chemical Engineering Journal*, *396*, p.125154.
125. Zhang, J., Sun, X., Liu, Y., Hou, L. and Yuan, C., 2020. Design and construction of bi-metal MOF-derived yolk–shell Ni 2 P/ZnP 2 hollow microspheres for efficient electrocatalytic oxygen evolution. *Materials Chemistry Frontiers*, *4*(5), pp.1366-1374.
126. Li, Z., Song, M., Zhu, W., Zhuang, W., Du, X. and Tian, L., 2021. MOF-derived hollow heterostructures for advanced electrocatalysis. *Coordination Chemistry Reviews*, *439*, p.213946.
127. Wang, J., Li, S., Lin, R., Tu, G., Wang, J. and Li, Z., 2019. MOF-derived hollow β-FeOOH polyhedra anchored with α-Ni (OH) 2 nanosheets as efficient electrocatalysts for oxygen evolution. *Electrochimica Acta*, *301*, pp.258-266.

128. Wang, J., Li, S., Lin, R., Tu, G., Wang, J. and Li, Z., 2019. MOF-derived hollow β-FeOOH polyhedra anchored with α-Ni (OH) 2 nanosheets as efficient electrocatalysts for oxygen evolution. *Electrochimica Acta*, *301*, pp.258-266.

129. Wang, J., Wang, J., Zhang, M., Li, S., Liu, R. and Li, Z., 2020. Metal-organic frameworks-derived hollow-structured iron-cobalt bimetallic phosphide electrocatalysts for efficient oxygen evolution reaction. *Journal of Alloys and Compounds*, *821*, p.153463.

130. Wang, C., Shang, H., Li, J., Wang, Y., Xu, H., Wang, C., Guo, J. and Du, Y., 2021. Ultralow Ru doping induced interface engineering in MOF derived ruthenium-cobalt oxide hollow nanobox for efficient water oxidation electrocatalysis. *Chemical Engineering Journal*, *420*, p.129805.

131. Meng, W., Zeng, Y., Liang, Z., Guo, W., Zhi, C., Wu, Y., Zhong, R., Qu, C. and Zou, R., 2018. Tuning expanded pores in metal–organic frameworks for selective capture and catalytic conversion of carbon dioxide. *ChemSusChem*, *11*(21), pp.3751-3757.

132. Wu, S., Qin, L., Zhang, K., Xin, Z. and Zhao, S., 2019. Ultrathin 2D metal–organic framework nanosheets prepared via sonication exfoliation of membranes from interfacial growth and exhibition of enhanced catalytic activity by their gold nanocomposites. *RSC advances*, *9*(17), pp.9386-9391.

133. Jung, D.W., Yang, D.A., Kim, J., Kim, J. and Ahn, W.S., 2010. Facile synthesis of MOF-177 by a sonochemical method using 1-methyl-2-pyrrolidinone as a solvent. *Dalton Transactions*, *39*(11), pp.2883-2887.

134. Bohigues, B., Rojas-Buzo, S., Moliner, M. and Corma, A., 2021. Coordinatively Unsaturated Hf-MOF-808 Prepared via Hydrothermal Synthesis as a Bifunctional Catalyst for the Tandem N-Alkylation of Amines with Benzyl Alcohol. *ACS Sustainable Chemistry & Engineering*, *9*(47), pp.15793-15806.

135. Wu, J., Dai, Q., Zhang, H. and Li, X., 2021. A defect-free MOF composite membrane prepared via in-situ binder-controlled restrained second-growth method for energy storage device. *Energy Storage Materials*, *35*, pp.687-694.

136. Qin, X., Kim, D. and Piao, Y., 2021. Metal-organic frameworks-derived novel nanostructured electrocatalysts for oxygen evolution reaction. *Carbon Energy*, *3*(1), pp.66-100.

137. Wang, X., Chai, L., Ding, J., Zhong, L., Du, Y., Li, T.T., Hu, Y., Qian, J. and Huang, S., 2019. Chemical and morphological transformation of MOF-derived bimetallic phosphide for efficient oxygen evolution. *Nano Energy*, *62*, pp.745-753.

138. Yuan, Q., Yu, Y., Sherrell, P.C., Chen, J. and Bi, X., 2020. Fe/Co-based Bimetallic MOF-derived Co3Fe7@ NCNTFs Bifunctional Electrocatalyst for High-Efficiency Overall Water Splitting. *Chemistry–An Asian Journal*, *15*(11), pp.1728-1735.

139. He, D., Ooka, H., Kim, Y., Li, Y., Jin, F., Kim, S.H. and Nakamura, R., 2020. Atomic-scale evidence for highly selective electrocatalytic N− N coupling on metallic MoS2. *Proceedings of the National Academy of Sciences*, *117*(50), pp.31631-31638.

140. Wang, Y., Wang, M., Lu, Z., Ma, D. and Jia, Y., 2021. Enabling multifunctional electrocatalysts by modifying the basal plane of unifunctional 1T′-MoS 2 with anchored transition metal single atoms. *Nanoscale*, *13*(31), pp.13390-13400.

141. Qin, J., Xi, C., Zhang, R., Liu, T., Zou, P., Wu, D., Guo, Q., Mao, J., Xin, H. and Yang, J., 2021. Activating edge-Mo of 2H-MoS2 via coordination with pyridinic N–C for pH-universal hydrogen evolution electrocatalysis. *ACS Catalysis*, *11*(8), pp.4486-4497.

142. Guo, Y., Park, T., Yi, J.W., Henzie, J., Kim, J., Wang, Z., Jiang, B., Bando, Y., Sugahara, Y., Tang, J. and Yamauchi, Y., 2019. Nanoarchitectonics for transition-metal-sulfide-based electrocatalysts for water splitting. *Advanced Materials*, *31*(17), p.1807134.

143. Zhang, B., Ji, X., Xu, K., Chen, C., Xiong, X., Xiong, J., Yao, Y., Miao, L. and Jiang, J., 2016. Unraveling the different charge storage mechanism in T and H phases of MoS2. *Electrochimica Acta*, *217*, pp.1-8.

144. Gao, Y., Wang, S., Wang, B., Jiang, Z. and Fang, T., 2022. Recent progress in phase regulation, functionalization, and biosensing applications of polyphase MoS2. *Small*, *18*(34), p.2202956.

145. Hinnemann, B., Moses, P.G., Bonde, J., Jørgensen, K.P., Nielsen, J.H., Horch, S., Chorkendorff, I. and Nørskov, J.K., 2005. Biomimetic hydrogen evolution: MoS2 nanoparticles as catalyst for hydrogen evolution. *Journal of the American Chemical Society*, *127*(15), pp.5308-5309.

146. Zhang, Y., Lin, Y., Duan, T. and Song, L., 2021. Interfacial engineering of heterogeneous catalysts for electrocatalysis. *Materials Today*, *48*, pp.115-134.

147. Zhao, G., Jiang, Y., Dou, S.X., Sun, W. and Pan, H., 2021. Interface engineering of heterostructured electrocatalysts towards efficient alkaline hydrogen electrocatalysis. *Science Bulletin*, *66*(1), pp.85-96.

148. Wang, C., Bai, S. and Xiong, Y., 2015. Recent advances in surface and interface engineering for electrocatalysis. *Chinese Journal of Catalysis*, *36*(9), pp.1476-1493.

149. Zhang, Y., Yang, J., Yu, Z., Hou, Y., Jiang, R., Huang, J., Yang, F., Yao, S., Gao, L. and Tang, W., 2021. Modulating carbon-supported transition metal oxide by electron-giving and electron-absorbing functional groups towards efficient overall water splitting. *Chemical Engineering Journal*, *416*, p.129124.

150. Tian, L., Chen, H., Lu, X., Liu, D., Cheng, W., Liu, Y., Li, J. and Li, Z., 2022. Local photothermal and photoelectric effect synergistically boost hollow CeO2/CoS2 heterostructure electrocatalytic oxygen evolution reaction. *Journal of Colloid and Interface Science*, *628*, pp.663-672.

151. Huang, C., Zhang, Y., Li, X., Cao, H., Guo, Y. and Zhang, C., 2022. Mn-incorporated Co3O4 bifunctional electrocatalysts for zinc-air battery application: An experimental and DFT study. *Applied Catalysis B: Environmental*, *319*, p.121909.

152. Maccato, C., Bigiani, L., Girardi, L., Gasparotto, A., Lebedev, O.I., Modin, E., Barreca, D. and Rizzi, G.A., 2021. Plasma-Assisted Synthesis of Co3O4-Based Electrocatalysts on Ni Foam Substrates for the Oxygen Evolution Reaction. *Advanced Materials Interfaces*, *8*(18), p.2100763.

153. Zhang, X., Li, J., Yang, Y., Zhang, S., Zhu, H., Zhu, X., Xing, H., Zhang, Y., Huang, B., Guo, S. and Wang, E., 2018. Co3O4/Fe0. 33Co0. 66P interface nanowire for enhancing water oxidation catalysis at high current density. *Advanced Materials*, *30*(45), p.1803551.

154. Yu, X., Chen, G., Wang, Y., Liu, J., Pei, K., Zhao, Y., You, W., Wang, L., Zhang, J., Xing, L. and Ding, J., 2020. Hierarchical coupling effect in hollow Ni/NiFe2O4-CNTs microsphere via spray-drying for enhanced oxygen evolution electrocatalysis. *Nano Research*, *13*(2), pp.437-446.

155. Dutta, S., Indra, A., Feng, Y., Han, H. and Song, T., 2019. Promoting electrocatalytic overall water splitting with nanohybrid of transition metal nitride-oxynitride. *Applied Catalysis B: Environmental*, *241*, pp.521-527.

156. Meng, Z., Zheng, S., Luo, R., Tang, H., Wang, R., Zhang, R., Tian, T. and Tang, H., 2022. Transition Metal Nitrides for Electrocatalytic Application: Progress and Rational Design. *Nanomaterials*, *12*(15), p.2660.

157. Yu, X., Zhou, T., Ge, J. and Wu, C., 2020. Recent advances on the modulation of electrocatalysts based on transition metal nitrides for the rechargeable Zn-Air battery. *ACS Materials Letters*, *2*(11), pp.1423-1434.

158. Peng, X., Pi, C., Zhang, X., Li, S., Huo, K. and Chu, P.K., 2019. Recent progress of transition metal nitrides for efficient electrocatalytic water splitting. *Sustainable Energy & Fuels*, *3*(2), pp.366-381.

159. Wang, W., Liu, C., Zhou, D., Yang, L., Zhou, J. and Yang, D., 2019. In-situ synthesis of coupled molybdenum carbide and molybdenum nitride as electrocatalyst for hydrogen evolution reaction. *Journal of Alloys and Compounds*, *792*, pp.230-239.

160. Tareen, A.K., Priyanga, G.S., Khan, K., Pervaiz, E., Thomas, T. and Yang, M., 2019. Nickel-based transition metal nitride electrocatalysts for the oxygen evolution reaction. *ChemSusChem*, *12*(17), pp.3941-3954.

161. Wu, A., Gu, Y., Yang, B., Wu, H., Yan, H., Jiao, Y., Wang, D., Tian, C. and Fu, H., 2020. Porous cobalt/tungsten nitride polyhedra as efficient bifunctional electrocatalysts for overall water splitting. *Journal of Materials Chemistry A*, *8*(43), pp.22938-22946.

162. Avasarala, B. and Haldar, P., 2010. Electrochemical oxidation behavior of titanium nitride based electrocatalysts under PEM fuel cell conditions. *Electrochimica Acta*, *55*(28), pp.9024-9034.

Chapter 2

Ultrathin MoS_2 wrapped N-doped carbon-coated cobalt nanospheres for OER applications

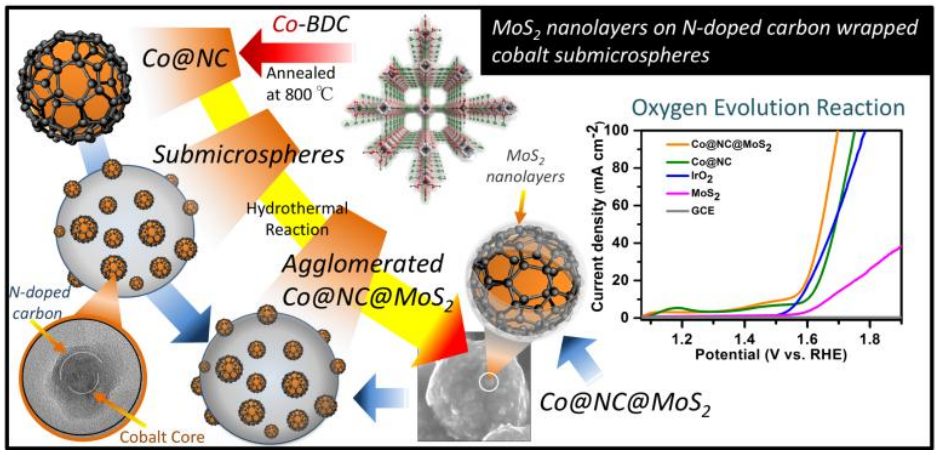

Brief Outcome:*In this chapter, the catalyst named "Co@NC@MoS_2" consist of three phases cobalt nanoparticles, N-doped carbon and ultrathin MoS_2 layers has been demonstrated for oxygen evolution reaction(OER.The possibilities to resolve the exponential increasein the energy demand using water splitting has also triggered huge worldwide attention towards oxygen evolution reaction using efficient, earth-abundant and low-cost electrocatalyst. Transition metal sulfides have been established as an excellent hydrogen evolution reaction catalyst but their oxygen evolution reaction behaviour is still less explored and needs further investigations. Oxygen evolution reaction has a huge potential for fuel cell and metal-air battery applications. Herein MoS_2nanolayers having interlayer spacing hierarchically grown over N-doped carbon wrapped cobalt nanospheres derived from cobalt-based metal-organic framework. The catalyst Co@NC@MoS_2 have a low overpotential of 297 mV vs RHE at 10 mA cm^{-2} current density. The catalysthas long term stability with a Tafel slope value of 70 mV dec^{-1}. A chronoamperometric study for more than 10 hours does not show any significant change in the current density of the catalyst.*

2.1. Introduction

The seizure of human activities during the recent pandemic has possibly made mankind realize that still there is a chance to revive the environment from the existing mess. A complete lockdown in most of the countries had actually brought huge positive change in the environment[1] but with a huge cost. Blue sky, clean beaches, clear water,fresh air to breath, and in some region, a lowered temperature than usual was observed. Therefore, it is a high time that we switch to greener technologies. In this context, Oxygen evolution reaction has an immense potential to resolve the twin problem of exhaustive usage of fossil fuel and massive carbon emission by supporting environment-friendly devices such as fuel cell and metal-air batteries.[2, 3] These energy-conversion and energy storage devices can trigger the industrial-scale production of energy materials.[4-6] The essential pre-requisites of OER catalyst are high abundance and low cost for a large-scale application.Due to the involvement of multistep electron-transfer process from water to oxygen via catalyst ($4OH^- \rightarrow 2H_2O + O_2 + 4e^-$), oxygen evolution reaction (OER) becomes a challenging affair.[7,8] This proton-coupled electron transfer lowers the efficiency of the electrocatalyst. Presently IrO_2 and RuO_2 are the benchmark electrocatalyst for OER, but their high cost and low abundance severely averted large-scale production.[9-11] Recently tremendous efforts have been devoted towards a low-cost, transition metal (Fe, Ni, Co, Mo) based substitutes for the precious metal electrocatalyst.[12] The study of transition metal compounds including phosphides (FeP, NiP,CoP),[13-16] oxides (Co_3O_4, NiO)[17, 18] and sulphides ($CoSe_2$, Ni_3S_2, FeS_2),[19-21] in oxygen evolution reaction is well-explored area. However, catalysts for oxygen evolution reaction using transition metal dichalcogenides are still less explored. MoS_2 is an exemplary two-dimensional material which attracts the attention due to the edge rich functionality.[22] The number of active sites in MoS_2 is more on exposed edges while the interlayer stacking leads by Van der Waals forces lacks the exposed active sites.[23] The performance of MoS_2 is quite low compared to the commercially available RuO_2 and IrO_2. To improve the catalytic activity of MoS_2, researchers used different strategies such as heteroatom doping,[24] constructing three-dimensional MoS_2,[25] and by increasing interlayer spacing to increase the number of active sites on the basal planes. Recently Tang et al. reported the enhanced oxygen evolution behavior of MoS_2nanosheets by Fe

doping.[26] At the same time, the Zhao et al. reported the doping of FeS_2 in MoS_2 basal planes resulting in the effective electronic structure tuning.[27]Herein, we synthesized N-doped carbon-wrapped cobalt nanospheres (Co@NC) from the pyrolysis of cobalt and H_2BDC (1,4-Benzenedicarboxylic acid) based metal-organic framework. The Co@NCnanospheresare electrochemically active towardsoxygen evolution reaction, which shows an overpotential of 365 mV at 10 mA cm^{-2} current density. Further growing few nanolayers of MoS_2 sheets on Co@NCnanospheresenhances the OER activity. The OER performance of the Co@NC nanoparticles with the mutual contribution of MoS_2nanolayers exhibits an overpotential of 297 mV at 10 mA cm^{-2} current density. These values are the lowest among all known MoS_2 based compounds for the oxygen evolution reaction using glassy carbon electrode.To the best of our knowledge, such an approach towards designing an OER catalyst which significantly reduces the overpotential was not observed in the recent literature.

2.2. Experimental section

2.2.1. Materials

The chemicals involved in this work were purchased from different sources and used without further modification. Cobalt (II) nitrate hexahydtate ($Co(NO_2)_2$. $6H_2O$, 99%), triethylenediamine ($C_6H_{12}N_2$, 99%) and 1,4-benzenedicarboxylic acid (C_6H_4-$1,4(COOH)_2$, 98%) and Ammonium molybdatetetrahydrate ($(NH_4)_6 \cdot Mo_7O_{24} \cdot 4H_2O$), 99.0%)were purchased from Sigma Aldrich. N,N-dimethylformamide anhydrous, Nafionperfluorinated resin solution were also purchased from Sigma Aldrich. L-Cysteine ($C_3H_7NO_2S$, 99%) was purchased from TCI. Deionised water was used in all preparation.

2.2.2. Methodology

2.2.2.1. Synthesis of Catalyst

The synthesis of catalyst involves two major steps and is described as follows.

Step 1.Synthesis of Co-based MOF derived Co@NCnanospheres:

The synthesis of MOF was done by using 2 mmol of $Co(NO_3)_2.6H_2O$, 0.8 mmol of triethylenediamine and 2 mmol of 1,4-benzenedicarboxylic acid (H_2BDC). All these chemicals were dissolved in 50 mL of N,N-dimethylformamide (DMF). The resulting solution was then heated at 120°C for 24 hrs then the mixture was cooled down and the pinkcolour precipitates were collected using centrifugation and washed with DMF and ethanol several times. After washing, the precipitate was dried in a vacuum oven at 50°C overnight. For the synthesis of Co@NC, the Co-based MOF was used as a precursor for annealing the sample in the furnace. After inserting the sample, and before starting the reaction, the tube was purged with argon gas for 20 min for making an inert environment. Then the temperature raised to 800°C at the rate of 5°/min and held at this temperature for 3 hrs under argon flow at 110 sccm.

Step 2.Synthesis of Co@NC@MoS_2 catalyst:

The Co@NC@MoS_2 catalyst was synthesized using a hydrothermal treatment of the Co@NC nanoparticles. Herein, 200 mg of Co@NC nanoparticles was dispersed in 25 ml of deionised water and sonicated for 1 hr. and, 0.20 mmol of $(NH_4)_6Mo_7O_{24} . 4H_2O$ and 2.14 mmol of L-cysteine were added to the Co@NC dispersion and again sonicated for 1 hr. The uniformly dispersed solution was then transferred into the 50 mL autoclave (with a Teflon lining) and heated at 200°C for 20 hrs. After cooling down, the precipitates were collected by centrifugation and washed with ethanol and water several times. After washing the as obtained Co@NC@MoS_2 catalyst was dried in a vacuum oven at 50°C overnight.

2.2.2.2. Physical characterization

The phase and structural elucidation of the synthesized catalyst was analyzed by Bruker Eco D8 ADVANCE X Powder X-ray diffractometer using the Ni filter applying Cu Kα radiation (λ = 1.54056 Å, 40 kV and 25 mA) in the 2θ range of 5°−80° with a rise of 0.00190/step. Autosorb IQ Quantachrome instrument was used for surface area calculation by nitrogen adsorption desorption isotherm at 77 K. The morphological

analysis of the catalyst was done by using a scanning electron microscope (SEM) from JEOL (JSM IT-300) provided with energy-dispersive X-ray diffractometer (Bruker). The microstructure and size of the product were examined by transmission electron microscopy (TEM), JEOL-2100 operated at 200 kV. XPS was done on ESCALab: 220-IXL with Mg Kα nonmonochromated X-ray beam having photon energy 1253.6 eV.

2.2.2.3. Electrochemical measurements

All the electrochemical measurements were done using CHI 760E electrochemical workstation at 25°C temperature. In the conventional three-electrode setup carbon-based electrode is used as a counter electrode,Ag/AgClas a reference electrode and catalyst coated glassy carbon electrode as a working electrode. The catalyst ink for coating the glassy carbon electrode was prepared by dispersing 5 mg of the catalyst in 500 μL of dimethylformamide containing 5 μL of 5 wt % Nafion and was sonicated for 120 min to prepare a homogeneous suspension. Out of this dispersion, only 5 μL was coated on glassy carbon electron and dried in vacuum. All the polarization data were collected at the scan rate of 5 mV s^{-1} in 1M KOH. The equation used for the conversion to reversible hydrogen electrode is $E_{RHE} = E_{Ag/AgCl} + 0.197 + 0.059*pH$. The determination of Tafel slope was done by fitting the linear region of the Tafel plot to the Tafel equation ($\eta = b \log(j) + a$) by again plotting the polarization curve. The iR correction was done by the elimination of Ohmic drop as stated by the equation $\eta_{corrected} = \eta - iR_s$ in which R_s denotes the solution resistance. Electrochemical impedance spectroscopy (EIS) was performed at different overpotential, that is, 200, 250 and 300 mV and a frequency range of 100000-1 Hz. For the stability study, we have used chronoamperometry at an applied potential of 305 mV. The double-layer capacitance was calculated for the determination of electrochemically active surface area ECSA analysis by the CV scans in a non-Faradaic potential range of as-prepared catalysts electrodes in 1 M KOH at a scan rate of 10 to 100 mV/s. Half of the differences in current density variation ($\Delta J = (J_{anodic}-J_{cathodic})/2$) at apotential of 1.16 V vs RHE plotted against scan rate fitted to a linear regression that allows thedetermination of double-layer capacitance (C_{dl}).

2.2.2.4. Theoretical methodology

The adsorption of oxygen atom and hydroxide molecule on Co@NC@MoS_2 heterostructure for oxygen evolution reaction is investigated by density functional theory (DFT) using the Vienna ab initio simulation package (VASP)[28] based on the projector augmented wave method (PAW)[29, 30] with a plane-wave basis set and periodic boundary conditions. The exchange correlation energy was calculated using the Perdew-Burke-Ernzerhof(PBE) functional.[31]The two-dimensional graphene/MoS_2heterostructure is constructed using 4*1*1 supercell of graphene and 3*1*1 supercellof MoS_2, resulting in lattice parameters a=9.82 Å , b=4.91 Å and c=30 Å. The c-direction is kept long enough to accommodate the heterostructure layers and the adsorbates with negligible interaction between their periodic layers. The optimized interlayer distance between the graphene and MoS_2 sheets is 3.63 Å. The nanospheres of Co@NC@MoS_2 are simulated with the layered heterostructure model in DFT. The cutoff energy for the plane wave basis is set to 550 eV with an energy convergence threshold of 10^{-4}eV. All the atoms are relaxed until the forces on them are less than 0.01 eV/Å. The supercell is sampled with 7*7*1 gamma-centered k-mesh. The van der Waals interactions in the bilayer have been accounted using the vdW exchange-correlation functional DFT-D2 method of Grimme.[32]

2.3. Result and Discussion The structural elucidation of the catalyst was done by using Powder X-ray diffractometer in the 2θ range of 5°−80°.The PXRD pattern of MoS_2 (Figure 2.1a) shows hexagonal crystal structure with two different diffraction peaks at a 2θvalue of 32.2°, and 57.1° which can be assigned to (100), and (110) crystal planes of MoS_2 (JCPDS No. 37-1492).[33]The absence of (002) plane and the broadening of the peaks indicate the presence of few layers of MoS_2 or the graphene-like MoS_2 in the sample.As for the PXRD pattern of the Co@NC@MoS_2 (Figure 2.1a), the peaks at 43.9°, 51.2°, and 75.5° attributed to (111), (200), and (220) crystal planes of cubic Co (JCPDS No. 15-0806).[34] The broad and less intense peak around 26° can be ascribed to the presence of a minute amount of graphitic carbon.[35] Apart from the above discussed peaks, there is a less intense peak at 32.3° and 57.2° attributed to the crystalplanes of MoS_2. The (002) plane is absent in the catalyst as well, which is again indicating the presence of few-layer MoS_2 over Co@NC nanoparticles.

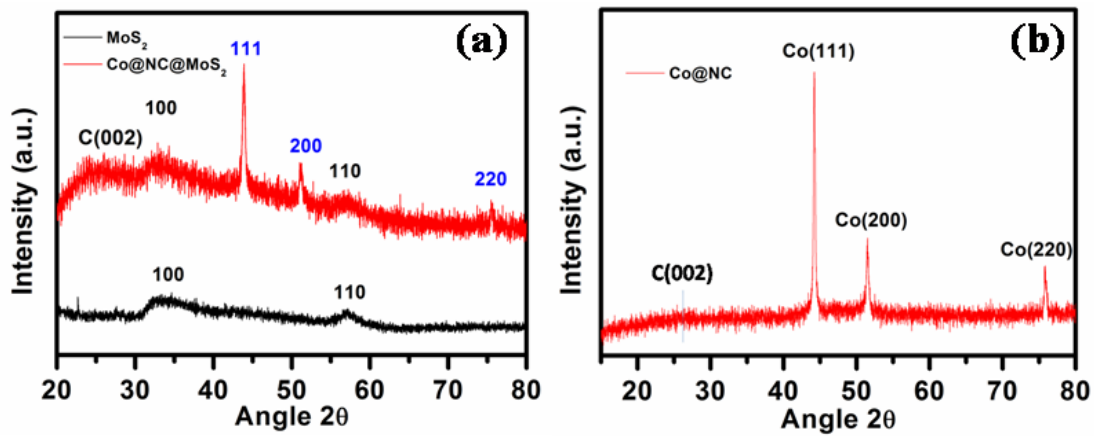

Figure2.1.*PXRD spectrum (a) of MoS_2 and Co@NC@$MoS_2$and (b) Co@NCnanospheres obtained from pyrolysis of MOF.*

In the PXRD pattern of as-synthesized Co@NC nanoparticles (Figure 2.1 b), the peaks located at 44.1°, 51.4° and 75.8° correspond to the presence of (111), (200) and (220) plane of cubic Co. The other very less intense peak around 25.6° show the presence of a very small amount of graphitic carbon present in the catalyst.Raman spectra of Co@NC precursor and Co@NC@MoS_2 catalyst were shown in Figure 2.2. For Co@NC, the peaks centred at 1350 cm^{-1} and 1585 $cm^{-1}$are ascribed to the well-known D and G bands of the carbon sheets.[36] The presence of both the peaks is consistent in Co@NC@MoS_2 demonstrating the presence of graphitic carbon on the cobalt nanosphere present in the catalystThe morphological analysis ofCo@NC and Co@NC@MoS_2 were shown in Figure 2.3. The SEM images of Co@NC (Figure 2.3a) shows theagglomerated cobalt nanoparticles formingsubmicrospheres. The morphology is retained even after the formation of the Co@NC@MoS_2 catalyst (Figure2d&e) with a few layers of MoS_2 grown on the surface of Co@NCspheres.The transmission electron micrographs of Co@NC(Figure 2.3 b&c) also confirms the spherical shape of nanoparticles with the presence of N-dopes carbon layer around the nanoparticles resulting in the formation of core-shell type nanostructures. The HRTEM images (inset Figure 2.3b) confirmthe presence of cobalt nanoparticles with the d-spacing of 0.205

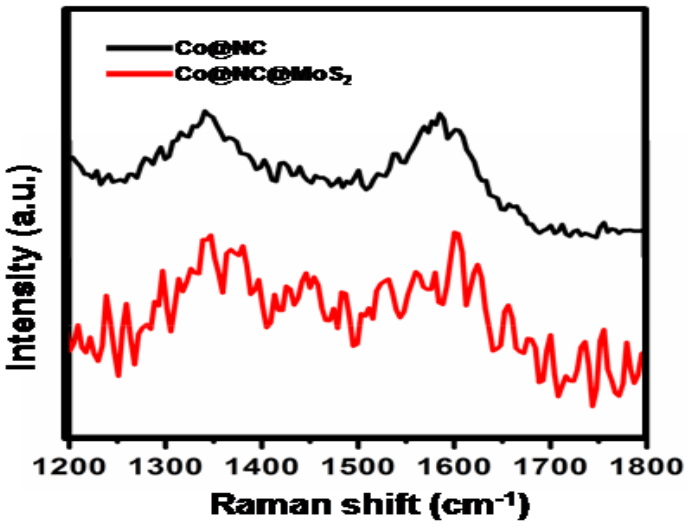

Figure 2.2 *Raman spectra showing the presence of graphitic carbon in the both Co@NC and Co@NC@MoS_2*

nm. The shell of the cobalt nanoparticles is having a lattice d-spacing 0.34 nm, which can be correlated to the presence of graphitic carbon.[37] The HRTEM images of the catalyst (Figure 2.3f) show the presence of MoS_2 layers over Co@NC with the d-spacing value of 0.27 nm corresponding to the (100) plane of hexagonal MoS_2.[38]

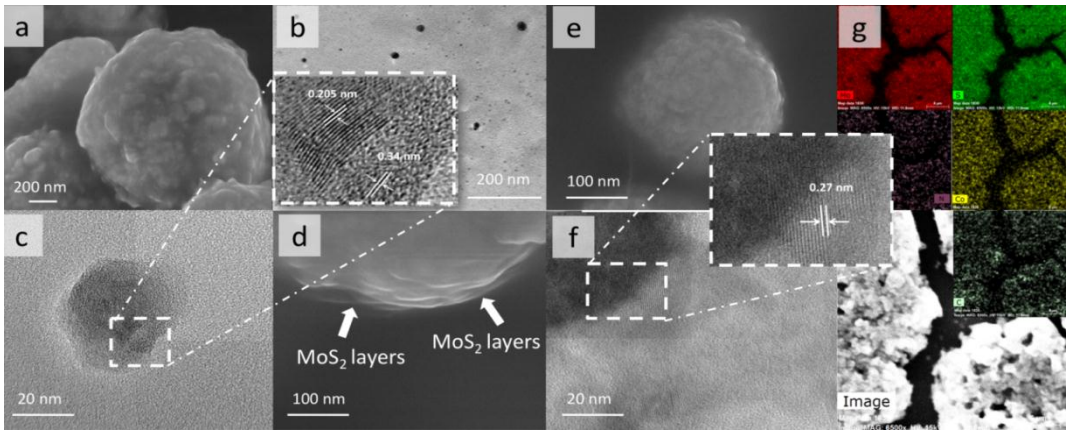

Figure.2.3 *(a) FESEM and (b) TEM images of Co@NC. (c) HRTEM image of Co@NC (d) and (e) FESEM images of Co@NC@MoS_2 showing the growth of a few layers of MoS2. (f) HRTEM images of Co@NC@MoS2 and (g) elemental mapping of the Co@NC@MoS2 showing the presence of Mo, S, Co, N and C in the catalyst.*

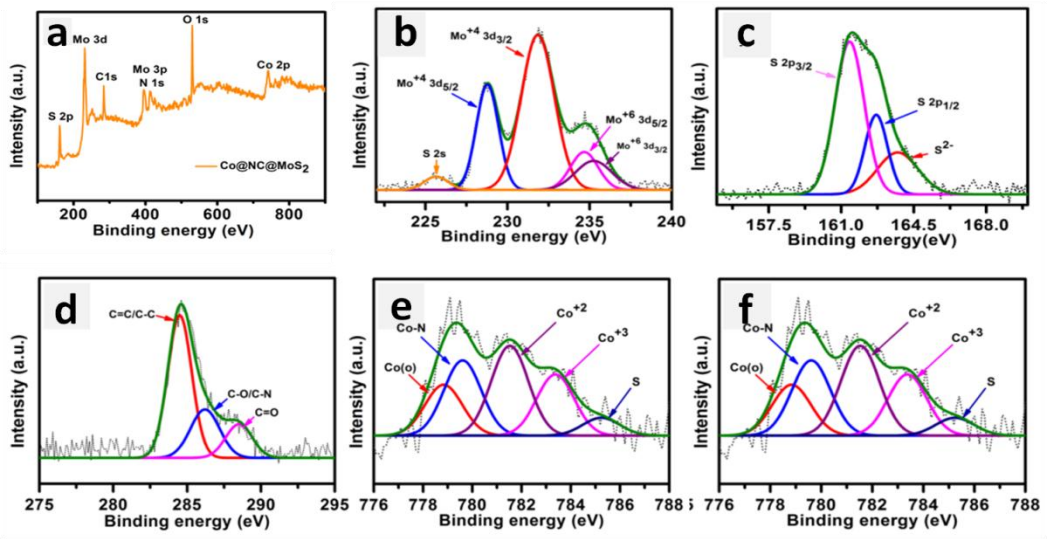

Figure2.4*shows the X-ray photoelectron spectra (XPS) of the Co@NC@MoS₂ catalyst. (a) wide scan XPS spectra The high-resolution spectra of Mo 3d, S2p, C 1s, Co 2p and N1s were expressed in b,c,d&f plots respectively. Experimental data were plotted using the dotted curve, and the fitting results were shown with solid curves. The peaks are assigned by oxidation states of different elements with theirsplitting term.*

The elemental mapping of Co@NC@MoS_2 displays the presence of Mo, S, Co, C and N in the catalyst (Figure 2.3 g). The electronic interaction and chemical composition of the catalyst can be understood from the X-ray photoelectron spectroscopy (XPS) measurements. The XPS survey spectrum indicates the presence of Mo, S, Co, C, and N elements in the Co@NC@MoS2 catalyst (Figure 2.4a). This is in-line with the results obtained from EDAX and elemental mapping. The deconvoluted Mo 3d peaks (Fig. 2.4b) appeared at 228.7 eV and 231.8 eV corresponding to Mo $3d_{5/2}$ and Mo $3d_{3/2}$ of Mo^{4+} spectral lines. The other two peaks at 234.6 eV and 235.2 eV can be assigned to Mo 3d5/2 and Mo 3d3/2 of Mo^{6+} spectral lines. The peak for Mo^{6+} was observed due to surface oxidation of MoS_2. [39] The peak at 225.6 eV can be allocated to S 2s. The peaks (Figure 2.4c) located at 161.4 eV and 162.6 eV can be attributed to S $2p_{3/2}$ and S $2p_{1/2}$ manifesting the binding energies of S2. The other peak at 163.7 eV can be assigned to the binding energy of bridging S in the catalyst.[39] The peak located at 284.4 eV shown in Figure2.4d corresponds to C=C/C–C of C 1s spectra. The intensity of this peak is still

higher for the catalyst showing the presence of the graphitized carbon shell after the

Element	Peak	BE (eV)	FWHM	Area (%)
Mo 3d	Mo^{4+} Mo^{6+} S 2s	228.7and 231.8 234.6 and 235.2 225.6	1.7 and 1.8 2.0 and 2.06 1.7	23.7 and 51.9 10.5 and 10.6 3.2
S 2p	S^{2-} S^{2-}(bridging)	261.4 and 162.6 163.7	1.66 and 1.28 2.30	56.09 and 22.58 21.32
C 1s	C=C/C-C C-O/C-N C=O	284.4 286.2 288.5	2.674 2.638 2.312	59.7 24.6 15.6
Co 2p	Co(o) Co-N Co^{+2} Co^{+3}	778.8 779.6 781.5 783.3	1.78 1.77 1.78 1.76	17.24 25.50 30.43 20.07
Mo 3p& N1s	Mo^{4+} Mo^{6+} N-Pyridinic N-Pyrrolic N- Graphitic	395.1 397.5 398.9 399.5 401.1	3.37 2.24 2.57 1.24 1.8	53.74 17.82 16.84 4.59 6.98

Table 2.1 *Deconvoluted peak parameters of the XPS analysis*

growth of a few MoS_2nanolayers. The other two peaks at 286.2 eV and 288.5 eV isshowing the presence of C-O/C-N and C=O in the catalyst.[40] The spectra for Co 2p shown in Figure 2.4e reveals the intense metallic Co peaks located at 778.8 eV. The other less intense peak at 779.6 eV shows the presence of Co-N linkage present in the catalyst.[41] There are two other less intense peaks present at 781.5 eV and 783.3 eV show the existence of Co^{+2} and Co^{+3} appearing due to the presence of trace amount of cobalt oxide (Co_xO_y).[42] The peaks at 395.1 eV and 397.5 eV are attributed to the Mo 3p of Mo^{+4} and Mo^{+6} species respectively, and the other three peaks at 398.9 eV, 399.5 eV and 401.1 eV can be attributed to the presence of pyridinic, pyrrolic and graphitic N respectively in the N 1s spectra.[43, 44] The N 1s with Mo 3p overlapped spectra are given in the Figure 2.4 f . All the deconvoluted parameters are documented in Table 2.1The element percentage from XPS analysis was also evaluated and provided in Table 2.2. The OER activity of the Co@NC@MoS_2 was examined by using simple three-electrode

Elements	Atomic %
Mo	16.21
S	33.94
C	20.24
N	7.23
Co	15.14
O	7.04

Table 2.2*Elemental percentage obtained from XPS analysis*

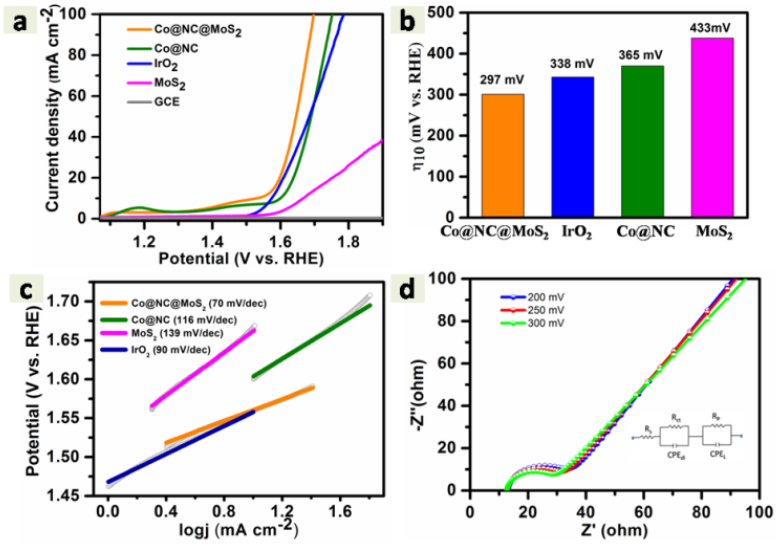

Figure 2.5 *Shows the electrochemical measurements of specific electrocatalysts for oxygen evolution in 1 M KOH alkaline medium. (a) Polarization curves (iR-corrected) of Co@NC@MoS_2 compared with Co@NC, IrO_2, Co@NC and MoS_2 respectively. (b)comparison of the overpotential values obtained from polarization curve at 10 mA cm^{-2}(c)the corresponding Tafel plots of all the above mentioned catalysts are displayed (d) Nyquist plot (with corresponding equivalent circuit) showing the Co@NC@MoS_2 @200, @250 mV, and @300 mV applied potential*

setup at 25°C in O_2 saturated 1M KOH. For a comparative study, the electrocatalytic activities of Co@NC, MoS_2 and commercial IrO_2 were also examined under the same condition. The performance of the Co@NC@MoS_2 was found to be superior to that of Co@NC, MoS_2 and commercially available IrO_2. The linear sweep voltammetry (LSV)

curves have shown in Figure 2.5a displays the comparison of the Co@NC@MoS_2electrocatalyst with MoS_2, Co@NC and commercially available IrO_2.The linear sweep voltammetry (LSV) curves have shown in Figure 2.5a displays the comparison of the Co@NC@MoS_2electrocatalyst with MoS_2, Co@NC and commercially available IrO_2.The Co@NC@MoS2 catalyst shows an onset potential of 200 mV and the minimum overpotential achieved at the current density of 10 mA cm-2is 297 mV. This obtained value is far better than that of Co@NC and MoS_2 catalysts. The Co@NC and MoS_2 show the overpotential of 365 mV and 433 mV, respectively (Figure 2.5b).From the post literature survey of the previously reported Co@NC based catalysts, we realized that, this is the best-known overpotential obtained at a current density of10 mA cm^{-2}For further insight, a study of the OER kinetics of the catalyst was carried out by plottingtheir Tafel slope as depicted in Figure 2.5c. The resulting Tafel slope values are 70, 90, 116 and 139 mV/dec for Co@NC@MoS_2, IrO_2, Co@NC and MoS_2 respectively.The lower Tafel slope value of catalyst renders a favourable OER kinetics than that of noblemetal-based catalyst (IrO_2).

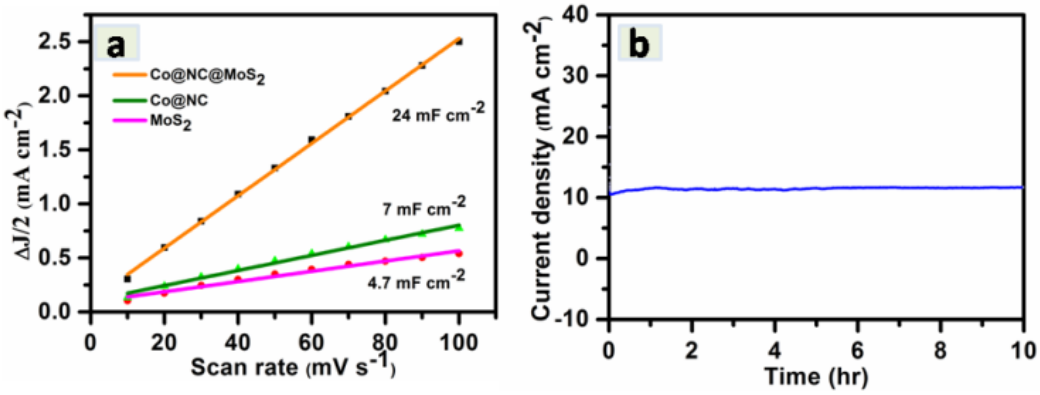

Figure 2.6 *(a) double layer capacitance calculation of Co@NC@MoS_2, Co@NC and MoS_2 (b) stability studies carried out using chronoamperometry*

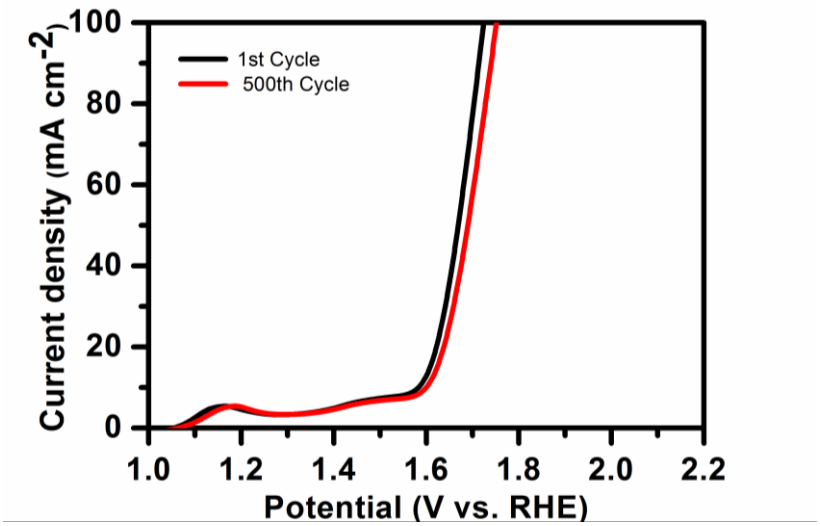

Figure 2.7 *Durability test of Co@NC using GCE in 1M KOH*

To understand the charge-transfer kinetics operating through the electrode-electrolyte interface, Electrochemical Impedance Spectroscopy (EIS) was performed.The corresponding Nyquist plot at various applied potentials is given inFigure 2.5d. All the spectra obtained in the measurement are fitted with the equivalent circuit depicted in Figure 2.5d. The equivalent circuit reveals two time-constant components R_{ct}-CPE_{dL} and R_p-CPE_L along with the solution resistance R_s. The constant phase angle element (CPE) explain the double-layer capacitance of the solid electrode. R_{ct}-CPE_{dL} gives information about the charge-transfer process, and the surface porosity can be correlated withR_p-CPE_L. The relationship between the charge transfer resistance and the applied potential is inversely proportional.The charge-transfer resistance (R_{ct}) of 12 Ω is obtained at an applied potential of 200 mV. The smaller value of R_{ct} demonstrates that the electrochemically active sites on the electrode surface are high, and the value of charge transfer between the electrode surface and electrolyte is also high. These observations from the Nyquist plot favors the overall OER process. For the determination of electrochemically active surface area (ECSA), the double-layer capacitance was measured at different scan rate (Figure 2.6 a). The C_{dl} values support the OER performance of all catalyst. The C_{dl} of Co@NC@MoS_2, Co@NC and MoS_2obtained as 24, 7 and 4.7 mF cm^{-2} respectively. The long term durability of the

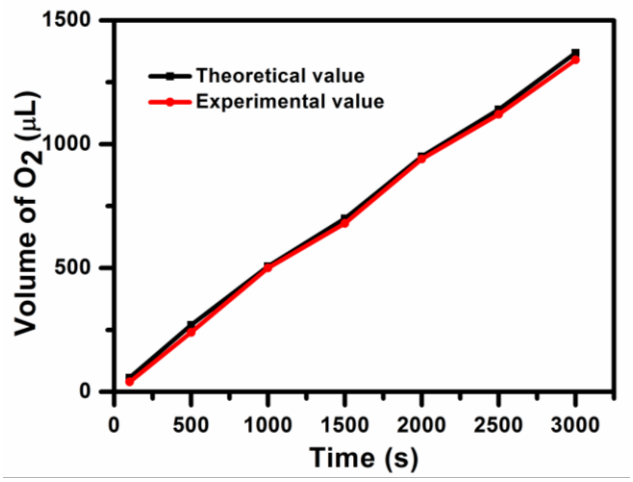

Figure 2.8 *volume of O_2 evolve at different time for the calculation of faradic efficiency the calculated value is the quantitative faradic yield for O_2 evolution*

catalyst was examined by the chronoamperometry (Figure 2.6 b)at an overpotential of 305 mV for 10 hr.. The longevity test of Co@NC catalyst is discussed in Figure 2.7. The durability test for the precursor Co@NC was done by continuously running 500 linear sweep voltammetry cycles. The significant change in the overpotential was found after 500 LSV cycles depicting the less stability of the precursor Co@NC.In order to calculate the faradic efficiency (Figure 2.8) and the amount of gas evolved,a water-gas displacement method is used in which the volume of the gas evolved noted with respect to the time. The ratio of experimental gas evolved with the theoretical gas evolved, isthe calculated faradic efficiency which is 97.9 % for Co@NC@MoS_2. The cyclic voltammetry curve for the calculation of double-layer capacitance (C_{dl}) is given in Figure 2.9. As oxygen evolution reaction is a four electron transfer process, we have studied its intermediate steps to observe the phenomenon at the surface of the heterostructure. This involves the calculation of adsorption energy of O-atom and OH^-molecule adsorbed on the surface of Co@NC@MoS_2heterostructure. In our theoretical model, we have tried to cover all the possible atomic sites. The strength of the adsorbate interaction with the absorbent and the amount of alteration of the properties of the system is described by the adsorption energy, which is given as

$$E_{ads} = E_{(surface\text{-}X)} - E_{(surface)} - E_{(X)}$$

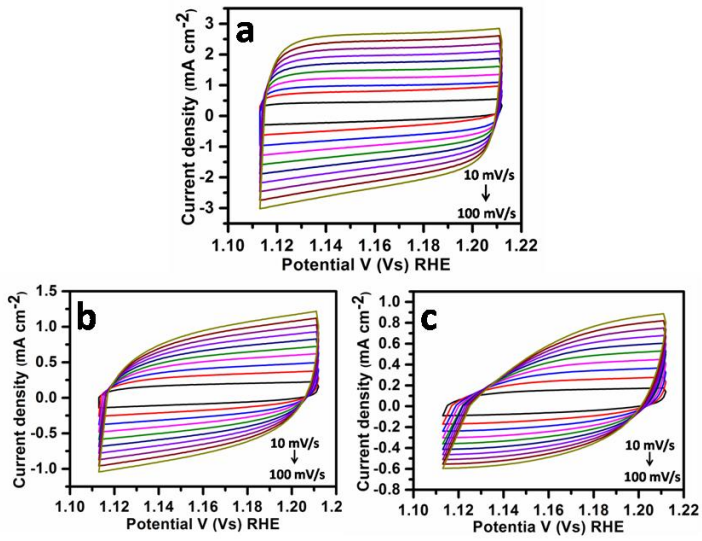

Figure 2.9 *Cyclic voltammetry curve of (a) Co@NC@MoS_2, (b) Co@NC and (c) MoS_2 for the calculation of C_{dl}*

where $E_{(surface-X)}$ is the total energy of the adsorbate and the surface together, $E_{(surface)}$ is the energy ofthe surface and $E_{(X)}$ is the energy of the O or OH molecules.Further, the Gibbs free energies are calculated at standard conditions (pH = 0, T = 298.15 K) and U = 1.23 V, the equilibrium potential for OER process.

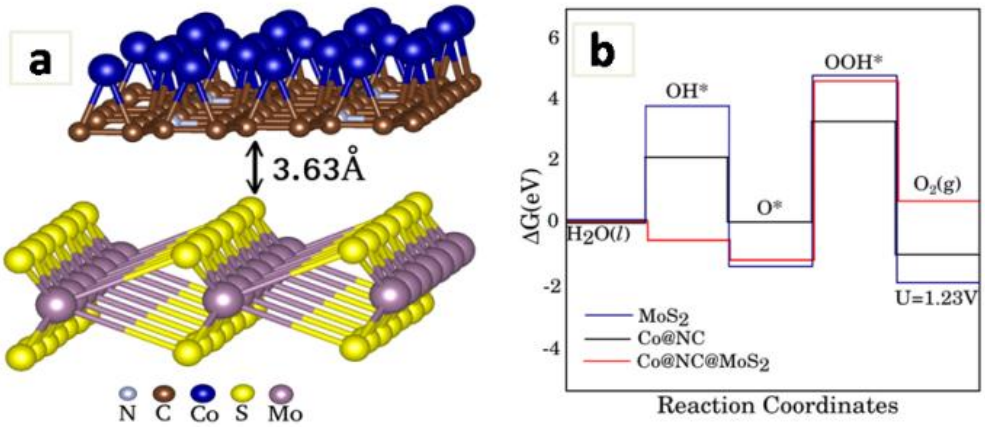

Figure 2.10 *(a) Co@NC@MoS_2 heterostructure is displayed, top layer Co, middle layer N-doped carbon and bottom layer MoS2, (b) Calculated Gibbs free energy diagram of MoS_2 and Co@NC and Co@NC@MoS_2, all energies are calculated on the surface of MoS_2 side*

S.No.	Surface	Total Energy	E ads (eV)	Bond length (Å)

		(eV)		
1.	MoS_2+O	-68.76584279	+1.26	d(Mo1-O) = 1.99 d(Mo2-O) = 1.89 d(Mo3-O) = 1.89
2.	MoS_2+OH	-71.93280111	+0.55	d(Mo1-O) = 2.16 d(Mo2-O) = 2.16 d(Mo3-O) = 2.05 d(O-H) = 0.99
3.	Co@NC+O (N-site)	-190.49062787	+1.42	d(N-O) = 1.83
4.	Co@NC+O (C-site)	-190.69369699	+1.21	d(C1-O) = 1.90 d(C1-O) = 1.71
5.	Co@NC+OH (N-site)	-195.59675697	-1.24	d(N-O) = 1.83 d(O-H) = 0.98
6.	Co@NC+OH (C-site)	-195.38499636	-1.02	d(C1-O) = 1.90 d(C1-O) = 1.71 d(O-H) = 0.98
7.	Co@NC@MoS2 + O (O on MoS2)	-242.87172627	-2.82	d(Mo -O)= 1.75
8.	Co@NC@MoS2+OH (OH on MoS2)	-246.27386288	-3.77	d(Mo -O)= 1.91 d(O-H) = 1.01

Table 2.3.*Total energy of adsorbtion of O atom and OH molecule.*

The Gibbs energy diagram (Figure 7b) represents all the intermediate steps providing the complete picture of the reaction path and the quality of the catalyst. For the comparison, Gibbs energies for MoS_2 and Co@NC are plotted along with Co@NC@MoS_2. We have adopted the intermediates particularly on MoS_2 surface of the heterostructure as a correlative theoretical model.All the theoretical binding energies are provided in the supplementary information. For Co@NC@MoS_2 heterostructure, steps 1, 2 and 4 are downhill whereas step 3 is uphill. So, step 3 that is O* transferring into OOH* is considered as the potential determining step for heterostructure. (Figure 2.It can be understood from the energy diagram that by growing few layers of MoS_2 on the surfaces of Co@NCnanospheres lowers the Gibbs energy values of the intermediates which means it makes the adsorption of O and OH easier than those of Co@NC and MoS_2. This can also be interpreted from the adsorption energy values provided in Table T3. The theoretical OER overpotential is calculated using the following expression[45]: η^{OER} = (

$\Delta G_2 + \Delta G_3)/2e$ -1.23 V, where ΔG_2 and ΔG_3 denote the Gibbs free energy of the intermediate steps of OER. A detailed discussion of how the Gibbs energy is calculated within the DFT framework is provided in the supplemental material. We obtain the over-potential value of 370 mV calculated theoretically for Co@NC@MoS_2 which is close to the experimental value of 297 mV. The theoretical simulations give the important insight of the electrocatalytic process that makes Co@NC@MoS_2 composite as a very effective catalyst for OER.

2.4 Conclsion

In summary, Co@NC@MoS_2 catalyst was synthesized through a hydrothermally grown few layers of MoS_2 over Co@NCnanospheres derived from metal-organic framework. The catalyst shows excellent OER activity with onset potential of 200 mV and overpotential of 297 mV at a current density of 10 mA cm^{-2} and a Tafel slope value of 70 mV/dec in 1M KOH solution. A durability tests up to 10 hrs using chronoamperometry, do not show any change in the current density of the catalyst. Few layer MoS_2 having defects in its basal plane enhances the electron transfer towards Co@NC,possibly due to the synergistic effect. The overall kinetics of the OER improved by the mutual interaction between MoS_2 layers and Co@NC nanoparticles. Similar methodology can be applied for the other metal nanoparticles for similar electrochemical applications.

Note:

- The permission has been granted by the authors and corresponding author of the published paper prior to adopting in the present thesis. The associated relevant publication is:

Gaur, Ashish, Parrydeep K. Sachdeva, Rajinder Kumar, Takahiro Maruyama, ChandanBera, and VivekBagchi. "Ultrathin MoS_2 wrapped N-doped carbon-coated cobalt nanospheres for OER applications." *Sustainable Energy & Fuels* 5, no. 3 (2021): 801-807.

References

1. M. A. Zambrano-Monserrate, M. A. Ruano and L. Sanchez-Alcalde, *Science of The Total Environment*, 2020, **728**, 138813.

2. Y. Li and J. Lu, *ACS Energy Letters*, 2017, **2**, 1370-1377.

3. N.-T. Suen, S.-F. Hung, Q. Quan, N. Zhang, Y.-J. Xu and H. M. Chen, *Chemical Society Reviews*, 2017, **46**, 337-365.

4. I. Roger, M. A. Shipman and M. D. Symes, *Nature Reviews Chemistry*, 2017, **1**, 0003.

5. Q. Shi, C. Zhu, D. Du and Y. Lin, *Chemical Society Reviews*, 2019, **48**, 3181-3192.

6. J. Lai, A. Nsabimana, R. Luque and G. Xu, *Joule*, 2018, **2**, 76-93.

7. Q. Qian, Y. Li, Y. Liu, L. Yu and G. Zhang, *Advanced Materials*, 2019, **31**, 1901139.

8. C. C. L. McCrory, S. Jung, I. M. Ferrer, S. M. Chatman, J. C. Peters and T. F. Jaramillo, *Journal of the American Chemical Society*, 2015, **137**, 4347-4357.

9. Y. Lee, J. Suntivich, K. J. May, E. E. Perry and Y. Shao-Horn, *The Journal of Physical Chemistry Letters*, 2012, **3**, 399-404.

10. P. Yu, J. Ma, R. Zhang, J. Z. Zhang and G. G. Botte, *ACS Applied Energy Materials*, 2018, **1**, 267-272.

11. J. Nai, Y. Lu, L. Yu, X. Wang and X. W. Lou, *Advanced Materials*, 2017, **29**, 1703870.

12. Z. Chen, X. Duan, W. Wei, S. Wang and B.-J. Ni, *Journal of Materials Chemistry A*, 2019, **7**, 14971-15005.

13. Y. Yao, N. Mahmood, L. Pan, G. Shen, R. Zhang, R. Gao, F.-e. Aleem, X. Yuan, X. Zhang and J.-J. Zou, *Nanoscale*, 2018, **10**, 21327-21334.

14. U. K. Sultana and A. P. O'Mullane, *ChemElectroChem*, 2019, **6**, 2630-2637.

15. Y. Bai, H. Zhang, Y. Feng, L. Fang and Y. Wang, *Journal of Materials Chemistry A*, 2016, **4**, 9072-9079.

16. L. Najafi, S. Bellani, R. Oropesa-Nuñez, A. Ansaldo, M. Prato, A. E. Del Rio Castillo and F. Bonaccorso, *Advanced Energy Materials*, 2018, **8**, 1703212.

17. B. Sidhureddy, J. S. Dondapati and A. Chen, *Chemical Communications*, 2019, **55**, 3626-3629.

18. A. Q. Mugheri, A. Tahira, U. Aftab, M. I. Abro, S. R. Chaudhry, L. Amaral and Z. H. Ibupoto, *RSC Advances*, 2019, **9**, 5701-5710.

19. G. Zhu, X. Xie, X. Li, Y. Liu, X. Shen, K. Xu and S. Chen, *ACS Applied Materials & Interfaces*, 2018, **10**, 19258-19270.

20. J.-Y. Wang, W.-T. Liu, X.-P. Li, T. Ouyang and Z.-Q. Liu, *Chemical Communications*, 2020, **56**, 1489-1492.

21. P. Ganesan, M. Prabu, J. Sanetuntikul and S. Shanmugam, *ACS Catalysis*, 2015, **5**, 3625-3637.

22. X. Yin, Y. Yan, M. Miao, K. Zhan, P. Li, J. Yang, B. Zhao and B. Y. Xia, *Chemistry – A European Journal*, 2018, **24**, 556-560.

23. M. Chatti, T. Gengenbach, R. King, L. Spiccia and A. N. Simonov, *Chemistry of Materials*, 2017, **29**, 3092-3099.

24. X. Kong, N. Wang, Q. Zhang, J. Liang, M. Wang, C. Wei, X. Chen, Y. Zhao and X. Zhang, *ChemistrySelect*, 2018, **3**, 9493-9498.

25. Z. Sun, M. Yang, Y. Wang and Y. H. Hu, *ACS Applied Energy Materials*, 2019, **2**, 1102-1110.

26. B. Tang, Z. G. Yu, H. L. Seng, N. Zhang, X. Liu, Y.-W. Zhang, W. Yang and H. Gong, *Nanoscale*, 2018, **10**, 20113-20119.

27. X. Zhao, X. Ma, Q. Lu, Q. Li, C. Han, Z. Xing and X. Yang, *Electrochimica Acta*, 2017, **249**, 72-78.

28. G. Kresse and D. Joubert, *Physical Review B*, 1999, **59**, 1758-1775.

29. P. E. Blöchl, *Physical Review B*, 1994, **50**, 17953-17979.

30. D. Vanderbilt, *Physical Review B*, 1990, **41**, 7892-7895.

31. J. P. Perdew, K. Burke and M. Ernzerhof, *Physical Review Letters*, 1996, **77**, 3865-3868.

32. S. Grimme, *Journal of Computational Chemistry*, 2006, **27**, 1787-1799.

33. C. P. Veeramalai, F. Li, Y. Liu, Z. Xu, T. Guo and T. W. Kim, *Applied Surface Science*, 2016, **389**, 1017-1022.

34. Y. Su, Y. Zhu, H. Jiang, J. Shen, X. Yang, W. Zou, J. Chen and C. Li, *Nanoscale*, 2014, **6**, 15080-15089.

35. B. Gupta, N. Kumar, K. Panda, V. Kanan, S. Joshi and I. Visoly-Fisher, *Scientific Reports*, 2017, **7**, 45030.

36. M. Pawlyta, J.-N. Rouzaud and S. Duber, *Carbon*, 2015, **84**, 479-490.

37. Y. Liu, P. Dong, M. Li, H. Wu, C. Zhang, L. Han and Y. Zhang, *Frontiers in Materials*, 2019, **6**.

38. L. Tian, R. Wu and H. Liu, *Journal of Materials Science*, 2019, **54**.

39. L. Zhao, J. Jia, Z. Yang, J. Yu, A. Wang, Y. Sang, W. Zhou and H. Liu, *Applied Catalysis B: Environmental*, 2017, **210**, 290-296.

40. A. Dolgov, D. Lopaev, C. Lee, E. Zoethout, V. Medvedev, O. Yakushev and F. Bijkerk, *Applied Surface Science*, 2015, **353**, 708-713.

41. Y. Chen, S. Zhao and Z. Liu, *Physical chemistry chemical physics : PCCP*, 2015, **17**.

42. C. Wu, D. Liu, H. Li and J. Li, *Small*, 2018, **14**, 1704227.

43. R. Li, L. Yang, T. Xiong, Y. Wu, L. Cao, D. Yuan and W. Zhou, *Journal of Power Sources*, 2017, **356**, 133-139.

44. H. Zhong, R. Tian, X. Gong, D. Li, P. Tang, N. Alonso-Vante and Y. Feng, *Journal of Power Sources*, 2017, **361**, 21-30.

45. I. C. Man, H.-Y. Su, F. Calle-Vallejo, H. A. Hansen, J. I. Martínez, N. G. Inoglu, J. Kitchin, T. F. Jaramillo, J. K. Nørskov and J. Rossmeisl, *ChemCatChem*, 2011, **3**, 1159-1165.

Chapter 3a

Intense nano-interfacial interactivity stimulates OER in MOF-derived superhydrophilic CuO-NiO heterostructure

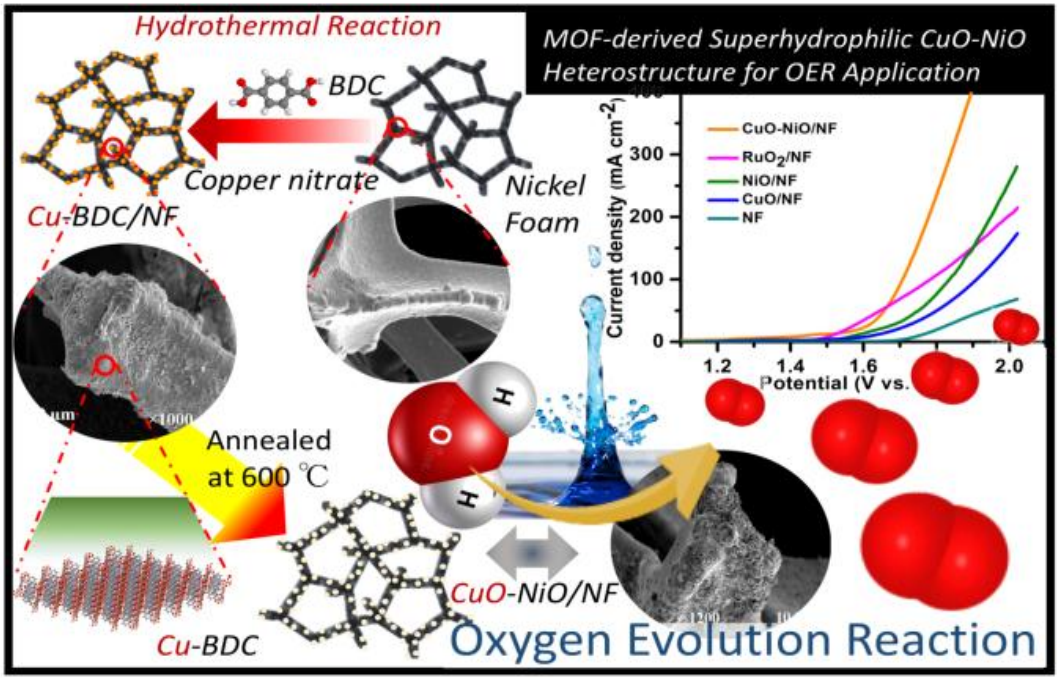

Brief Outcome: *Human survival might be at stake if the rate of carbon emission goes on like this in the near future. A clean energy alternative is a must to resolve the twin problem of CO2 emission and fossil fuel exhaustion. In this regard, hydrogen can be a promising carbon-neutral candidate which can effectively attenuate the global energy crises towards a sustainable solution. However, the large-scale hydrogen production from electrochemical water splitting is still a challenge that proceeds through a sophisticated four-electron transfer mechanism of oxygen evolution reaction (OER) at the anode. The development of efficient, durable, earth-abundant and cheap electrocatalysts for oxygen evolution reaction is a scorching area of research. Inspired by the synergistic effect existing along with the interfaces of the heterostructures, we designed the nanointerfaces between CuO and NiO phases in CuO-NiO hybrid nanostructures formed over NF, showing strong interactions. The catalyst was synthesized by the hydrothermal growth of metal-organic framework (Cu-BDC) on Nickel Foam (NF), followed by temperature-controlled calcination. The contact angle measurement was performed and found to be 0°, demonstrating the superhydrophilic nature of the catalyst. The catalyst CuO-NiO/NF shows a low overpotential of 231 mV in driving a current density of 10 mA cm-2 and exhibits a Tafel slope value of 100 mV/dec. The catalyst's durability was measured up to 20 hr using chronoamperometry technique. DFT calculations indicate the existence of strong interfacial interactions which is further manifested in the XPS analysis. The results obtained from DFT are also in line with the experimental data.*

3a.1. Introduction

Recently, a new climate prediction was issued by World Meteorological Organization (WMO), stating that, "There is a ~20% chance that one of the next 5 years will be at least 1.5°C warmer than pre-industrial levels, but the chance is increasing with time." The heat stress due to high surface temperature in the coming days would reach extreme affecting human health, productivity, and mortality in many places on Earth.[1] Rising levels of CO_2 in the ocean causing huge proliferation of toxic algae, which is a potential threat to marine life, coastal communities, aquaculture and fisheries and of course human health.[2] The ocean absorbs CO_2 at a rate of 22 million tons per day as revealed by the National Oceanic and Atmospheric Administration. Increased acidity of the ocean's surface water resulting in the dissolution of shells and skeletons causing the extinction of numerous species. An effort to obtain sustainable and clean energy,[3] using electrocatalytic hydrogen generation reactions[4,5] and oxygen evolution reactions [6-8] could be potential solutions towards environmental degradation. Well known Ru and Ir based catalysts are still the most efficient and productive electrocatalyst for oxygen evolution reaction.[9,10] However the extensive use of these catalysts are not commercially feasible due to less abundance and high cost. Organic-inorganic hybrid materials such as metal-organic framework (MOFs) and zinc-imidazole frameworks (ZIFs) with tunable porosity and morphology have shown immense potential in this regard. The MOF derived materials that contain controllable surface functionalities witha high surface area are promising materials for the electrocatalytic application.[11-16] Tremendous efforts have been devoted towards the investigation offirst-row transition metal-based substitutes of precious metal (Ir and Ru) electrocatalyst.[17-19]Among them, iron, cobalt, nickel and copper-based oxide,[20-22] sulphide,[23,24] nitride,[25,26] and phosphide [27,28] have attracted significant interest. Oxides due to their structural tenability and variable valence state, have attracted considerable attention for oxygen evolution reaction. The OER performance of binary-oxides prevails over single oxide phases. Copper-based compounds have great potential for electrocatalytic applications because of their low cost and high abundance.[29, 30] The redox-active properties of copperare also well known as it acts as a metal centre in many biological enzymatic reactions.[31, 32] The oxidation of Cu (II) to Cu (III) and the reduction

of Cu(II) to Cu(I) and Cu(0) is a well-knownredox property of copper oxide. Due to the high electron mobility within the electrocatalyst, copper oxide-based materials are highly active for oxygen evolution reaction.[33] The higher valence states of oxide materials act as an active site for the electrocatalytic process similarly in NiO the surface Ni^{3+} are considered as the most active adsorption site.[34,35] Several approaches have been devoted to improving the electrocatalyticperformance of the single-phase including the heteroatom doping,[36, 37] conducting carbon support.[38,39] The formation of heterointerfaces in oxide can also enhance the electrocatalytic performance by electronic structure modulation and synergistic effect. Xiong et al. have Shown Co-dopedCuOnanoarray on copper foam (Co-CuO NA/CF) via a cation exchange reaction as a 3D OER catalyst[29] while khan et al. has shown an increase in the OER activity of NiO phase by forming heterostructure with NiS phase.[40] Herein, we have created a nano-interface between CuO and NiOto avail the synergistic effect existing in between these phases for a better OER performance.The strong interaction between both the phases was confirmed by X-ray photoelectron spectroscopy (XPS). The *in-situ* synthesis of both the phases was done by using Cu-BDC MOF as a precursor. The MOF coated Nickel foam electrode then calcined in the tubular furnace in a temperature control solid-state reaction. The heterointerfaces between both phases enhance the OER activity resulting in a low overpotential of 231 mV at 10 mA cm^{-2} current density in 1 M KOH solution. This strong interaction between the two phases resulting in an excellent electrocatalytic activity was also studied using density functional theory (DFT), which provides the mechanistic insight of the reaction. Superhydrophilicbehaviour of the catalyst allows the transfer of the ions quickly from the electrolyte to the electrode surface and accelerates the mass transport process and thus enhances the electrocatalytic performance.

3a.2. Experimental section

3a.2.1. Materials

All chemicals were obtained from several commercial sources and used without further modification. Copper (II) nitrate hexahydrate ($Cu(NO_3)_2.\ 6H_2O$, 99%) and 1,4-benzenedicarboxylic acid (C_6H_4-1,4$(COOH)_2$, 98%) were purchased from Sigma Aldrich. N, N-dimethylformamide (99.8%), Nafion perfluorinatedresin (5 wt% in a mixture of the lower aliphatic alcohols and water, contains 45% water) were also purchased from Sigma Aldrich. Sodium hydroxide pellets and commercial RuO_2 were purchased from TCI. All the preparations were done using deionised water.

3a.2.2. Methodology

3a.2.2.1. Synthesis of Catalyst

Catalyst synthesis section is subdivided into two major steps as per following description

Step 1. Synthesis of Cu-BDC MOF: The metal-organic framework was synthesized using 4 mmol of $Cu(NO_3)_2.6H_2O$, and 4 mmol of 1,4-benzenedicarboxylic acid (H_2BDC), under alkaline condition usingN,N-dimethylformamide (DMF) as a solvent. Firstly, in 10 ml of N,N-dimethylformamide (DMF) containing 4 mmol of 1,4-benzenedicarboxylic acid (H_2BDC) were taken in a beaker and 1 mL of 0.5 M NaOH solution was added with vigorous stirring. In the second beaker, 4 mmol of $Cu(NO_3)_2.6H_2O$ were dissolved in 10 mL of N,N-dimethylformamide (DMF). Both the solutions were mixed in the 50 mL Teflon-lined stainless steel autoclave with a piece of nickel foam (0.5 cm × 0.5 cm). After the mixing of all the precursors, the autoclave was heated at 160°C for 24 hr.The as-obtained electrode was washed with DMF and DI water several times and dried at 60 degrees in the oven for 6 hours.

Step 1. Synthesis of CuO-NiO hybrid nanostructures: Heterostructures of CuO and NiO over NF were prepared by the controlled solid-state reaction of the Cu-BDC MOF under an inert atmosphere. The obtained Cu-BDC MOF on NF substrate was then calcined in the furnace at 600°C for 4 h. The ramp rate of heating was kept at 5°C per

minute. After calcination, flower-likeheterostructures of CuO-NiOwere formed over nickel foam (NF).

Synthesis of CuO nanoparticles : The synthesis of CuO nanoparticles are done by using metal organic framework as a precursor ($Cu_2(OH)_2(BDC)$)The metal organic framework was synthesized using 4mmolof $Cu(NO_3)_2.6H_2O$, and4mmolof 1,4-benzenedicarboxylic acid (H_2BDC), Sodium hydroxide and N,N-dimethylformamide (DMF). Firstly in 10 ml of N,N-dimethylformamide (DMF) 4 mmol of 1,4-benzenedicarboxylic acid (H_2BDC) were mixed in the beaker then 1 mL of 0.01 M NaOH solution added with rigorous stirring. In second beaker 4 mmol of $Cu(NO_3)_2.6H_2O$ were dissolve in 10 mL of N,N-dimethylformamide (DMF).Both the solutions were mixed together in the 50 mL teflon-lined stainless steel autoclave. The as obtained MOF was heated in furnace at 600°C for 3 hr at a ramp rate of 5°C/min. After annealing CuOwere obtained and used as it is.

Synthesis of NiO/NF: The NiO/NF electrode was obtained by heating the bare nickel foam at 600°C for 3 hr at a ramp rate of 5°C /min. After annealing the NiO nanostructures were formed over nickel foam.

3a.2.2.2. Physical characterization

The preliminary structural analysis of CuO-NiO/NF hybrid nanostructures were performedby Bruker Eco D8 ADVANCE X Powder X-ray diffractometer. The diffractometer consists of a Ni-filter that applies Cu K_α radiation (λ = 1.54056 Å, 40 kV and 25 mA) in the 2θ range of 5°−80° with a rise of 0.00190/step. The JEOL (JSM IT-300) scanning electron microscope SEM was used for the morphological analysis of the hybrid structure equipped with an energy-dispersive X-ray diffractometer (Bruker). The microstructure and the particle size analysis of the hybrid CuO-NiO/NF were examined by transmission electron microscopy (TEM) JEOL-2100 operated at 200 kV. X-ray Photoelectron Spectroscopy (XPS) was done onESCALab: 220-IXL with Mg K_α non-monochromated X-ray beam having photon energy 1253.6 eV.

3a.2.2.3. Electrochemical measurements

The electrochemical study was performed by using CHI 760E electrochemical workstation at room temperature. The three-electrode setup was used in which graphite electrode, Ag/AgCl electrode, were used as a counter electrode and reference electrode respectively. The as-synthesized catalyst over NF was used as a working electrode. A comparative study was performed by preparing separate ink of CuO and RuO_2 catalysts to fabricate respective working electrodes. Generally, catalyst inks (for the coating on the nickel foam) were prepared by using 10 mg of the corresponding catalyst in 500 µL of dimethylformamide containing 10 µL of 5 wt % Nafion solution. Before the fabrication of the working electrodes, the ink was sonicated for 120 min, to obtain a homogeneous suspension of the catalyst. Then 40 µL of ink was coated on the nickel foam and dried in a vacuum. All the polarization data were collected at the scan rate of 5 mV s^{-1} in 1M KOH. Theoretical of the OER reaction has been calculated by $E_{RHE} = E_{Ag/AgCl} + 0.197 + 0.059\times pH$ equation with iR correction $\eta_{corrected} = \eta - iR_s$in which R_s denotes the solution resistance. Electrochemical stability at a potential of 0.6 V for 20 hrwas measured by chronoamperometry. The Tafel slope was calculated by fitting the linear region of the Tafel curve to the Tafel equation ($\eta = b \log(j) + a$). Electrochemical impedance spectroscopy (EIS) was carried out with an applied potential of 100mV under a frequency range of 100000 Hz - 1Hz. The double-layer capacitance and electrochemically active surface area (ECSA) analysis completed by the CV scans in a non-Faradaic potential range in 1 M KOH at a scan rate of 20 to 200 mV/s.

3a.2.2.4. Theoretical methodology

The DFT calculations were carried out using VASP[41, 42] (Vienna Ab-initio Simulation Package) by calculating the E_{ads} of the intermediate species interacting with the different active sites on the heterostructure and individual phases. The calculation was carried out with projected augmented waves (PBE) in the generalized gradient approximation (GGA) with Perdew-Burke-Emzerhof (PBE) exchange-correlation function. For CuO, NiO and CuO-NiOheterostructure, 1 x 1 x 1 supercell were constructed for DFT calculations and 15 Å vacuum was allowed in the z-direction to restrict the periodic imaging interactions.

A 7 x 7 x 1 gamma-centered K-mesh was employed along with 520 eV cut-off energy. The energy conversion was set to be 10^{-4} eV and the forces were converged within 0.01 eV/Å for structural optimization.

3a.3. Result and Discussion

The primary structural elucidation of the catalyst was carried out by using powder X-ray diffraction spectroscopy and shown in figure (3a.1 (a)). The PXRD pattern of CuO-NiO/NF shows sharp and distinct reflections indicating the presence of both CuO and NiO phases revealing the existence of hybrid heterostructures over NF.

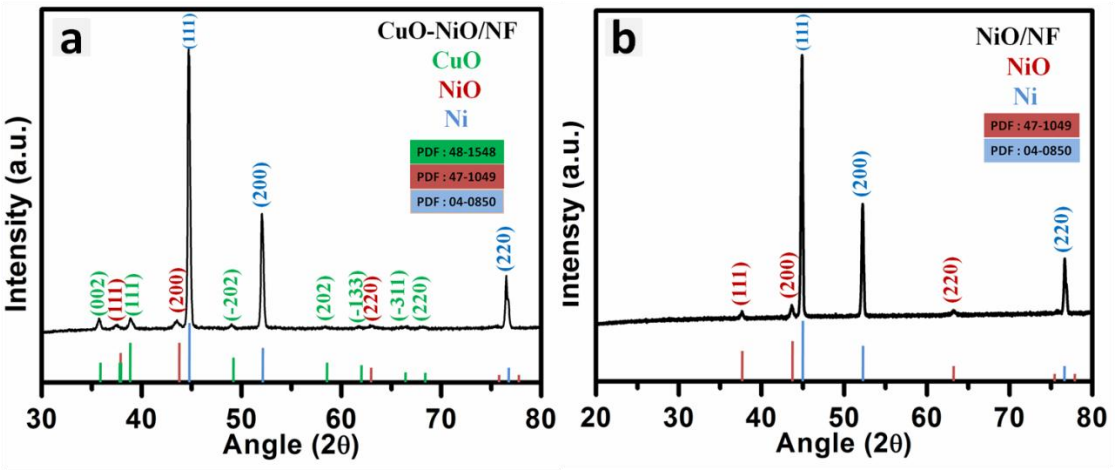

Figure 3a.1. *PXRD spectrum (a) CuO-NiO/NF (b) NiO/NF nanospheres obtained from pyrolysis of MOF.*

The diffraction peaks at 35.2°, 38.4°, 48.6°, 58.07°, 61.4°, 65.8° and 67.8° can be assigned to (002), (111), (-202), (202), (-133), (-311) and (220) crystal planes of CuO (JCPDS No. 48-1548).[43,44] The other peaks at 37.05°, 43.2° and 62.8° correspond to (111), (200) and (220) crystal plane of nickel oxide (JCPDS No. 47-1049).[45,46] The phase elucidation of bare nickel foam and NF after pyrolysis was performed using PXRD. Peaks of NiOwere observed in the PXRD pattern of pyrolyzed nickel foam showing the formation of nickel oxide on the surface of NF. In figure 3a.1 b, the peaks at 37.5°, 43.5° and 62.8° correspond to (111), (200) and (220) crystal planes of nickel oxide (JCPDS No. 47-1049). The results obtained from the PXRD spectra are also consistent with the HRTEM analysis.

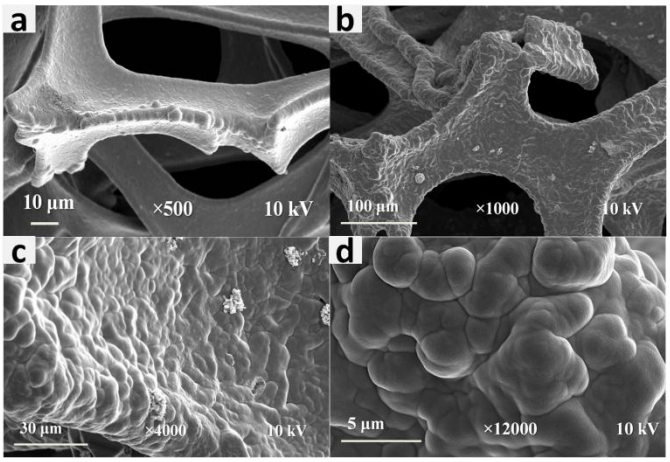

Figure 3a.2. *SEM images of bare nickel foam (a) and Co_3O_4-NiO/NF at different magnification for (b) 10µm (x500) (c) 10 µm (x1000) and (d) 10 µm (×1200) showing the presence of CuO-NiO nanoflowers uniformly grown over nickel foam*

The morphological analysis of the catalyst was done by scanning electron microscopy (SEM) and the corresponding images are shown in Figure 3a.2 . The SEM image of bare nickel foam is shown in Figure 3a.2 (a).The SEM images of the uniform growth of the Cu-BDC over NF is shown in Figure 3a. 2(b-c). The nickel foam electrode was perfectly coated with the Cu based metal-organic framework. The hybrid nanostructures of CuO-NiO over nickel foam can be seen in the SEM images of catalyst CuO-NiO/NF (Figure 3a.2(d)). The fine distribution of the heterostructure is uniform over the nickel foam.. The Transmission electron microscopy (TEM) analysis was also in line with the previous analysis. TEM image of CuO-NiO/NF (Figure 3a.3a&b) shows the uniform formation of CuO-NiO hybrid nanostructures of the range of 25 to 35 nm. The HRTEM images (Figure 3a.3(c-d)) of CuO-NiO/NF shows the formation of the interface between two phases. The interface is shown by the dotted line.

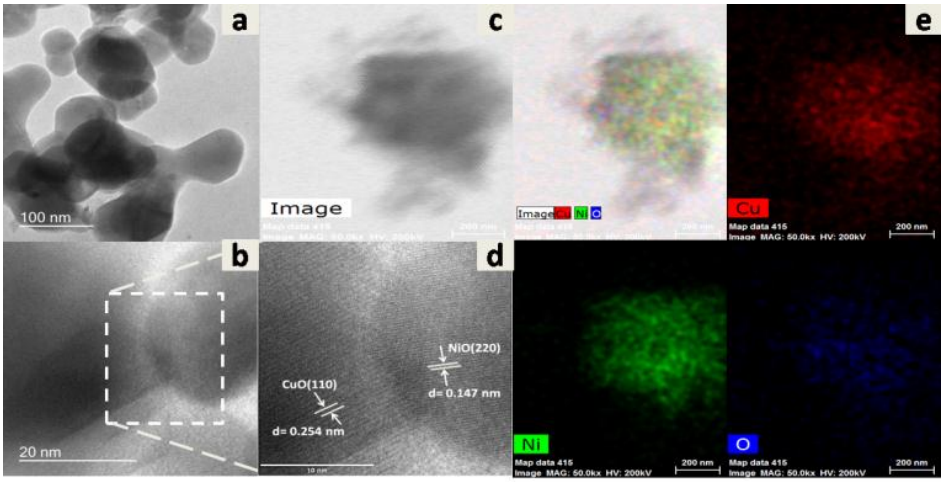

Figure 3a.3. *TEM images of (a) CuO-NiO hybrid nanostructures (b) HRTEM images of the catalyst (d) the interface formation between CuO and NiO in the catalyst with corresponding lattice fringe width (c) & (e) STEM elemental mapping of CuO-NiO/NF showing the presence of all Cu, Ni and O elements.*

The d spacing value of 0.274 nm corresponds to the (110) crystal plane of the CuO phase while the d spacing value of 0.147 nm corresponds to the (220) crystal plane of the NiO phase.[47, 48] The STEM elemental mapping of the CuO-NiO/NF (Figure 3a.3c, 3a.3e) confirms the presence of uniformly distributed Cu, Ni and O in the catalyst. For the elucidation of chemical composition and electronic interaction the X-ray photoelectron spectroscopy (XPS) measurement were conducted. The presence of Cu, Ni and O in the catalyst was confirmed from the XPS survey spectrum of the CuO-NiO/NF catalyst (Figure 3a.4). These results are very much aligned with the results obtained from the EDAX elemental mapping. The high-resolution Cu 2p XPS spectrum (Figure 3a.5a)shows two peaks at 934.1 and 942.9 eV corresponds to Cu $2p_{3/2}$ and satellite peak of Cu $2p_{3/2}$.[29, 49] For Ni 2p in figure (3a.5b),the peaks located at 856.8 and 862.3 eV are attributed to Ni $2p_{3/2}$ and satellite peak of Ni $2p_{3/2}$.[50, 51] The O 1s spectrum in figure (3a.5c), exhibitthe peaks located at 532.6 and 534.5 eVcorrespond to oxygen ions in the coordination states at the surface and the presence of lattice oxygen associated with CuO and NiO.[52] An investigation of the XPS spectra of the individual CuO phase revealed a shift of 1.4 eV in the binding energy of Cu $2p_{3/2}$ for CuO-NiO/NF[53] indicating interaction between the two phases (figure 3a.5d).

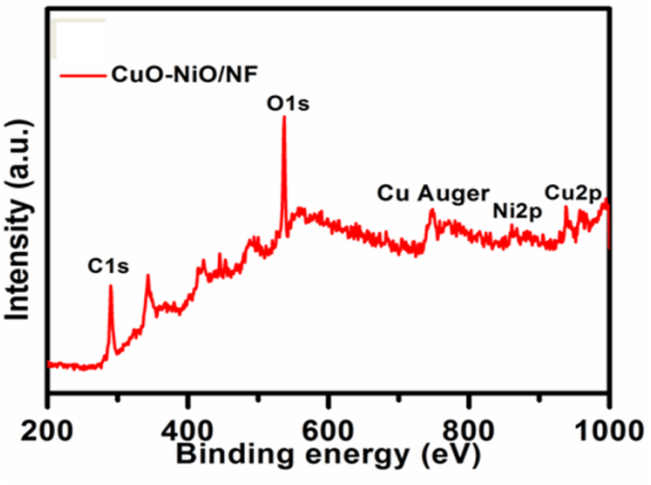

Figure 3a.4 *Wide scan XPS spectra of CuO-NiO/NF*

This result shows the presence of strong interaction between the two nano-interfaces of CuO and NiO in the CuO-NiO/NF catalyst.

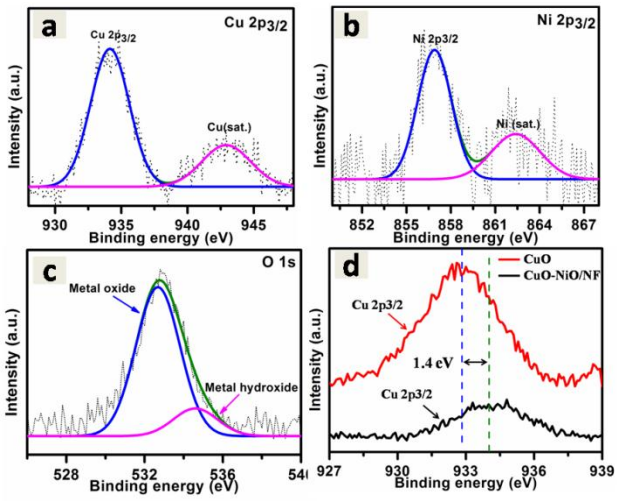

Figure 3a.5. *XPS of the CuO-NiO/NF catalyst (a) Cu 2p, (b) Ni 2p and (c) O 1s (d) comparison of the Cu 2p spectra of CuO-NiO/NF and individual CuO: experimental data (dotted curve) and fitting results (solid curve). The peaks are determinedby oxidation states of elements with their splitting term.*

The catalytic performance of CuO-NiO/NF and other supporting catalysts towards OER was evaluated in the basic medium using a graphitic rod as a counter electrode and Ag/AgCl (saturated KCl filled) as a reference electrode. All the data were taken at 25°C

in O_2 saturated 1M KOH. The table containing mass loading of all the catalyst on nickel foam is given in the Table 3a.1.

Catalyst	Mass loading (mg cm^{-2})
CuO-NiO/NF	2.9
CuO/NF	2.9
NiO/NF	1.6
RuO_2/NF	2.9

Table 3a.1 *Mass loading of all the catalyst over NF*

For comparative studies, the electrocatalytic activities of CuO/NF and NiO/NF and commercial RuO_2 over NFwere also investigated under the same experimental condition. Figure 3a.6a shows the $iR_{corrected}$ polarization curves for all the catalysts. The overpotential value of 231, 290, 343 and 350 mV obtained at 10 mA cm^{-2} current density respectively for CuO-NiO/NF, RuO_2/NF, CuO/NF and NiO/NF. The performance of CuO-NiO/NF was found to be superior to that of commercially available RuO_2 at 10 mA cm^{-2} and obtained at a higher current density**.** The comparison of the overpotential of all the catalyst at 10 mA cm^{-2} of current density is displayed in Figure 3a.6b. In order to understand the kinetics of the reaction, we have calculated the Tafel slope value by plotting the Tafel slope as depicted in figure 3a.6c.The resulting Tafel slope values are 100, 110, 145 and 154 and 300 mV/dec for CuO-NiO/NF, RuO_2/NF, CuO/NF, NiO/NF and bare NF respectively. The lower Tafel slope value of catalyst indicatesafavourable OER kinetics than that of noble metal-based catalyst (RuO_2). Electrochemical impedance spectroscopy shows a fast chargetransfer through the interface and indicates that the composite is performing far better than the individual phases in terms of charge transfer resistances. The corresponding Nyquist plots at an applied potential of 100 mV are displayed in figure 3a.6d. In all the spectra the two semi-circles are completely fitted with

the equivalent circuit displayed in figure 3a.6d.The fitted data displays two time-constant components R_{ct}-CPE_{dL} and Rp-CPE_L,in addition to the solution resistance.

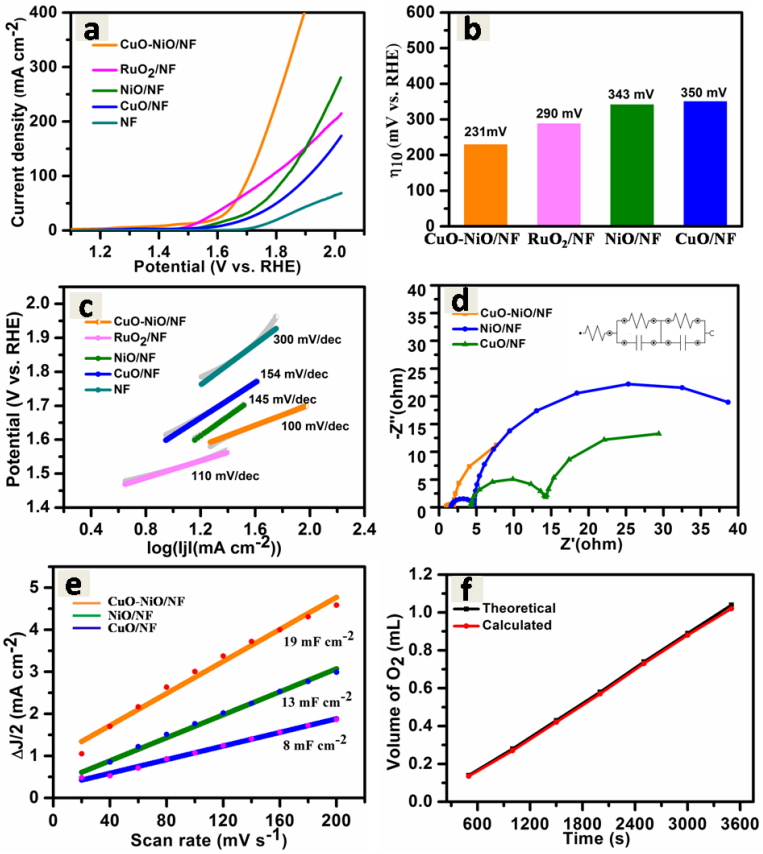

Figure 3a.6*. Electrochemical measurements of the corresponding electrocatalysts for oxygen evolution in 1 M KOH alkaline medium. (a) Polarization curves (iR-corrected) of CuO-NiO/NF compared with the other electrode (b) Bar-graph comparing the overpotential values obtained from polarization curve at 10 mA cm^{-2} current density (c) the respective Tafel plots derived from the Tafel equation (d) EIS Nyquist plot (with the corresponding equivalent circuit) of the electrode at 100mV of overpotential.(e) double-layer capacitance (C_{dl}) calculation for all the electrodes derived from the cyclic voltammetry curve taken in the non-faradic region. (f) For the calculation of faradic efficiency, the plot shows the volume of O_2 evolve at different time intervals.*

The constant phase angle element (CPE) explain the double-layer capacitance of the solid electrode. R_{ct}-C1 gives information about charge-transfer resistance and EDL capacitance, and the surface porosity can be correlated withRp-CPEL. The (R1C2) circuit signify the diffusion/adsorption of reaction intermediates due to very slow diffusion

through reaction interface and surface porosity. The species, such as MOH, can undergo oxidation to MO under the applied potential, resulting in the (R1C2) impedance at the low-frequency region in the semi-circle. The charge transfer resistance and the applied potential is inversely proportional. The charge-transfer resistance (R_{ct}) of 1.5 Ω was obtained with an applied potential of 100 mV.The lower value of R_{ct}indicates that the electrode surface has large number of electrochemically active sites and the charge transfer between the electrode surface and the electrolyte is fast.These observations from the Nyquist plot also rendering towards excellent OER activity. To calculate the electrochemically active surface area we have first calculated the double-layer capacitance (C_{dl}) of all the electrodes (Figure 3a.6e). The obtained C_{dl} values are 19, 13 and 8 mF cm^{-2} for CuO-NiO/NF, NiO/NF and CuO/NF respectively. The higher value of C_{dl} of the catalyst indicates higher OER activity. The catalyst's long-term durability was examined by the chronoamperometry at an overpotential of 0.6 V for 20 hr (Figre 3a.7). The catalyst seems significantly stable in alkaline media during the course of reaction.

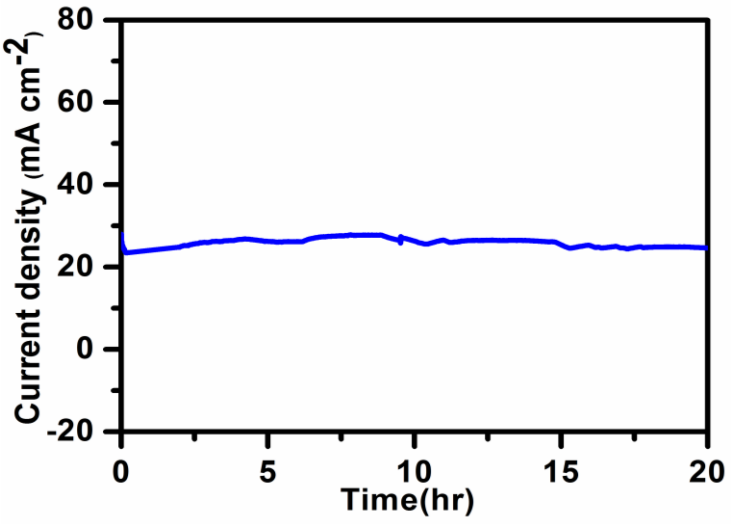

Figure 3a.7 *chronoamperometry curve of the catalyst showing the stability up to 20 hr with no change in the current density*

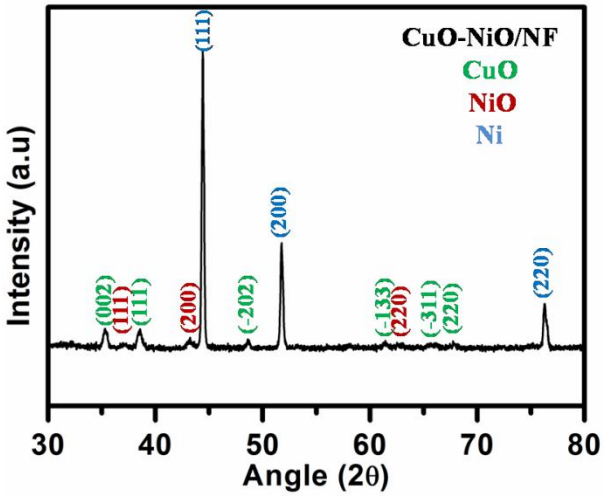

Figure 3a.8. *PXRD pattern of the catalyst after stability showing the retention of all the phases present*

The post-stability investigations of the catalyst were carried out using PXRD indicates that all the phases present in the catalysts remained intact even after prolong stability After stability PXRD is given in Figure 3a.8. The cyclic volatammetry curve for the determination of double-layer capacitance is provided in Figure 3a.9.

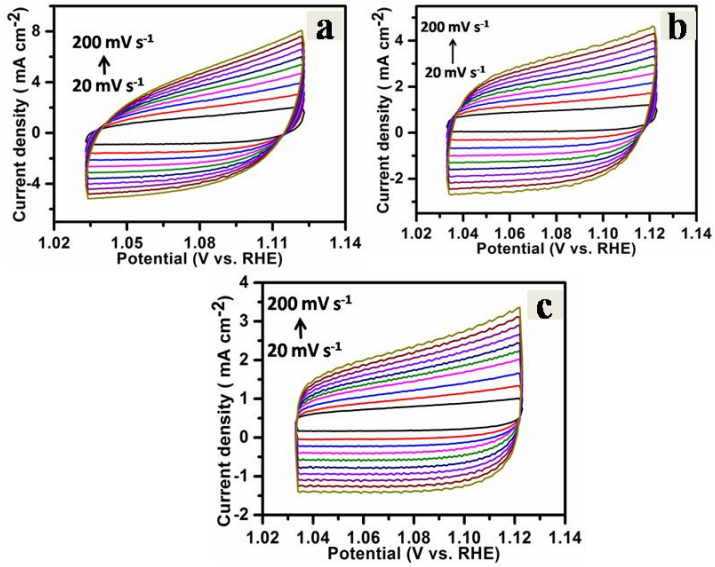

Figure 3a.9 *Cyclic voltammetry curve of (a)CuO-NiO/NF, (b)NiO/NF and (c) CuO/NF for the calculation of* C_{dl}

The faradic efficiency was calculated (figure 3a.6f) using water-gas displacement method, in which the percentage of the ratio of the amount of O_2 evolved experimentally to the amount of O_2 evolved theoretically. The faradic efficiency value for our catalyst was found to be 98.07 %.

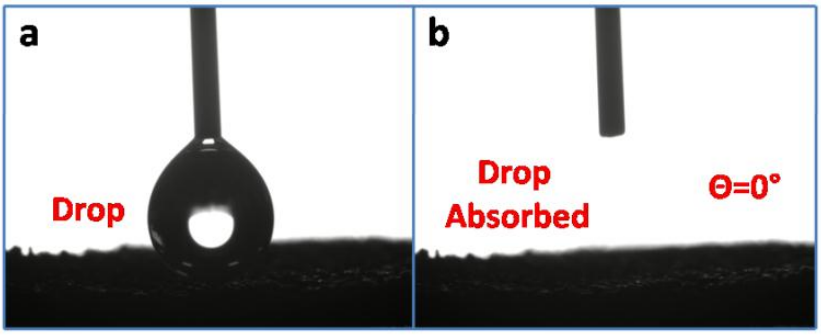

Figure 3a.10. (a) Hydrophilicity analysis of CuO-NiO/NF (a) before and (b) after dropping the liquid on the surface of the catalyst

Superhydrophilic surfaces have drawn significant interest in heterogeneous catalysis as it supports the low adsorption energies on the surface of the catalyst. In heterogeneous catalysis, the behaviour of the surface of the catalyst is also important. The surface of CuO-NiO/NF was inspected by carrying out a contact angle measurement (Figure 6a, b)and found to be superhydrophilicas the drop of water absorbs instantly after dropping on the surface. The contact angle was also found to be zero illustrating the super hydrophilic nature of the catalyst surface.Superhydrophilic catalyst allows the transfer of the ions quickly from the electrolyte to the electrode surface and accelerates the mass transport process and hence enhances the electrocatalytic performance.[54,55] As revealed by the electrochemical experimental results, the hybrid nanostructure exhibits significantly higher OER activity with respect to the individual phases, which motivated us to further investigate the reaction intermediates using density functional theory (DFT) as implemented in Vienna ab initio simulation package (VASP). All the expressions for calculating the free energies along with the calculated energy are given in supporting information Table 3a.2.

Surface	Total Energy (eV)	Free Energy (eV)	Bond Length (M-O) A°
Cu Site in CuO	-37.4328		
CuO-OH*	-36.4739	11.20989	1.77231
CuO-O*	-30.2592	1.591058	1.67332
CuO-OOH*	-41.0205	-0.51026	1.80632
Ni site in NiO	-48.6984		
NiO-OH*	-58.6504	0.29908	1.79504
NiO-O*	-52.0761	1.950604	1.72074
NiO-OOH*	-63.9306	-1.6034	1.82121
Cu site in CuO-NiO/NF	-156.928		
CuO-NiO/NF-OH*	-166.919	0.260269	1.78218
CuO-NiO/NF- O*	-160.054	2.240934	1.93789
CuO-NiO/NF- OOH*	-169.562	0.742975	1.83249
Ni site in CuO-NiO/NF			
CuO-**Ni**O/NF- OH*	-167.709	-0.53005	1.93755
CuO-**Ni**O/NF- O*	-164.132	-1.04614	1.83933
CuO-**Ni**O/NF- OOH*	-172.352	2.030719	1.94992

Table 3a.2 *Energy values of adsorption of all the intermediate species on different active sites.*

For DFT calculation, the reference values were taken for H_2 and H_2O. Further, the Gibbs free energies (ΔG)were calculated at normal condition (pH = 14, T = 298.15K) at equilibrium potential of 1.23 V. The E_{ads} was calculated by the following formula:[56]

$$E_{ads} = E_{(surf+x)} - E_{surf} - E_x$$

The free energy diagram of CuO-NiO heterostructure is shown in figure 3a.11(a), and the free energy calculations for different intermediates of the OER process were done by adsorbing them on both Cu and Ni sites present in the heterostructures. It was found that the Ni site in the heterostructure is more favourable and having a lower energy pathway for the OER kinetics, whereas for the Cu site we observe higher values of energy, as well as the potential limiting step (PLS) is more uphill than that of Ni site.

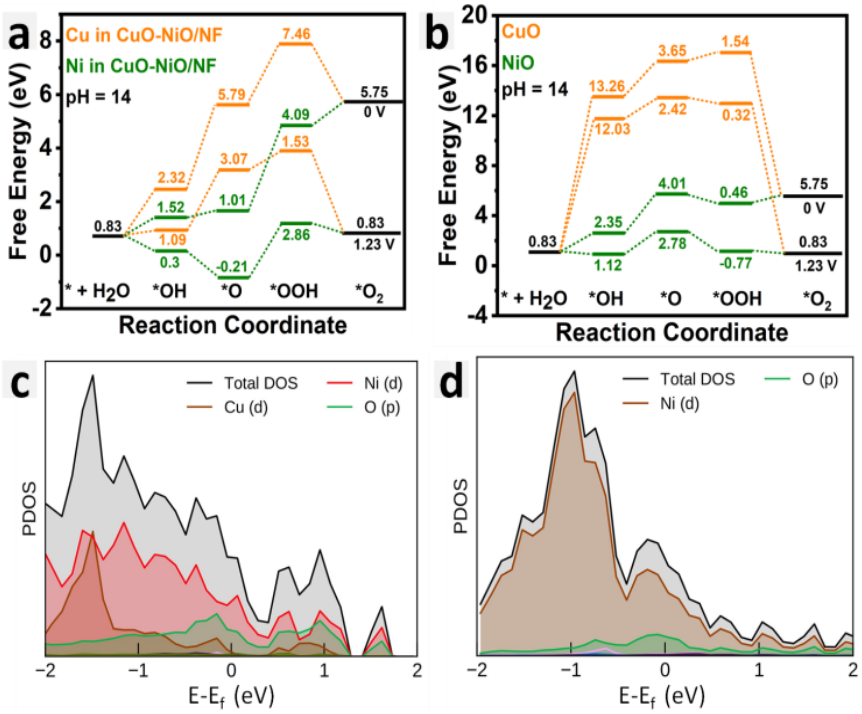

Figure 3a.11. *(a) free energy plot of CuO-NiO/NF at pH=14(b) individual CuO and NiO free energy plot at pH = 14 c) PDOS of CuO-NiOheterostructure (Cu d-orbital, Ni d-orbital & O p-orbital) d) PDOS of individual NiO (Ni d-orbital and O p-orbital)*

The PLS step for CuO-NiOheterostructure in case of Ni active site is *O to *OH (ΔG_2-ΔG_3) and that for Cu site is *OOH to $*O_2$ (ΔG_3-ΔG_4) and the PLS is lower for Ni than that of Cu (3.24 eV). For comparison we've also calculated the free energy of different

intermediates on individual NiOand CuO sites (figure 3a.11(b)), and the PLS step for NiO is *O to *OOH (ΔG_2-ΔG_3) and for Cu, it is *OOH to *O_2 (ΔG_3-ΔG_4), individually also NiO (PLS difference = 3.55 eV) is proved to be better for OER than that of CuO. It was observed that the CuO-NiOheterostructure is more facile for OER than that of individual NiO and CuO. Considering the whole scenario, the PLS values shows the effectiveness of active sites towards the OER mechanism, which proves that Ni and Cu active sites in heterostructure are more favourable than individual Ni and Cu sites in NiO and CuO. Projected density of states is calculated for CuO-NiOheterostructure (figure 3a.11(c)) as well as for individual NiO (figure 3a.11(d)) and CuO (3a.12).

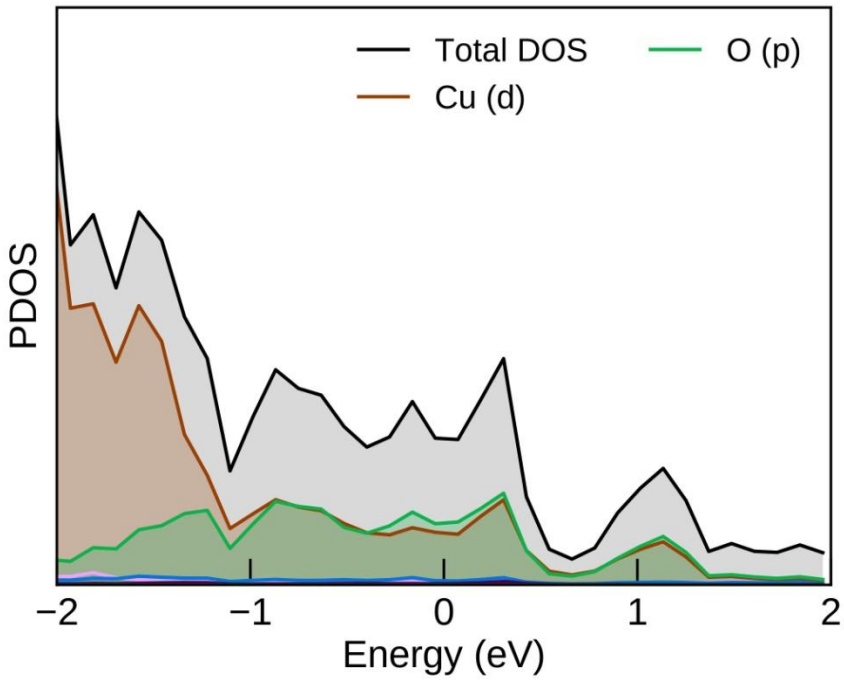

Figure 3a.12 *PDOS of individual CuO phase.*

The DOS plot describes the overall concentration of the accessible carrier states in a given energy range. As observed in DOS plot the area under the PDOS curve gives the total density of states available for electron occupation. The CuO-NiO/NF heterostructure has higher DOS as well as greater area as compared to individual NiO and CuO, revealing fater electron transfer and rendering towards the higher electrocatalytic performance. It is also observed that Ni d-orbital and oxygen p-orbitals have significant contribution for NiO-CuO heterostructure. As observed in figure 3a.11 (c) and (d) in case

of NiO oxygen p orbital have very low contribution in PDOS. In heterostructure the contribution of p-orbital mainly coming from CuO compound. It is also found that the peak distance between d-orbital and p-orbital reduces in case of heterostructure which is further enhancing the OER catalytic efficiency.

3a.4 Conclusion

In summary, the fabrication of an excellent OER catalyst using metal-organic framework as a precursor is depicted, where strongly interacted nano-interfaces of the hybrid nanostructures enhances the catalytic activity. The strong interaction between both the phases could be traced using X-ray photoelectron spectroscopy. Superhydrophilic catalyst augments the ionic transfer from the electrolyte to the electrode surface and accelerates the mass transport process and hence the overall electrocatalytic performance is enhanced. The catalyst CuO-NiO/NF shows a very low overpotential of 231 mV at 10 mA cm^{-2} current density and a Tafel slope value of 100 mV/dec. A chronoamperometry studies were performed up to 20 hr to exhibit the durability of the catalyst. The electrocatalytic activity of the catalyst can be explained by the formation of heterointerfaces, highly exposed active sites and synergistic effect.The experimental observations are also supported by the DFT calculations. The DFT results also show that Ni and Cu active sites in heterostructure are more favourable than individual Ni and Cu sites in NiO and CuO. This work has open up a new window, where similar methodology can be applied for the other metal oxide nanoparticles for several electrochemical applications.

Note:

- The permission has been granted by the authors and corresponding author of the published paper prior to adopting in the present thesis. The associated relevant publication is:

Gaur, Ashish, Vikas Pundir, Ashwinder Singh, Takahiro Maruyama, Chandan Bera, and Vivek Bagchi. "Intense nano-interfacial interactivity stimulates the OER in a MOF-derived superhydrophilic CuO–NiO heterostructure." *Sustainable Energy & Fuels* 5, no. 21 (2021): 5505-5512.

References

1. N. J. Lutsko, *Journal of Climate*, 2021, 34, 901-917.

2. S. K. Moore, V. L. Trainer, N. J. Mantua, M. S. Parker, E. A. Laws, L. C. Backer and L. E. Fleming, *Environmental Health*, 2008, 7, S4.

3. N. S. Lewis, *Science*, 2016, 351, aad1920.

4. K. Zeng and D. Zhang, *Progress in Energy and Combustion Science*, 2010, 36, 307-326.

5. X. Zou and Y. Zhang, *Chemical Society Reviews*, 2015, 44, 5148-5180.

6. Y. Yao, N. Mahmood, L. Pan, G. Shen, R. Zhang, R. Gao, F.-e. Aleem, X. Yuan, X. Zhang and J.-J. Zou, *Nanoscale*, 2018, 10, 21327-21334.

7. J. Song, C. Wei, Z.-F. Huang, C. Liu, L. Zeng, X. Wang and Z. J. Xu, *Chemical Society Reviews*, 2020, 49, 2196-2214.

8. G. Zhu, X. Xie, X. Li, Y. Liu, X. Shen, K. Xu and S. Chen, *ACS Applied Materials & Interfaces*, 2018, 10, 19258-19270.

9. Y. Lee, J. Suntivich, K. J. May, E. E. Perry and Y. Shao-Horn, *The Journal of Physical Chemistry Letters*, 2012, 3, 399-404.

10. J. Yu, Q. He, G. Yang, W. Zhou, Z. Shao and M. Ni, *ACS Catalysis*, 2019, 9, 9973-10011.

11. R. Zhu, J. Ding, Y. Xu, J. Yang, Q. Xu and H. Pang, *Small*, 2018, 14, 1803576.

12. L. Chen, R. Luque and Y. Li, *Dalton Transactions*, 2018, 47, 3663-3668.

13. Q. Shi, S. Fu, C. Zhu, J. Song, D. Du and Y. Lin, *Materials Horizons*, 2019, 6, 684-702.

14. F. Zheng, Z. Zhang, C. Zhang and W. Chen, *ACS Omega*, 2020, 5, 2495-2502.

15. W. Li, S. Watzele, H. A. El-Sayed, Y. Liang, G. Kieslich, A. S. Bandarenka, K. Rodewald, B. Rieger and R. A. Fischer, *Journal of the American Chemical Society*, 2019, 141, 5926-5933.

16. C. A. Downes and S. C. Marinescu, *ChemSusChem*, 2017, 10, 4374-4392.

17. W.-J. Dang, Y.-Q. Shen, M. Lin, H. Jiao, L. Xu and Z.-L. Wang, *Journal of Alloys and Compounds*, 2019, 792, 69-76.

18. F. Lyu, Q. Wang, S. M. Choi and Y. Yin, *Small*, 2019, 15, 1804201.

19. D. Gao, R. Liu, J. Biskupek, U. Kaiser, Y.-F. Song and C. Streb, *Angewandte Chemie International Edition*, 2019, 58, 4644-4648.

20. X. Li, J. Wei, Q. Li, S. Zheng, Y. Xu, P. Du, C. Chen, J. Zhao, H. Xue, Q. Xu and H. Pang, *Advanced Functional Materials*, 2018, 28, 1800886.

21. L. Pei, Y. Song, M. Song, P. Liu, H. Wei, B. Xu, J. Guo and J. Liang, *Electrochimica Acta*, 2021, 368, 137651.

22. M. Wu, G. Zhang, H. Tong, X. Liu, L. Du, N. Chen, J. Wang, T. Sun, T. Regier and S. Sun, *Nano Energy*, 2021, 79, 105409.

23. P. Thangasamy, S. Oh, S. Nam, H. Randriamahazaka and I.-K. Oh, *Small*, 2020, 16, 2001665.

24. W. Zhang, X. Zhao, Y. Zhao, J. Zhang, X. Li, L. Fang and L. Li, *ACS Applied Materials & Interfaces*, 2020, 12, 10280-10290.

25. A. K. Tareen, G. S. Priyanga, K. Khan, E. Pervaiz, T. Thomas and M. Yang, *ChemSusChem*, 2019, 12, 3941-3954.

26. M. E. Kreider, A. Gallo, S. Back, Y. Liu, S. Siahrostami, D. Nordlund, R. Sinclair, J. K. Nørskov, L. A. King and T. F. Jaramillo, *ACS Applied Materials & Interfaces*, 2019, 11, 26863-26871.

27. G. Yuan, J. Bai, L. Zhang, X. Chen and L. Ren, *Applied Catalysis B: Environmental*, 2021, 284, 119693.

28. K. Liu, C. Zhang, Y. Sun, G. Zhang, X. Shen, F. Zou, H. Zhang, Z. Wu, E. C. Wegener, C. J. Taubert, J. T. Miller, Z. Peng and Y. Zhu, *ACS Nano*, 2018, 12, 158-167.

29. X. Xiong, C. You, Z. Liu, A. M. Asiri and X. Sun, *ACS Sustainable Chemistry & Engineering*, 2018, 6, 2883-2887.

30. S. M. Pawar, B. S. Pawar, B. Hou, J. Kim, A. T. Aqueel Ahmed, H. S. Chavan, Y. Jo, S. Cho, A. I. Inamdar, J. L. Gunjakar, H. Kim, S. Cha and H. Im, *Journal of Materials Chemistry A*, 2017, 5, 12747-12751.

31. X. Kuang, S. Chen, L. Meng, J. Chen, X. Wu, G. Zhang, G. Zhong, T. Hu, Y. Li and C.-Z. Lu, *Chemical Communications*, 2019, 55, 1643-1646.

32. C. Wang, H. Tissot, C. Escudero, V. Pérez-Dieste, D. Stacchiola and J. Weissenrieder, *The Journal of Physical Chemistry C*, 2018, 122, 28684-28691.

33. A. Rajput, A. Kundu and B. Chakraborty, *ChemElectroChem*, 2021, 8, 1698-1722.

34. J. Zhang, J. Qian, J. Ran, P. Xi, L. Yang and D. Gao, *ACS Catalysis*, 2020, 10, 12376-12384.

35. M. Tahir, L. Pan, R. Zhang, Y.-C. Wang, G. Shen, I. Aslam, M. A. Qadeer, N. Mahmood, W. Xu, L. Wang, X. Zhang and J.-J. Zou, *ACS Energy Letters*, 2017, 2, 2177-2182.

36. C. Li, P. Tian, H. Pang, W. Gong, J. Ye and G. Ning, *Sustainable Energy & Fuels*, 2020, 4, 2792-2799.

37. C.-W. Wu, B. Unnikrishnan, A. P. Periasamy, I. W. P. Chen, Y.-T. Tseng, Y.-Y. Yang, W.-J. Lin, C.-C. Huang and H.-T. Chang, *ACS Sustainable Chemistry & Engineering*, 2020, 8, 9794-9802.

38. V. Shokhen, M. Zysler, M. Shviro, D. Zitoun and M. Chatenet, *ACS Applied Energy Materials*, 2020, 3, 8858-8870.

39. A. Gaur, P. K. Sachdeva, R. Kumar, T. Maruyama, C. Bera and V. Bagchi, *Sustainable Energy & Fuels*, 2021, 5, 801-807.

40. N. A. Khan, N. Rashid, M. Junaid, M. N. Zafar, M. Faheem and I. Ahmad, *ACS Applied Energy Materials*, 2019, 2, 3587-3594.

41. P. E. Blöchl, *Physical Review B*, 1994, 50, 17953-17979.

42. D. Vanderbilt, *Physical Review B*, 1990, 41, 7892-7895.

43. M. Qiu, N. Wang, Z. Cui, J. Liu, L. Hou, J. Liu, R. Hu, H. Zhang and Y. Zhao, *Journal of Materials Chemistry A*, 2018, 6, 817-822.

44. X. Zhang, S. Sun, J. Lv, L. Tang, C. Kong, X. Song and Z. Yang, *Journal of Materials Chemistry A*, 2014, 2, 10073-10080.

45. Y. He, L. Xu, Y. Zhai, A. Li and X. Chen, *Chemical Communications*, 2015, 51, 14768-14771.

46. Y. Zhou, H. Liu, S. Zhu, Y. Liang, S. Wu, Z. Li, Z. Cui, C. Chang, X. Yang and A. Inoue, *ACS Applied Energy Materials*, 2019, 2, 7913-7922.

47. F. Lin, Z. Shao, P. Li, Z. Chen, X. Liu, M. Li, B. Zhang, J. Huang, G. Zhu and B. Dong, *RSC Advances*, 2017, 7, 15053-15059.

48. K. Nguyen, N. D. Hoa, C. M. Hung, D. T. Thanh Le, N. Van Duy and N. Van Hieu, *RSC Advances*, 2018, 8, 19449-19455.

49. F. Yu, F. Li, B. Zhang, H. Li and L. Sun, *ACS Catalysis*, 2015, 5, 627-630.

50. G. Zhou, D.-W. Wang, L.-C. Yin, N. Li, F. Li and H.-M. Cheng, *ACS Nano*, 2012, 6, 3214-3223.

51. M. ul Haq, Z. Wen, Z. Zhang, S. Khan, Z. Lou, Z. Ye and L. Zhu, *Scientific Reports*, 2018, 8, 1705.

52. C. V. V. M. Gopi, R. Vinodh, S. Sambasivam, I. Obaidat, R. M. N. Kalla and H. Kim, *Materials Today Energy*, 2019, 14, 100358.

53. H. Yan, Y. Xie, Y. Jiao, A. Wu, C. Tian, X. Zhang, L. Wang and H. Fu, *Advanced Materials*, 2018, 30, 1704156.

54. X. Xu, T. Wang, L. Su, Y. Zhang, L. Dong and X. Miao, *ACS Sustainable Chemistry & Engineering*, 2021, 9, 5693-5704.

55. X. Shan, J. Liu, H. Mu, Y. Xiao, B. Mei, W. Liu, G. Lin, Z. Jiang, L. Wen and L. Jiang, *Angewandte Chemie International Edition*, 2020, 59, 1659-1665.

56. G. Kresse and D. Joubert, *Physical Review B*, 1999, 59, 1758-1775.

Chapter 3b

Interfacial interaction induced OER activity of MOF derived superhydrophilic Co_3O_4-NiO hybrid nanostructures

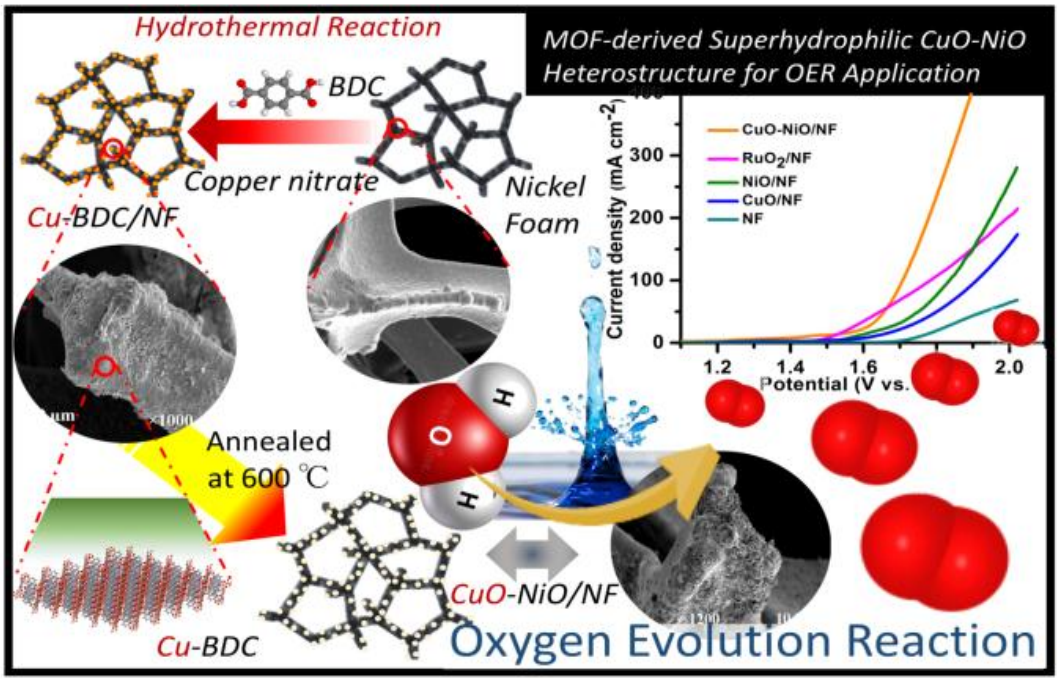

Brief Outcome:*Electrocatalytic water splitting is one of the key technology for the future energy systems envisioned for the storage of energy obtained from variable renewables and green fuels. The development of efficient, durable, earth-abundant and cheap electrocatalysts for oxygen evolution reaction is a scorching area of research. Oxygen evolution reaction has a huge potential for fuel cell and metal-air battery applications. Herein we reported the interfacially interacted and uniformly decorated Co_3O_4-NiO hybrid nanostructures formed by the metal-organic framework (Co_2-BDC(OH)$_2$) using BDC as a linker to the metal center. The fine nanosheets of the Co2-BDC(OH)$_2$ was first uniformly grown oven the honeycomb-like structure of nickel foam (NF). After controlled calcination of these nanosheets/NF composite, a uniformly decorated, binder-free Co_3O_4-NiO/NF electrocatalyst was synthesized. The transformation of Co_2-BDC(OH)2/NF into Co_3O_4-NiO/NF is characterized by employing several techniques such as powder X-ray diffraction (PXRD), X-ray photoelectron spectroscopy and Transmission electron microscopy, etc. The catalyst exhibits a low overpotential of 311 mV vs. RHE at 10 mA cm-2 current density. The catalyst also displays long term stability (24 h) with a Tafel slope value of 90 mV dec^{-1}. The obtained experimental results are also in-line with the theoretical data acquired from the model systems.*

3b.1. Introduction

Rising ocean waters will completely engulf many coastal land areas of several nations within the next few decades, according to the report produced by Climate Central.[1]Increasing carbon footprint, environmental contamination and depletion of fossil energies are the major threats to such climate changes.[2]Electrocatalytic water splitting is one such system which has obtained worldwide attention for being the most feasible technology for electrochemical hydrogen production,[3-5] but the sluggish proton-coupled electron transfer process at the anodic part for the oxygen evolution reaction affects the overall efficiency of the production.[6-8] RuO2 and IrO2are still known as one of the most productive electrocatalysts for oxygen evolution reaction.[9,10] However, the less abundance and high cost, limit the extensive use of these catalysts. Tremendous attempts have been devoted in the recent past for exploring transition metal (Fe, Ni, Co, Mo) based cost-effective substitutes to replace precious IrO_2 and RuO_2 electrocatalysts.[10-14] The development of transition metalbasedelectrocatalysts including phosphides, oxides and sulphides [15-17]for oxygen evolution reaction is a well-studied area and currently under exploration. Among these, oxides due to their structural tenability and high valence state, have attracted considerable attention for oxygen evolution reaction. The activity-enhancement of a new generation of catalyst focuses on the synergic approach among specific solids which exploit the mutual coactions of these materials. These strategies based on synergistic effects due to the combination of different phases further excavate the potential of transitional oxide-based electrocatalysts. In Co_3O_4 the Co^{3+} site considered as electrocatalitically active towards OER by enhancing the deprotonation of OOH* species[11] to O_2 similarly in the nickelxide surface Ni^{3+} considered as a highly active site for OER.[12]Several techniques have been applied to improve the electrocatalytic activities, such as utilizing conductive carbon supports,[13,14]introducing heterointerfaces[15,16] and doping elements.[17, 18] Among these approaches, fabricating heterostructures could modulate the surface electronic structure, induce synergistic effect among different components, and expose more active sites. The in-situ formation of these oxides having intermingled interfaces between nanoparticles of different phases accelerate the OER performance. The surface morphology of the catalyst also affects the

overall OER performance by influencing the active sites and mass transport. Metal-organic framework (MOFs) and zinc-imidazole frameworks (ZIFs) are the class of organic-inorganic hybrid materials with tuneable porosity and morphology. The MOF derived materials contain controllable surface functionalities and a very high surface area and hence can be used as a promising material for several electrocatalytic application.[19-26] Herein, we have synthesized the two-dimensional Co_2-BDC$(OH)_2$ MOF over NF hydrothermally followed by controlled calcination leading to the generation of a uniform heterostructure of spinel cobalt oxide/nickel oxide over NF. The interface formation between Co_3O_4 and NiO nanoparticles induces a synergistic effect leading to an excellent OER performance with the overpotential value of 311 mV at 10 mA cm-2 current density in 1M KOH. The OER activity of the Co_3O_4-NiO/NF nanocomposite is much superior to the individual Co_3O_4 and NiO phases and reveals an interesting insight towards the OER activity of a biphasic system.

3b.2. Experimental section

3b.2.1. Materials

All chemicals were purchased from different sources and used without further modification. Cobalt (II) nitrate hexahydrate ($Co(NO_2)_2.6H_2O$, 99%), 1,4-benzenedicarboxylic acid (C_6H_4-1,4$(COOH)_2$,98%), N,N-dimethylformamide(anhydrous, 99.8%), Nafionperfluorinated resin solution (5 wt% in a mixture of lower aliphatic alcohols and water, contains 45% water) were purchased from Sigma Aldrich.Sodium hydroxide pallets and commercial RuO_2 were purchased fromTCI Chemicals (India) Pvt. Ltd. Deionised water was used in all preparation.

3b.2.2. Methodology

3b.2.2.1. Synthesis of Catalyst

Catalyst synthesis section is subdivided into two major stepsas per following description

Step 1.Synthesis of $Co_2(OH)_2$(BDC) MOF: The synthesis of MOF was carried out by using previously reported method method[27] with slight modification in which, 2 mmol of

$Co(NO_3)_2.6H_2O$, and 2 mmol of 1,4-benzenedicarboxylic acid (H_2BDC). At the outset, 2 mmol of 1,4-benzenedicarboxylic acid (H_2BDC) were dissolved in 10 mL of N,N-dimethylformamide (DMF),followed by the addition of 1 mL of 0.5 M NaOH solution under continuous stirring. In another flask, 2 mmol of $Co(NO_3)_2.6H_2O$ were dissolved in 10 mL of N,N-dimethylformamide (DMF). Both the solutions were mixed together in the 50 mL Teflon-lined stainless steel autoclave with a piece of nickel foam (0.5 cm×0.5 cm). The autoclave was then heated for 20 h at 110°C temperature. The asobtained$Co_2(OH)_2(BDC)$ MOF over NF was washed three times with DMF and ethanol respectively and dried at 60 °C.

Step 1.Synthesis of CO_3O_4-NiO hybrid nanostructures: The Co3O4-NiO hybrid nanostructures were formed over the NF when Co-BDC/NF substrate was calcined at moderate temperature. The asobtained Co-BDC/NF substrate was heated in a furnace at 500°C for 3 h at a ramp rate of 5°C per minute. After annealing Co3O4-NiO hybrid nanostructures were formed over NF.

Synthesis of CO_3O_4 nanoparticles :Co_3O_4 nanoparticles were synthesized by using metal organic framework as a precursor ($Co_2(OH)_2(BDC)$)The synthesis of MOF is done by using previously reported method with slight modification in which 2 mmol of $Co(NO_3)_2.6H_2O$, and 2 mmol of 1,4-benzenedicarboxylic acid (H_2BDC). Firstly the 2 mmol of 1,4-benzenedicarboxylic acid (H_2BDC) were dissolve in 10 mL of N,N-dimethylformamide (DMF) then 1 mL of 0.5 M NaOH solution was added under continuous stirring. In other flask 2 mmol of $Co(NO_3)_2.6H_2O$ were dissolve in 10 mL of N,N-dimethylformamide (DMF). Both the solutions were mixed together in the 50 mL Teflon-lined stainless steel autoclave and the autoclave was heated was heated for 20 h at 110°C temperature. The as obtained $Co_2(OH)_2(BDC)$ MOF was washed three times with DMF and ethanol and dried naturally. The as obtained MOF was heated in furnace at 500°C for 3 hr at a ramp rate of 5°C/min. After annealing Co_3O_4 were obtained and used as it is.

Synthesis of NiO/NF: The NiO/NF electrode was obtained by heating the bare nickel foam at 600°C for 3 hr at a ramp rate of 5°C /min. After annealing the NiO nanostructures were formed over nickel foam.

3b.2.2.2. Physical characterization

The phase and structural information of the catalyst was obtained by Bruker Eco D8 ADVANCE X Powder Xraydiffractometer with Ni filter applying Cu Kα radiation (λ = 1.54056 Å, 40 kV and 25 mA) in the 2θ range of 5°−80° with a rise of 0.00190/step. The surface morphological analysis of the catalyst was done by using a scanning electron microscope (SEM) from JEOL (JSM IT-300) provided with an energy-dispersive X-ray diffractometer (Bruker). The microstructure of the grain and size of the obtained product were investigated by transmission electron microscopy (TEM) JEOL-2100 operated at 200 kV. X-ray Photoelectron Spectroscopy (XPS) was done on ESCA Lab: 220-IXL with Mg Kα nonmonochromated X-ray beam with photon energy 1253.6 eV.

3b.2.2.3. Electrochemical measurements

All electrochemical tests were carried out at room-temperature (25°C)using a CHI 760E electrochemical workstation. A graphite electrode was used as a counter electrode, a saturated Ag/AgCl electrode as a reference electrode, and a synthesised catalyst over NF as a working electrode in the standard three-electrode setup. Separate inks for Co_3O_4 and RuO_2 were prepared for comparative analysis. The ink (for the coating on the nickel foam) was prepared by using 10 mg of the corresponding catalyst in 1000 μL of dimethylformamide containing 10 μL of 5 wt % Nafion solution. This mixture was sonicated for 120 min and a homogeneous suspension was prepared. Out of these suspensions, only 335 μL was coated on the nickel foam and kept in a vacuum for drying. All the electrochemical data were collected in 1 M KOH at the scan rate of 5 mVs^{-1}. Conversion of all the polarization curves to RHE were done by using the equation, $E_{RHE} = E_{Ag/AgCl} + 0.197 + 0.059 \times pH$. Electrochemical stability was measured by running chronoamperometry at a potential of 0.5 V for 24 hr. The calculation of the Tafel slope was carried out by fitting the linear region of the Tafel curve to the Tafel equation (η = b

log(j) + a) by plotting all the comparative polarization curves. The iR compensation was done by the exclusion of Ohmic drop as stated by the equation $\eta corrected = \eta - iR_s$, where, Rs denotes the solution resistance. For the calculation of charge transfer resistance electrochemical impedance spectroscopy (EIS) was performed at an overpotential of 100mV under a frequency range of 100000- 1 Hz. To know the number of active sites, present on the surface of the catalyst electrochemically active surface area (ECSA) was determined by calculating double-layer capacitance (C_{dl}). For the calculation of C_{dl}, we took CV scans in the non-Faradic region of all the supporting catalysts electrodes by varying the scan rate from 20 to 200 mV s^{-1}.

3b.2.2.4. Theoretical methodology

For oxygen evolution reaction (OER) the adsorption of the oxygen atom on different sites of heterostructure is investigated withdensity functional theory (DFT) by using the Vienna ab initio simulation package (VASP) based on the projector augmented wave method (PAW). The exchange-correlation energy was determined using the Perdew-Burke-Ernzerh of (PBE) functional. The two-heterostructure is constructed using 120 atoms, resulting in lattice parameters a=18.43 Å, b=8.43 Å and c=19.40 Å. The direction along "a" is kept long enough to take in the heterostructure layers and the adsorbates with negligible interaction between their periodic layers. The cutoff energy for the plane-wave basis is set to 450 eV with an energy convergence threshold of 10^{-4}eV. All the atoms are relaxed until the forces on them are less than 0.01 eV/Å.

3b.3. Result and Discussion

The structural elucidation of Co_3O_4-NiO/NF catalyst was done by using powder X-ray diffraction spectroscopy and shown in figure 3b.1(a). The PXRD pattern shows the presence of both Co_3O_4 and NiO phases which are grown over nickel foam under hydrothermal reaction. The diffraction peaks at 31.3°, 36.9°, 59.4° and 65.3°can be assigned to (220), (311), (511) and (440) crystal planes of Co3O4 (JCPDS No. 42- 1467). [28,29] The other peaks at 37.4°, 43.4° and 62.9° corresponds to (111), (200) and (220) crystal plane of nickel oxide (JCPDS No. 47- 1049). [30, 31]

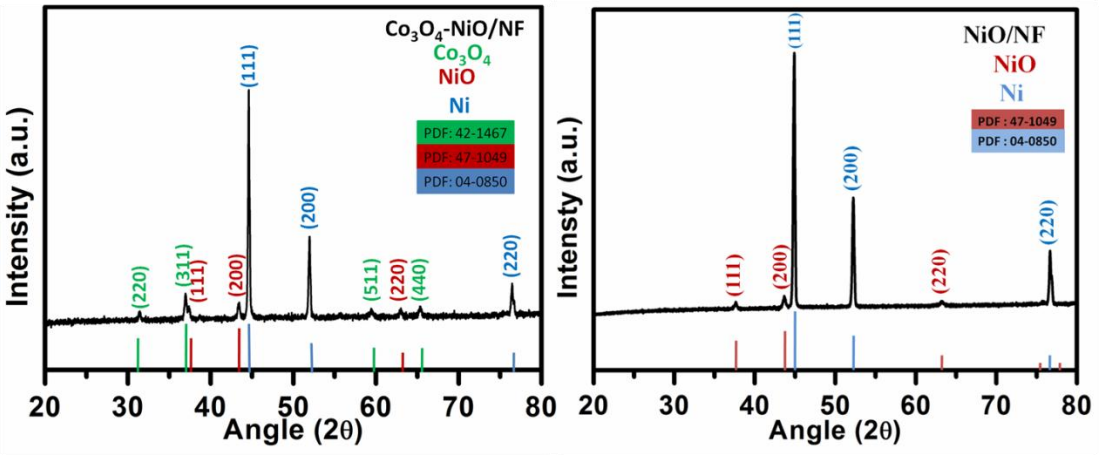

Figure3b.1.*PXRD pattern (a) Co_3O_4-NiO/NF (b) NiO/NFnanospheres obtained from pyrolysis of MOF.*

We have also checked the PXRD spectra of bare nickel foam and after the pyrolysis of nickel foam. As for the PXRD spectra of pyrolyzed nickel foam peaks for NiO was observed, showing the formation of nickel oxide on the surface. In figure 3b.1(b), the peaks at 37.4°, 43.4° and 62.9° corresponds to (111), (200) and (220) crystalplane of nickel oxide (JCPDS No. 47-1049). All the results obtained from PXRD are consistent with the HRTEM analysis. The PXRD pattern of as-synthesized Co_3O_4, bare Nickel foam and the Co-BDC MOF is given in Figure3b.2(a&b) and Figure 3b.3.

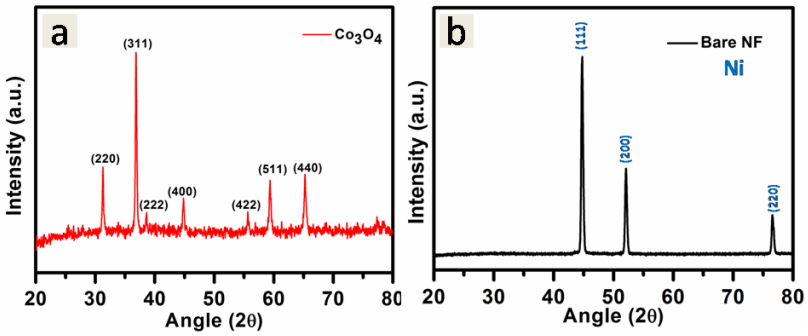

Figure 3b.2.*PXRD psttern (a) Co_3O_4-NiO/NF (b) NiO/NFnanospheres obtained from pyrolysis of MOF.*

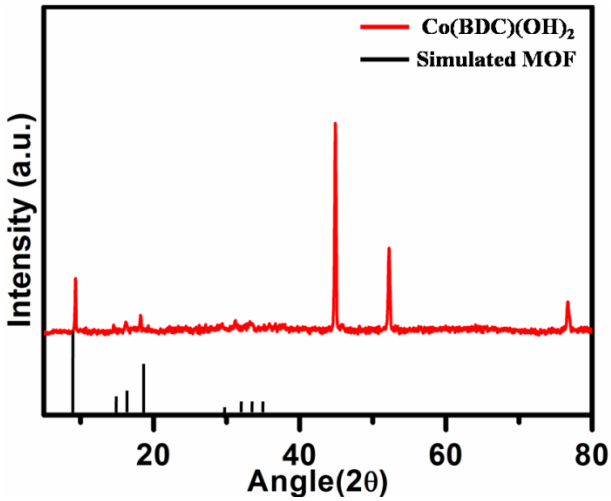

Figure 3b.3 *PXRD pattern of MOF over NF overlapped with the simulated MOF*

The morphological analysis of the catalyst was done by scanning electron microscopy (SEM) and the images were shown in Figure 3b.4. The SEM image of bare NF is shown in Figure 3b.4(a). The flower-shaped hybrid nanostructures of Co_3O_4-NiO/NF catalyst can be identified from the SEM images at different magnifications displayed in Figure 3b.4(b-e). The images show a uniform distribution of the nanostructures over the honeycomb skeleton of the NF.

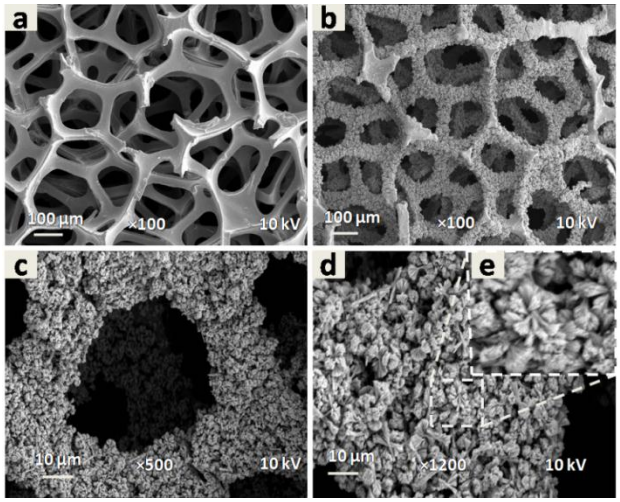

Figure 3b.4.*SEM images of bare nickel foam (NF) (a) and Co_3O_4-NiO/NF at different magnification for (b) 100 µm (c) 10 µm and (d) 10 µm (×1200) showing the presence of Co_3O_4-NiO nanoflowers uniformly grown over NF (e) zoomed in image of showing the formation of nanoflowers on the surface of NF*

The transmission electron microscopy (TEM) analysis also depict the formation of the above-mentioned composite. The TEM image of Co_3O_4-NiO/NF (Figure 3b.5(a)) shows a uniformly formedCo_3O_4-NiO hybrid nanostructures having a size range of 20 to 30 nm. The HRTEM images (Figure 3b.5(b, d)) of Co_3O_4-NiO/NF shows the formation of an interface between two phases and is shown by thedotted line. The d spacing value of 0.24 nm corresponds to the (311) crystal plane of the Co_3O_4 phase while the d spacing value of 0.147 nm corresponds to (220) crystal plane of the NiO phase.[32-35]

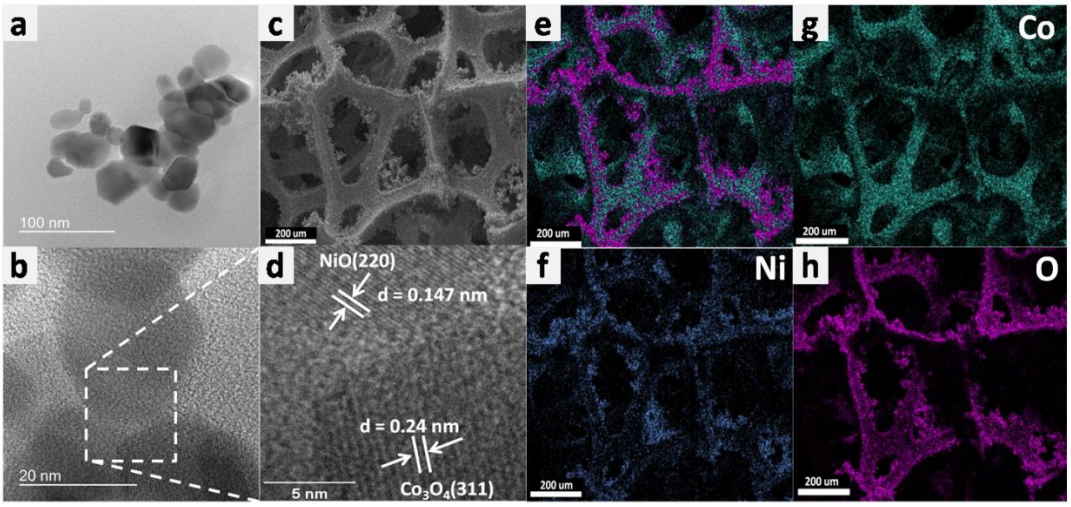

Figure 3b.5 *(a) TEM image of Co_3O_4-NiO/NF (b) & (d) HRTEM image with fringe width corresponding to the respective plane (c,e,f,g&h) dark field STEM elemental mapping showing the uniform distribution of all the elements.*

The FESEM elemental mapping of the Co_3O_4-NiO/NF (Figure 3b.5 (c, e, f, g & h)) reveals the presence of uniformly distributed Co, Ni and O in the catalyst.For the investigation of electronic interaction and chemical composition, the X-ray photoelectron spectroscopy (XPS) measurement was conducted. The survey spectrum (Figure 3b.6(a)) confirms the presence of Co, Ni, and O in the Co_3O_4-NiO/NF catalyst. The results are in line with the elemental mapping obtained from EDAX. The high-resolution Co 2p XPS spectrum (Figure 3b.6(b)) shows three peaks at 779.6, 781.3 and 781.8 eV corresponds to Co^{3+}, Co^{2+} and a satellite peak of Co $2p_{3/2}$. 36, 37 For Ni 2p, shown in figure (3b.6(c)),the peaks located at 853.7 and 871.7 eV attributed to Ni^{3+} of Ni $2p_{3/2}$ andNi $2p_{1/2}$.

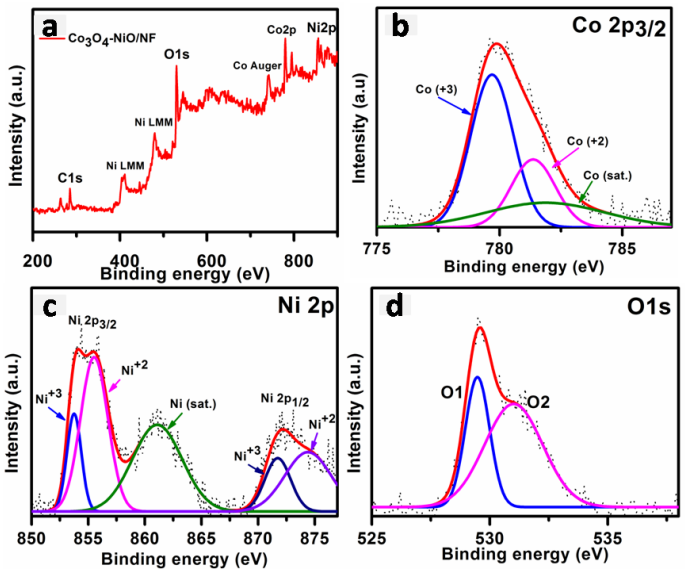

Figure 3b.6. *XPS of the Co_3O_4-NiO/NF catalyst (a) survey spectrum of catalyst . HR spectra of (b) Co 2p, (c) Ni 2p and (d) O 1s electron: experimental data (dotted curve) and fitting results (solid curve). The peaks are assigned by oxidation states of different elements with their splitting term.*

The other peaks at 855.5 and 874.3 eV can be assigned for the binding energy of Ni^{2+} of Ni $2p_{3/2}$ and Ni $2p_{1/2}$ .Interfacial interaction between the two phases can be investigated by using X-ray photoelectron spectroscopy. Any shift in the binding energy toward the positive value shows the interfacial interaction between two phases.[41]In our case, we have performed the XPS analysis of Co_3O_4-NiO and individual Co_3O_4 and NiO. When we compared the peak positions of Co $2p_{3/2}$ in Co_3O_4-NiO and individual Co_3O_4, we got the positive shift of 1.3 eV. When we compared the peak position of Ni 2p in Co_3O_4-NiO and individual NiO, we got a positive shift of 0.9 eV. The XPS results indicate that the electronic interaction between Co_3O_4-NiO leads to the redistribution of charge on their coupling interface. The graphs showing the shift in the XPS are given in Figure 3b.7. The catalytic activity of the sample towards OER was evaluated in basic medium using Ag/AgCl (saturated KCl filled) as a reference electrode and graphitic rod as a counter electrode All the data were taken at 25°C in O_2 saturated 1M KOH. The table containing mass loading of all the catalyst on NF is given in the Table 3b.1. For comparisons, the electrocatalyticactivities of NiO/NF and Co_3O_4/NF and commercial RuO_2/NFwas also examined under the identical condition.

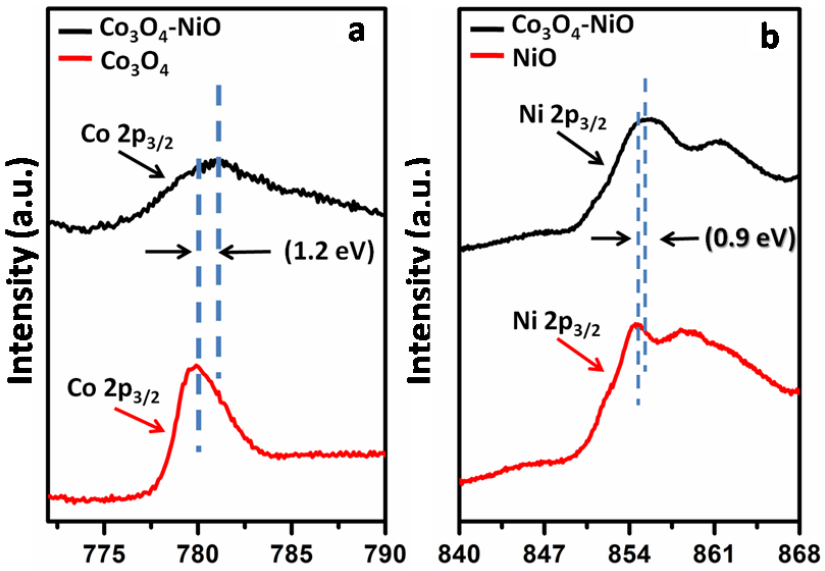

Figure 3b.7*(a)High resolution $Co2p_{3/2}$ XPS spectra of Co_3O_4-NiO and Co_3O_4 (b) high resolution XPS Ni 2p spectra of Co_3O_4-NiO and NiO*

Catalyst	Mass loading (mg cm^{-2})
Co_3O_4-NiO/NF	3.35
Co_3O_4/NF	3.35
NiO/NF	1.4
RuO_2/NF	3.35

Table 3b.1 *Mass loading of all the catalyst over NF*

Figure 3b.8(a) indicates the iR- corrected polarization curves for all the catalysts. The overpotential value of 311, 290, 339 and 343 mV obtained at 10 mA cm-2 current density respectively for Co_3O_4- NiO/NF, RuO_2/NF, Co_3O_4/NF and NiO/NF. The performance of the commercially available $RuO_2$was found to be superior to that of Co_3O_4-NiO/NF at 10 mA cm^{-2} current density. However, at the higher current densities (50 mA cm^{-2} and beyond), our catalyst shows superior activity than that of all the other supporting catalysts. The overpotential required to achieve the current densityof

50 mA cm^{-2} is 390, 415, 432 and 520 mV respectively for the Co_3O_4-NiO/NF,RuO_2/NF, Co_3O_4/NF and NiO/NF (Figure 3b.8(b)).

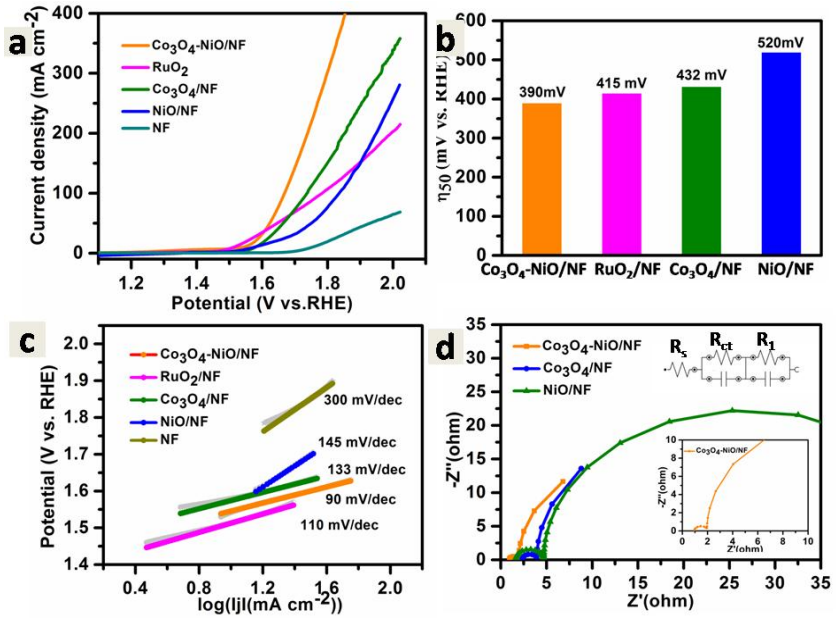

Figure 3b.8.*Electrochemical measurements of specific electrocatalysts for oxygen evolution in 1 M KOHalkaline medium. (a)Polarization curves (iR-corrected) of Co_3O_4-NiO/NF compared with theother electrode (b) comparison of the overpotential values obtained from polarization curve at 50 mA cm^{-2} current density (c) the corresponding Tafel plots derived from the (d) EIS Nyquist plot (with corresponding equivalent circuit) of the electrode at 100mV of overpotential*

Furthermore, to investigate the kinetics of the reaction, we have calculated the Tafel slope value by plotting the Tafel plot as depicted in figure 3b.8(c). The resulting Tafel slope values obtained are 90, 110, 133 and 145mV/dec for Co_3O_4- NiO/NF, RuO_2/NF, Co_3O_4/NF and NiO/NF respectively. The lower Tafel slope value of catalyst rendering a favourable OER kinetics than that of noble metal-based catalyst (RuO_2). To evaluate the interfacialinteractions of the catalyst and the charge transfer through the interface, we performed electrochemical impedance spectroscopy. The corresponding Nyquist plot at an applied overpotential of 100 mV are given in figure 3b.8(d). All the semi circles were fitted with the equivalent circuit depicted in figure 3b.8(d). along with the solution resistance, the fitted data exhibits two time-constant components R_{ct}-CPE_{dL} and R_p-CPE_L. The constant phase angle element (CPE) explain the double layer capacitance of the solid

electrode. R_{ct}-C1 gives information about charge-transfer resistance and EDL capacitance, and the surface porosity can be correlated with R_p-CPE_L. The (R1C2) circuit signify the diffusion/adsorption of reaction intermediates due to very slow diffusion through the reaction interface and surface porosity.

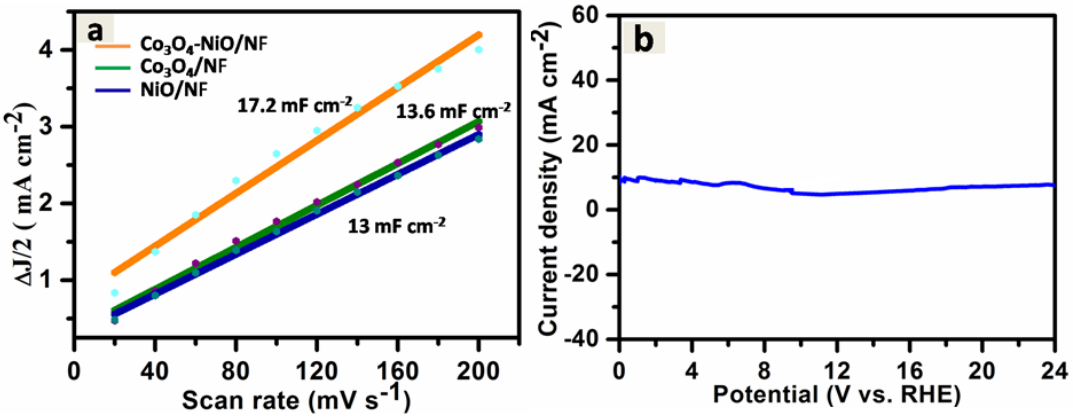

Figure 3b.9. *(a) double-layer capacitance (C_{dl}) calculation for all the electrodes obtained from the cyclic voltammetry curve taken in the non-faradic region (b) stability studies using chronoamperometry for 24 hr*

The species, such as MOH, can undergo oxidation to MO in apotential, resulting in the (R1C2) impedance at the low-frequency region in the semi-circle.The relationship between the charge transfer resistance and the applied potential is inversely proportional. A charge transfer resistance (R_{ct}) of 1.3Ω is obtained when the potential of100 mV is applied to the Co_3O_4-NiO/NF catalyst.The smaller value of Rct demonstrates that the electrochemically active sites on the electrode exhibit low resistance during the charge transfer between the electrode surface and the electrolyte. These observations from Nyquist plot explains the rationale behind a higher rate of electron transfer in the overall OER process. To calculate the electrochemically active surface area, we have first calculated the double-layer capacitance (Cdl) of all the electrodes as shown in Figure 3b.9(a). The obtained Cdl value is 17.2, 13.6 and 13 mF cm^{-2} for Co_3O_4- NiO/NF, Co_3O_4/NF and NiO/NF respectively.The higher value of C_{dl} for the catalyst indicates higher OER activity per unit area of the electrode of the corresponding catalyst.The long term durability of the catalyst was examined by the chronoamperometry at an overpotential of 311 mV for 24hr (Figure 3b.9(b)).

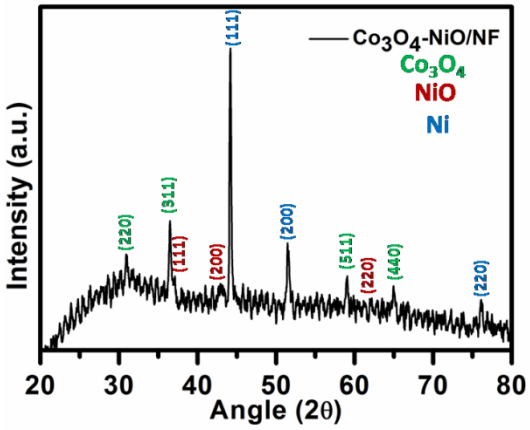

Figure 3b.10.*PXRD pattern of the catalyst after stability showing the retention of all the phases present*

The post stability studies using PXRD shows that, all the phases remain intact in the catalysts even after performing long duration stability experiment. The PXRD pattern taken after stability is given in Figure 3b.10. The cyclic volatametry curve for the calculation of double layer capacitance is given in Figure 3b.11

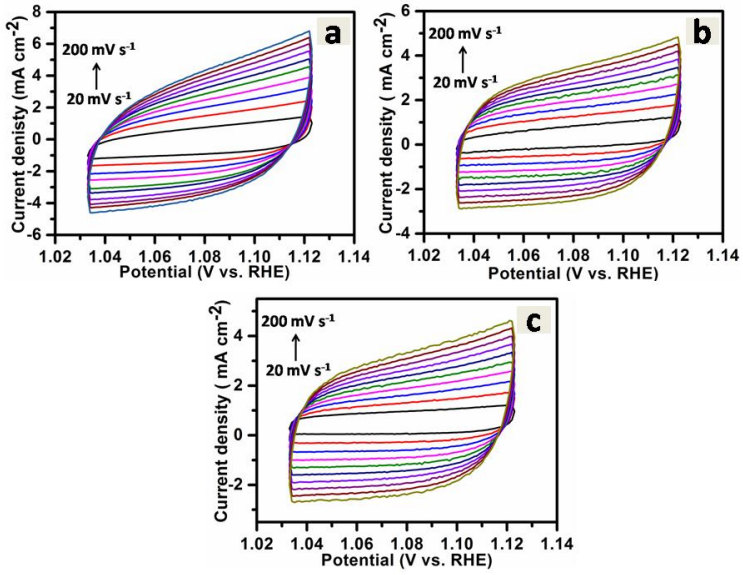

Figure 3b.11 *Cyclic voltammetry curve of (a)Co_3O_4-NiO/NF, (b) Co_3O_4/NF and (c) NiO/NF for the calculation of C_{dl}*

In order to calculate the faradic efficiency, a water-gas displacement method is used in which, the percentage of the ratio of the amount of O_2 evolved experimentally to the theoretically calculated amount of O_2 evolved. The faradic efficiency valueobtained for our catalyst was found to be 98.6 % (Figure 3b.12(a)). As oxygen evolution reaction is a 4 electron transfer process with a sluggish mechanism, we have calculated all adsorption values of different intermediates on the surface of the heterostructure. In our theoretical model, we have constructed all the atomic sites as per crystallographic information file and optimization thereafter, revealing the Co_3O_4-NiO heterostructure.

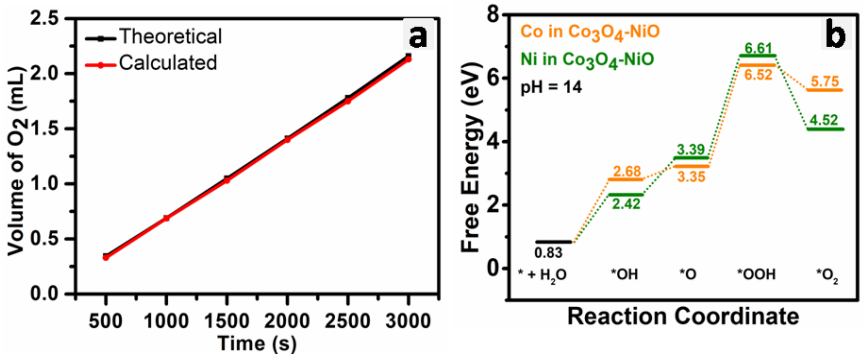

Figure 3b.12. *(a)Volume of O_2 evolve atdifferent time for the calculation offaradic efficiency the calculated value is the quantitative faradicyield for O2 evolution (b) calculated Gibbs free energies diagram for Co_3O_4-NiO/NF heterostructure*

The strength of adsorption was determined by calculating the adsorption energies, which is given as $E_{ads} = E_{(surface-X)} - E_{(surface)} - E_{(X)}$ where $E_{(surface-X)}$ depicts the overall energy of the adsorbate and the surface, $E_{(surface)}$ is the surface energy and $E_{(X)}$ is the total energy of the O or OH molecules. Furthermore, the free energies are obtained at standard conditions (pH = 14, T = 298.15 K) and at equilibrium potential, ie.,U = 1.23V,[42]for OER process. The Gibbs free energy diagram shown in Figure 3b.12(b), demonstrate the value of adsorption energies for different intermediates. We did the calculation on both Ni as well as on Co-site present in the Co_3O_4-NiO/NF heterostructure and found that the Ni is the most active site for the OER process. For Ni and Co both, the OER step involving O* to OOH* is an uphill process and a rate-determining step (R.D.S.). The theoretically calculated overpotential for Co_3O_4-NiO/NF heterostructure is 364 mV which is closed to the experimentally calculated one. We have also calculated the cohesive energy. The

calculations indicate the stable formation of oxide heterostructure with the cohesive energy of -5.3238 eV. The negative cohesive energy indicates a strong interaction between two phases. We have also calculated the Bader charge analysis for the charge transfer at the interface. The Bader charge analysis was carried out with the Co_3O_4-NiO heterostructure and it appeared that NiO loses a charge of +0.035138 to Co_3O_4 and Co_3O_4 gain charge of - 0.035123 through the interface conveys a significant charge transfer taking place across the phases in the heterostructure. A detail discussion of how the different adsorption energies calculated with obtained values are provided in Table 3b.2. Superhydrophilic surfaces have drawn significant attention in heterogeneous catalysis as it favours the low adsorption energies on the catalyst surface. It is also important to know the nature and behaviour of the surface of the catalyst in water bases heterogeneous catalysis.[43]

S. No.	Surface	Total energy (eV)
1.	**Co3O4-NiO+O (Ni-site)**	-725.68981
2.	**Co3O4-NiO+O (Co-site)**	-725.7282
3.	**Co3O4-NiO+OH (Ni-site)**	-730.49719
4.	**Co3O4-NiO+OH (Co-site)**	-730.23927
5.	**Co3O4-NiO+OOH (Ni-site)**	-733.50533
6.	**Co3O4-NiO+OOH (Co-site)**	-733.58578

Table 3b.2. *Adsorption energies at different sites*

The surface of Co_3O_4-NiO/NF was analyzed by performing hydrophilicity test (Figure 3b.13(a&b)) and found to be superhydrophilic as the drop of water absorb immediately after falling on to the surface. The contact angle was also found to be closed to 0° depicting the superhydrophilicity of the catalyst surface.

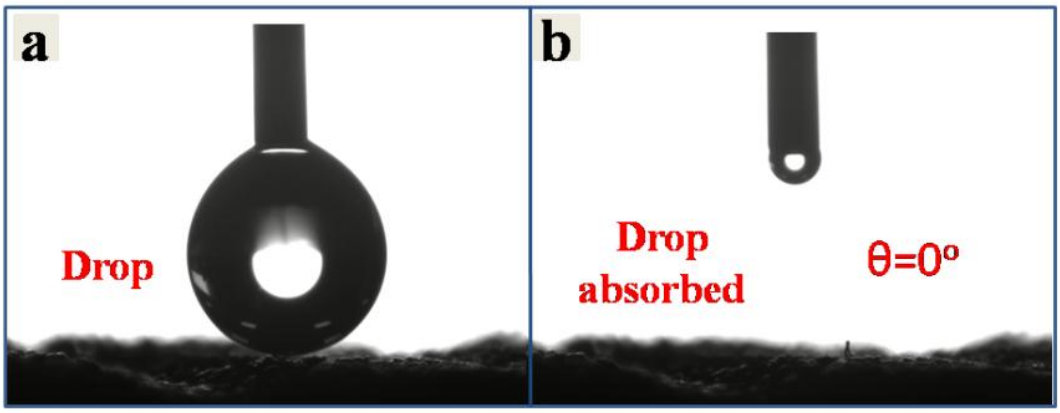

Figure 3b.13.*(a) Hydrophilicity analysis of Co_3O_4-NiO/NF (a) before and (b) after dropping the liquid on the surface ofthe catalyst*

3b.4 Conclusion

In summary, we could demonstrate the fabrication of nanointerfaces between Co3O4 and NiO by using Co2(OH)2(BDC)as a precursor. The catalyst shows nanoflowers like morphology with superhydrophilic nature. The resulting Co3O4-NiO hybrid nanostructures show excellent OER activity with onset overpotential of 290 mV and overpotential of 311 mV at 10 mA cm-2 current density and a Tafel slope of 90 mV/dec in 1M KOH solution. The catalyst shows durability up to 24 hr in chronoamperometry. The electrocatalytic activity of the catalyst can be explained by the formation of heterointerfaces, highly exposed active sites and synergistic effect. The DFT results supports the experimental findings which can be applied for the other metal oxide nanoparticles for several electrochemical applications.

Note:

- The permission has been granted by the authors and corresponding author of the published paper prior to adopting in the present thesis. The associated relevant publication is:

Gaur, Ashish, VikasPundir, RituRai, BaljeetKaur, Takahiro Maruyama, ChandanBera, and VivekBagchi. "Interfacial interaction induced OER activity of MOF derived superhydrophilic Co 3 O 4–NiO hybrid nanostructures." *Dalton Transactions* 51, no. 5 (2022): 2019-2025.

References

(1)Lewis, N. S. *Science* 2016, *351*, aad1920.

(2) Zeng, K.; Zhang, D. *Progress in Energy and Combustion Science* 2010, *36*, 307.

(3)Zou, X.; Zhang, Y. *Chemical Society Reviews* 2015, *44*, 5148.

(4) Chen, Z.; Duan, X.; Wei, W.; Wang, S.; Ni, B.-J. *Journal of Materials Chemistry A* 2019, *7*, 14971.

(5) Yao, Y.; Mahmood, N.; Pan, L.; Shen, G.; Zhang, R.; Gao, R.; Aleem, F.-e.; Yuan, X.; Zhang, X.; Zou, J.-J. *Nanoscale* 2018, *10*, 21327.

(6) Song, J.; Wei, C.; Huang, Z.-F.; Liu, C.; Zeng, L.; Wang, X.; Xu, Z. J. *Chemical Society Reviews* 2020, *49*, 2196.

(7) Zhu, G.; Xie, X.; Li, X.; Liu, Y.; Shen, X.; Xu, K.; Chen, S. *ACS Applied Materials & Interfaces* 2018, *10*, 19258.

(8) Lee, Y.; Suntivich, J.; May, K. J.; Perry, E. E.; Shao-Horn, Y. *The Journal of Physical Chemistry Letters* 2012, *3*, 399.

(9) Yu, J.; He, Q.; Yang, G.; Zhou, W.; Shao, Z.; Ni, M. *ACS Catalysis* 2019, *9*, 9973.

(10) Li, Y.; Li, F.-M.; Meng, X.-Y.; Li, S.-N.; Zeng, J.-H.; Chen, Y. *ACS Catalysis* 2018, *8*, 1913.

(11) Han, H.; Park, S.; Jang, D.; Kim, W. B. *Journal of Alloys and Compounds* 2021, *853*, 157338.

(12) Fan, H.; Yu, H.; Zhang, Y.; Zheng, Y.; Luo, Y.; Dai, Z.; Li, B.; Zong, Y.; Yan, Q. *AngewandteChemie International Edition* 2017, *56*, 12566.

(13) Gaur, A.; Sachdeva, P. K.; Kumar, R.; Maruyama, T.; Bera, C.; Bagchi, V. *Sustainable Energy & Fuels* 2021, *5*, 801.

(14) Zhang, J.; Qian, J.; Ran, J.; Xi, P.; Yang, L.; Gao, D. *ACS Catalysis* 2020, *10*, 12376.

(15) Kwon, T.; Jun, M.; Joo, J.; Lee, K. *Journal of Materials Chemistry A* 2019, *7*, 5090.

(16) Li, Q.; Wang, X.; Tang, K.; Wang, M.; Wang, C.; Yan, C. *ACS Nano* 2017, *11*, 12230.

(17) Xiong, X.; You, C.; Liu, Z.; Asiri, A. M.; Sun, X. *ACS Sustainable Chemistry & Engineering* 2018, *6*, 2883.

(18) Sahoo, M. K.; Samantara, A. K.; Behera, J. N. *Inorganic Chemistry* 2020, *59*, 12252.

(19) Wang, X.; Li, B.; Wu, Y.-P.; Tsamis, A.; Yu, H.-G.; Liu, S.; Zhao, J.; Li, Y.-S.; Li, D.-S. *Inorganic Chemistry* 2020, *59*, 4764.

(20) Zhu, R.; Ding, J.; Yang, J.; Pang, H.; Xu, Q.; Zhang, D.; Braunstein, P. *ACS Applied Materials & Interfaces* 2020, *12*, 25037.

(21) Abdelkader-Fernández, V. K.; Fernandes, D. M.; Balula, S. S.; Cunha-Silva, L.; Freire, C. *Journal of Materials Chemistry A* 2020, *8*, 13509.

(22) Chen, L.; Luque, R.; Li, Y. *Chemical Society Reviews* 2017, *46*, 4614.

(23) Zhu, R.; Ding, J.; Xu, Y.; Yang, J.; Xu, Q.; Pang, H. *Small* 2018, *14*, 1803576.

(24) Zheng, S.; Li, Q.; Xue, H.; Pang, H.; Xu, Q. *National Science Review* 2020, *7*, 305.

(25) Li, X.; Wei, J.; Li, Q.; Zheng, S.; Xu, Y.; Du, P.; Chen, C.; Zhao, J.; Xue, H.; Xu, Q.; Pang, H. *Advanced Functional Materials* 2018, *28*, 1800886.

(26) Xue, Z.; Liu, K.; Liu, Q.; Li, Y.; Li, M.; Su, C.-Y.; Ogiwara, N.; Kobayashi, H.; Kitagawa, H.; Liu, M.; Li, G. *Nature Communications* 2019, *10*, 5048.

(27) Zhou, J.; Zheng, H.; Luan, Q.; Huang, X.; Li, Y.; Xi, Z.; Lu, G.; Xing, L.; Li, Y. *Sustainable Energy & Fuels* 2019, *3*, 3201.

(28) Jin, B.; Li, Y.; Wang, J.; Meng, F.; Cao, S.; He, B.; Jia, S.; Wang, Y.; Li, Z.; Liu, X. *Small* 2019, *15*, 1903847.

(29) Chen, H.; Ge, D.; Chen, J.; Li, R.; Zhang, X.; Yu, T.; Wang, Y.; Song, S. *Chemical Communications* 2020, *56*, 10529.

(30) Long, H.; Shi, T.; Hu, H.; Jiang, S.; Xi, S.; Tang, Z. *Scientific Reports* 2014, *4*, 7413.

(31) Muráth, S.; Alsharif, N. B.; Sáringer, S.; Katana, B.; Somosi, Z.; Szilagyi, I. *Crystals* 2020, *10*.

(32) Liu, L.; Yang, M.; Zhao, H.; Xu, Y.; Cheng, X.; Zhang, X.; Gao, S.; Song, H.; Huo, L. *MicrochimicaActa* 2019, *186*, 184.

(33) Harilal, M.; Krishnan, S. G.; Vijayan, B. L.; Venkatashamy Reddy, M.; Adams, S.; Barron, A. R.; Yusoff, M. M.; Jose, R. *Materials & Design* 2017, *122*, 376.

(34) Nguyen, K.; Hoa, N. D.; Hung, C. M.; Thanh Le, D. T.; Van Duy, N.; Van Hieu, N. *RSC Advances* 2018, *8*, 19449.

(35) Natile, M. M.; Glisenti, A. *Chemistry of Materials* 2003, *15*, 2502.

(36) Liotta, L. F.; Di Carlo, G.; Pantaleo, G.; Venezia, A. M.; Deganello, G. *Applied Catalysis B: Environmental* 2006, *66*, 217.

(37) Huang, W.; Ding, S.; Chen, Y.; Hao, W.; Lai, X.; Peng, J.; Tu, J.; Cao, Y.; Li, X. *Scientific Reports* 2017, *7*, 5220.

(38) Zhou, G.; Wang, D.-W.; Yin, L.-C.; Li, N.; Li, F.; Cheng, H.-M. *ACS Nano* 2012, *6*, 3214.

(39) Gopi, C. V. V. M.; Vinodh, R.; Sambasivam, S.; Obaidat, I.; Kalla, R. M. N.; Kim, H. *Materials Today Energy* 2019, *14*, 100358.

(40) Yan, H.; Xie, Y.; Jiao, Y.; Wu, A.; Tian, C.; Zhang, X.; Wang, L.; Fu, H. *Advanced Materials* 2018, *30*, 1704156.

(41) Man, I. C.; Su, H.-Y.; Calle-Vallejo, F.; Hansen, H. A.; Martínez, J. I.; Inoglu, N. G.; Kitchin, J.; Jaramillo, T. F.; Nørskov, J. K.; Rossmeisl, J. *ChemCatChem* 2011, *3*, 1159.

(42) Wang, J.-Y.; Liu, W.-T.; Li, X.-P.; Ouyang, T.; Liu, Z.-Q. *Chemical Communications* 2020, *56*, 1489.

Chapter 3c

Electronic Redistribution Over the Active Sites of $NiWO_4$-NiO Induces Collegial Enhancement in Hydrogen Evolution Reaction

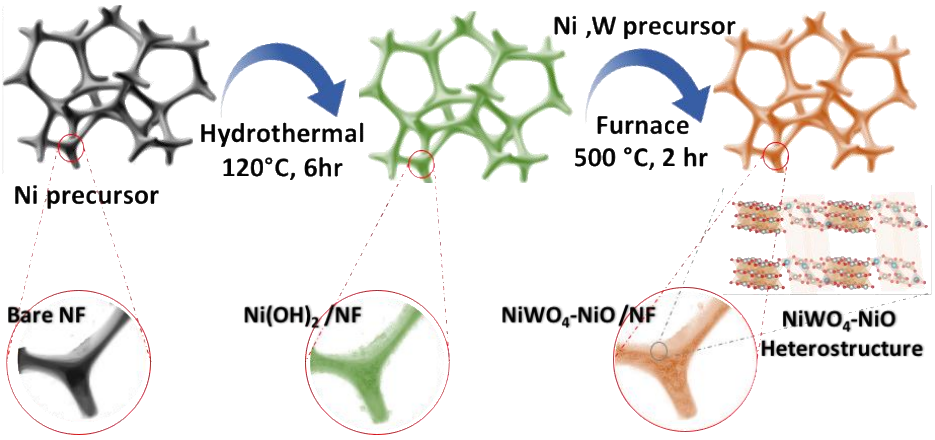

Brief Outcome: *The activity-enhancement of a new-generation catalyst focuses on the collegial approach among specific solids which exploit the mutual coactions of these materials for HER applications. Strategic manipulation of these solid interfaces typically reveals unique electronic states different from their pure phases, thus, providing a potential passage to create catalysts with excellent activity and stability. Herein, the formation of the $NiWO_4$-NiO interface has been designed and synthesized via a three-step method. This strategy enhances the chance of the formation of abundant heterointerfaces due to the fine distribution of $NiWO_4$ nanoparticles over$Ni(OH)_2$ sheets. $NiWO_4$-NiO has superior HER activity in alkaline (1M KOH) electrolyte with modest overpotential of 71 mV at 10 mA cm^{-2} current density. The catalyst is highly stable in an alkaline medium and negligible change was observed in the overpotential after 10,000 cycles upto 100 hrs. This study explores a unique method for high-performance hydrogen generation by constructing transition metal-oxides heterojunction. The XPS studie sreveal an electronic redistribution driven by charge transfer through the $NiWO_4$-NiO interface. The density functional theory (DFT) calculations show that the $NiWO_4$-NiO exhibits a Pt-like activity with the hydrogen Gibbs free energy (ΔG_H*) value of 0.06 eV compared to the Pt(ΔG_H*=-0.02eV).*

3c.1. Introduction

Biodiversity is the heart of our existence, where millions of different species depend someway on each other. Our planet operates like a living, breathing organism with countless species working like its organs, each with a different role to play in keeping the planet healthy. However, extreme human activity with an unending non-cyclic pattern of usage of carbon-based fuel, and unsustainable exploitation of resources have affected the climate adversely.[1] In the recent past, 23,000 spectacled flying foxes (Pteropusconspicillatus), also known as the spectacled fruit bat killed in heat stress in Australia.[2] Extreme heat events are just one of many symptoms of climate change.[3] Therefore, it is high time that we make a move towards a sustainable energy source. Green hydrogen is one of the most promising energy carriers, which can be generated using environment friendly technologies.[4-6] Water electrolysis is an excellent method for generating hydrogen energy, which completes the hydrogen cycle loop.[7-9] Owing to high intrinsic activity and low acid corrosion resistance, Pt and Pt-based catalysts are commonly used as cathode material for hydrogen evolution reaction (HER) in water electrolysis.[10-14] However, the restricted supply and high cost of noble metals prevent them from being used commercially on a significant scale. As a result, various efforts have been made to produce noble-metal-free HER catalysts, based on metal sulphides[15-17], carbides[18-21], oxides[19,22,23], and phosphides.[24,25] The transition zones between two crystals or phases are referred to as interfaces that manifest unique physicochemical properties due to atomic misarrangement. Controlled manipulation of these interfaces can be used to tune the mechanical, electrical, optical, and catalytic properties of materials.[26-28] The activity and stability of electrocatalysts are determined by the electronic structure and strain.[29] Atomic misalignment at the contact can cause strain within the solid, resulting in a change in the electronic structures which are completely different from the original electronic structures of the pure phases. For example, Wang et al. show the superior electrocatalytic activity towards hydrogen evolution reaction by the formation of interfaces between Ni_2P-$Ni_{12}P_5$.[29] Furthermore, Jiao et al. show the enhanced overall water splitting by interface engineering between Co, CoP and N, P doped carbon nanotubes.[30] Appropriately engineered interfaces can promote fast electron transport and

create isolated active sites which in turn enhances the catalytic activity. The electrocatalytic activity of the individual NiO phase is poor due to the low electrical conductivity and low specific surface area, however, the electrocatalytic activity of single-phase NiO can be improved by the introduction of foreign active components.[31,32] One such solid is nickel tungstate ($NiWO_4$) which exhibits superior electrochemical activities and has recently been used for biosensors, hydrodesulphurization (HDS), photoelectrocatalysis (PEC), photocatalysis, supercapacitor, and electrocatalytic applications.[33-35] Very limited work has been reported on $NiWO_4$ nanomaterials for cathodic reduction and anodic oxidation. Herein, we have integrated $NiWO_4$ and NiO into a unique heterointerface that excels HER in an alkaline medium.

3c.2. Experimental section

3c.2.1. Materials

The chemicals used in this work were procured from different suppliers and are used without further purification. Nickel (II) nitrate hexahydrate ($Ni(NO_3)_2.\ 6H_2O$, 99%), Sodium tungstate dihydrate ($Na_2WO_4{\cdot}2H_2O$, 99.9%), Ammonium fluoride (NH_4F, 99.9%), Nafion perfluorinated resin solution (5 wt% in a mixture of lower aliphatic alcohol and water, contains 45% water) were purchased from Sigma Aldrich. Potassium hydroxide pellets were purchased from TCI. Nickel foam (NF) was purchased from Nanoshel. In all the preparation, Milli Q water having a conductivity of 0.056 μS/cm was used.

3c.2.2. Methodology

3c.2.2.1. Synthesis of Catalyst

Catalyst synthesis section is subdivided into three major steps as per following description**.**

Step 1. Synthesis of $Ni(OH)_2$/NF: To remove surface oil and oxide coatings, the NF was cleaned with 3M HCl solution under ultrasonication and thereafter washed with DI water and acetone. The cleaned NF was cut into small pieces with a cross-section of 1 cm

x 1.2 cm. Nanosheets of $Ni(OH)_2$were grown over NF using hydrothermal methods. Nickel(II) nitrate hexahydrate, ($Ni(NO_3)_2.6H_2O$, 1mmol) and carbamide (urea, 2 mmol) were mixed in 15 mL of deionized water. The above solution was then transferred into the 30 mL Teflon autoclave containing a piece of nickel foam and was kept at a temperature of 100°C for 6 h. The obtained $Ni(OH)_2$/NF was washed with water and ethanol several times and dried in the oven at 60°C.

Step 2. Synthesis of $NiWO_4$-$Ni(OH)_2$/NF: Synthesis of $NiWO_4$ nanoparticles over $Ni(OH)_2$ was carried out using 2 mmol of sodium tungstate dihydrate ($Na_2WO_4 \cdot 2H_2O$) and 2 mmol of nickel nitrate hexahydrate ($Ni(NO_3)_2.6H_2O.2$). The mixture was dissolved in 15 mL of water and the solution was transferred into the 30 mL Teflon autoclaves containing $Ni(OH)_2$/NF. The autoclave was heated at 180°C for 18 h. After the reaction is over, the obtained $NiWO_4$-$Ni(OH)_2$/NF electrode was washed with water and ethanol and dried in the oven at 60°C.

Step 3. Synthesis of $NiWO_4$-NiO/NF:

In order to prepare $NiWO_4$ – NiO hetero-nanostructures over NF, the above electrode was calcinated in the oven at 500°C for 2 h in the air at a heating rate of 5°C per minute. During this process, NiO was formed from $Ni(OH)_2$ and $NiWO_4$became more crystalline. After cooling down, the electrode was removed from the furnace and washed with water and ethanol. The as-obtained $NiWO_4$-NiO was used as an electrocatalyst for hydrogen evolution reaction.

Synthesis of $NiWO_4$ nanoparticles: Synthesis of $NiWO_4$ nanoparticles was done by using sodium tungstate dihydrate ($Na_2WO_4 \cdot 2H_2O$) and $Ni(NO_3)_2.6H_2O$. 2 mmol of sodium tungstate and 2 mmol of nickel nitrate hexahydrate was dissolve in 15 mL of water . After that the solution was transferred into the 30 mL teflon autoclave containing NF. The autoclave was heated at 180°C for 18 h. After that the obtained NiWO4/NF electrode was washed with water and ethanol and dried in the oven at 60°C.

Synthesis of NiO/NF: To remove surface oil and oxide coatings, the NF was cleaned ultrasonically in 3M HCl solution, acetone, and DI water for 20 minute. The cleaned NF was cut into small pieces with a cross section of 1cm x 1.2cm. $Ni(OH)_2$ nanosheets were

grown over NF by using hydrothermal method. 1 mmol of $Ni(NO_3)_2.6H_2O$ and 2 mmol of urea were mixed in 15 mL of deionized water. The above solution was transferred into the 30 mL teflon autoclave containing a piece of nickel foam, then the autoclave was heated at 100°C for 6 h. After that the obtained $Ni(OH)_2$/NF was washed with water and ethanol several times and dried in oven at 60°C .After that the as obtained $Ni(OH)_2$/NF electrode was calcinated in furnace at 550°C for 2 hr in the presence of air. The as obtained NiO/NF was washed and used as a electrode as it is.

3c.2.2.2. Physical characterization

The $NiWO_4$-NiO/NF hybrid heterostructured catalyst was physically characterised using several techniques. Preliminarily it was analysed using a Bruker Eco D8 ADVANCE X Powder X-ray diffractometer that consists of a Ni filter. The Cu K_α radiation (λ = 1.54056 Å, 40 kV and 25 mA) was used in the 2θ range of 5°−80° with a step size of 0.00190/step. The morphological characterisation of the hybrid nanostructure was performed by JEOL (JSM IT-300) scanning electron microscope equipped with an energy-dispersive X-ray diffractometer (Bruker). The nanostructured $NiWO_4$-NiO/NF material and the particle gross size were examined by transmission electron microscopy (TEM) JEOL-2100 operated at 200 kV. The elemental analysis is performed by X-ray Photoelectron Spectroscopy (XPS) on ESCA Lab: 220-IXL with Mg K_α non-monochromated X-ray beam having photon energy 1253.6 eV.

3c.2.2.3. Electrochemical measurements

The electrochemical experiment was carried out at room temperature using a CHI 760E electrochemical workstation. A three-electrode arrangement was set up with graphite electrodes as counter electrodes and saturated Ag/AgCl serving as the reference electrode. The as-synthesized $NiWO_4$-NiO/NF catalyst formed over the NF was used as a working electrode. An ink of commercially available Pt/C catalyst was separately prepared for the comparative analysis. Following a general procedure, the ink for the nickel foam coating was prepared by dissolving 10 mg of the catalyst in 500 µL of dimethylformamide containing 10 µL of a 5% Nafion solution. After sonication for 120 minutes, a homogenous catalyst suspension was formed before it could be drop-casted

onto the nickel foam. The nickel foam was then coated with 40 μL of ink and cured under vacuum which makes it ready for further analysis. Scan rates for all of the polarisation data were kept at 5 mV/s^{-1} in 1M KOH. Equation $E_{RHE} = E_{Ag/AgCl} + 0.197 + 0.059$ pH has been used for conversion of all the electrochemical data into RHE. Electrochemical stability was performed by running 10,000 LSV cycles on a continuous mode. The Tafel slope was calculated by fitting the linear region of the Tafel curve following the Tafel equation ($\eta = b \log(j) + a$). Electrochemical impedance spectroscopy (EIS) was performed at an overpotential of 100 mV under a frequency range of 100000 Hz - 1 Hz. The double-layer capacitance and electrochemically active surface area ECSA analysis were performed using the CV scans in a non-Faradaic potential range in 1 M KOH at a scan rate of 20 to 200 mV/s.

3a.2.2.4. Theoretical methodology

The Gibbs free energy (ΔG_H) of hydrogen adsorption to the catalyst surface is intimately associated with hydrogen evolution activity.[36,37] Free energy is a conventional parameter employed to measure hydrogen-metal bond strength. When ΔG_H is close to 0.0 eV, it implies an optimised intermediate binding energy and leads to a high HER efficiency because of equilibrium between the rate of proton reduction and ease of desorption of the protons from the active surface.[38]

For HER catalysts, the ΔG_H value was calculated by DFT, which provides a suitable description of hydrogen evolution activity. The hydrogen atoms adsorption energy of the heterostructure is computed as:

$$\Delta E_{ads} = E_{surface + H^*} - E_{surface} - \tfrac{1}{2} E_{(H2)}$$

Here, $E_{surface + H^*}$ refers to the energy of adsorbate and adsorbent, $E_{surface}$ is the energy of pristine surface and $E(H_2)$ is the energy of hydrogen gas. ΔG_H is calculated from ΔE_{ads}using the following equation:

$$\Delta G = \Delta E_{ads} + 0.24\ eV$$

The DFT calculations was done by assuming a supercell having lattice parameters: $a = 6.71$ Å, $b = 16.36$ Å, $c = 12.96$ Å, with $\alpha = \beta = \gamma = 89.98°$ using Vienna Ab initio Simulation Package (VASP) with projector-augmented wave method. The exchange-

correlation functional is preserved with the PBE (Perdew, Burke, and Ernzerhof) version of generalized gradient approximation. Approximately 10*Å* vacuum was added along the c-axis to prevent interaction between adjacent layers. For structure relaxation, the plane wave energy cut-off was set to 520 eV, and the k-point mesh was taken as 7 X 7 X 1. For geometry optimisation, the forces and energy conversion threshold were set at 0.01eV/A and 10^{-4} eV respectively.

3c.3. Result and Discussion

Primarily the fabricated catalyst was investigated through; powder X-ray diffraction (PXRD) as shown in Figure 3c.1(a). The $NiWO_4$-NiO/NF PXRD pattern reveals crisp and distinct reflections with both $NiWO_4$ and NiO phases present, indicating the existence of hybrid heterostructures over NF. The diffraction peaks at 15.86°, 19.34°, 24.16°, 25.13°, 31.11°, 31.83°, 36.83°, 39.40°, 41.90°, 46.5°,49.2°,52.6°,54.81°, 65.83°, and 72.90° can be assigned to (010), (100), (011), (110), (T00), (020), (002), (200), (T02), (011), (T12), ($\bar{2}$11), (130), ($\bar{2}$02), (T32), and (302), crystal planes of $NiWO_4$ (JCPDS No. 15-0755).[33,43,44] The other peaks at 37.47°, 43.53° and 62.90°, 76.45° and 79.53° correspond to (111), (200), (220), (311) and (222) crystal plane of nickel oxide (JCPDS No. 47-1049).[45,46]

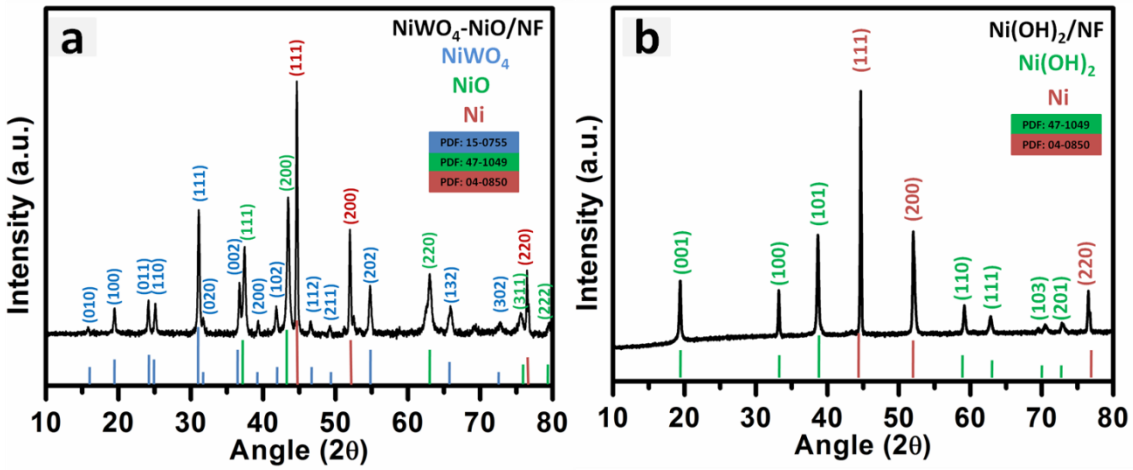

Figure 3c.1 *PXRD spectrum of (a) Catalyst showing the presence of both $NiWO_4$ and NiO phases (b) pre-catalyst showing the formation of $Ni(OH)_2$ over nickel foam.*

The PXRD pattern of the as-synthesized $Ni(OH)_2$ (Figure 3c.1(b)) shows seven peaks centered at 19.3°, 33.2°, 38.7°, 59.1°, 62.9°, 70.9°, and 72.9° corresponds to (001), (100), (101), (110), (111), (103), and (201) crystal planes of $Ni(OH)_2$ (JCPDS No. 22-0444).[44,47] The other three peaks at 44.61°, 52.07°, and 76.6° corresponds to the (111), (200), and (220) crystal planes of Ni which is coming from the nickel foam (JCPDS No. 04-0850).[48] All the results obtained from PXRD are consistent with the HRTEM analysis, discussed in the later section.

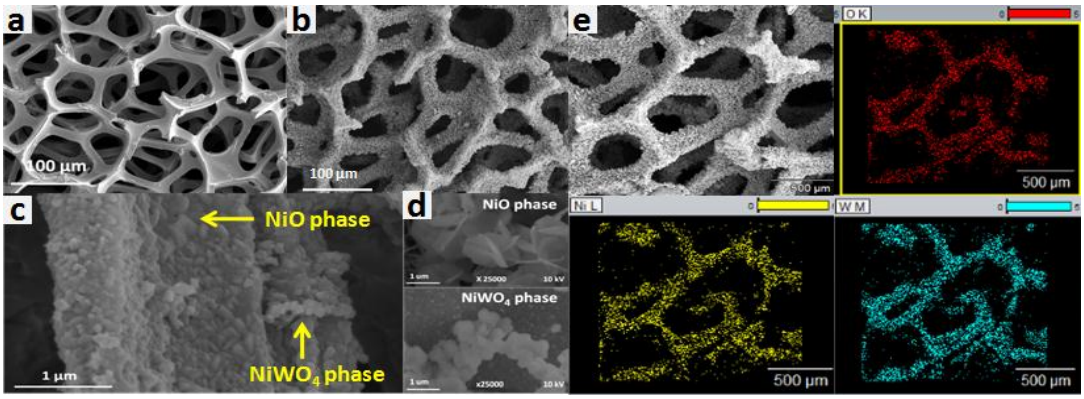

Figure 3c.2. *FESEM images of (a) bare nickel foam and (b & c) $NiWO_4$-NiO/NF at different magnifications showing the presence of $NiWO_4$ nanoparticles over NiO sheet. (d) images of individual NiO and $NiWO_4$ phases(e) The FESEM elemental mapping of $NiWO_4$-NiO/NF showing the uniform distribution of Ni, W and O over the catalyst surface*

Scanning electron microscopy (SEM) was used to examine the morphology of the catalyst and the resulting images are shown in Figure 3c.2.The SEM images of bare nickel foam (NF) are depicted in Figure 3c.2(a)., while Figures 3c.2(b & c) are showing the SEM images of $NiWO_4$-NiO at different magnifications. These images show the uniform distribution of $NiWO_4$ nanoparticles over NiO sheets. Figure 3c.2(d) depicts the image of individual $NiWO_4$ and NiO phases. To further check the elemental distribution of the corresponding elements over the catalyst ($NiWO_4$-NiO/NF) surface, we have shown the EDX mapping using FESEM (Figure 3c.2(e)). The images show that all the elements (Ni, W, O) are uniformly distributed over the catalyst surface.

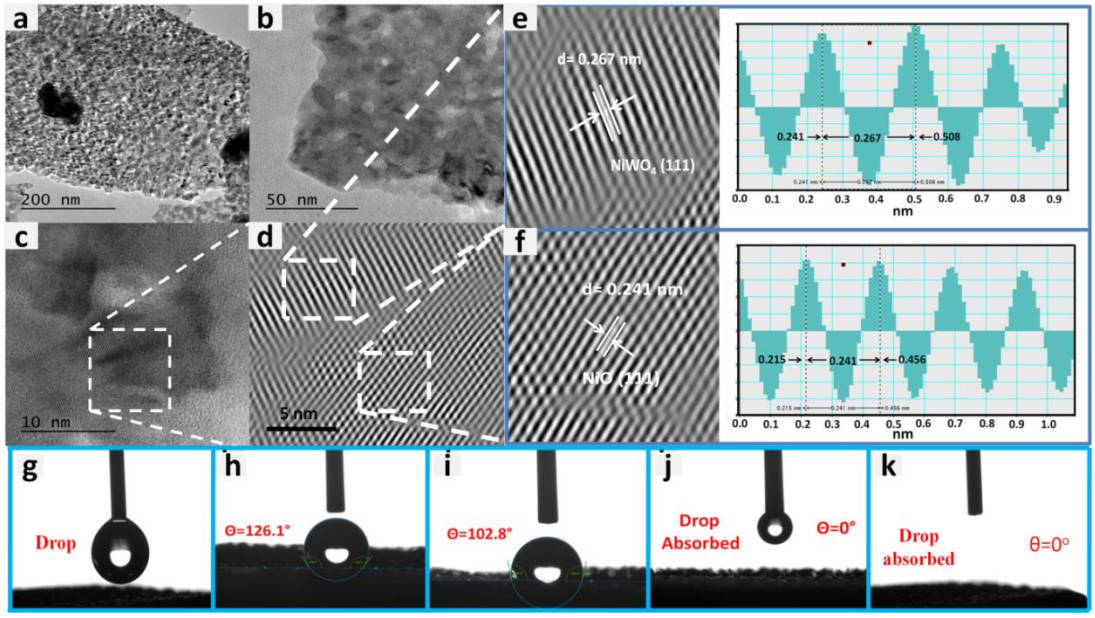

Figure 3c.3. *TEM images (a&b) of $NiWO_4$-NiO heterostructure at different magnification showing the presence of $NiWO_4$ nanoparticles over NiO, (c &d) HRTEM images of $NiWO_4$-NiO heterostructure, (e &f) shows the respective fringe-width of $NiWO_4$ and NiO with corresponding planes.*

We have also used transmission electron microscopy (TEM) and high-resolution TEM imaging (HRTEM) to confirm the crystal structures of these nanomaterials. Figure 3c.3(a&b) shows the TEM images of $NiWO_4$-NiO at two different resolutions. These images also indicate the presence of $NiWO_4$ nanoparticles over NiO sheets.The HRTEM analysis of $NiWO_4$-NiO (Figure 3c.3(c, d) confirms the presence of two different lattice fringes forming the interface between them. The d-spacing value of these phases was found to be 0.267 nm (Figure 3c.3(e)) and 0.241 nm (Figure 3c.3(f)) corresponding to the (111) planes of $NiWO_4$ and NiO.[49,50] These sharp lattice fringes are indicating the high crystallinity of the sample. In heterogeneous catalysis, the surface behaviour of the catalyst is extremely important. Heterogeneous catalysis is highly favoured by the superhydrophilic surfaces, as they support the low adsorption energies on their surfaces[51]. By measuring the contact angle between the surface of the electrode material and the water droplet, the hydrophilicity may be measured. Superhydrophilicity of a material facilitates the electrolytes to diffuse more efficiently toward the accessible active sites, reducing the ohmic resistance at the electrode-electrolyte interface and promotes a faster

charge transfer during the electrochemical reaction. It was found that the surface of bare NF is hydrophobic in nature with contact angle of 126.1˚ (Figure 3c.3(g&h)). NiO was also hydrophobic in nature with contact angle of 102.8˚ (Figure 3c.3(i)) whereas individual $NiWO_4$ and $NiWO_4$-NiO/NF are superhydrophilic in nature (Figure 3c.3(j&k)) with contact angle of 0˚.

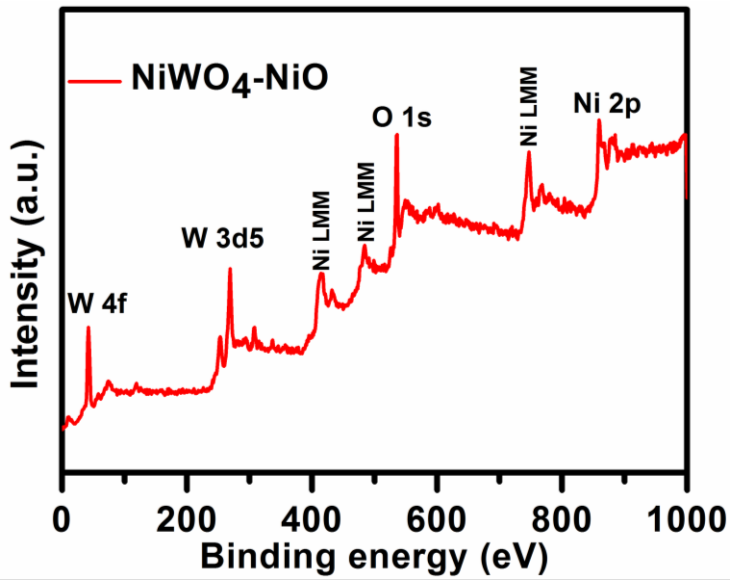

Figure 3c.4. *XPS wide scan spectrum of $NiWO_4$-NiO confirms the presence of Ni, W and O in $NiWO_4$-NiO/NF heterostructure*

The investigation of the chemical states of Ni, W and O in $NiWO_4$-NiO was done by using X-ray photoelectron spectroscopy (XPS). The XPS survey spectrum of $NiWO_4$-NiO is given in Figure 3c.4. The high-resolution XPS spectra of Ni 2p (Figure 3c.5(a)) shows three peaks at 854.4eV, 855.3 eV and 860.8 eV attributed to Ni^{+2}, Ni^{+3} and one satellite peak of Ni $2p_{3/2}$ [48,52] whereas the high-resolution XPS spectrum of W 4f (Figure 3c.5(b)) shows two peaks at 36.01 eV and 38.11 eV which correspond to $W4f_{7/2}$ and $W4f_{5/2.}$.[43,44] In O1s XPS spectra (Figure 3c.5(c)), the peak located at 530.2 eV corresponds to the metal-oxygen bonding while the other peak present at 531.5 eV shows the presence of metal hydroxide bonding and surface adsorbed species in the sample.[43] The binding energy of an elements in XPS depends on the surrounding electronic environment, therefore any variations owing to the formation of interfaces between two phases can also be detected. Hence, For the study of the interaction between different

phases at the interface, we did the XPS analysis of individual $NiWO_4$ and NiO samples and we found that there is a significant shift in the Ni 2p XPS spectra (Figure 3c.5(d)).

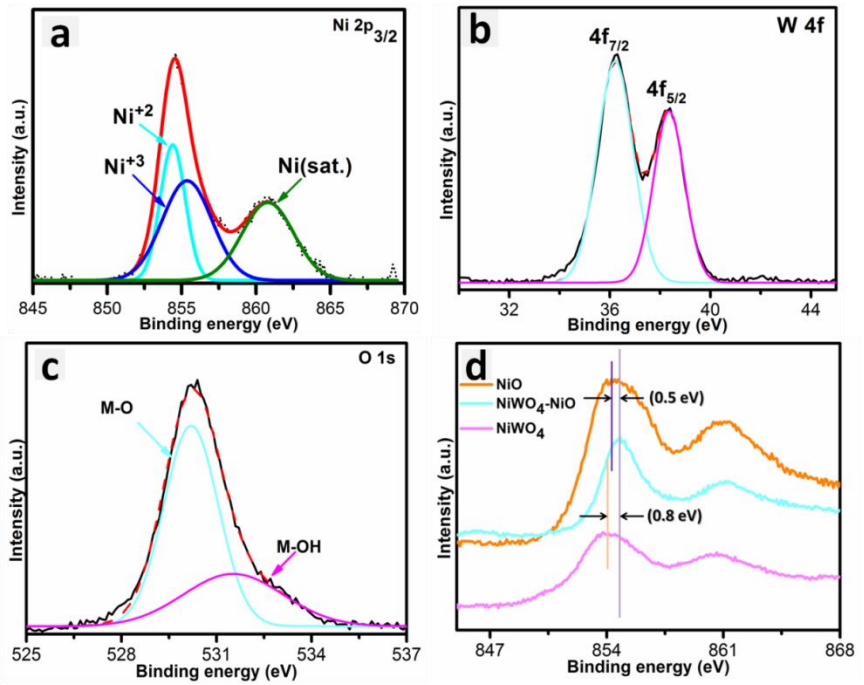

Figure 3c.5. *XPS of the $NiWO_4$-NiO/NF catalyst (a) high resolution XPS spectrum of Ni2p in $NiWO_4$-NiO (b) high resolution XPS spectrum of W4f in $NiWO_4$-NiO (c) high resolution XPS spectrum of O1s in $NiWO_4$-NiO (d) a comparison of the Ni2p spectra of $NiWO_4$-NiO and individual NiO and $NiWO_4$ phases.*

The positive shift of 0.5 eV was observed in the case of $NiWO_4$-NiO when compared to the individual NiO while there is negative shift of 0.35 eV observed in the case of W4f spectra when compared to the individual $NiWO_4$. These observations show that there is an electronic redistribution driven by charge transfer from NiO to $NiWO_4$ through the strong interfacial interactions in $NiWO_4$-NiO heterointerface. This also increases the availability of the electrons for the adsorption of H ion on the surface of $NiWO_4$.[53,54] The XPS spectra showing shift in W 4f is given Figure 3c.6.

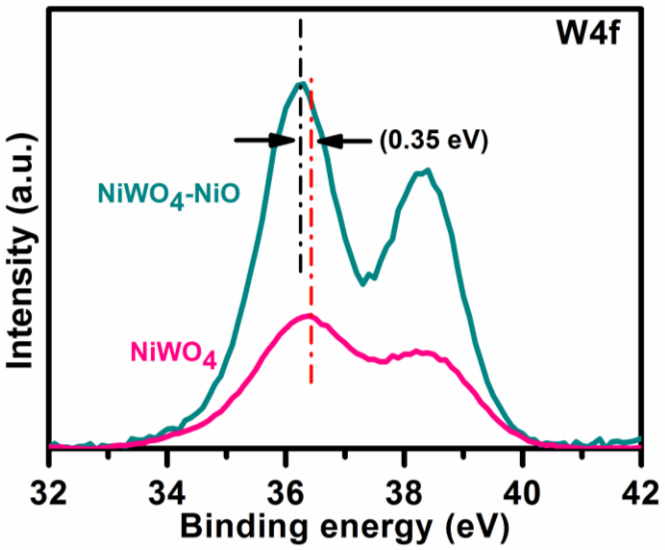

***Figure 3c.6**: XPS spectra of W4f showing negative shift after the formation $NiWO_4$-NiO*

The catalytic performance of $NiWO_4$-NiO/NF, $NiWO_4$, NiO and $Ni(OH)_2$ towards hydrogen evolution reaction (HER) was first evaluated in 1M KOH (pH=14) using a graphitic rod as a counter electrode and Ag/AgCl (saturated KCl filled) as a reference electrode. All the measurements in this section were done at room temperature (25°C) and 1M KOH. The Table 3c.1 includes a table that shows the mass loading of each catalyst on nickel foam. Under the same experimental conditions, the electrocatalytic activities of Pt/C (drop casted over nickel foam) were studied for comparison. Figure 3c.7(a) shows the iRcorrected polarization curves for all the catalysts. The overpotential value of 44, 71, 143, 248 and 328 mV were obtained at a current density of 10 mA cm^{-2} respectively for Pt/C, $NiWO_4$-NiO/NF, $Ni(OH)_2$NF, NiO/NF and $NiWO_4$/NF. The HER

Catalyst	Mass loading (mg cm^{-2})
$NiWO_4$-NiO/NF	2.9
$NiWO_4$/NF	2.6
NiO/NF	2.5
Pt/C/NF	2.9
$Ni(OH)_2$	2.1

Table 3c.1 *Mass loading of all the catalyst on nickel foam*

performance of $NiWO_4$-NiO/NF was found to be very close to that of commercially available Pt/C. The overpotential values of all the catalysts at 10 mA cm^{-2} current density are given in Figure 3c.7(b). To learn more about the reaction's kinetics, we measured the Tafel slope value by plotting the Tafel's equation as shown in Figure (3c.7(c)). The HER follows two pathways in alkaline media, these are Volmer-Tafel and Volmer-Heyrovsky pathways and are shown below:

$$H_2O + M + e^- \rightarrow M - H_{ads} + OH^- \text{ (Volmer)}$$

$$H_2O + M - H_{ads} + e^- \rightarrow H_2 + M + OH^- \text{ (Heyrovsky)}$$

$$2M - H_{ads} + e^- \rightarrow H_2 + 2M \text{ (Tafel)}$$

The first step is common for both processes which is the adsorption of the hydrogen on the catalyst surface (M). "M-H_{ads}"$depicts$ hydrogen intermediates adsorbed on the catalyst surface. The onset potential of HER can be evaluated by a Volmer step. On the basis of the above observations, it would be rational to conclude that the water dissociation is greatly enhanced at the Volmer step, especially in the case of $NiWO_4$-NiO/NF. The Tafel slope value gives crucial information regarding the rate-determining

step in HER. From Butler−Volmer kinetics, it can be deduced that the theoretically Tafel slope values are 120, 30 and 40 mV dec^{-1} when the Volmer, Tafel or Heyrovsky, steps are the rate-determining steps respectively.[55,56] In our case, we got the Tafel slope value of 68 mV/dec for $NiWO_4$-NiO revealing that the reaction predominantly proceeds through the Volmer-Heyrovsky pathway. The Tafel slope values for NiO, $Ni(OH)_2$ and $NiWO_4$ were evaluated to be 145, 185 and 229 mV/dec respectively.

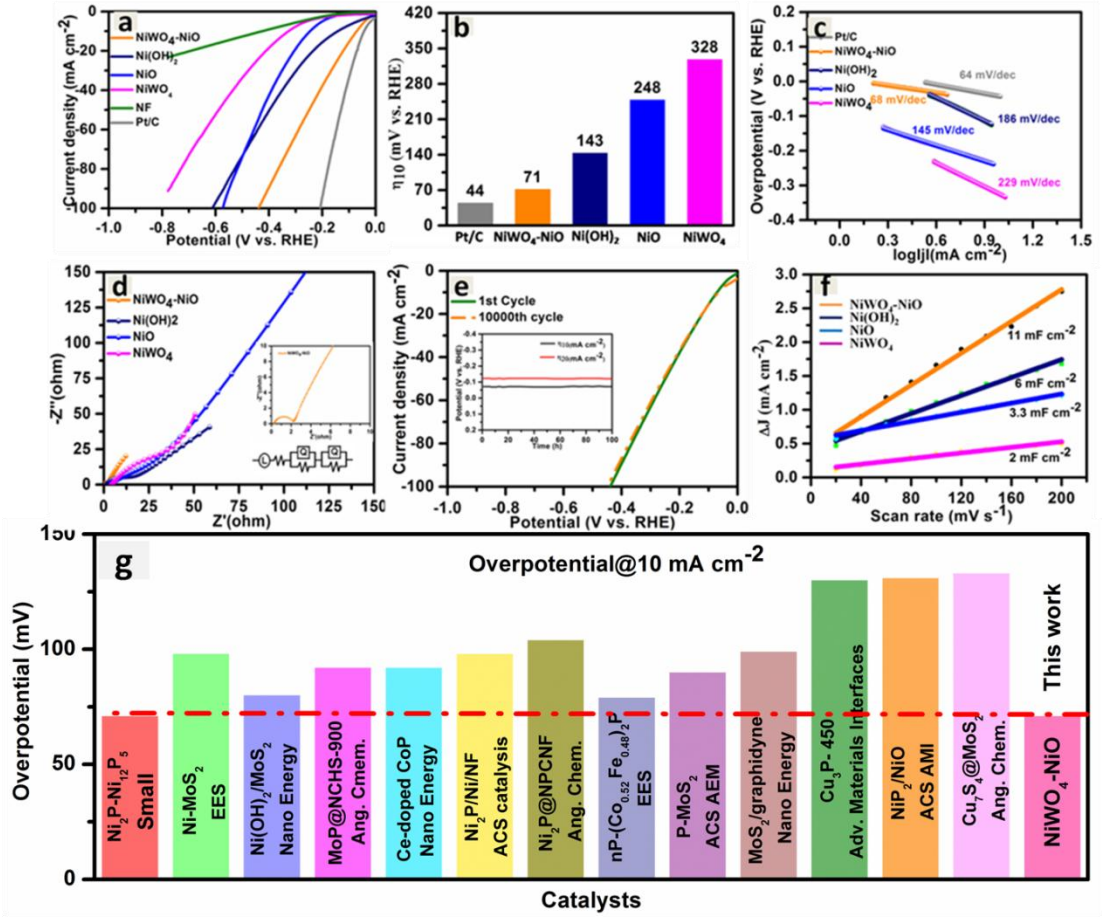

Figure 3c.7. *Electrochemical measurements of electrocatalysts for hydrogen evolution reaction in alkaline medium (1M KOH).The plots shows (a) polarization curves (iR-corrected) of $NiWO_4$-NiO/NF compared with $NiWO_4$, NiO, $Ni(OH)_2$ and Pt/C. (b) comparative bar-graph presentation of overpotential at 10 mA cm^{-2} current density. (c) the corresponding Tafel plots (d) Nyquist plot (with corresponding equivalent circuit) of the corresponding catalysts at an applied potential of 100mV. (e) Stability studies showing the overpotential at 1st cycle and after 10000 cycles. (f) Double-layer capacitance (C_{dl}) of all the catalyst. (g) Comparison of overpotential of our catalyst with recently reported catalyst.*

The lower Tafel slope value of catalyst renders a favourable HER kinetics with respect to the individual phases. The charge transfer resistance was evaluated using electrochemical impedance spectroscopy, which reveals a faster electron transfer through the interface possibly because of the strong electrode-electrolyte interfacial contacts. Figure 3c.7(d) shows the Nyquist plot at an applied overpotential of 100 mV. All of the spectra were fitted with the equivalent circuit represented in the above figure. The fitted data has two time-constant components, R_{ct}-CPE1 and R_p-CPE2, in addition to the solution resistance. The electrode's double-layer capacitance is indicated by the constant phase angle element (CPE). R_{ct}-CPE1 provides information on charge-transfer resistance, CPE_{dl} correlates the capacitance, while R_p-CPE2 can be used to correlate surface porosity. R_p-CPE2 is also associated with the slow solvent diffusion over the reaction interface and surface porosity, hence the corresponding value indicates the diffusion/adsorption of reaction intermediates.

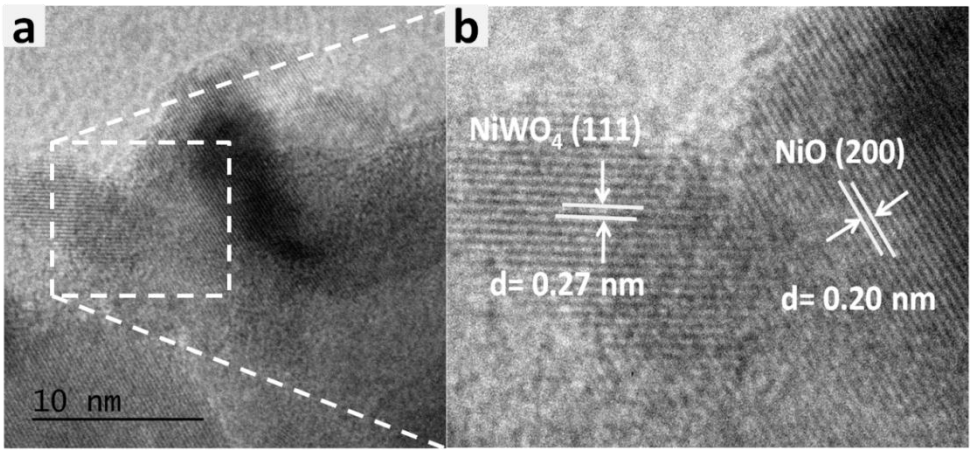

Figure 3c.8 *(a)HRTEM images of the $NiWO_4$-NiO after stability test in alkaline medium with (b) corresponding fringe width*

The species, such as MOH, may oxidise to MO at a particular potential, resulting in the (R_p-CPE2) impedance in the low-frequency region. The charge transfer resistance is inversely proportional to the applied potential. The charge-transfer resistance (R_{ct}) for $NiWO_4$-NiO at an applied potential of 100 mV was found to be 1.88 ohms. The low R_{ct} value in the Nyquist plot indicates a high charge transfer through the electrode-electrolyte interface, which also imply a possibility of finding a large number of electrochemically

active sites on the catalyst surface, and exhibits an excellent HER activity. The long-term stability of the $NiWO_4$-NiO/NF towards HER was measured by continuously running 10,000 LSV cycles (up to 100 hrs) as shown in Figure 3c.7(e).

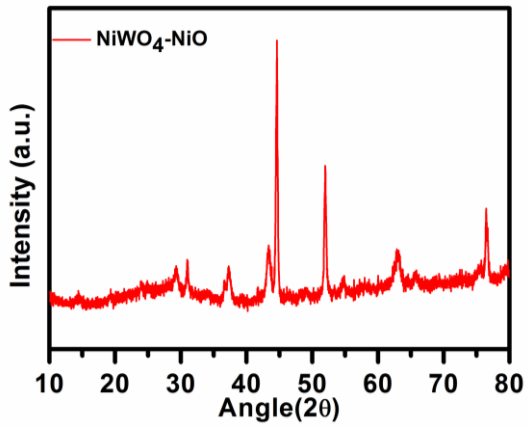

Figure 3c.9 *PXRD pattern of the $NiWO_4$-NiO after stability test in alkaline medium*

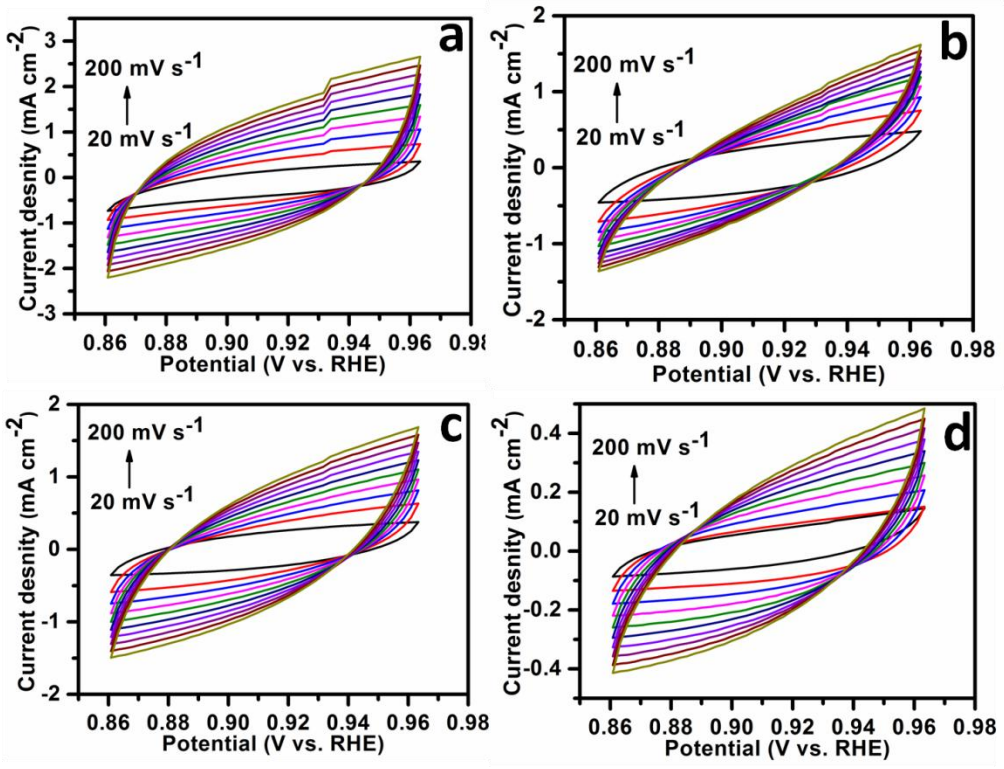

Figure 3c.10 *Cyclic voltammetry curve for the calculation of double layer capacitance of (a) $NiWO_4$-NiO (b) NiO (c) $Ni(OH)_2$ and $NiWO_4$*

No significant change was observed in the overpotential even after the stability experiment, indicating the excellent stability of $NiWO_4$-NiO/NF in an alkaline medium. HRTEM and PXRD spectra of the catalysts after stability are provided in Figure 3c.8 and 3c.9. No change was observed in the PXRD and HRTEM of the catalyst after stability. The double-layer capacitance (Cdl) extracted from cyclic voltammetry cycles in the non-Faradaic region with a potential window of 0.86 to 0.96 V vs RHE (Figure 3c.10) was used to calculate electrochemically active surface area (ECSA). The calculated value of Cdl is 11, 6, 3.3 and 2 mF cm-2 respectively for $NiWO_4$-NiO, $Ni(OH)_2$, NiO and $NiWO_4$ (Figure 3c.7(f)). The higher value of double-layer capacitance (Cdl) for $NiWO_4$-NiO also indicates the presence of a large number of HER active sites. Figure 3c.7(g) shows the comparison of the overpotential of our catalyst with the recently reported materials displayed in Table 3c.2. In addition, we have also calculated the apparent turnover frequency (TOF) of all the catalysts and we found TOF values of 0.041 s-1 , 0.0001s-1 and 0.0005 s-1 for $NiWO_4$-NiO, $NiWO_4$ and NiO respectively. The higher value of TOF for $NiWO_4$-NiO renders the higher catalytic efficiency of the catalyst. The 'TOF' plot 3c.11.

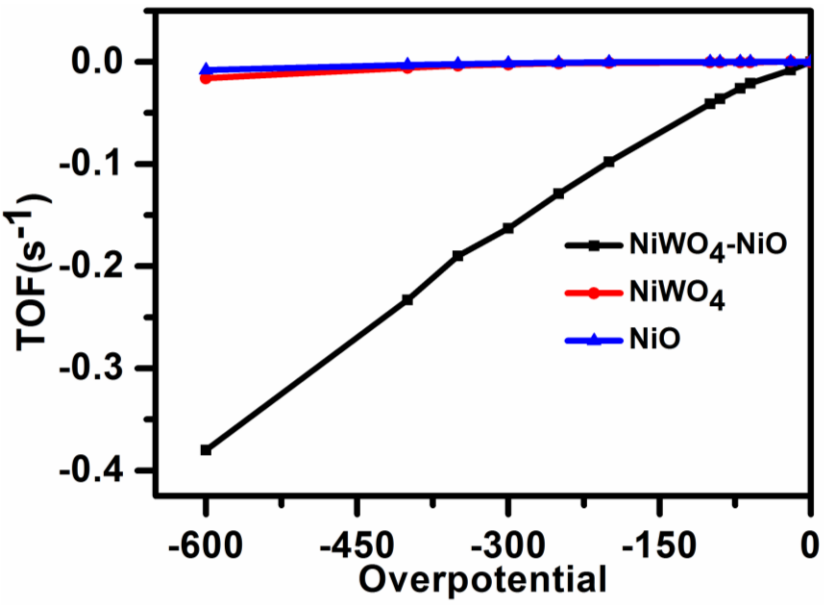

Figure 3c.11 *TOF value with the corresponding overpotential of all the catalyst in alkaline medium*

For investigating the effect of the interfaces on the HER performance of $NiWO_4$-NiO, DFT calculations has been performed on $NiWO_4$-NiO and pure $NiWO_4$ and NiO.The Gibbs freeenergy of hydrogen on $NiWO_4$-NiO and pure $NiWO_4$ and NiO were calculated to assess the HER activity. The ideal value of ΔG_{H^*} for hydrogen evolution reaction should be close to zero indicating that the adsorption of the hydrogen on the catalyst surface is neither too strong nor too weak.[38] Figure 3c.12(a) is depicting the free energy plot of adsorb H^* on the surface of $NiWO_4$-NiO, $NiWO_4$ and NiO. The ΔG_{H^*} value for the adsorption of hydrogen on the interface $NiWO_4$-NiO is 0.06 eV which is very close to zero indicating the surface energy is conducive for adsorption as well as desorption. This value is also way smaller than that of NiO (0.72 eV) and $NiWO_4$ (0.91 eV). This low ΔG_{H^*} value accounts for the higher hydrogen evolution performance of $NiWO_4$-NiO in comparison with the individual phases. A volcano plot shown in Figure 3c.12(b), relates the overpotential with hydrogen adsorption energies, which reveals that

Catalyst	**η_{10} (mV vs RHE) at J = 10 mA/cm^2**	**Tafel Slope**	**Reference**
1T-MoS_2/CoS_2	71	60	1
Ni_2P–$Ni_{12}P_5$/NF	76	68	2
Ni- MoS_2	98	60	3
Ni_2P-NiP_2 HNPs/NF	59.7	58.8	4
Ni-Mo-N	109	95	5
np-$(Co_{0.52}Fe_{0.48})_2P$	79	40	6
$Ni(OH)_2$/MoS_2	80	60	7
CoP/NPC/TF	80	54	8
C_3N_4 @MoN	110	57.8	9
MoP@NCHSs-900	92	62	10
Co@N-CNTs@rGO	108	64	11
FeP/Ni_2P	14	24.2	12
O-Co_2P	160	61.1	13
Ce-doped CoP	92	63.5	14

NF-NiS_2	67	63	15
Ni_2P/Ni/NF	98	72	16
MoS_2/graphdiyne	99	89	17
Ni_2P@NPCNFs	104.2	79.7	18
Co/MoS_2	158	58	19
Cu_3P-450 microsheets-	130	83	20
1T-2H MoS_2	280	65	21
v-$Ni_{12}P_5$	27.7	30.88	22
1T'-$MoTe_2$/GC	230	44	23
NiP_2/NiO Nanorod Arrays	131	93	24
NiS_2/MoS_2	98	88	25
NiCoP/rGO	209	124.1	26
MOF/MoS_2	248	86	27
FeP NAs/CC	218	146	28
1T-MoS_2/CoS_2	26	43	1
$MoS_{2(1-x)}Se_{2x}$	273	100	29
EA-2H/1T/RGO	186	49	30
$MoS_{2(1-x)}Se_2$	164	48	31
1T $MoSe_2$	152	52	30
Double-gyroid MoS_2	240	50	32
Ni-Co-MoS_2nanobox	155	51	33
$MoSe_2$/$NiSe_2$	210	56	34
Cu_7S_4@MoS_2nanoframes	133	48	35
$MoSe_2$/ CNT	178	58	36
MoS_2/HG	124	41	37
$MoSe_2$/graphene	159	61	38
1T' MoS_2Nanosheet	175	100	39
$MoSe_2$	250	80	40

P-MoS_2	90	47	41
$MoSe_2$	250	59.8	42
Ni2P/MoS_2	39.5	39.5	43
$MoSe_2$/Mo	166	34.7	44
O, P- MoS_2	230	53	45
MS_2/MO_2 (M = W, Mo)	147	63	46
Co-1T MoS_2	50	32	47
$MoSe_2/MoO_2$/Mo	142	48.9	48
NiCoP@NiMn-LDH	293	43.7	49
Mo-doped CoP/NF	305	56	50
Co-Fe Oxyphosphide/NF	280	53	51
Fe-doped Co-Mo-S Microtube	268	79.3	52
CoP(MoP)$CoMoO_3$@CN	296	105	53
np-$(Ni_{0.67}Fe_{0.33})_4P$	245	32.9	54
Co-P@Porous Carbon	280	53	55
Mo-doped Ni_2P/NF	270	68.5	56
CoFe-P/NF	250	35	57
Ni-Co/Ni-Fe phosphides	251	56	58
NiFeP@C	268	38.7	59
$NiCo_2S_4$/NF	260	40.1	60
$NiWO_4$-NiO	**71**	**68**	**This work**

Table 3c.2. *Comparison of HER activity of recently reported catalyst in alkaline medium*

position of the catalyst is very close to that of the Pt/c. There is an overall concentration of accessible carrier states in a particular energy range, as seen by the density of states (DOS) plot as shown in Figure 3c.12(c). The area under the PDOS curve gives an overall density of electron states available for occupation. The $NiWO_4$-NiO hybrid heterostructure system is shown to have a high density of states crossing the Fermi level,

indicating that the $NiWO_4$-NiO has better carrier transfer rate than that of NiO and $NiWO_4$ individual phases. All the equations used and energy values obtained from the theoretical calculation are given Table 3c.3.

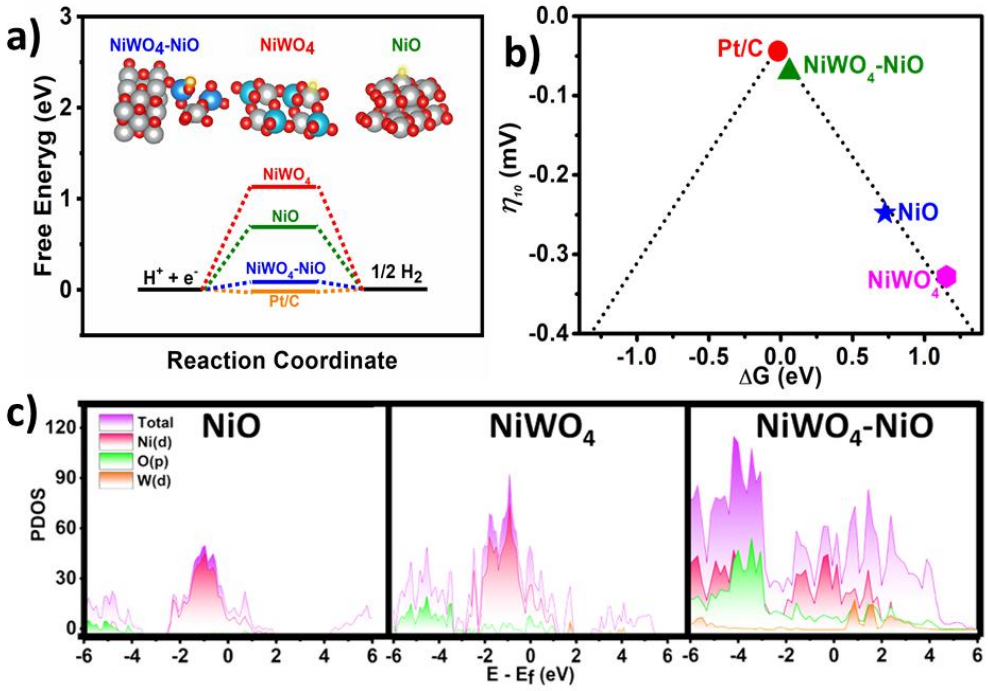

Figure 3c.12 *(a) HER free energy diagram of $NiWO_4$-NiO and pure $NiWO_4$ and NiO calculated at equilibrium potential (b) volcano plot showing the activity of $NiWO_4$-NiO (c) PDOS plot of $NiWO_4$-NiO, $NiWO_4$ and pristine NiO.*

Catalyst	Adsorption Energy (eV)	Gibbs Free Energy (eV)
H@NiO	0.4847	0.7247
H@$NiWO_4$	0.91	1.1538
H@$NiWO_4$-NiO	-0.175	0.065

Table 3c.3: *Gibbs free energy (ΔG_{H^*}) and Adsorption energy (ΔE_{H^*}) of the catalyst and its precursors.*

Conclusion

In summary, herein, we have developed a $NiWO_4$-NiO heterostructure over NF, which showed outstanding HER activity in an alkaline (1M KOH) medium with an overpotential of 71 mV at a current density of 10 mA cm-2 . The catalyst is highly stable in an alkaline medium and negligible change was observed in the overpotential even after 10000 cycles (100 hrs). We have also demonstrated that the abundant interfaces of $NiWO_4$-NiO over NF exhibit enhanced HER activity compared to the pure $NiWO_4$ and NiO phases. Furthermore, the strong interaction between both phases in the heterostructure was investigated by the shift in the XPS data. The superhydrophilicity of the NiWO4-NiO/NF electrode enhances ionic transfer from the electrolyte to the electrode surface and accelerates the mass transport process. DFT studies demonstrated that the electronic states of the NiWO4-NiO interface have been significantly altered, which indicates a favourable hydrogen adsorptivity on $NiWO_4$-NiO catalyst. This, in turn, lowers the Gibbs free energy significantly (as low as 0.06 eV) and speeds up charge-transfer kinetics to 21 boost HER activity. This work indicates that appropriate heterostructuring in abundance can improve the catalytic activity immensely as shown in the case of $NiWO_4$-NiO/NF. The catalyst is not only highly durable but also performs extremely well in alkaline media.

Gaur, Ashish, Krishankant, Vikas Pundir, Takahiro Maruyama, Chandan Bera, and Vivek Bagchi. "Electronic Redistribution Over the Active Sites of $NiWO_4$-NiO Induces Collegial Enhancement in Hydrogen Evolution Reaction in Alkaline Medium" *Under minor revision in Journal of Colloid and Interface Science*

References

(1) Perera, F. *Int J Environ Res Public Health* **2017**, *15*, 16.

(2) Bittel, J. *Natural Resources Defense Council Report* **2019**.

(3) Lutsko, N. J. *Journal of Climate* **2021**, *34*, 901.

(4) Lewis, N. S.; Nocera, D. G. *Proceedings of the National Academy of Sciences* **2006**, *103*, 15729.

(5) Zhu, J.; Hu, L.; Zhao, P.; Lee, L. Y. S.; Wong, K.-Y. *Chemical Reviews* **2020**, *120*, 851.

(6) Abdelkader-Fernández, V. K.; Fernandes, D. M.; Balula, S. S.; Cunha-Silva, L.; Pérez-Mendoza, M. J.; López-Garzón, F. J.; Pereira, M. F.; Freire, C. *ACS Applied Energy Materials* **2019**, *2*, 1854.

(7) Wu, D.; Kusada, K.; Yoshioka, S.; Yamamoto, T.; Toriyama, T.; Matsumura, S.; Chen, Y.; Seo, O.; Kim, J.; Song, C.; Hiroi, S.; Sakata, O.; Ina, T.; Kawaguchi, S.; Kubota, Y.; Kobayashi, H.; Kitagawa, H. *Nature Communications* **2021**, *12*, 1145.

(8) Liu, H.; Zhang, R.; Chen, L.; Wang, L.; Guo, Y.; Yang, Y. *Advanced Sustainable Systems* **2021**, *5*, 2000184.

(9) Shao, H.; Wu, Y.; Xu, X.; Xian, Y.; Shi, Y.; Wang, F.; Lv, K.; Tan, C.; Hao, L.; Dong, B.; Agathopoulos, S. *Advanced Sustainable Systems* **2022**, *6*, 2200196.

(10) Dubouis, N.; Grimaud, A. *Chemical Science* **2019**, *10*, 9165.

(11) Tavakkoli, M.; Holmberg, N.; Kronberg, R.; Jiang, H.; Sainio, J.; Kauppinen, E. I.; Kallio, T.; Laasonen, K. *ACS Catalysis* **2017**, *7*, 3121.

(12) Qu, K.; Zheng, Y.; Zhang, X.; Davey, K.; Dai, S.; Qiao, S. Z. *ACS Nano* **2017**, *11*, 7293.

(13) Zhu, R.; Ding, J.; Xu, Y.; Yang, J.; Xu, Q.; Pang, H. *Small* **2018**, *14*, 1803576.

(14) Zheng, S.; Li, Q.; Xue, H.; Pang, H.; Xu, Q. *National Science Review* **2020**, *7*, 305.

(15) Anantharaj, S.; Kundu, S.; Noda, S. *Journal of Materials Chemistry A* **2020**, *8*, 4174.

(16) Huang, C.; Yu, L.; Zhang, W.; Xiao, Q.; Zhou, J.; Zhang, Y.; An, P.; Zhang, J.; Yu, Y. *Applied Catalysis B: Environmental* **2020**, *276*, 119137.

(17) Sharma, L.; Botari, T.; Tiwary, C. S.; Halder, A. *ACS Applied Energy Materials* **2020**, *3*, 5333.

(18) Yang, C.; Zhao, R.; Xiang, H.; Wu, J.; Zhong, W.; Li, W.; Zhang, Q.; Yang, N.; Li, X. *Advanced Energy Materials* **2020**, *10*, 2002260.

(19) Xie, W.; Yu, T.; Ou, Z.; Zhang, J.; Li, R.; Song, S.; Wang, Y. *ACS Sustainable Chemistry & Engineering* **2020**, *8*, 9070.

(20) Kumar, R.; Gaur, A.; Maruyama, T.; Bera, C.; Bagchi, V. *ACS Applied Materials & Interfaces* **2020**, *12*, 57898.

(21) He, C.; Tao, J. *Advanced Sustainable Systems* **2018**, *2*, 1700136.

(22) Jian, C.; Cai, Q.; Hong, W.; Li, J.; Liu, W. *Small* **2018**, *14*, 1703798.

(23) Zhang, T.; Wu, M.-Y.; Yan, D.-Y.; Mao, J.; Liu, H.; Hu, W.-B.; Du, X.-W.; Ling, T.; Qiao, S.-Z. *Nano Energy* **2018**, *43*, 103.

(24) Wang, X.; Li, W.; Xiong, D.; Petrovykh, D. Y.; Liu, L. *Advanced Functional Materials* **2016**, *26*, 4067.

(25) Yu, X.; Yu, Z.-Y.; Zhang, X.-L.; Zheng, Y.-R.; Duan, Y.; Gao, Q.; Wu, R.; Sun, B.; Gao, M.-R.; Wang, G.; Yu, S.-H. *Journal of the American Chemical Society* **2019**, *141*, 7537.

(26) Feng, Y.; Zhang, T.; Zhang, J.; Fan, H.; He, C.; Song, J. *Small* **2020**, *16*, 2002850.

(27) Zhou, Y.; Pondick, J. V.; Silva, J. L.; Woods, J. M.; Hynek, D. J.; Matthews, G.; Shen, X.; Feng, Q.; Liu, W.; Lu, Z.; Liang, Z.; Brena, B.; Cai, Z.; Wu, M.; Jiao, L.; Hu, S.; Wang, H.; Araujo, C. M.; Cha, J. J. *Small* **2019**, *15*, 1900078.

(28) Wang, H.; Fu, W.; Yang, X.; Huang, Z.; Li, J.; Zhang, H.; Wang, Y. *Journal of Materials Chemistry A* **2020**, *8*, 6926.

(29) Wang, Z.; Wang, S.; Ma, L.; Guo, Y.; Sun, J.; Zhang, N.; Jiang, R. *Small* **2021**, *17*, 2006770.

(30) Jiao, J.; Yang, W.; Pan, Y.; Zhang, C.; Liu, S.; Chen, C.; Wang, D. *Small* **2020**, *16*, 2002124.

(31) Lovell, E. C.; Lu, X.; Zhang, Q.; Scott, J.; Amal, R. *Chemical Communications* **2020**, *56*, 1709.

(32) Kou, T.; Chen, M.; Wu, F.; Smart, T. J.; Wang, S.; Wu, Y.; Zhang, Y.; Li, S.; Lall, S.; Zhang, Z.; Liu, Y.-S.; Guo, J.; Wang, G.; Ping, Y.; Li, Y. *Nature Communications* **2020**, *11*, 590.

(33) Ji, Y.; Yang, L.; Ren, X.; Cui, G.; Xiong, X.; Sun, X. *ACS Sustainable Chemistry & Engineering* **2018**, *6*, 9555.

(34) Bi, Y.; Nie, H.; Li, D.; Zeng, S.; Yang, Q.; Li, M. *Chemical Communications* **2010**, *46*, 7430.

(35) Chen, S.; Yang, G.; Jia, Y.; Zheng, H. *Journal of Materials Chemistry A* **2017**, *5*, 1028.

(36) Blöchl, P. E. *Physical Review B* **1994**, *50*, 17953.

(37) Vanderbilt, D. *Physical Review B* **1990**, *41*, 7892.

(38) Wang, Z.-L.; Hao, X.-F.; Jiang, Z.; Sun, X.-P.; Xu, D.; Wang, J.; Zhong, H.-X.; Meng, F.-L.; Zhang, X.-B. *Journal of the American Chemical Society* **2015**, *137*, 15070.

(39) Huang, S.; Meng, Y.; Cao, Y.; Yao, F.; He, Z.; Wang, X.; Pan, H.; Wu, M. *Applied Catalysis B: Environmental* **2020**, *274*, 119120.

(40) Qian, Z.; Wang, K.; Shi, K.; Fu, Z.; Mai, Z.; Wang, X.; Tang, Z.; Tian, Y. *Journal of Materials Chemistry A* **2020**, *8*, 3311.

(41) Kim, S. Y.; Yun, T. Y.; Yu, K. S.; Moon, H. C. *ACS Applied Materials & Interfaces* **2020**, *12*, 51978.

(42) Prajesh, R.; Goyal, V.; Nahid, M.; Saini, V.; Singh, A. K.; Sharma, A. K.; Bhargava, J.; Agarwal, A. *Sensors and Actuators B: Chemical* **2020**, *318*, 128166.

(43) Zhao, G.; Li, P.; Cheng, N.; Dou, S. X.; Sun, W. *Advanced Materials* **2020**, *32*, 2000872.

(44) Du, X.; Shao, Q.; Zhang, X. *International Journal of Hydrogen Energy* **2019**, *44*, 2883.

(45) Sun, B.; Zhao, W.; Wei, L.; Li, H.; Chen, P. *Chemical Communications* **2014**, *50*, 13142.

(46) Gao, W.; Xia, Z.; Cao, F.; Ho, J. C.; Jiang, Z.; Qu, Y. *Advanced Functional Materials* **2018**, *28*, 1706056.

(47) Shan, X.; Liu, J.; Mu, H.; Xiao, Y.; Mei, B.; Liu, W.; Lin, G.; Jiang, Z.; Wen, L.; Jiang, L. *Angewandte Chemie International Edition* **2020**, *59*, 1659.

(48) Gao, Z.-W.; Liu, J.-Y.; Chen, X.-M.; Zheng, X.-L.; Mao, J.; Liu, H.; Ma, T.; Li, L.; Wang, W.-C.; Du, X.-W. *Advanced Materials* **2019**, *31*, 1804769.

(49) Yan, H.; Xie, Y.; Jiao, Y.; Wu, A.; Tian, C.; Zhang, X.; Wang, L.; Fu, H. *Advanced Materials* **2018**, *30*, 1704156.

(50) Gao, M.-R.; Xu, Y.-F.; Jiang, J.; Zheng, Y.-R.; Yu, S.-H. *Journal of the American Chemical Society* **2012**, *134*, 2930.

(51) Conway, B. E.; Tilak, B. V. *Electrochimica Acta* **2002**, *47*, 3571.

(52) Mahmood, N.; Yao, Y.; Zhang, J.-W.; Pan, L.; Zhang, X.; Zou, J.-J. *Advanced Science* **2018**, *5*, 1700464.

Chapter 4

An Electronegativity Induced Valence States Augmentation of Ni and Co through Electronic Redistribution in Co-Ni_3N/CeF_3 for Oxygen Evolution Reaction

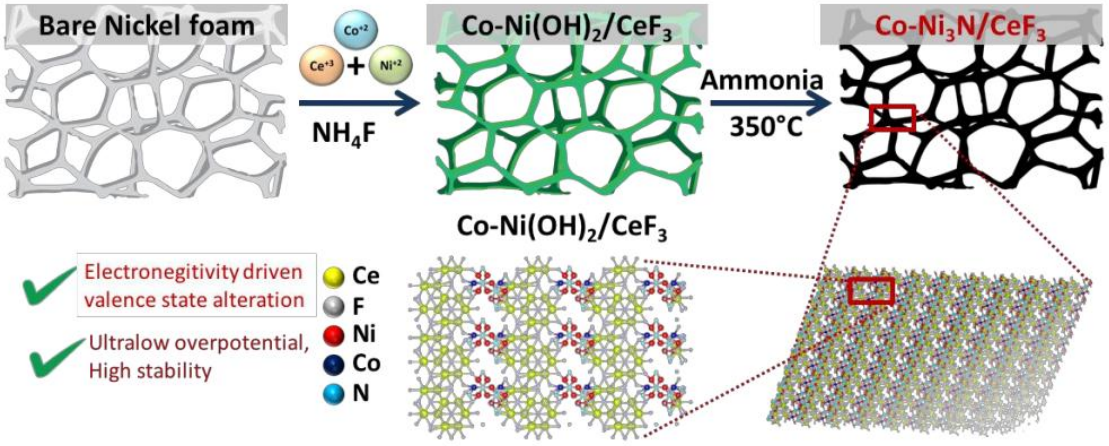

Brief Outcome:*The development of high-performance and inexpensive electrocatalysts for the oxygen evolution reaction (OER) is one of the most desired objectives in energy conversion reactions. Due to sluggish reaction kinetics, the commercialization of such processes could not be achieved yetChoosing an appropriate coupling interface to boost the catalyst performance is essential for the creation of high-efficiency electrocatalysts. Herein, metal-nitride and metal-fluoride heterostructure is reported with an extremely low overpotential of 180 mV at a current density of 10 mA* cm^{-2} *for OER application. The Co-*Ni_3N/CeF_3 *catalyst shows strong interfacial interaction causing significant electronic redistribution between Co-*Ni_3N *and* CeF_3 *phases. XPS studies reveal the charge transfer from Co-*Ni_3N *to the* CeF_3 *phase resulting in the augmentation in the valence states of Co and Ni making them highly active sites for the adsorption of intermediates (O*, OH*, HOO*). This phenomenon is possibly driven by the high polarity of CeF3 due to the presence of highly electronegative F atoms. The stability study of the catalyst was performed for 120 h at large current densities of 110 and 200 mA* cm^{-2}*. The detailed analysis of the surface reconstruction of Co-*Ni_3N/CeF_3 *is also carried out after a long-term stability test. This work offers a fresh look at the possibilities of the design and fabrication of an efficient and low-cost catalyst.*

4.1. Introduction

We were never being so vulnerable towards the ill effects of climate change as we are today. Extreme human activities such as warfare, extensive space exploration and otherinnumerable processes expelling greenhouse gases, have led to an abrupt change in the temperature and weather patterns causing huge threats to planetary life.[1] Hence, it is vital to develop viable and green energy sources to confront the ever-increasing usage of fossil fuels and environmental pollution. Electrochemical water splitting has been envisioned as a rapid, highly productive and environmentally benign process for producing high-purity hydrogen.[2-4] In addition, the lousy kinetics of the anodic oxygen evolution reaction (OER) makes it difficult to make progress in the field of water-splitting technology, which requires a significant overpotential in order to achieve the necessary current density.[5-7] While pricey metal oxides such as IrO_2 and RuO_2 demonstrate effective OER performance but their paucity, exorbitant prices, and poor stability limit their broad utilization.[8-12] The fabrication of highly active electrocatalysts based on earth-abundant elements would be a very promising answer to the aforesaid problem. In this perspective, non-noble metals (Ni, Co, Fe) and their related sulfides,[13-16] oxides,[17-20] and phosphides[21-23] are being intensively explored as electrocatalysts for the OER. Recent research has demonstrated that transition metal nitrides (Co_2N, Co_4N, Ni3N, etc) might function as promising OER electrocatalysts within an alkaline medium.[24-26] Nickel nitride (Ni_3N) is a popular material among researchers due to its high conductivity and stability.[27-28] However, the OER performance for Ni_3N is low, possibly because of the low adsorption of the reaction intermediate (O*, OH*, HOO*) on its surface. The impact of interface coupling plays a crucial role in enhancing electrocatalytic performance by legislating the electronic structure proximal to the interface, tweaking orbital overlap among different atoms, and eventually optimizing the adsorption and desorption energies among the reaction intermediates and catalyst. Therefore, it is crucial to select the right solid for Ni_3N in order to produce a composition where the interface can considerably improve electrocatalytic performance.[29-31]Recently, Wang et al. reported Co-doped Ni_3N nanosheets with the overpotential of 270 mV for OER. The Co-Ni_3N nanosheets promote electron redistribution and also optimized the

adsorption energies of intermediates (O*, OH*, HOO*). The significance of Co doping in the oxidation of Ni in Co-Ni_3N is also discussed, along with how this affects the adsorption energy and energetic barrier of separation of intermediates (O*, OH*, HOO*) in the oxygen evolution process.[32] Cerium trifluoride (CeF_3), on the other hand, has poor electrocatalytic performance despite having outstanding photocatalytic efficacy. CeF_3 has an active redox pair composed of Ce^{3+} and Ce^{4+} that can be alternatively changed by sharing or gaining electrons, resulting in high mobility of electrons.[33] Based on the aforementioned reports, Co-Ni_3N/CeF_3heterointerface are designed. To the best of our knowledge, there are no such reports on the construction of heterostructure of metal nitride with metal fluorides in the recent literature. The resulting $CoNi_3N$/CeF_3heterostructure outperforms Co-Ni_3N in oxygen evolution due to the electronicredistribution and interface coupling effect generated by the addition of CeF_3. The high electronegativity of fluorine atom makes CeF_3 of high polarity than that of Co-Ni_3N, this difference in electronegativity will enhance the electron redistribution from Co-Ni_3N to CeF_3 resulting in the augmentation in valence stated of Ni and Co. The catalyst shows an ultralow overpotential of 180 mV at 10 mA cm-2 of current density. This value is the lowest among the Ni_3N-based compounds reported up to date. The catalyst was studied for the long-term durability at higher current densities of 110 and 200 mA cm^{-2}, shows no significant change in the current density after 120 h. A detailed study of the catalyst transformation after stability has been carried out using XPS and HRTEM analysis.

4.2. Experimental section

4.2.1. Materials

Chemicals were bought from several commercial sources and used as it is. Cerium (III) nitrate hexahydrate ($Ce(NO_3)_3.6H_2O$, 99%), Cobalt (II) nitrate hexahydrate ($Co(NO_3)_2.6H_2O$, 98%), Nickel (II) nitrate hexahydrate ($Ni(NO_3)_2.6H_2O$, 98%), Ammonium fluoride (NH_4F, 99.9%), Urea (NH_2CONH_2, 99.5%), Nafionperfluorinated resin solution (5 wt. % in a mixture of water and alcohol, possesses 45% water), Potassium hydroxide pallet (KOH) and Ruthenium (IV) oxide (RuO_2, 99.9% trace metal

basis) were bought from Sigma Aldrich. Nickel foam (NF) was purchased from Nanoshel. In all the preparation, Milli Q water having a conductivity of 0.056 μS/cm was used.

4.2.2. Methodology

4.2.2.1. Synthesis of Catalyst

Catalyst synthesis section is subdivided into two major stepsas per following description**.**

Step 1.Synthesis of Co- $Ni(OH)_2/CeF_3$nanosheets: Hydrochloric acid (3M HCl) was used to remove the oxide layer and other surface impurities from the nickel foam substrate. Deionized water and ethanol were then used to clean the material repeatedly. Cobalt- doped nickel hydroxide nanosheets grown over nickel foam substrate were fabricated by an improvised autoclave process. Typically, 0.95 mmol$Ni(NO_3)_2 \cdot 6H_2O$, 0.05 mmol $Co(NO_3)_2 \cdot 6H_2O$, 0.5 mmol of $Ce(NO_3)_3.6H_2O$, 5 mmol NH_4F and 5 mmol of $CO(NH_2)_2$ were dissolved in 20 mL deionized water and a homogenous solution was obtained by mixing and stirring. The above solution was transferred into the 50 mL Teflon-lined autoclave containing NF substrate and heated for 12h at 160 °C. The obtained Co-$Ni(OH)_2/CeF_3$nanosheets array is washed with DI and ethanol and dried in an oven overnight at 60 °C.

Step 2.Synthesis of Co-Ni_3N/CeF_3: The as-obtained Co-$Ni(OH)_2/CeF_3$ was kept in a furnace at 350 °C for 2h under the influence of continuous flow of high-purity ammonia @26 sccm. After cooling down, the sample was removed and named as Co-Ni_3N/CeF_3. For a comparative study, individual Co-Ni_3N and CeF_3 were also made by using similar method. In the case of Co-Ni_3N, above method was used but without cerium salt, while the individual CeF_3 was formed by mixing 0.5 mmol of $Ce(NO_3)_3.6H_2O$and 5 mmol NH_4F in 20 mL deionized water. The solution was kept in a Teflon-lined autoclave at 160 °C for 12 h.

4.2.2.2. Physical characterization

The physical characterization of the as-prepared Co-$Ni_3N/CeF_3$was done using various techniques. First of all, byaBruker Eco D8 ADVANCED X powder X-ray diffractometerconsisting of a Ni filter was used for its initial steps of examination. The radiations of CuK (=1.5405, 40 KV and 25 mA) was used for the study. The examination was done in the 2Θ range of 20°- 80° and step size of about 0.0020/step was given. Scanning electron microscope from JEOL (JSM 17-300) was used for studying the morphology of the catalyst. The energy-dispersive X-ray diffractometer (Bruker) study was also done by the same scanning electron microscope. The complete information about the structure of Co-Ni_3N/CeF_3 and the average particle size was measured by Transmission electron microscope (TEM) JEOL-2100 which was operated at 200 KV. X-ray photoelectron spectroscopy (XPS) on ECSA: 220-IXL with MgKα is used for further investigation of elements. The MgKα used is non-monochromated X-ray beam with photon energy 1253.6 eV.

3c.2.2.3. Electrochemical measurements

All the electrochemical measurements were carried out in CHI 760E electrochemical workstation. In the three-electrode system, saturated Ag/AgCl electrode is used as a reference electrode and graphite rod used as a counter electrode. Firstly, the prepared electrode was used for taking all the polarization data at a scan rate 5 mV s^{-1} in 1 M KOH. After all the polarization data was collected, it was converted to Reversible hydrogen electrode (RHE) by the use of equation $E_{RHE} = E_{Ag/AgCl} + 0.197 + 0.059*pH$. For the calculation of Tafel slope, polarisation curves were again plotted, and the linear region of Tafel plot was fitted to the Tafel equation i.e., $\eta = b \log(j) + a$. The electrochemical surface area (ECSA) was determined by the calculation of double layer capacitance, in which CV scans of the as prepared electrode were taken at a scan rate of 20 to 200 mV/s in 1M KOH in non-faradaic potential range. when ΔJ = (Janodic-Jcathodic)/2 was plotted against the scan rate at a potential of 1.08 V vs RHE and was fitted linearly, it gave the value of double layer capacitance (Cdl). The faradic efficiency was calculated by taking the ratio of experimental and theoretical oxygen evolution in the reaction

4.3. Result and Discussion

The catalyst Co-Ni_3N/CeF_3 was synthesized under the controlled nitridation of Co-$Ni(OH)_2/CeF_3$ at a fixed temperature. The formation of Co-Ni_3N/CeF_3heterostructure was primarily characterized using powder X-ray diffraction (PXRD). The PXRD pattern of Co-Ni_3N/CeF_3 is given in Figure 4.1(a). The peak positioned at 24.5°, 25.01°, 27.8°, 35.2°, 44.1°, 45.1°, 51.07°, 52.9°, 64.8°, 68.8°, 69.8°, 71.2° and 78.4° corresponds to (002), (110), (111), (112), (300), (113), (221), (214), (304), (115) and (411) crystal planes of hexagonal CeF_3.[34-35] The other peak centered at 38.9°, 42.0°, 44.4°, 58.5°, 70.6° and 78.4° corresponds to (110), (002),(200), (112), (300) and (113) crystal planes of hexagonal Ni_3N.[36-37]

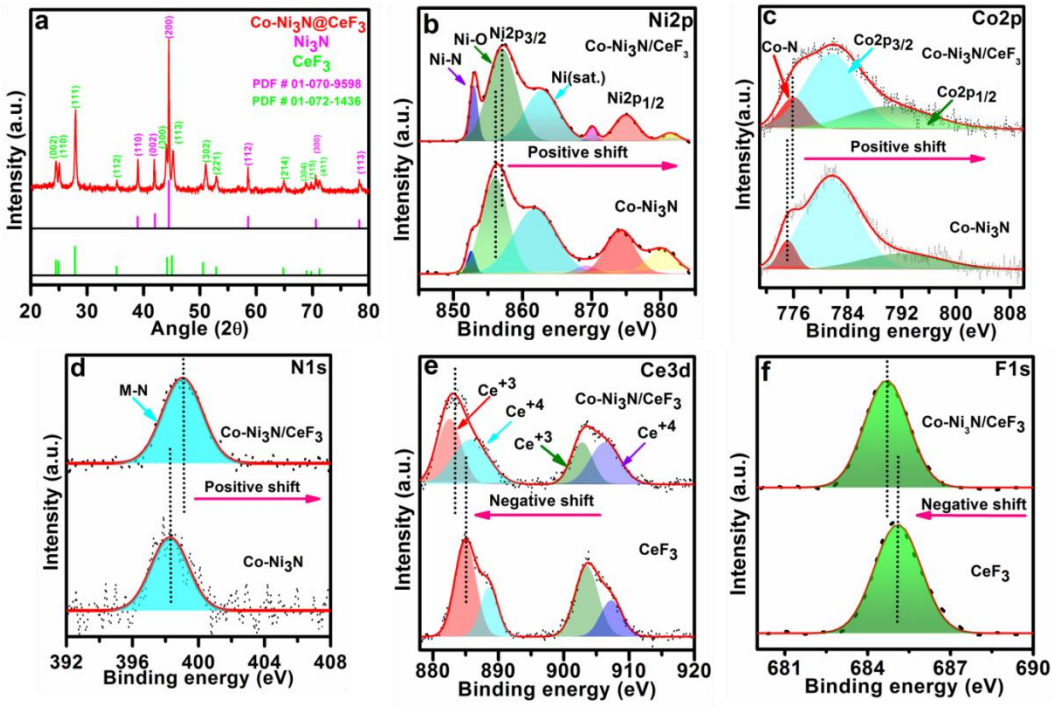

Figure 4.1. *(a) PXRD spectra of Co-Ni_3N/CeF_3 showing the formation of both Ni_3N and CeF_3 phase, high resolution XPS spectra of (b) Ni2p (c) Co2p (d) N1s (e) Ce3d and (f) F1s present in Co-Ni_3N/CeF_3, Co-Ni_3N and CeF_3*

X-ray photoelectron spectroscopy (XPS) was used to investigate the valence states and electronic redistribution between Co-Ni_3N and CeF_3 in Co-Ni_3N/CeF_3. The high-resolution XPS spectraof Ni2p present in Co-Ni_3N/CeF_3 and Co-Ni_3N are provided in Figure 4.1(b). In the Ni2p spectra of Co-Ni_3N/CeF_3, we observed three peaks centered at 852.9, 857.0 and 862.7eV corresponding to the presence of Ni-N, Ni-O and one satellite peak of $Ni2p_{3/2}$. Similarly, the other three peaks at 870.0, 874.9 and 881.3eV correspond to the presence of Ni-N, Ni-O and one satellite peak of $Ni2p_{1/2}$.All these peaks are also observed for the Ni2p spectra of Co-Ni_3N but at slightly lower binding energy.[37-38] The higher binding energy of Ni2p in Co-Ni_3N/CeF_3 indicates the charge transfer from Ni to some other element. The high-resolution XPS spectra of Co2p (Figure 4.1c) present in Co-Ni_3N/CeF_3 can be deconvoluted into three peaks. The peak centered at 781.4 and 792.0 eV attributed to the surface oxidized Co(II) species.[32] The peak at 775.1 eV corresponds to the Co species present in aforementioned catalyst. These three peaks are also present in the Co2p spectra of Co-Ni_3N. The binding energy of the Co-N is higher in Co-Ni_3N/CeF_3 confirming the possibility of charge transfer from Co. XPS spectra of N1s (Figure 4.1d) present in Co-Ni_3N/CeF_3 show one peak at 399.0 eV corresponding to the M-N bond.[39] The N1s spectra of Co-Ni_3N/CeF_3 were also observed at higher binding energy than that of N1s present in Co-Ni_3N. The XPS spectra of Ce3d (Figure 1e) present in Co-Ni_3N/CeF_3 shows four peaks at 882.5, 885.7, 902.7 and 906.3 eV corresponds to the $Ce^{3+}$and Ce^{4+} peak of $Ce3d_{5/2}$ and $Ce3d_{3/2}$. The similar peaks are also observed for Ce3d spectra present in CeF_3.[40] When we compared the binding energy of Ce 3d present in both the species we notice the negative shift in the binding energy. This negative shift confirms that the Ce is gaining electrons from the other species. Similarly, the F1s spectra (Figure 4.1f) alsoshift towards the lower binding energy when compared to the individual CeF_3.[33] The positive shift in the binding energy of Ni, Co and N and the negative shift in the binding energy of Ce and F indicate the charge transfer from Co-Ni_3N to the CeF_3.This charge transfer results in the augmentation of the valence states of Ni and Co, making them highly active catalytic sites for the adsorption of electron-rich intermediated (O*, OH*, HOO*) responsible for oxygen evolution reaction. The PXRD pattern of Co-Ni_3N and wide scan XPS spectra of Co-Ni_3N/CeF_3 is given in Figure 4.2 & 4.3.

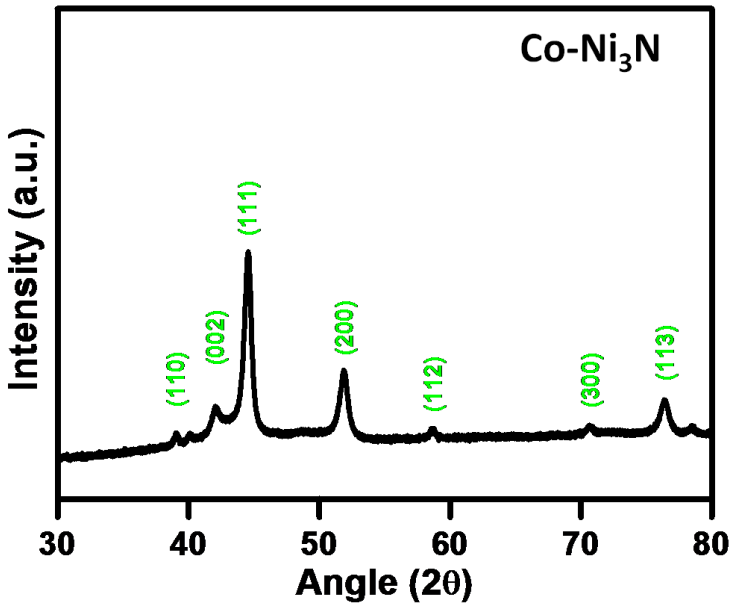

Figure 4.2 .*PXRD pattern of Co-Ni_3N*

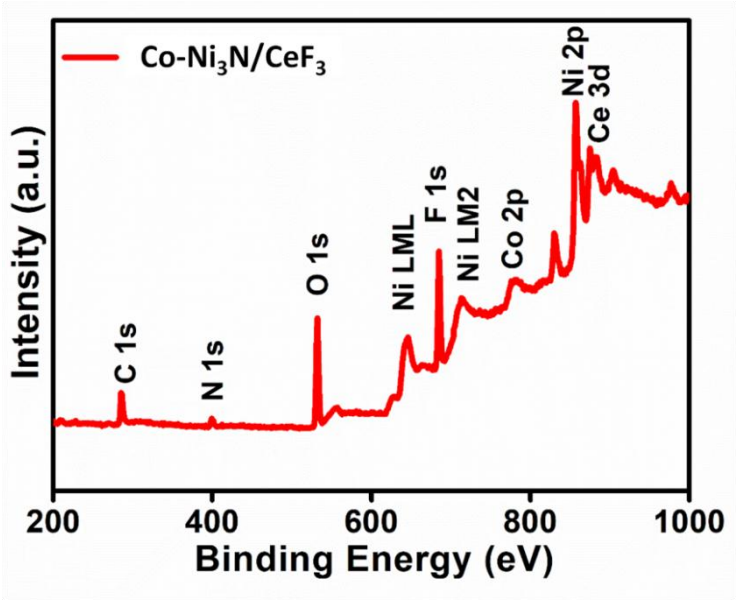

Figure 4.3.*XPS wide scan spectra of Co-Ni_3N/CeF_3*

Scanning electron microscopy (SEM) images with different magnifications are provided in Figure 4.4(a-d). The SEM images of Co-Ni_3N/CeF_3 show a sheet-like structure. The uniform distribution of all the elements over the catalyst surface is confirmed using

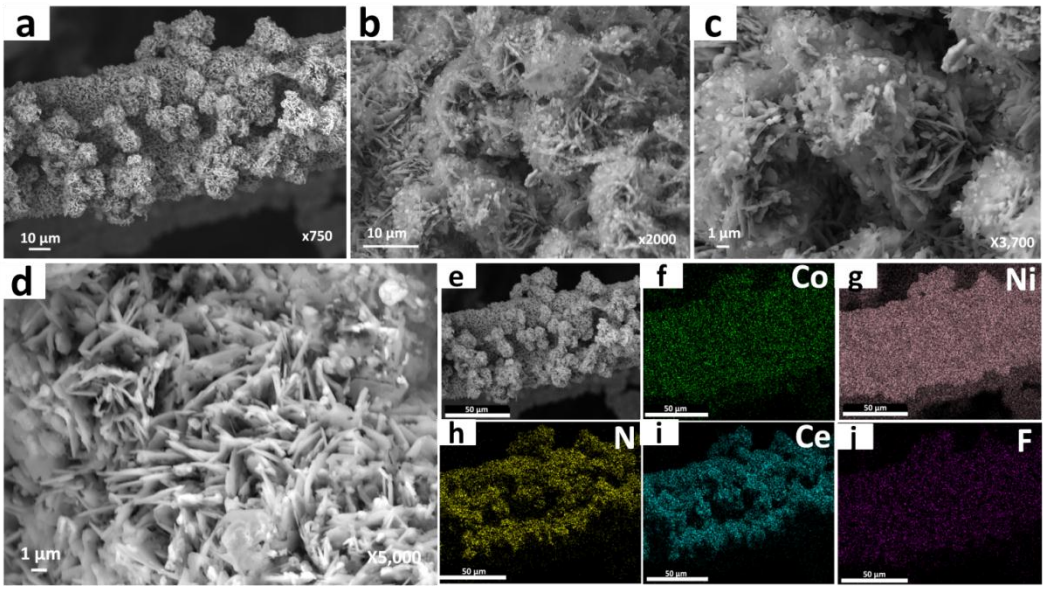

Figure 4.4*. (a-d) FESEM images of Co-Ni_3N/CeF_3 at different magnification showing sheet like structure (e-j) FESEM elemental mapping of Co-Ni_3N/CeF_3 showing the uniform distribution of Co, Ni, N, Ce and F over the catalyst surface.*

SEM elemental mapping. Figure 4.4(e-j) shows the elemental mapping for Co, Ni, N, Ce and F.TEM images of Co-Ni_3N/CeF_3 show the formation of Co-Ni_3N nanosheets with anchored CeF_3 nanoparticles (Figure 4.5(a)). The formation of a heterointerface between Co-Ni_3N and CeF_3 is confirmed using HR-TEM analysis. HR-TEM images (Figure 4.5b & c) confirm the presence of CeF_3 and Ni_3N phases in the catalyst. Figure 3d shows the presence of Ni_3N phase with the dspacing of 0.23 nm corresponds to the (110) crystal plane of Ni_3N.[41] The presence of CeF_3 was also confirmed with the d-spacing value of 0.319 and 0.205 nm corresponding to (111) and (300) crystal planes of CeF_3[33] (Figure 4.5e,f). From HR-TEM images we can observe the formation of an interface between Co-Ni_3N and CeF_3. The behaviour of the catalyst's surface is crucial in heterogeneous catalysis. The superhydrophilic surfaces strongly favour heterogeneous catalysis because they can support low adsorption energies on their surfaces.[42-43] It was found that the surface of bare nickel foam is hydrophobic with a contact angle of 116.7° while the surface of $CoNi_3N/CeF_3$ was found to be superhydrophilic with a contact angle of 0° (Figure 4.5g-i).

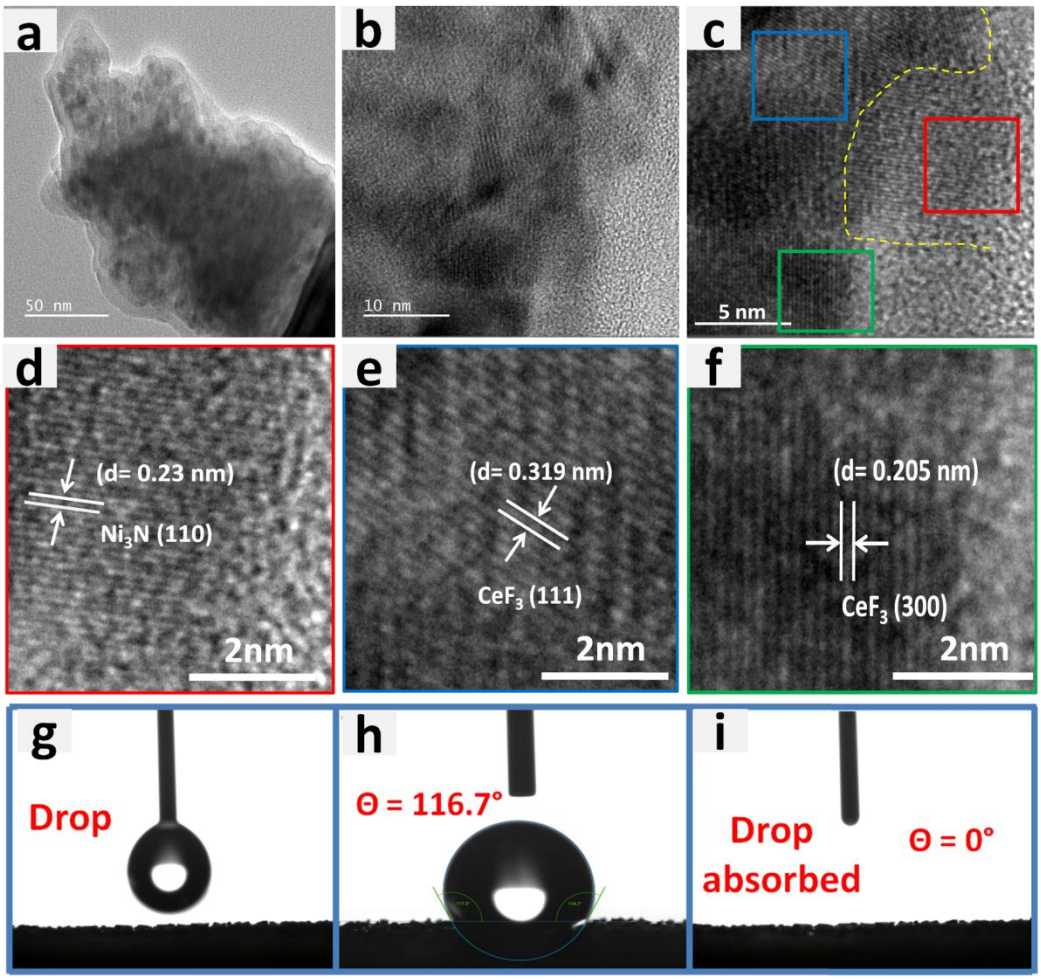

Figure4.5. *(a) TEM image of Co-Ni_3N/CeF_3 (b,c) HRTEM image of Co-Ni_3N/CeF_3 showing the presence of (d) Ni_3N and (e,f) CeF_3 phase with corresponding fringe width. (g,h) drop shape analysis of bare NF showing hydrophobic behaviour and (i) Co-Ni_3N/CeF_3 with zero contact angle showing superhydrophilic behaviour*

The catalytic performance of Co-Ni_3N/CeF_3 towards oxygen evolution reaction was studied in three-electrode electrochemical setup and in general, 1M KOH solution was used in the experiment, unless mentioned otherwise. The comparison of the catalytic performance was done with Co-Ni_3N, CeF_3, commercially available RuO_2 and bare nickel foam. Notably, the $CoNi_3N/CeF_3$ catalyst demonstrated an excellent OER activity that is far better than the commercially available RuO_2, specifically, the overpotential of

180 mV was achieved at a current density of 10 mA cm^{-2} (Figure 4.6a). This performance is the highest among the Ni_3N-based catalyst up to date.

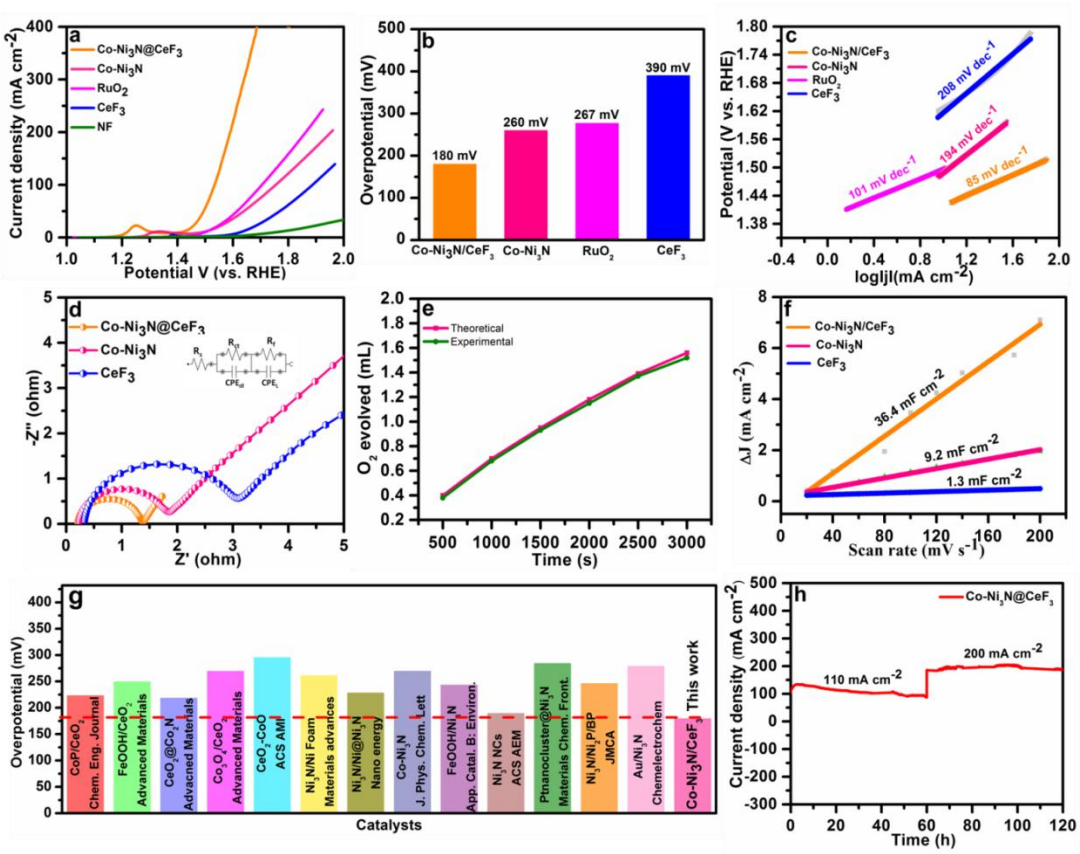

Figure 4.6*. (a) polarization curve of Co-Ni_3N/CeF_3 and other supporting catalyst. (b) overpotential value of all the catalyst at 10 mA cm^{-2} of current density (c) tafel plot derived from polarization curve (d) EIS nyquist plot of all the catalysts (e) faradic efficiency calculation using water displacement method (f) double- layer capacitance value of all the catalyst (g) comparison of Co-Ni_3N/CeF_3 with recently reported Ni_3N and Ce based highly active catalysts (h) durability test using chronoamperometry*

The catalytic performance of individual Co-Ni_3N, RuO_2 and CeF_3 are 260, 267 and 390 mV at a current density of 10 mA cm^{-2}. Figure 4.6b shows the corresponding overpotentials of all the catalysts at a current density 10 mA cm^{-2}. The Tafel plot derived from the polarisation curves(figure 4.6c) shows the low Tafel slope value of 85 mV dec^{-1} for Co-Ni_3N/CeF_3. This value is lower than that of Co-Ni_3N (194 mV dec^{-1}), RuO_2 (101 mV dec^{-1}) and CeF_3 (208 mV dec^{-1}). The lower Tafel slope value of Co-Ni_3N/CeF_3

suggests the fast OER kinetics as compared to the commercially available RuO_2. The charge transfer resistance was studied using electrochemical impedance spectroscopy to identify strong interfacial contacts for faster electron transit across the electrode-electrolyte interface. Figure 4.6d shows the Nyquist plot with the equivalent circuit used for fitting the plot and obtained the desired parameters which significantly define a good catalyst. An Rct value of 1.16 Ω was obtained for Co-Ni_3N/CeF_3 catalyst which indicates a rapid electron transfer and hence follows a superior OER kinetics. The R_{ct} values of 1.57 and 2.74 Ω were obtained for Co-Ni_3N and CeF_3. These higher values of R_{ct} indicate relatively slower charge transfer in both the catalyst than that of Co-Ni_3N/CeF_3. The faradic efficiency (Figure 4.6e) is estimated using the water-gas displacement technique, in which the estimated faradic efficiency is the percentage of the ratio of the quantity of O_2 evolved empirically to the amount of O_2 evolved theoretically. The faradic efficiency value for our catalyst is 96.1%. The aforesaid apparent OER performance could be inflated as a result of the large specific surface area of nanomaterials. To precisely assess the inherent OER activity of the reported catalyst, we evaluated theelectrochemical C_{dl} of the Co-Ni_3N/CeF_3 catalyst to compute their ECSA and normalized the resulting current in comparison to Co-Ni_3N and CeF_3 catalysts. The double-layer capacitance (Cdl) value was calculated using cyclic voltammetry (CV) measurements carried out at different scan rates (20-200 mVs-1). The obtained C_{dl} values are 36.4, 9.2 and 1.3 mF cm^{-2} for Co-Ni_3N/CeF_3, Co-Ni_3N and CeF_3 respectively (Figure 4.6f). The higher values of Cdl indicate a higher number of active sites present in Co-Ni_3N/CeF_3. The OER activity of Co-Ni_3N/CeF_3 is obviously higher than the other catalysts after the ECSA normalization. The ECSA normalized polarization curve is provided in Figure 4.7 and the cyclic voltammetry curve used for the calculation of Cdl is provided inFigure 4.8. The activity of the catalyst was compared with most of the Ni_3N and Cerium-based catalysts (Figure 4.6g) and we found the highest activity of our catalyst with the least overpotential among all. The table containing different parameters of these catalysts is given in Table 4.1. The long-term durability of Co-Ni_3N/CeF_3 for OER was performed using the chronoamperometry method. As seen in figure 4h, 120 h of continuous durability study was performed using chronoamperometry at 110 and 200 mA cm^{-2} current densities.

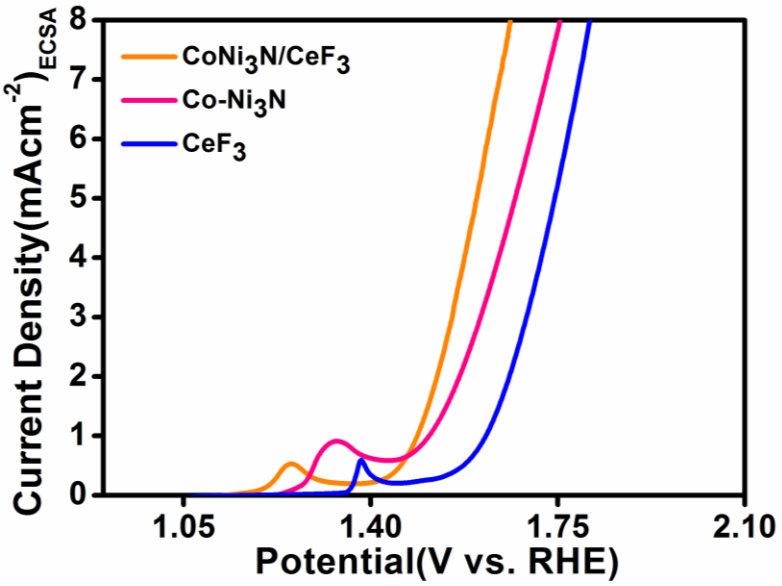

Figure 4.7. *ECSA normalised OER activity of Co-Ni_3N/CeF_3, Co-Ni_3N and CeF_3*

In the beginning, slight decrease in the current density was witnessed possibly due to minute peeling of the catalyst, however it becomes stable later, even at higher current density of 200 $mAcm^{-2}$. This experimentshows that the Co-Ni_3N/CeF_3 catalyst is enormously stable even under extreme condition.

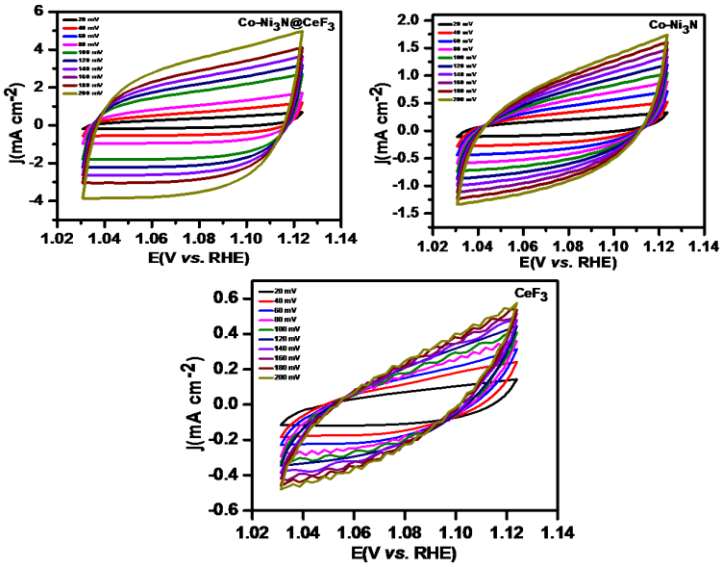

Figure 4.8.*Cyclic voltammetry curves of Co-Ni_3N/CeF_3, Co-Ni_3N, CeF_3at different scan rates.*

Catalyst Name	Overpotential@10 mA cm^{-2}	Reference
CoP/CeO_2	224	1
$FeOOH/CeO_2$	250	2
CeO_2-Co_2N	219	3
Co_3O_4/CeO_2	270	4
CeO_2-CoO	296	5
Ni_3N/Ni foam	262	6
Ni_3N/Ni@Ni_3N	229	7
Co-Ni_3N	270	8
$FeOOH/Ni_3N$	244	9
Ni_3N/NCs	190	10
Ptnanocluster@Ni_3N	285	11
Ni_3N/Ni_2P/BP	247	12
Au-Ni_3N	280	13
Co-Ni_3N/CeF_3	180	This work

Table 4.1 *Table containing the OER activity Ce and Ni_3N based reported catalyst*

Poststability studies of catalyst were carried out using XPS and HRTEM analysis.For a better understanding of the surface reconstruction of Co-Ni_3N/CeF_3 after OER, Ar beam XPS depth profiles are used to study the near-surface composition to provide further insights (Figure 4.9 a). The surface of the catalyst was etched using continuous Ar sputtering for 100 s. The XPS data were recorded before and after etching the surface of Co-Ni_3N/CeF_3. In the highresolution XPS spectra of Ni2p (Figure 4.9b), we did not get any peak for Ni-N bonding but after etching the surface Ni-N peak was observed in Ni2p spectra.

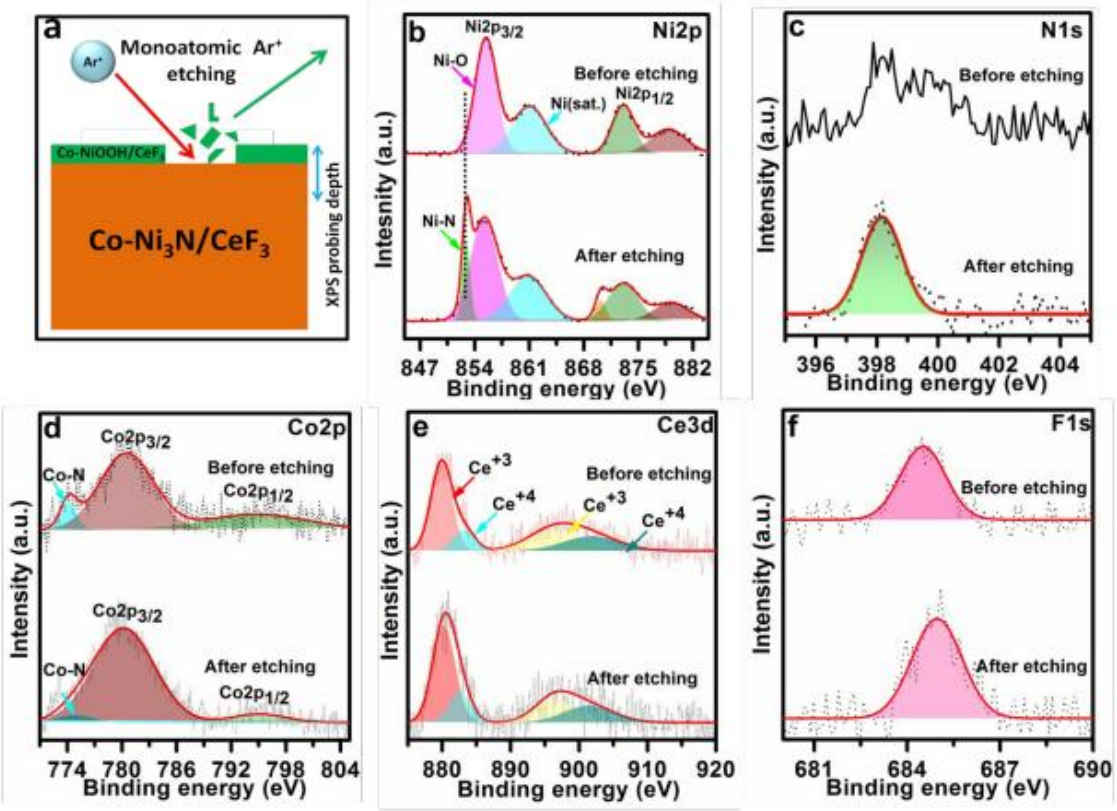

***Figure 4.9**. (a) Schematic showing the XPS depth profiling experiment. After stability analysis of Co-Ni_3N/CeF_3 XPS, high resolution XPS spectra of (b) Ni2p, (c) N1s, (d) Co2p, (e) Ce3d and (f) F1s present in Co-Ni_3N/CeF_3 before and after etching using Ar sputtering for 100s.*

These results indicate that the surface of Ni3N was oxidized to form NiOOH during OER. The surface reconstruction of Ni_3N into NiOOH was previously studied in different literature.[44-45]The intensity of the N1s peak was very weak on the surface, however after etching, the intensity increases (Figure 4.9c). This also confirms the surface oxidation of the Ni_3N. No significant change has been observed in the XPS spectra of Co, Ce and F (Figure 4.9(d-f)). This study reveals that the CeF_3 phase was retained in the catalyst and nevertheless, the surface Ni_3N was oxidized to NiOOH. The formation of NiOOH was further confirmed using high resolution-TEM analysis. The HRTEM image of Co-Ni3N/CeF3 (Figure 4.10) confirms the presence of NiOOH with the d-spacing of 0.24 nm corresponding to the (100) plane of NiOOH and another fringe-width of 0.205 nm corresponding to the (300) plane of CeF3.[46]

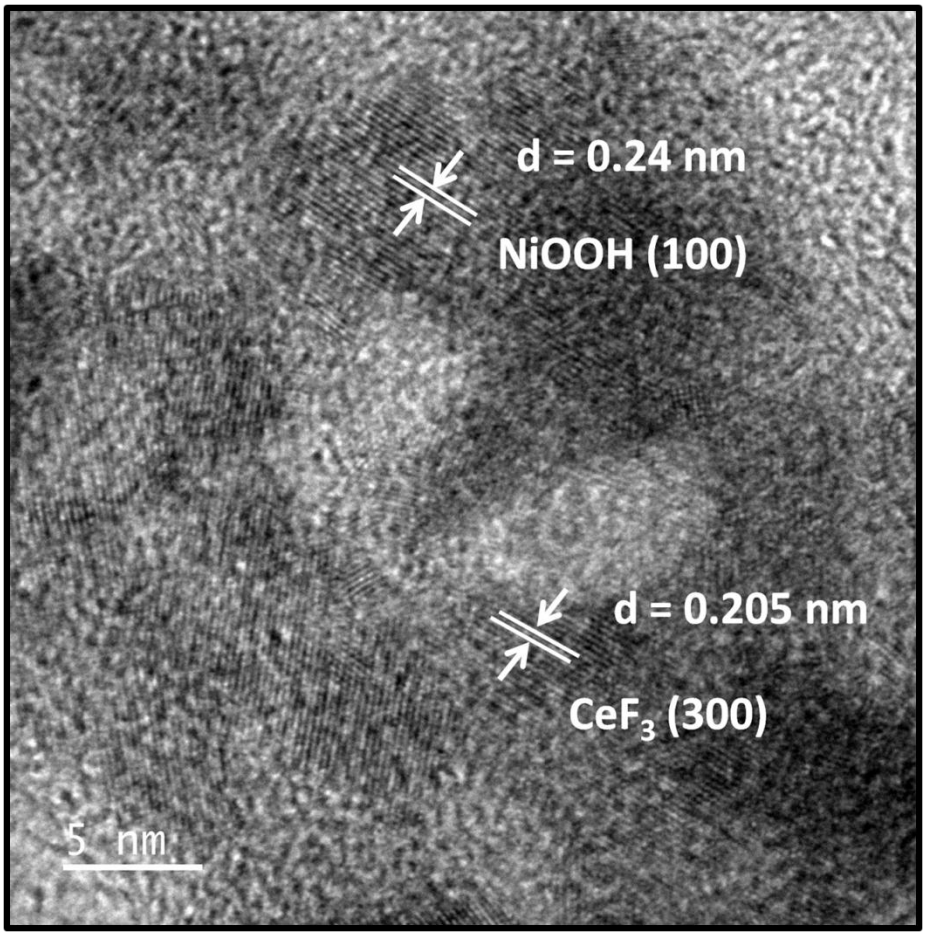

Figure 4.10. *HRTEM image of Co-Ni_3N/CeF_3 after durability test showing the formation of NiOOH over the catalyst surface*

4.4 Conclusion

In conclusion, the Co-Ni_3N/CeF_3 electrode was prepared by a two-step process. The high electronegativity of fluorine atoms in CeF_3 facilitates the charge transfer from Ni and Co to Ce and F. Furthermore, the strong interfacial interaction between Co-Ni_3N and CeF_3 increases the valence states of Ni and Co. The catalyst Co-Ni_3N/CeF_3 shows an ultralow overpotential of 180 mV and is far superior to those of Co-Ni_3N and CeF_3. This value is the lowest among the Ni_3Nbased compounds reported till date. The catalyst is highly stable and studied for 120 h under the high current densities of 110 and 200 mA cm^{-2} respectively. Post-stability studies using XPS depth profiling measurements reveal that the surface Ni_3N was further oxidizing to form NiOOH species and CeF_3 remained stable

after 120 h of stability. Achieving such nanostructures with appropriate engineering of the interfaces would pave the future technology in energy conversion reactions.

Gaur, Ashish,Joel Mathew John, VikasPundir, RajdeepKaur, and VivekBagchi. "An Electronegativity Induced Valence States Augmentation of Ni and Co through Electronic Redistribution in Co-Ni_3N/CeF_3 for Oxygen Evolution Reaction" *Under minor revision in ACS Applied Energy Materials.*

References

(1) Sanati, S.; Morsali, A.; García, H. *Energy & Environmental Science***2022**, *15*, 3119.

(2) Sun, H.; Xu, X.; Song, Y.; Zhou, W.; Shao, Z. *Advanced Functional Materials***2021**, *31*, 2009779.

(3) Han, H.; Qiu, Y.; Zhang, H.; Bi, T.; Yang, Q.; Liu, M.; Zhou, J.; Ji, X. *Sustainable Energy & Fuels***2022**, *6*, 3008.

(4) Zheng, M.; Guo, K.; Jiang, W.-J.; Tang, T.; Wang, X.; Zhou, P.; Du, J.; Zhao, Y.; Xu, C.; Hu, J.-S. *Applied Catalysis B: Environmental***2019**, *244*, 1004.

(5) Lu, S.-S.; Zhang, L.-M.; Dong, Y.-W.; Zhang, J.-Q.; Yan, X.-T.; Sun, D.-F.; Shang, X.; Chi, J.-Q.; Chai, Y.-M.; Dong, B. *Journal of Materials Chemistry A***2019**, *7*, 16859.

(6) Zhang, L.; Wang, J.; Liu, P.; Liang, J.; Luo, Y.; Cui, G.; Tang, B.; Liu, Q.; Yan, X.; Hao, H.; Liu, M.; Gao, R.; Sun, X. *Nano Research***2022**, *15*, 6084.

(7) Wu, Z.-P.; Lu, X. F.; Zang, S.-Q.; Lou, X. W. *Advanced Functional Materials***2020**, *30*, 1910274.

(8) Anantharaj, S.; Ede, S. R.; Karthick, K.; Sam Sankar, S.; Sangeetha, K.; Karthik, P. E.; Kundu, S. *Energy & Environmental Science***2018**, *11*, 744.

(9) Chemelewski, W. D.; Lee, H.-C.; Lin, J.-F.; Bard, A. J.; Mullins, C. B. *Journal of the American Chemical Society***2014**, *136*, 2843.

(10) Ye, C.; Zhang, L.; Yue, L.; Deng, B.; Cao, Y.; Liu, Q.; Luo, Y.; Lu, S.; Zheng, B.; Sun, X. *Inorganic Chemistry Frontiers***2021**, *8*, 3162.

(11) Qiu, Y.; Liu, Z.; Zhang, X.; Sun, A.; Ji, X.; Liu, J. *Journal of Colloid and Interface Science***2022**, *610*, 194.

(12) Cui, M.; Yang, C.; Li, B.; Dong, Q.; Wu, M.; Hwang, S.; Xie, H.; Wang, X.; Wang, G.; Hu, L. *Advanced Energy Materials***2021**, *11*, 2002887.

(13) Biswas, R.; Thakur, P.; Kaur, G.; Som, S.; Saha, M.; Jhajhria, V.; Singh, H.; Ahmed, I.; Banerjee, B.; Chopra, D.; Sen, T.; Haldar, K. K. *Inorganic Chemistry***2021**, *60*, 12355.

(14) Luo, Y.; Qin, J.; Yang, G.; Luo, S.; Zhao, Z.; Chen, M.; Ma, J. *Chemical Engineering Journal***2021**, *410*, 128394.

(15) Tabassum, L.; Khairul Islam, M.; Perera, I. P.; Li, M.; Huang, X.; Tasnim, H.; Suib, S. L. *ACS Applied Energy Materials***2022**, *5*, 12039.

(16) Wang, J.; Chen, C.; Cai, N.; Wang, M.; Li, H.; Yu, F. *Nanoscale***2021**, *13*, 1354.

(17) Wang, D.; Wang, Y.; Fu, Z.; Xu, Y.; Yang, L.-X.; Wang, F.; Guo, X.; Sun, W.; Yang, Z.-L. *ACS Applied Materials & Interfaces***2021**, *13*, 34507.

(18) Zhang, G.; Li, Y.; Xiao, X.; Shan, Y.; Bai, Y.; Xue, H.-G.; Pang, H.; Tian, Z.; Xu, Q. *Nano Letters***2021**, *21*, 3016.

(19) Taylor, A. K.; Prabhudev, S.; Botton, G. A.; Gates, B. D. *ACS Applied Energy Materials***2022**.

(20) Gao, R.; Deng, M.; Yan, Q.; Fang, Z.; Li, L.; Shen, H.; Chen, Z. *Small Methods***2021**, *5*, 2100834.

(21) Ding, H.; Liu, H.; Chu, W.; Wu, C.; Xie, Y. *Chemical Reviews***2021**, *121*, 13174.

(22) Gaur, A.; Krishankant; Pundir, V.; Singh, A.; Maruyama, T.; Bera, C.; Bagchi, V. *Sustainable Energy & Fuels***2021**, *5*, 5505.

(23) Sun, X.; Zhang, Y.; Xiao, Y.; Li, Z.; Wei, L.; Yao, G.; Niu, H.; Zheng, F. *Inorganic Chemistry***2022**, *61*, 14140.

(24) Liu, D.; Ai, H.; Li, J.; Fang, M.; Chen, M.; Liu, D.; Du, X.; Zhou, P.; Li, F.; Lo, K. H.; Tang, Y.; Chen, S.; Wang, L.; Xing, G.; Pan, H. *Advanced Energy Materials***2020**, *10*, 2002464.

(25) Chen, P.; Xu, K.; Tong, Y.; Li, X.; Tao, S.; Fang, Z.; Chu, W.; Wu, X.; Wu, C. *Inorganic Chemistry Frontiers***2016**, *3*, 236.

(26) Gao, M.; Chen, L.; Zhang, Z.; Sun, X.; Zhang, S. *Journal of Materials Chemistry A***2018**, *6*, 833.

(27) Ray, C.; Lee, S. C.; Jin, B.; Kundu, A.; Park, J. H.; Chan Jun, S. *Journal of Materials Chemistry A***2018**, *6*, 4466.

(28) Zhou, P.; Zhai, G.; Lv, X.; Liu, Y.; Wang, Z.; Wang, P.; Zheng, Z.; Cheng, H.; Dai, Y.; Huang, B. *Applied Catalysis B: Environmental***2021**, *283*, 119590.

(29) Zheng, X.; Cui, P.; Qian, Y.; Zhao, G.; Zheng, X.; Xu, X.; Cheng, Z.; Liu, Y.; Dou, S. X.; Sun, W. *AngewandteChemie International Edition***2020**, *59*, 14533.

(30) Chen, H.; Shi, L.; Liang, X.; Wang, L.; Asefa, T.; Zou, X. *AngewandteChemie International Edition***2020**, *59*, 19654.

(31) Wang, M.; Ma, W.; Lv, Z.; Liu, D.; Jian, K.; Dang, J. *The Journal of Physical Chemistry Letters***2021**, *12*, 1581.

(32) Chen, J.; Qi, X.; Liu, C.; Zeng, J.; Liang, T. *ACS Applied Materials & Interfaces***2020**, *12*, 51418.

(33) Zuo, S.; Zhang, H.; Li, X.; Han, C.; Yao, C.; Ni, C. *ACS Sustainable Chemistry & Engineering***2022**, *10*, 1440.

(34) Yuan, Z.; Zhang, D.; Fan, G.; Chen, Y.; Fan, Y.; Liu, B. *ACS Applied Energy Materials***2021**, *4*, 2820.

(35) Sun, J.; Lu, J.; Huang, C.; Wu, Q.; Xia, L.; Xu, Q.; Yao, W. *ACS Sustainable Chemistry & Engineering***2021**, *9*, 1994.

(36) Shanker, G. S.; Ogale, S. *ACS Applied Energy Materials***2021**, *4*, 2165.

(37) Gao, D.; Zhang, J.; Wang, T.; Xiao, W.; Tao, K.; Xue, D.; Ding, J. *Journal of Materials Chemistry A***2016**, *4*, 17363.

(38) Guan, J.; Li, C.; Zhao, J.; Yang, Y.; Zhou, W.; Wang, Y.; Li, G.-R. *Applied Catalysis B: Environmental***2020**, *269*, 118600.

(39) Han, B.; Lou, Y.; Liu, Z.; Zhou, C.; Wang, Z.; Qian, G. *Advanced Materials Interfaces***2021**, *8*, 2101161.

(40) Zhang, B.; Wang, J.; Liu, J.; Zhang, L.; Wan, H.; Miao, L.; Jiang, J. *ACS Catalysis***2019**, *9*, 9332.

(41) Xu, X.; Wang, T.; Su, L.; Zhang, Y.; Dong, L.; Miao, X. *ACS Sustainable Chemistry & Engineering***2021**, *9*, 5693.

(42) Shan, X.; Liu, J.; Mu, H.; Xiao, Y.; Mei, B.; Liu, W.; Lin, G.; Jiang, Z.; Wen, L.; Jiang, L. *AngewandteChemie International Edition***2020**, *59*, 1659.

(43) Gao, X.; Liu, X.; Zang, W.; Dong, H.; Pang, Y.; Kou, Z.; Wang, P.; Pan, Z.; Wei, S.; Mu, S.; Wang, J. *Nano Energy***2020**, *78*, 105355.

(44) Shalom, M.; Ressnig, D.; Yang, X.; Clavel, G.; Fellinger, T. P.; Antonietti, M. *Journal of Materials Chemistry A***2015**, *3*, 8171.

(45) Kim, B.; Oh, A.; Kabiraz, M. K.; Hong, Y.; Joo, J.; Baik, H.; Choi, S.-I.; Lee, K. *ACS Applied Materials & Interfaces***2018**, *10*, 10115.

Chapter 5

Augmenting the Ni-valence state in $MnCo_2O_4$-Ni_3N and $MnCo_2O_4$@Co-Ni_3N via interfacial charge transfer for oxygen evolution reaction

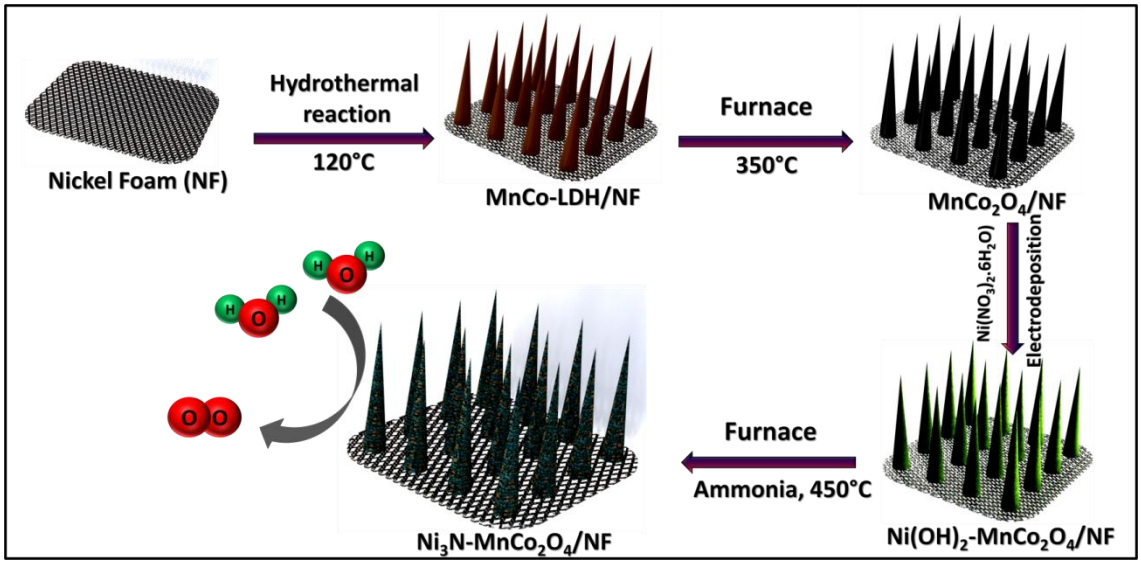

Brief Outcome: *Technologies for electrochemical conversion rely on the development of novel electrocatalysts. In these processes, the oxygen evolution reaction (OER) plays a critical role; it can be used in water splitting and metal-air batteries, for example. Herein using interfacial interaction technique we formed the novel heterointerfaces of $MnCo_2O_4$-Ni_3N and $MnCo_2O_4$@Co-Ni_3N over nickel foam. Electrodeposition technique was used for the synthesis of $Ni(OH)_2$ and Co-$Ni(OH)_2$ nanosheets over the $MnCo_2O_4$ nanowire. Further nitridation in the presence of ammonia produces the Ni_3N and Co-Ni_3N nanosheets over the $MnCo_2O_4$ nanowire scaffold. The $MnCo_2O4$-Ni_3N heterostructure shows excellent OER activity with the overpotential of 224 mV at 10 mA cm^{-2} of current density. The durability of the catalyst is also excellent with no change in current density (100 mA cm^{-2}) even after 100 hr of stability. Whereas $MnCo_2O_4$@Co-Ni_3N is active for overall water splitting with the cell volatage of 1.45V.*

5.1. Introduction

The most successful species on Earth, humans, have altered their surroundings, disrupting billions of years of careful evolution. Humanity has created a vicious, unrelenting inertia that will soon bring about a mass extinction, and the time left to respond is rapidly diminishing. The enormous increase in the release of CO_2 has destabilised the fine ecological equilibrium of the global eco-system. Since the petrochemical energy crisis and environmental pollution concerns are only expected to grow worse, it is crucial to create sustainable and green energy sources.[1,2] Because of its abundance and purity, water is a great material for using in the electrolysis process that generates hydrogen (H_2).[3,4] However, due to slow kinetics that involve several electron and proton exchanges, the OER requires a rather large overpotential. The scarcity of certain pricey metals and oxides, such as Pt, RuO_2, and IrO_2, makes them impractical to use as catalysts for the hydrogen evolution process (HER) or the oxygen evolution reaction (OER).[5-8] Consequently, metal-free catalysts, Transition metal oxides, and other active, cheap, and powerful electrocatalysts are needed.[9-12] Recent theoretical and experimental investigations have already shown that Ni_3N is a very intriguing material in this scenario, since it has certain surface terminations and crystal facets that can provide optimal energetics for water dissociation.[13-15] Different designs of metal nitride catalysts have been developed in order to further increase the effectiveness of the water splitting activity of metal nitrides such as Ni_3N−NiMoN/CC, Ru/Ni_3N−Ni and Co-Ni_3N.[16-18] In all these materials Ni atom is having low oxidation state which makes it electron rich with the completely filled e_g orbital. However the activity of the Ni-based materials can be further enhanced by the enhanced valence state of Ni atom. Higher valent metal atom can tremendously enhance the OER by enhancing the rate of adsorption of intermediates (OH^*,O^* and OOH^*) on the active sites.[19] However, the activity of the Ni-containing compounds would be greatly increased by combining Ni with other transition metals, as they have lower e_g-orbit filling.[20-25]

Herein using interfacial interaction technique we formed the novel heterointerfaces of $MnCo_2O_4$-Ni_3N and $MnCo_2O_4$@Co-Ni_3N over nickel foam. Electrodeposition technique was used for the synthesis of $Ni(OH)_2$ and Co-$Ni(OH)_2$ nanosheets over the $MnCo_2O_4$ nanowire. Further nitridation in the presence of ammonia produces the Ni_3N and Co-Ni_3N nanosheets over the $MnCo_2O_4$ nanowire scaffold. The $MnCo_2O_4$-Ni_3N heterostructure shows excellent OER activity with the overpotential of 224 mV at 10 mA cm^{-2} of current density. The durability of the catalyst is also excellent with no change in current density (100 mA cm^{-2}) even after 100 hr of stability. Whereas $MnCo_2O_4$@Co-Ni_3N exhibit the overpotential of 52 and 170 mV at 10 and 20 mA cm^{-2} of current density. The cell potential was found to be 1.45 V which is lowest among the known Ni_3N based catalyst for water splitting reation. Charge transfer from Ni to Mn and Co has been observed and characterized using X-ray photoelectron spectroscopy (XPS). This charge transfer results in the augmentation of Ni-valence state and will leads to the strong adsorption of OH^- ions which simultaneously increases the catalytic activity towards oxygen evolution reaction (OER).

5.2. Experimental section

5.2.1. Materials

All chemicals are bought from various sources and used as it is. Manganese (II) chloride tetrahydrate ($MnCl_2.\ 4H_2O$, 99.9%), Cobalt (II) nitrate hexahydrate ($Co(NO_3)_2.6H_2O$, 98%), Nickel (II) nitrate hexahydrate ($Ni(NO_3)_2.6H_2O$, 98%), Ammonium fluoride (NH_4F, 99.9%), Urea (NH_2CONH_2, 99.5%), Nafion perfluorinated resin solution (5 wt. % in mixture of lower aliphatic alcohols and water, contains 45% water), Potassium hydroxide pallet (KOH) and Ruthenium (IV) oxide (RuO_2, 99.9% trace metal basis) were purchased from sigma Aldrich. Nickel foam (NF) was purchased from Nanoshel. In all the preparation, Milli Q water having conductivity of 0.056 μS/cm was used.

5.2.2. Methodology

5.2.2.1. Synthesis of Catalyst

Catalyst synthesis section is subdivided into two major steps as per following description.

Synthesis of $MnCo_2O_4$ nanowire on NF: The NF was cleaned with 3M HCl solution under ultrasonication and then washed with DI water and acetone to remove surface grime and oxide coatings. The cleaned NF was divided into little pieces with a 1 cm × 1.5 cm of cross section area. Hydrothermal method is used to grow nanowire of $MnCo_2O_4$. Homogeneous solution of 0.280 g $Co(NO_3)_2 \cdot 6H_2O$, 0.088 g $MnCl_2 \cdot 4H_2O$, 0.068 g NH_4F and 0.051 g urea were made using 5 ml of ethanol and 25 ml of DI water. The aforesaid solution was placed to a Teflon-lined stainless steel autoclave, and one piece of NF was placed in the autoclave. The autoclave was heated at 120°C for 12h. The as synthesized MnCoLDH/NF was removed from autoclave and rinsed with ethanol and DI water. After washing, the electrode was kept for drying at 60°C for overnight. Finally, the as-prepared MnCoLDH/NF electrode was calcined in air for 2 hours at 400 °C to form $MnCo_2O_4$ over nickel foam.

Synthesis of $MnCo_2O_4$-Ni_3N:

Nickel hydroxide nanosheets were electrodeposited over $MnCo_2O_4$/NF. The fabrication of Ni $(OH)_2$ was done in three electrode setup where $MnCo_2O_4$/NF, Ag/AgCl and Pt used as a working, reference and counter electrode respectively. The electrolyte was made using aqueous solution of 0.2 M $Ni(NO_3)_2.6H_2O$. The deposition potential was kept -2.0V for 600 seconds. After this the deposition of $Ni(OH)_2$ over $MnCo_2O_4$/NF was takes place. This $MnCo_2O_4$-$Ni(OH)_2$ electrode was kept in furnace at 350°C for 2 h under continuous ammonia flow. $Ni(OH)_2$ transformed into the Ni_3N sheets over $MnCo_2O_4$ nanowire. The as obtained $MnCo_2O_4$-Ni_3N catalyst was washed with DI and ethanol several times and used as a working electrode.

Synthesis of $MnCo_2O_4$@Co-Ni_3N:

Nickel hydroxide nanosheets were electrodeposited over $MnCo_2O_4$/NF. The fabrication of Co-Ni $(OH)_2$ was done in three electrode setup where $MnCo_2O_4$/NF, Ag/AgCl and Pt used as a working, reference and counter electrode respectively. The electrolyte was made using aqueous solution of 0.2 M $Ni(NO_3)_2.6H_2O$ and 0.02M $Co(NO_3)_2.6H_2O$. The deposition potential was kept -2.0V for 600 seconds. After this the deposition of Co-$Ni(OH)_2$ over $MnCo_2O_4$/NF was takes place. This $MnCo_2O_4$@Co-$Ni(OH)_2$ electrode was kept in furnace at 350°C for 2 h under continuous ammonia flow. Co-$Ni(OH)_2$ transformed into the Co-Ni_3N sheets over $MnCo_2O_4$ nanowire. The as obtained $MnCo_2O_4$@Co-Ni_3N catalyst was washed with DI and ethanol several times and used as a working electrode.

5.2.2.2. Physical characterization

The physical characterization of the as-prepared $MnCo_2O_4$-Ni_3N and $MnCo_2O_4$@Co-Ni_3N was done using various techniques. First of all, bya Bruker Eco D8 ADVANCED X powder X-ray diffractometer consisting of a Ni filter was used for its initial steps of examination. The radiations of CuK (=1.5405, 40 KV and 25 mA) was used for the study. The examination was done in the 2Ɵ range of 20°- 80° and step size of about 0.0020/step was given. Scanning electron microscope from JEOL (JSM 17-300) was used for studying the morphology of the catalyst. The energy-dispersive X-ray diffractometer (Bruker) study was also done by the same scanning electron microscope. The complete information about the structure of $MnCo_2O_4$-Ni_3N and $MnCo_2O_4$@Co-Ni_3N and the average particle size was measured by Transmission electron microscope (TEM) JEOL-2100 which was operated at 200 KV. X-ray photoelectron spectroscopy (XPS) on ECSA: 220-IXL with MgKα is used for further investigation of elements. The MgKα used is non-monochromated X-ray beam with photon energy 1253.6 eV.

5.2.2.3. Electrochemical measurements

All the electrochemical measurements were carried out in CHI 760E electrochemical workstation. In the three-electrode system, saturated Ag/AgCl electrode is used as a

reference electrode and graphite rod used as a counter electrode. Firstly, the prepared electrode was used for taking all the polarization data at a scan rate 5 mV s^{-1} in 1 M KOH. After all the polarization data was collected, it was converted to Reversible hydrogen electrode (RHE) by the use of equation $E_{RHE} = E_{Ag/AgCl} + 0.197 + 0.059*pH$. For the calculation of Tafel slope, polarisation curves were again plotted, and the linear region of Tafel plot was fitted to the Tafel equation i.e., $\eta = b \log(j) + a$. The electrochemical surface area (ECSA) was determined by the calculation of double layer capacitance, in which CV scans of the as prepared electrode were taken at a scan rate of 20 to 200 mV/s in 1M KOH in non-faradaic potential range. when ΔJ = (Janodic-Jcathodic)/2 was plotted against the scan rate at a potential of 1.08 V vs RHE and was fitted linearly, it gave the value of double layer capacitance (C_{dl}). The faradic efficiency was calculated by taking the ratio of experimental and theoretical oxygen evolution in the reaction.

6.3. Result and Discussion

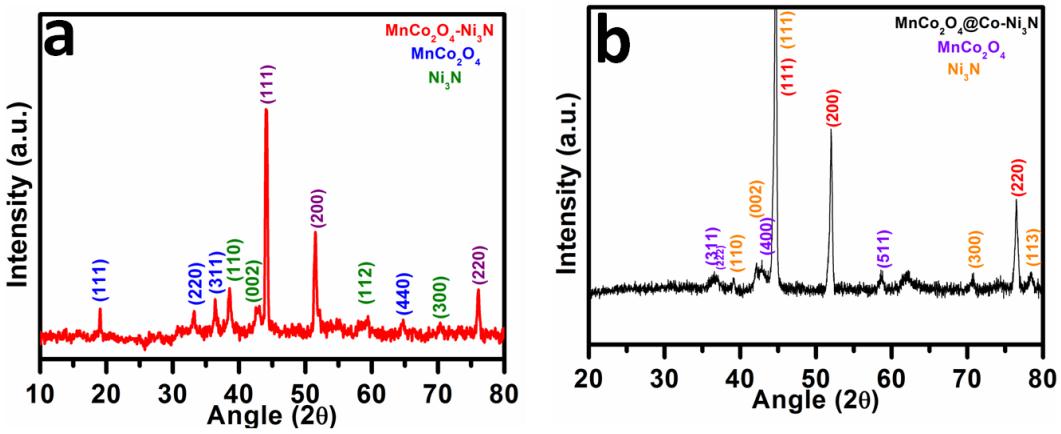

Figure 5.1. *(a) PXRD pattern of $MnCo_2O_4$-Ni_3N and $MnCo_2O_4$@Co-Ni_3N*

The structural elucidation of $MnCo_2O_4$-Ni_3N and $MnCo_2O_4$@Co-Ni_3N was done by using powder X-ray diffaraction analysis (PXRD). PXRD pattern of $MnCo_2O_4$-Ni_3N and $MnCo_2O_4$@Co-Ni_3N is given in Figure 5.1(a) and 5.1(b). The peaks were matched with the correpsong JCPDS data of $MnCo_2O_4$-Ni_3N.[26,27]

The morphological examination was done by scanning electron microscopy (SEM). The nano-urchin like shape of $MnCo_2O_4$ was observed these nano-urchins are having sharp edges. Further the coating of Ni_3N and Co-Ni_3N was done over $MnCo_2O_4$ and the very fine coating of Ni_3N and Co-Ni_3N can be observed in SEM images. The SEM images of $MnCo_2O_4$-Ni_3N with elemental mapping is given in Figure 5.2 whereas the SEM images of $MnCo_2O_4$@Co-Ni_3N is provided in Figure 5.3.

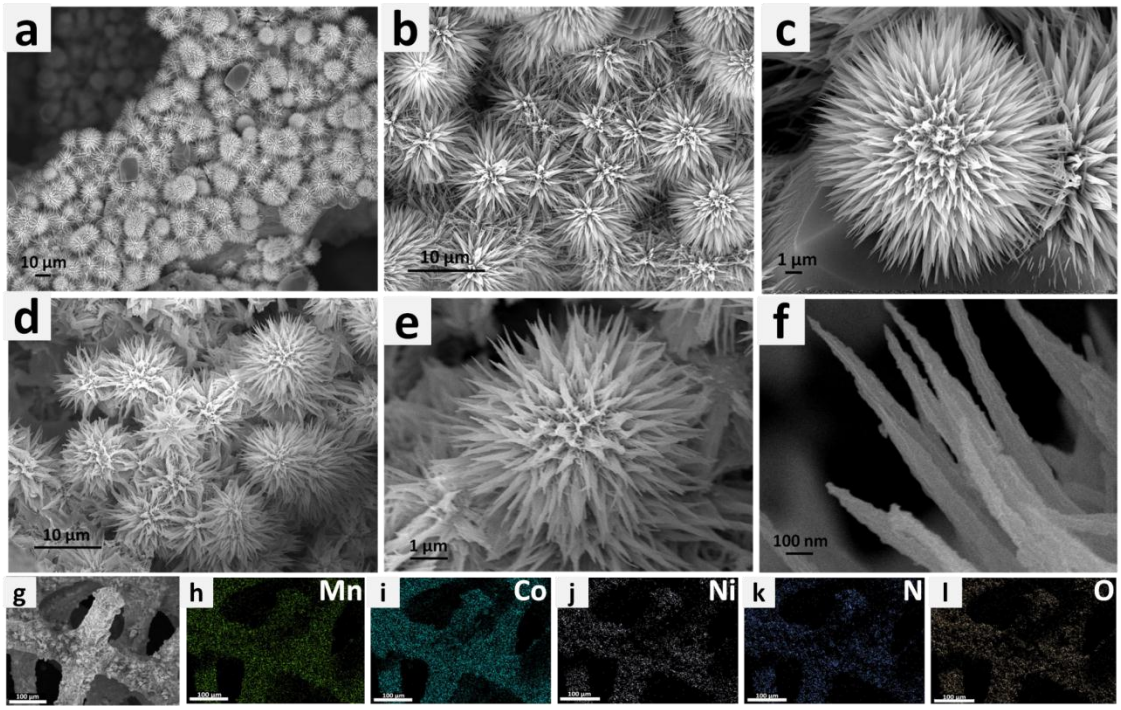

Figure 5.2. *(a), (b) and (c) $MnCo_2O_4$ nanoflowers (d), (e) and (f) Ni_3N coated $MnCo_2O_4$ nanoflowers (g-i) SEM elemental mapping confirming the presence of all the elements*

TEM image of rod shape $MnCo_2O_4$ is shown in Figure 5.4(a). TEM images of $MnCo_2O_4$-Ni_3N show the formation of Ni_3N nanosheets over $MnCo_2O_4$ nanorods (Figure 5.4(b&c)). The formation of a heterointerface between Ni_3N and $MnCo_2O_4$ is confirmed using HR-TEM analysis. HR-TEM images (Figure 5.4(d,e&f) confirm the presence of $MnCo_2O_4$ and Ni_3N phases in the catalyst. Figure 5.4e shows the presence of $MnCo_2O_4$ phase with the dspacing of 0.25 nm corresponds to the (311) crystal plane of $MnCo_2O_4$. The presence of Ni_3N was also confirmed with the d-spacing value of 0.21 corresponding to (111) crystal planes of Ni_3N (Figure 5.4f). From HR-TEM images we can observe the formation of an interface between $MnCo_2O_4$ and Ni_3N.

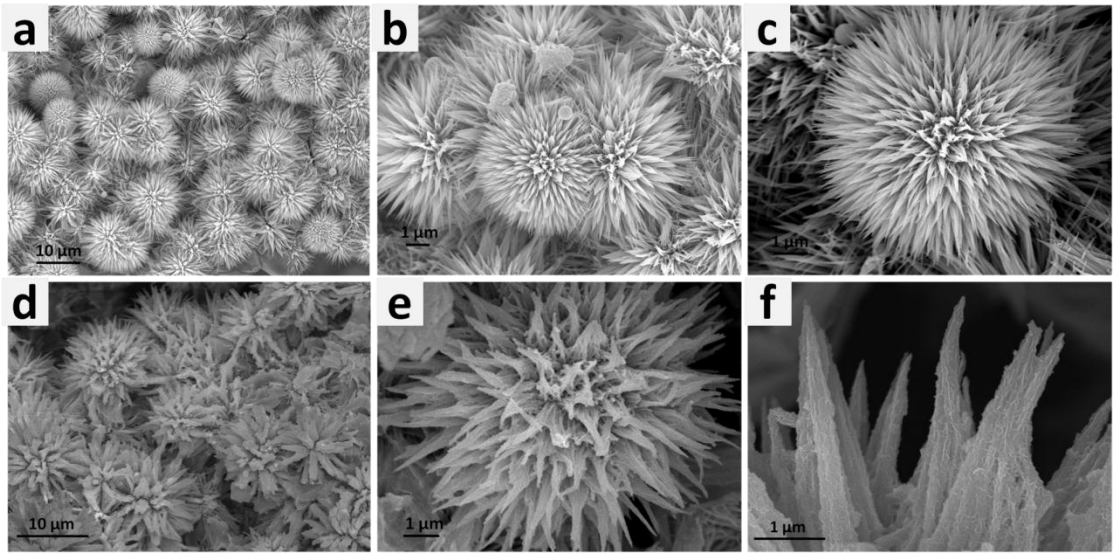

Figure 5.3. *(a), (b) and (c) $MnCo_2O_4$ nanoflowers (d), (e) and (f) Co-Ni_3N coated $MnCo_2O_4$*

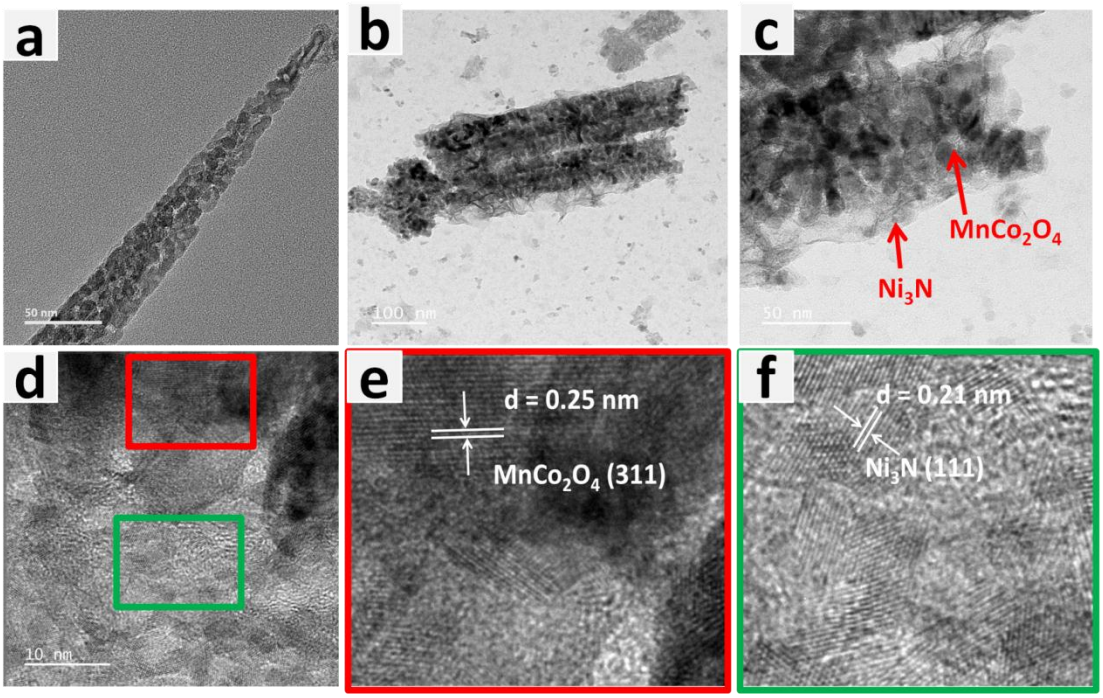

Figure 5.4. *(a)$MnCo_2O_4$ nanowires (b-c) Ni_3N coated $MnCo_2O_4$ nanowire (d-f) HRTEM image showing the presence of $MnCo_2O_4$ and Ni_3N*

TEM image of rod shape $MnCo_2O_4$ is shown in Figure 5.5(a). TEM images of $MnCo_2O_4$@Co-Ni_3N show the formation of Co-Ni_3N nanosheets over $MnCo_2O_4$ nanorods (Figure 5.5(b&c)). The formation of a heterointerface between Co-Ni_3N and $MnCo_2O_4$ is confirmed using HR-TEM analysis. HR-TEM images (Figure 5.5(d,e&f) confirm the presence of $MnCo_2O_4$ and Ni_3N phases in the catalyst. Figure 5.45e shows the presence of $MnCo_2O_4$ phase with the dspacing of 0.25 nm corresponds to the (311) crystal plane of $MnCo_2O_4$. The presence of Ni_3N was also confirmed with the d-spacing value of 0.21 corresponding to (111) crystal planes of Ni_3N (Figure 5.5f). From HR-TEM images we can observe the formation of an interface between $MnCo_2O_4$ and Co-Ni_3N.

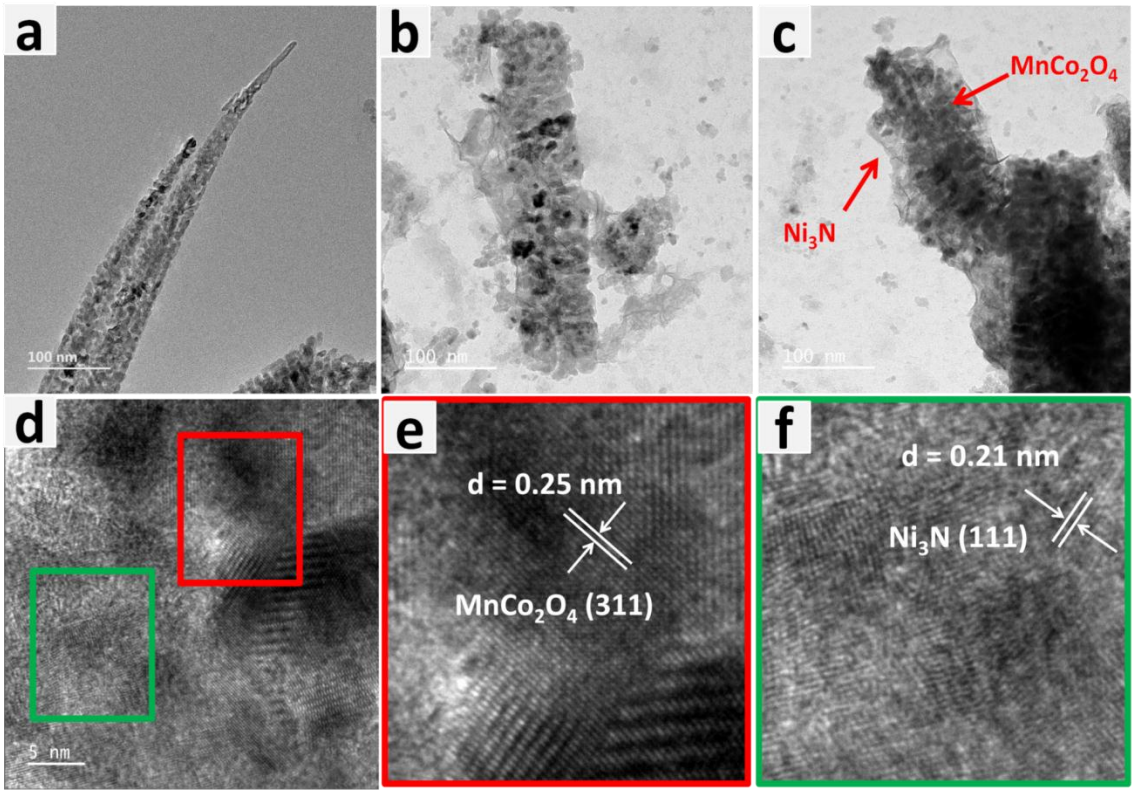

Figure 5.5. *(a) $MnCo_2O_4$ nanowires (b-c) Ni_3N coated $MnCo_2O_4$ nanowire (d-f) HRTEM image showing the presence of $MnCo_2O_4$ and Ni_3N*

The catalytic performance of $MnCo_2O_4$-Ni_3N towards oxygen evolution reaction was studied in three-electrode electrochemical setup and in general, 1M KOH solution was used in the experiment, unless mentioned otherwise. The comparison of the catalytic performance was done with $MnCo_2O_4$, Ni_3N, commercially available RuO_2 and bare nickel foam. Notably, the $MnCo_2O_4$-Ni_3N catalyst demonstrated an excellent OER activity that is far better than the commercially available RuO_2. The overpotential of 224 mV (Figure 5.6a) was achieved for the catalyst which was far better than that of individual $MnCo_2O_4$ and Ni_3N. The overpotential of 270 mV, 300 mV and 350 mV was obtained for RuO_2, $MnCo_2O_4$ and Ni_3N (Figure 5.6(b) The Tafel plot derived from the polarisation curves (figure 5.6c) shows the low Tafel slope value of 111 mV dec^{-1} for $MnCo_2O_4$-Ni_3N. This value is lower than that of Ni_3N (142 mV dec^{-1}), RuO_2 (115 mV dec^{-1} and $MnCo_2O_4$ (194 mV dec^{-1}). The lower Tafel slope value of $MnCo_2O_4$-Ni_3N suggests the fast OER kinetics as compared to the commercially available RuO_2. The charge transfer resistance was studied using electrochemical impedance spectroscopy to identify strong interfacial contacts for faster electron transit across the electrode-electrolyte interface. Figure 5.6d shows the Nyquist plot with the equivalent circuit used for fitting the plot and obtained the desired parameters which significantly define a good catalyst. Lower R_{ct} value was obtained for $MnCo_2O_4$-Ni_3N catalyst which indicates a rapid electron transfer and hence follows a superior OER kinetics. To precisely assess the inherent OER activity of the reported catalyst, we evaluated the electrochemical C_{dl} of the $MnCo_2O_4$-Ni_3N catalyst to compute their ECSA and normalized the resulting current in comparison to $MnCo_2O_4$ and Ni_3N catalysts. The double-layer capacitance (Cdl) value was calculated using cyclic voltammetry (CV) measurements carried out at different scan rates (20-200 mVs^{-1}). The obtained C_{dl} values are 30, 8.1 and 5.8 mF cm^{-2} for $MnCo_2O_4$-Ni_3N, Ni_3N and $MnCo_2O_4$ respectively (Figure 5.6e). The higher values of C_{dl} indicate a higher number of active sites present in $MnCo_2O_4$-Ni_3N. The faradic efficiency (Figure 5.6f) is estimated using the water-gas displacement technique, in which the estimated faradic efficiency is the percentage of the ratio of the quantity of O_2 evolved empirically to the amount of O_2 evolved theoretically. The faradic efficiency value for our catalyst is 97.3%.

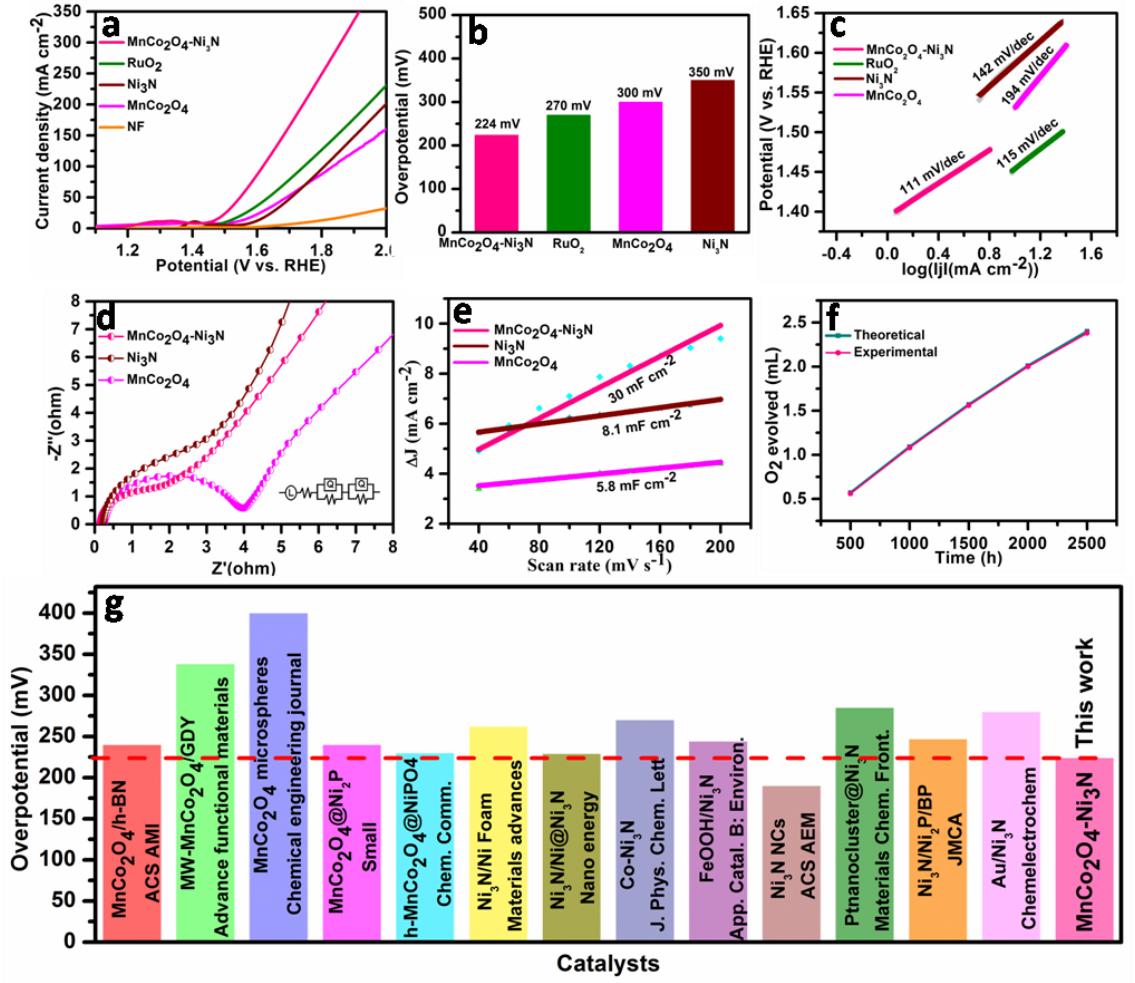

Figure 5.6. *(a) polarization curve of $MnCo_2O_4$-Ni_3N and other supporting catalyst. (b) overpotential value of all the catalyst at 10 mA cm^{-2} of current density (c) tafel plot derived from polarization curve (d) EIS nyquist plot of all the catalysts (e) double- layer capacitance value of all the catalyst (f) faradic efficiency calculation using water displacement method (g) comparison of $MnCo_2O_4$-Ni_3N with recently reported Ni_3N and $MnCo_2O_4$ based highly active catalysts*

The activity of the catalyst at 10 mA cm^{-2} was also compared with the recently reported Ni_3N and $MnCo_2O_4$ based catalysts. The overpotential of the catalyst was found to be second highest among the recently repored Ni_3N based catalyst. The stability of the catalyst was checked by using chronoamperometry measurement and the electrode was found to be stable for more than 100 h at higher current density of 100 mA cm^{-2} also (Figure 5.7) . No significant change in the current density was observed even after 100 h of atbility.

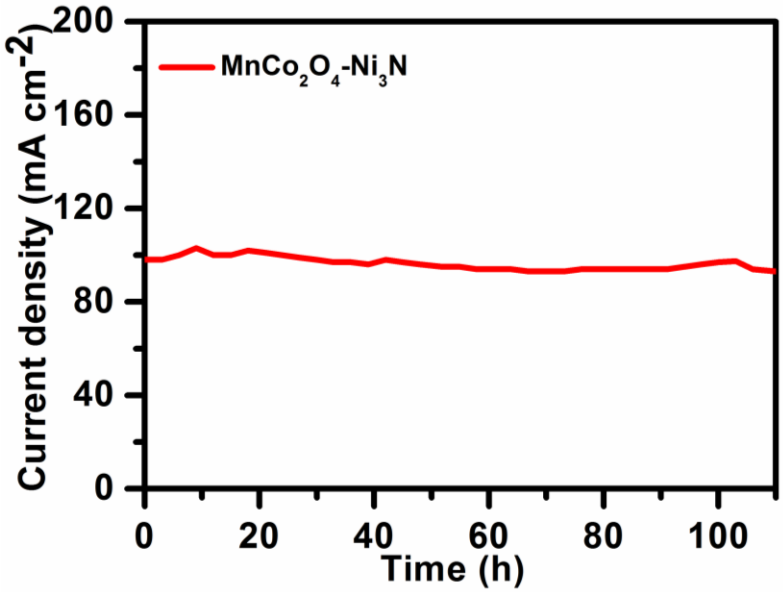

***Figure 5.7**.Durability test of the catalyst using chronoamperometry*

The catalytic performance of $MnCo_2O_4$@Co-Ni_3N towards oxygen evolution reaction was studied in three-electrode electrochemical setup and in general, 1M KOH solution was used in the experiment, unless mentioned otherwise. The comparison of the catalytic performance was done with $MnCo_2O_4$, Co-Ni_3N, commercially available RuO_2 and bare nickel foam. Notably, the $MnCo_2O_4$-Ni_3N catalyst demonstrated an excellent OER activity that is far better than the commercially available RuO_2. The overpotential of 170 mV (Figure 5.8a) was achieved for the catalyst which was far better than that of individual $MnCo_2O_4$ and Co-Ni_3N. The overpotential of 330 mV, 340 mV and 310 mV was obtained for RuO_2, $MnCo_2O_4$ and Co-Ni_3N (Figure 5.8(b) The charge transfer resistance was studied using electrochemical impedance spectroscopy to identify strong interfacial contacts for faster electron transit across the electrode-electrolyte interface. Figure 5.8c shows the Nyquist plot with the equivalent circuit used for fitting the plot and obtained the desired parameters which significantly define a good catalyst. Lower R_{ct} value was obtained for $MnCo_2O_4$-Ni_3N catalyst which indicates a rapid electron transfer and hence follows a superior OER kinetics.

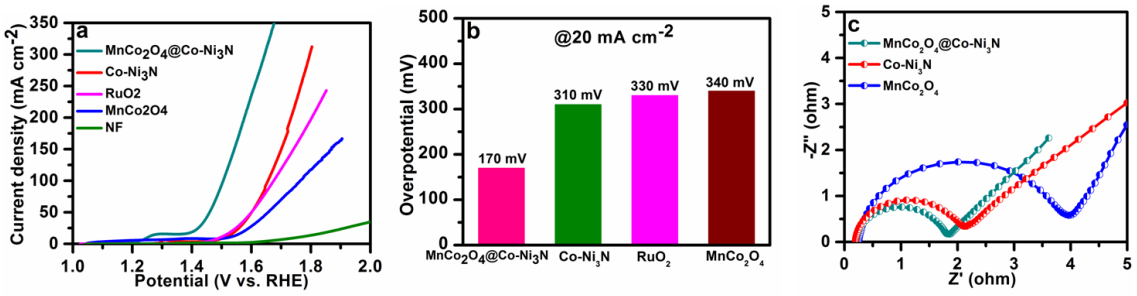

***Figure 5.8**. (a) polarization curve of $MnCo_2O_4$@Co-Ni_3N and other supporting catalyst. (b) overpotential value of all the catalyst at 10 mA cm^{-2} of current density (c) EIS nyquist plot of all the catalysts*

The stability of the catalyst was checked by chronoamperometry meanurement by continuously running for 100 h (Figure 5.9) and no change has been observed in the current density.

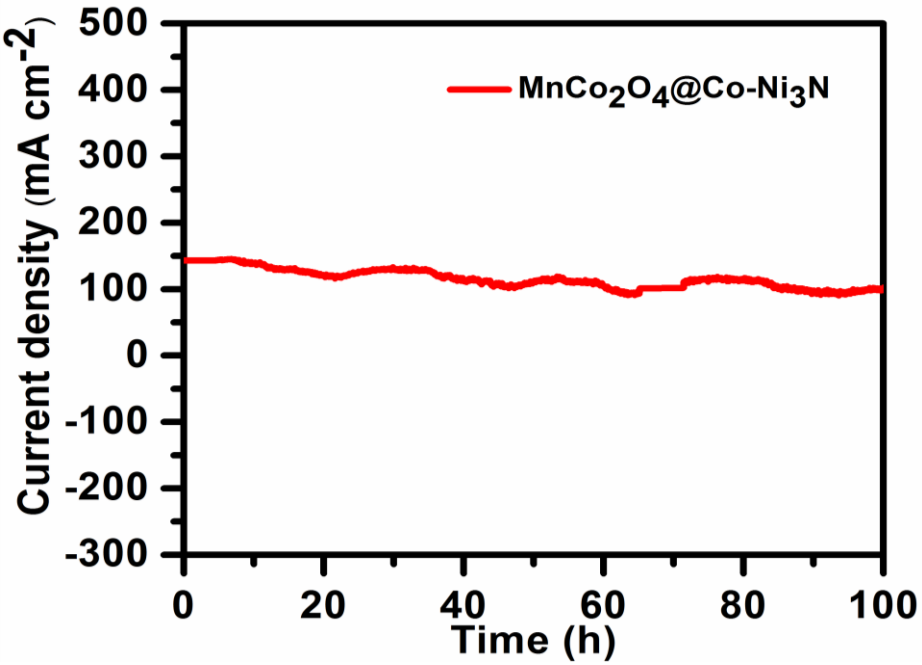

***Figure 5.9.** Durability test of the catalyst using chronoamperometry*

The catalytic performance of $MnCo_2O_4$@Co-Ni_3N towards hydrogen evolution reaction (HER) was studied in three-electrode electrochemical setup and in general, 1M KOH solution was used in the experiment, unless mentioned otherwise.

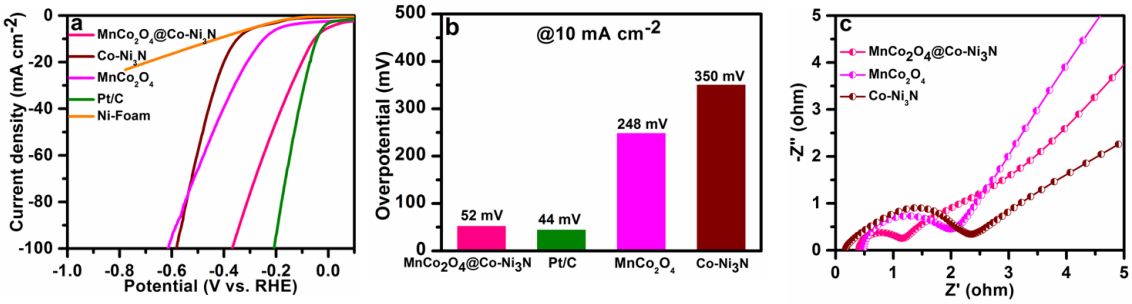

***Figure 5.10**. (a) polarization curve of $MnCo_2O_4$@Co-Ni_3N and other supporting catalyst. (b) overpotential value of all the catalyst at 10 mA cm^{-2} of current density (c) EIS nyquist plot of all the catalysts*

The comparison of the catalytic performance was done with $MnCo_2O_4$, Co-Ni_3N, commercially available Pt/C and bare nickel foam. Notably, the $MnCo_2O_4$@Co-Ni_3N catalyst demonstrated an excellent HER activity that is far better than the commercially available RuO_2. The overpotential of 52 mV (Figure 5.10a) was achieved for the catalyst which was far better than that of individual $MnCo_2O_4$ and Co-Ni_3N. The overpotential of 44 mV, 248 mV and 350 mV was obtained for Pt/C, $MnCo_2O_4$ and Co-Ni_3N (Figure 5.10(b) The charge transfer resistance was studied using electrochemical impedance spectroscopy to identify strong interfacial contacts for faster electron transit across the electrode-electrolyte interface.

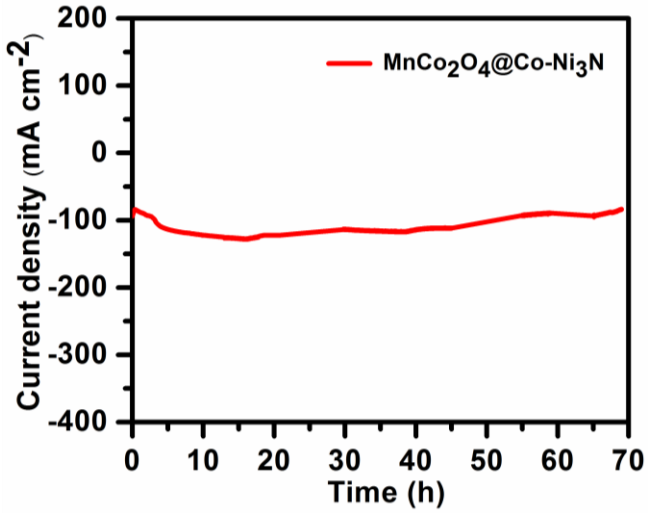

***Figure 5.11.** Durability test of the catalyst using chronoamperometry*

5.4. Conclusion

In conclusion we have formed two heterostructure $MnCo_2O_4$-Ni_3N and $MnCo_2O_4$@Co-Ni_3N over nickel foam. Electrodeposition technique was used for the synthesis of $Ni(OH)_2$ and Co-$Ni(OH)_2$ nanosheets over the $MnCo_2O_4$ nanowire. Further nitridation in the presence of ammonia produces the Ni_3N and Co-Ni_3N nanosheets over the $MnCo_2O_4$ nanowire scaffold. The $MnCo_2O4$-Ni_3N heterostructure shows excellent OER activity with the overpotential of 224 mV at 10 mA cm^{-2} of current density. The durability of the catalyst is also excellent with no change in current density (100 mA cm^{-2}) even after 100 hr of stability. Whereas $MnCo_2O_4$@Co-Ni_3N is active for overall water splitting with the cell volatage of 1.45V.

References

1. Muntean, Marilena, et al. "Fossil CO_2 emissions of all world countries." *Luxembourg: Publications Office of the European Union* 2 (2018).

2. Razmjoo, Armin, et al. "A Technical analysis investigating energy sustainability utilizing reliable renewable energy sources to reduce CO2 emissions in a high potential area." *Renewable Energy* 164 (2021): 46-57.

3. Sui, Yiming, and Xiulei Ji. "Anticatalytic strategies to suppress water electrolysis in aqueous batteries." *Chemical Reviews* 121.11 (2021): 6654-6695.

4. Vidas, Leonardo, and Rui Castro. "Recent developments on hydrogen production technologies: state-of-the-art review with a focus on green-electrolysis." *Applied Sciences* 11.23 (2021): 11363.

5. Zhao, Fang, et al. "Increasing iridium oxide activity for the oxygen evolution reaction with hafnium modification." *Journal of the American Chemical Society* 143.38 (2021): 15616-15623.

6. Joshi, Prerna, et al. "Contribution of B, N-co-doped reduced graphene oxide as a catalyst support to the activity of iridium oxide for oxygen evolution reaction." *Journal of Materials Chemistry A* 9.14 (2021): 9066-9080.

7. El-Refaei, Sayed M., Patrícia A. Russo, and Nicola Pinna. "Recent advances in multimetal and doped transition-metal phosphides for the hydrogen evolution reaction at different pH values." *ACS Applied Materials & Interfaces* 13.19 (2021): 22077-22097.

8. Cheng, Zhihua, et al. "All-pH-tolerant in-plane heterostructures for efficient hydrogen evlution reaction." *ACS nano* 15.7 (2021): 11417-11427.

9. Hu, Chuangang, and Liming Dai. "Carbon-based metal-free catalysts for electrocatalysis beyond the ORR." *Angewandte Chemie International Edition* 55.39 (2016): 11736-11758.

10. Wang, Bin, et al. "Recent advances in energy chemistry of precious-metal-free catalysts for oxygen electrocatalysis." *Chinese Chemical Letters* 29.12 (2018): 1757-1767.

11. Hong, Wesley T., et al. "Toward the rational design of non-precious transition metal oxides for oxygen electrocatalysis." *Energy & Environmental Science* 8.5 (2015): 1404-1427.

12. Al-Naggar, Ahmed H., et al. "Water splitting performance of metal and non-metal-doped transition metal oxide electrocatalysts." *Coordination Chemistry Reviews* 474 (2023): 214864.

13. Xu, Kun, et al. "Metallic nickel nitride nanosheets realizing enhanced electrochemical water oxidation." *Journal of the American Chemical Society* 137.12 (2015): 4119-4125.

14. Gao, Daqiang, et al. "Metallic Ni 3 N nanosheets with exposed active surface sites for efficient hydrogen evolution." *Journal of Materials Chemistry A* 4.44 (2016): 17363-17369.

15. You, Bo, et al. "Universal surface engineering of transition metals for superior electrocatalytic hydrogen evolution in neutral water." *Journal of the American Chemical Society* 139.35 (2017): 12283-12290.

16. Wu, Aiping, et al. "Integrating the active OER and HER components as the heterostructures for the efficient overall water splitting." *Nano Energy* 44 (2018): 353-363.

17. Liu, Zong, et al. "Overall water-splitting reaction efficiently catalyzed by a novel bi-functional Ru/Ni 3 N–Ni electrode." *Chemical Communications* 56.15 (2020): 2352-2355.

18. Wang, Meng, et al. "Co-doped Ni_3N nanosheets with electron redistribution as bifunctional electrocatalysts for efficient water splitting." *The Journal of Physical Chemistry Letters* 12.6 (2021): 1581-1587.

19. Tahir, Muhammad, et al. "High-valence-state NiO/Co3O4 nanoparticles on nitrogen-doped carbon for oxygen evolution at low overpotential." *ACS Energy Letters* 2.9 (2017): 2177-2182.

20. Suntivich, Jin, et al. "A perovskite oxide optimized for oxygen evolution catalysis from molecular orbital principles." *Science* 334.6061 (2011): 1383-1385.

21. He, Qing, et al. "Constructing 3D hierarchical MOFs nanospheres for oxygen evolution from high-throughput calculations." *Journal of Colloid and Interface Science* 607 (2022): 1944-1952.

22. Tareen, Ayesha Khan, et al. "Nickel-based transition metal nitride electrocatalysts for the oxygen evolution reaction." *ChemSusChem* 12.17 (2019): 3941-3954.

23. Kreider, Melissa E., et al. "Precious metal-free nickel nitride catalyst for the oxygen reduction reaction." ACS applied materials & interfaces 11.30 (2019): 26863-26871.

24. Saad, Ali, et al. "Ordered mesoporous cobalt–nickel nitride prepared by nanocasting for oxygen evolution reaction electrocatalysis." *Advanced Materials Interfaces* 6.20 (2019): 1900960.

25. Chen, Qiming, et al. "Surface Phase Engineering Modulated Iron-Nickel Nitrides/Alloy Nanospheres with Tailored d-Band Center for Efficient Oxygen Evolution Reaction." *Small* 18.4 (2022): 2105696.

26. Luo, Xinyue, et al. "Nickel-Rich Ni3N Particles Stimulated by Defective Graphitic Carbon Nitrides for the Effective Oxygen Evolution Reaction." *Industrial & Engineering Chemistry Research* 61.5 (2022): 2081-2090.

27. Zeng, Kai, et al. "Multilayer hollow MnCo2O4 microsphere with oxygen vacancies as efficient electrocatalyst for oxygen evolution reaction." *Chemical Engineering Journal* 421 (2021): 127831.

Chapter 6

Curtailing the excess e_g-orbital filling of Ni-atom by enhanced inter-atomic charge transfer within bimetallic 2-D MOF nanoribbons for electrocatalytic oxygen evolution reaction

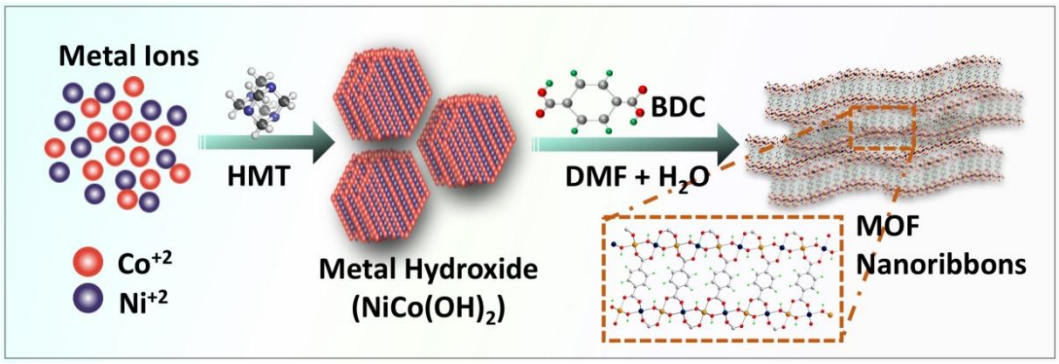

Brief Outcome: *Electrochemical conversion technologies rely on the design and creation of highly efficient electrocatalysts. The oxygen evolution reaction (OER), which has applications in water splitting and metal-air batteries, is a crucial process in such conversions. Herein,a bimetallic Co, Ni-based ultrathin metal-organic framework nanoribbons (NiCo-NR) is reported for an efficient OER. It is proposed that in the ultrathin MOF nanoribbons, the surface atoms (Co,Ni) are coordinatively unsaturated, due to which, the inter-atomic electron transfer within the MOF makes more active adsorption sites on the surface. Our findings showed that the coordinatively unsaturated transition metal atoms are the dominant active sites and the electrocatalytic activity can be tuned by the coupling interactions of Ni and Co metals. The excess eg-orbital filling of Ni-atom which limits the electrocatalytic performance can be reduced by π-donation from Ni to Co through the oxygen atom.*

6.1. Introduction

Humans, the most dominant species existing on the earth, have transformed the environment, undermining billions of years of meticulous evolutionary processes. Vicious unending inertia created by human activities is about to bring a Mass extinction, with just a short window of time in which to act.[1] The astronomical increase in the emission of CO_2 has destabilized the subtle ecological balance of the global eco-system. Therefore, It is imperative to develop sustainable and green energy sources to deal with the ever-increasing petrochemical energy crisis and environmental pollution challenges.[2] Water is an excellent resource for producing high-quality hydrogen (H_2) through water electrolysis because it is clean and abundant on Earth.[3] However, the OER demands a relatively high overpotential resulting fromsluggish kinetics that includes numerous electron and proton exchanges.[4, 5] Ir/Ru-based oxides have been identified as the most efficient OER catalysts. Nonetheless, the expensive price, paucity of reserves, and poor stability of these precious metal-based electrocatalysts have prevented large-scale commercial applications of the water electrolysis technique.[6, 7] Furthermore, substantial overpotential to trigger the reaction reduces energy conversion efficiency and makes it difficult to use in devices for practical applications. On the other hand, two-dimensional (2D) nanomaterials like graphitic carbon nitride, transition-metal oxides, layered double hydroxides and transition-metal dichalcogenidesexhibit distinct chemical and physical properties.[8, 9]Their huge lateral size, atomic thickness, large specific surface area and high surface-to-volume atom ratio make them suitable for a wide range of applications including energy storage, electrocatalysis, electronics, sensors, and so on. These intriguing features and broad uses have also fuelled researchers to fabricate 2D metal–organic framework (MOF) nanosheets. Current findings on water splitting electrocatalysts have also focused on increasing the activation and stability of MOF-based electrocatalysts.[10-13]Some of the unusual features of MOFsespecially, their atomically distributed metal ions and coordinatively unsaturated metal sites can be used as highly active electrocatalytic sites.[14-16]Because of the high mass resistivity in their micro-pores, it is difficult to entirely remove the solvent molecules from bulk MOFs to displaybehavioural aspects of coordinatively unsaturated transition metal sites. MOFs

prepared as 2D nanosheets have inherent advantages that are generally associated with 2D materials, such as highly exposed surface atoms and high specific surface area.[17] These facilitate the interaction between reactive intermediates and the catalyst surface.[18, 19] Such distinctive features make the MOF perform better in oxygen evolution reactions (OER), supercapacitors, hydrogen evolution reactions (HER), oxygen reduction reactions (ORR), and electrochemical CO_2 reduction (ECR).[9, 20-23] The production of 2D MOF nanosheets, however, remains a substantialchallenge since MOF crystal growth should be limited to a few nanometres in thickness without affecting lateral direction growth.[8] Ni-based materials have gotten a lot of interest, as a result of their inexpensive cost and high electrocatalytic performance including Ni_3Se_2nanoforest/NF, $NiCo_2O_4$-Ni_3S_2/NF, NiP-NiS and Ni-based MOFs.[24-27]Nevertheless, the OER activity of such Ni-based materials is minimal, and their electrochemical performance deteriorated fast.[28] The fundamental cause for their inadequate activity is the excessive e_g-orbital filling of nickel, which limits OER performance. The problem can be circumvented by integrating nickel with other metals which results in lowering of the Ni-e_g-orbital filling, thereby significantly boosting the activity of Ni-containing bimetal compounds. Herein we report a 2D bimetallic metal-organic framework nanoribbons (NiCo-NR), which shows excellent oxygen evolution reaction (OER) with an overpotential of 244 mV at a current density of 10 mA $cm^{-2,}$and exhibits aTafel slope value of 85 mV/dec. The low overpotential was considerably lowered when Ni and Co atoms were coupled in the form of ultrathin nanoribbons. The inter-atomic electron transfer from the e_g orbital of Ni to the e_g orbital of Co through an oxygen atom, results in the attainment of a partially positive charge on the Ni atom, making it more active for the adsorption of the intermediate involved in the OER. The charge transfer process is explicitly explained using synchrotron radiation-based X-ray absorption near-edge structure (XANES), extended X-ray absorption fine structure (EXAFS), X-ray photoelectron spectroscopy (XPS) and is elucidated in the later section of this article.

6.2. Experimental section

6.2.1. Materials

All chemicals are bought from various sources and used as it is. Cobalt (II) chloride hexahydrate ($CoCl_2.6H_2O$, 98%) , Nickel(II) acetate tetrahydrate ($Ni(OCOCH_3)_2.4H_2O$, 98%) and nickel(II) chloride hexahydrate ($NiCl_2 \cdot 6H_2O$, 98%) were purchased from sigma Aldrich. 1,4-benzenedicarboxylic acid (C_6H_4-1,4$(COOH)_2$, 98%) ,N,N-dimethylformamide anhydrous ($HCON(CH_3)_2$, 99.5%) and Hexamethylenetetramine ($C_6H_{12}N_4$, 99.0%) were purchased from TCI chemicals. Nafion perfluorinated resin solution (5 wt. % in mixture of lower aliphatic alcohols and water, contains 45% water), Potassium hydroxide pallet (KOH) and Ruthenium (IV) oxide (RuO_2, 99.9% trace metal basis) were also purchased from sigma Aldrich.

6.2.2. Methodology

6.2.2.1. Synthesis of Catalyst

Catalyst synthesis section is subdivided into two major steps as per following description**.**

Step 1. Synthesis of $NiCo(OH)_2$ nanosheets: The synthesis of $NiCo(OH)_2$ nanosheets was adapted from previous report with minor modifications. In a standard procedure, $CoCl_2 \cdot 6H_2O$ (1.0 mmol) and $NiCl_2 \cdot 6H_2O$ (1.0 mmol) were firstly dissolved in 300 mL of deionized water. Then 25 mmol of hexamethylenetetramine (HMT) was added into the above solution. The solution was refluxed at 105°C for 5 hr with continuous stirring. After that the solid product was obtained by centrifugation of the above solution at 7000 RPM. The obtained $NiCo(OH)_2$ was washed with deionized water and ethanol several times. The pure $NiCo(OH)_2$ nanosheets were obtained by drying the above product at 60°C in Oven.

Step 2. Synthesis of NiCo-NR: The $NiCo(OH)_2$ nanosheets (0.04 mmol) and 1,4 benzenedicarboxylic acid (0.042 mmol) were mixed together in a 40 mL capped vial with 15 mL N,N-dimethylformamide and 2 mL deionized water and stirred. The vial was then heated to 60°C and kept at this temperature for 12 hours with continuous stirring. The

light green NiCo-NR were obtained and washed with DMF and ethanol several times. The nanoribbons were redispursed into the ethanol and used for further characterization and electrocatalysis.

Synthesis of Co-NR: The Co-NR was produced by two step synthesis method. In the first step the $Co(OH)_2$ hydroxide nanosheets were synthesized while in the second step the MOF nanoribbons were synthesized by using Co(OH)2 hydroxide nanosheets and 1,4-benzenedicaboxylic acid (BDC). The synthesis of $Co(OH)_2$ nanosheets was adapted from previous report with minor modifications.In a standard procedure, $CoCl_2 \cdot 6H_2O$ (2 mmol) was firstly dissolved in 300 mL of deionized water. Then 50 mmol of hexamethylenetetramine (HMT) was added into the above solution. The solution was refluxed at 100°C for 1 hr with continuous stirring. After that the solid product was obtained by centrifugation of the above solution at 7000 RPM. The obtained $Co(OH)_2$ was washed with deionized water and ethanol several times. The pure $Co(OH)_2$ nanosheets were obtained by drying the above product at 60°C in Oven. After that the $Co(OH)_2$ nanosheets (0.04 mmol) and 1,4 benzenedicarboxylic acid (0.042 mmol) were mixed together in a 40 mL capped vial with 15 mL N,N-dimethylformamide and 2 mL deionized water and stirred. The vial was then heated to 60°C and kept at this temperature for 12 hours with continuous stirring. The light green Co-NR were obtained and washed with DMF and ethanol several times. The nanoribbons were redispersed into the ethanol and used for further characterization and electrocatalysis.

Synthesis of Ni-NR: The Ni-NR was produced by two step synthesis method. In the first step the $Ni(OH)_2$ hydroxide nanosheets were synthesized while in the second step the MOF nanoribbons were synthesized by using Ni(OH)2 hydroxide nanosheets and 1,4-benzenedicaboxylic acid (BDC). The synthesis of $Ni(OH)_2$ nanosheets was adapted from previous report with minor modifications.In a standard procedure, $Ni(CH_3COO)_2 \cdot 4H_2O$ (2.0 mmol) was dissolved in a 30.0 mL deionized water, and then 1.0 mL of 6.0 M $NH_3 \cdot H_2O$ was poured in drop by drop during magnetic stirring. The solution was then sealed in a 30 mL Teflon autoclave and heated for 5 hours at 200 °C. A green suspension resulted from the hydrothermal reaction were obtained by centrifuging at 7000rpm and washing with deionized water for 3 times.The pure $Ni(OH)_2$ nanosheets were obtained by

drying the above product at 60°C in Oven. After that the $Ni(OH)_2$ nanosheets (0.04 mmol) and 1,4 benzenedicarboxylic acid (0.042 mmol) were mixed together in a 40 mL capped vial with 15 mL N,N-dimethylformamide and 2 mL deionized water and stirred. The vial was then heated to 60°C and kept at this temperature for 12 hours with continuous stirring. The light green Ni-NR were obtained and washed with DMF and ethanol several times. The nanoribbons were redispersed into the ethanol and used for further characterization and electrocatalysis.

6.2.2.2. Physical characterization

The Bruker Eco D8 ADVANCE X Powder X-ray diffractometer was used to investigate the structural properties of NiCo-NR, Ni-NR and Co-NR.The diffractometer consists of a Ni filter that provides Cu K radiation (= 1.54056, 40 kV, and 25 mA) in the 2θ range of 5°-80° with a rise of 0.00190/step. The morphological examination of the nanoribbons is performed using a JEOL JSM-7600F (FESEM) scanning electron microscope SEM equipped with an energy-dispersive X-ray diffractometer (Bruker). Transmission electron microscopy (TEM) JEOL-2100 operating at 200 kV was used to analyse the length and breadth of the NiCo-NR, Ni-NR and Co-NR nanoribbons. X-Ray photoelectron (XPS) spectroscopy was executed on a K-Alpha plus XPS system of Thermo Fisher Scientific instruments in an ultrahigh vacuum chamber ($7x10^{-9}$ torr) using Al-Kα radiation (1486.6 eV). AFM imaging was done by using a Bruker multimode and scanning probe microscope with TAP 150-AL-G cantilevers (budget sensor).

6.2.2.3. Electrochemical measurements

At a temperature of 25°C, all electrochemical measurements were performed on a CHI 760E electrochemical workstation. A graphite electrode serves as a counter electrode, and a saturated Ag/AgCl electrode serves as a reference electrode in the traditional three-electrode arrangement. The ink for coating graphitic strip electrodes was made by dissolving 2 mg of the catalyst in 300μL of ethanol containing 10μL of 5% Nafion. The mixture was sonicated for 120 minutes to create a homogenous suspension. Only 50 μL of the fluid were deposited on graphitic strip electrodes and dried in vacuum. All of the

polarisation data was obtained in 1 M KOH at a scan rate of 5 mV s^{-1}. $E_{RHE} = E_{Ag/AgCl} + 0.197 + 0.059\times pH$ is the equation used to convert to a reversible hydrogen electrode. The Tafel slope was determined by plotting the polarisation curve again and fitting the linear portion of the Tafel plot to the Tafel equation ($\eta = b \log(j) + a$). The elimination of Ohmic drop was used to correct the iR_s, as stated by the equation $\eta_{corrected} = \eta - iR_s$, where Rs signifies the solution resistance. Electrochemical impedance spectroscopy (EIS) was carried out at a frequency range of 1 to 100000 Hz with an overpotential of 200 mV. We employed chronoamperometry with a 244 mV applied voltage for the stability study. The double layer capacitance was determined using CV scans in a non-Faradaic potential range of as-prepared catalyst electrodes in 1 M KOH at a scan rate of 10 to 100 mV/s for the calculation of electrochemically active surface area ECSA study. Half of the variations in current density ($J = (J_{anodic}-J_{cathodic})$) shown against scan rate at a potential of 1.16 V versus RHE fit to a linear regression that allows the measurement of double layer capacitance (Cdl). The faradic efficiency was calculated by dividing the experimental oxygen evolution by the theoretical oxygen evolution.

6.3. Result and Discussion

The core metal ions in the MOFs have a crucial role in the reaction mechanism; hence, appropriate metal ions is critical for the synthesis of a highly active MOF-based electrocatalyst. The structural elucidation of the as-synthesized metal-organic framework nanoribbons is done by using PXRD. The XRD peaks of the NiCo-NR (Figure 6.1(a)) are consistent with the reported MOF (CCDC No. 638866, Cambridge Crystallographic Data Centre).[29] The Ni-NR is also isostructural with the NiCo-NR. The structure of Co-NR is also consistent with the reported Co-BDC MOF.[30] The PXRD data of both Ni-NR and Co-NR are discussed Figure 6.2.

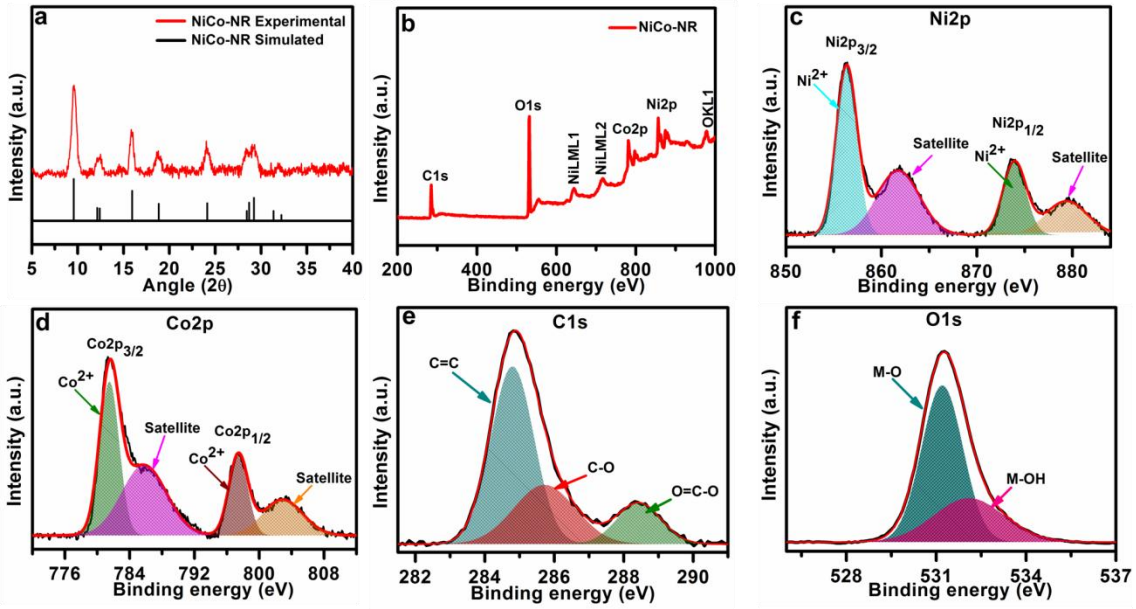

Figure 6.1. *(a) PXRD spectra NiCo-NR with the simulated one (b) wide scan XPS spectra of NiCo-NR (c) high resolution XPS spectra of Ni2p (d) Co2p (e) C1s and (f) O1s*

The chemical valence state and surface composition of NiCo-NR are examined by X-ray photoelectron spectroscopy (XPS) and are displayed in Figure 6.1. The survey spectra (Figure 6.1(b)) confirm the presence of Co, Ni, C and O in NiCo-NR. The narrow scan spectra of Ni 2p (Figure 6.1(c)) show four peaks at 856.3, 861.7, , 873.9 and 879.3 eV attributed to the Ni^{2+} oxidation state and one satellite peak respectively for the Ni $2p_{3/2}$ and Ni $2p_{1/2}$.[31]

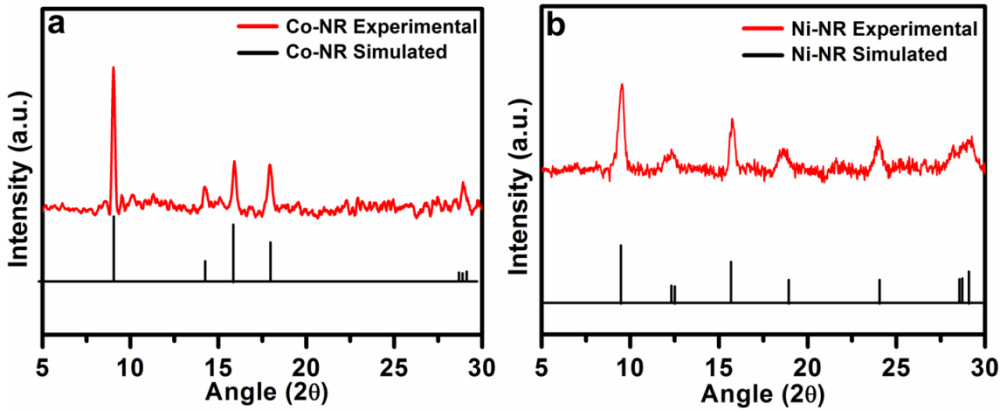

Figure 6.2 *(a) PXRD spectraof Co-NR and (b) Ni-NR*

Similarly four peaks were observed for high-resolution XPS spectra of Co2p respectively at 781.5, 785.7, 797.4 and 802.8 eV attributed to the Co^{2+} oxidation state and one satellite peak respectively for the Co $2p_{3/2}$ and Co $2p_{1/2}$. For C1s (figure 1e) three peaks appeared at 284.8, 285.7, and 288.4 eV corresponding to C=C, C-O and O-C=O bonds respectively which are present in BDC.[32] The high-resolution O1s show two peaks at 531.2 and 532 eV for the metal oxide and metal hydroxide linkage respectively.[33] The XPS data confirms the exact valence states of each elements present in NiCo-NR. We have also performed a detailed XPS analysis of individual Ni-NR, Co-NR and $NiCo(OH)_2$ to investigate the change in the electronic structure (Information is provided in Figure 6.2, 6.4 and 6.5. The elemental percentage of each element present in the NiCo-NR revealed that the elemental ratio of Ni and Co are almost equal. The table containing the percentage value of all the elements in NiCo-NR is provided in Table 6.1. All the parameters obtained from the deconvolution of all the catalyst is provided in Table 6.2, 6.3, 6.4 & 6.5.

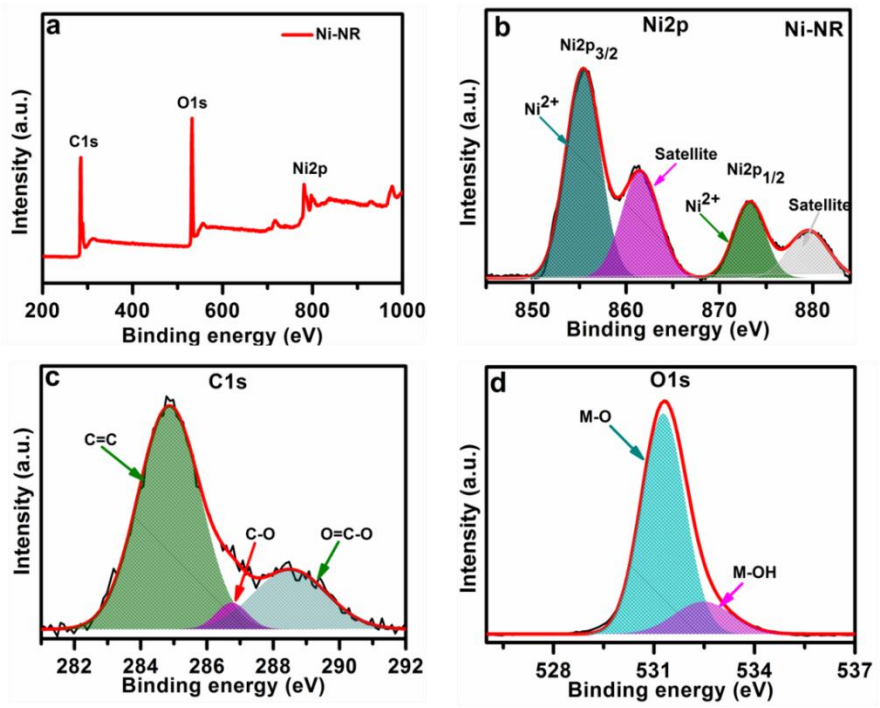

Figure 6.3 *(a) Wide scan XPS spectra of Ni-NR and (b) high resolution XPS spectra of Ni2p (c) C1s and (d) O1s*

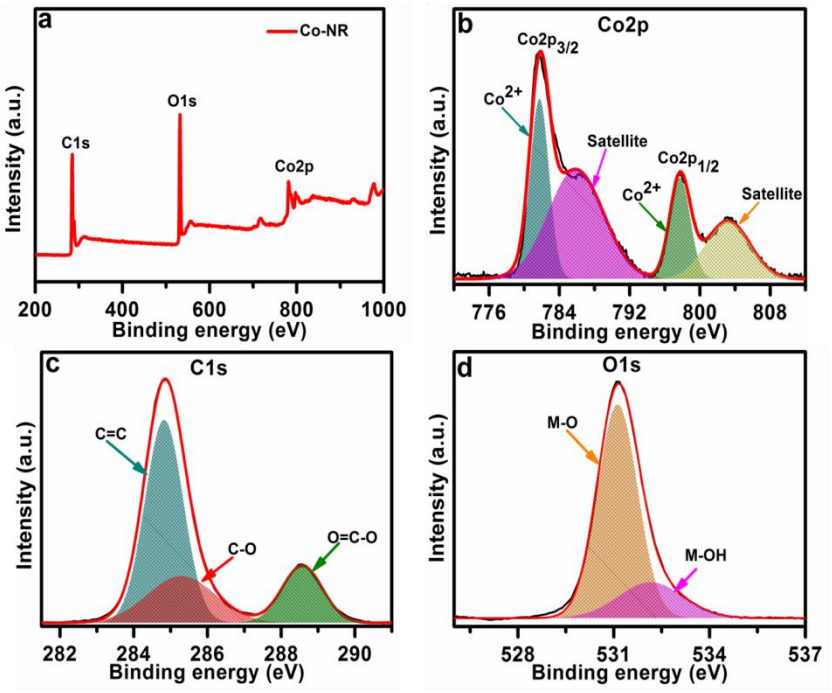

***Figure 6.4**. (a) Wide scan XPS spectra of Co-NR and (b) high resolution XPS spectra of Co2p (c) C1s and (d) O1s*

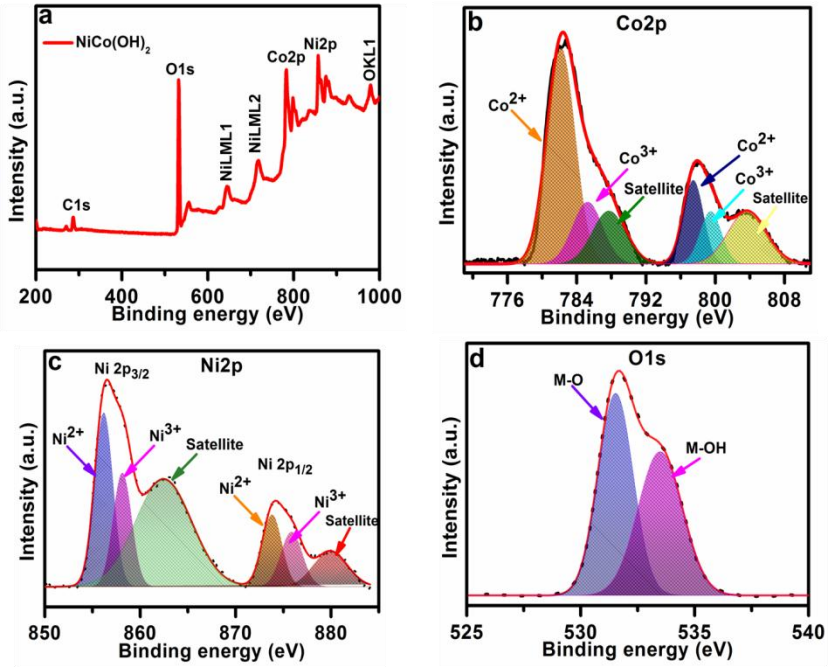

***Figure 6.5** (a) Wide scan XPS spectra of $NiCo(OH)_2$ and (b) high resolution XPS spectra of Co2p (c) Ni2p and (d) O1s*

Element	%
Co	3.1
Ni	2.9
C	52
O	33

Table 6.1. *elemental percentage obtained from XPS analysis of NiCo-NR*

Element	Peak	BE (eV)	FWHM	Area (%)
Ni 2p	$2p_{3/2}$ (Ni^{+2}) $2p_{3/2}$ (Sat.) $2p_{1/2}$ (Ni^{+2}) $2p_{1/2}$ (Sat.)	856.3 861.7 873.9 879.3	2.57 5.23 2.85 5.19	37.43 29.35 18.06 15.13
Co 2p	$2p_{3/2}$ (Co^{+2}) $2p_{3/2}$ (Sat.) $2p_{1/2}$ (Co^{+2}) $2p_{1/2}$ (Sat.)	781.4 785.7 797.4 802.8	2.82 6.54 2.75 5.86	32.83 34.78 16.50 15.88
C 1s	C=C C-O O-C=O	284.8 285.7 288.4	1.45 2.09 1.50	58.17 27.91 13.91
O 1s	Metal oxide Metal hydroxide	531.2 532.0	1.62 2.76	67.65 32.34

Table 6.2 *Peak parameters obtained from the XPS analysis of NiCo-NR*

Element	Peak	BE (eV)	FWHM	Area (%)
Ni 2p	$2p_{3/2}$ (Ni^{+2}) $2p_{3/2}$ (Sat.) $2p_{1/2}$ (Ni^{+2}) $2p_{1/2}$ (Sat.)	855.6 861.4 873.2 879.5	4.35 4.73 3.94 5.01	46.66 25.92 15.35 12.04
C 1s	C=C C-O O-C=O	284.8 286.7 288.5	2.21 1.11 2.59	72.69 4.38 22.9
O 1s	Metal oxide Absorbed water	531.2 532.4	1.53 2.03	83.68 16.31

Table 6.3 *Peak parameters obtained from the XPS analysis of Ni-NR*

Element	Peak	BE (eV)	FWHM	Area (%)
Co 2p	$2p_{3/2}$ (Co^{+2}) $2p_{3/2}$ (Sat.) $2p_{1/2}$ (Co^{+2}) $2p_{1/2}$ (Sat.)	781.7 785.8 797.7 803.1	2.52 7.40 2.73 5.92	24.07 43.01 14.67 18.23
C 1s	C=C C-O O-C=O	284.8 285.2 288.5	1.22 2.15 1.28	58.64 23.93 17.42
O 1s	Metal oxide Absorbed water	531.1 532.1	1.48 2.36	78.83 21.16

Table 6.4 *Peak parameters obtained from the XPS analysis of Co-NR*

Element	Peak	BE (eV)	FWHM	Area (%)
Ni 2p	$2p_{3/2}$ (Ni^{+2})	856.1	2.23	21.23
	$2p_{3/2}$ (Ni^{+3})	858.7	2.37	15.72
	$2p_{3/2}$ (Sat.)	862.4	6.81	40.81
	$2p_{1/2}$ (Ni^{+2})	873.7	2.28	8.25
	$2p_{1/2}$ (Ni^{+3})	875.7	2.75	8.67
	$2p_{1/2}$ (Sat.)	879.7	3.57	5.29
Co 2p	$2p_{3/2}$ (Co^{+2})	782.1	3.85	41.92
	$2p_{3/2}$ (Co^{+3})	785.2	4.12	12.89
	$2p_{3/2}$ (Sat.)	787.7	4.53	12.14
	$2p_{1/2}$ (Co^{+2})	797.4	2.75	11.64
	$2p_{1/2}$ (Co^{+3})	799.4	2.91	6.70
	$2p_{1/2}$ (Sat.)	803.6	5.15	14.6
O 1s	Metal oxide	531.1	1.25	5.75
	Metal hydroxide	531.6	1.89	51.13
	Absorbed water	533.5	2.19	43.11

Table 6.5 Peak parameters obtained from the XPS analysis of $NiCo(OH)_2$

The morphological study of the catalyst was performed by using scanning electron microscopy (SEM). The SEM images of the NiCo-NR catalyst with different magnifications are depicted in figure 6.6 (a, b & c), confirming the nanoribbons-like morphology. The micrographs shared in Figure 6.6(d & e) display the transmission electron microscopy (TEM) analysis of NiCo-NR at different resolutions. The images ratify the formation of NiCo-NR and also show that nanoribbons are very thin and uniform throughout the length. The TEM images of individual Co-NR and Ni-NR catalysts are provided in Figure 6.7 & 6.8. The percentage of exposed active surfaces is determined by the thickness of NiCo-NR. The atomic force microscopy (AFM) shows the emergence of the 2D nanoribbons in NiCo-NR (Figure 6.6f). The thickness of the nanoribbons is varying between 2.6 to 3.6 nm possibly because of the minute overlapping of the nanostructures. The thickness of NiCo(OH)2 nanosheets, Ni-NR and Co-NR were

studied and the corresponding images are provided in Figure 6.9,6.10 &6.11. The elemental mapping shows the even allocation of all the elements over the surface of NiCo-NR (Figure 2 g-j). The elemental mapping for carbon is provided in Figure 6.12.

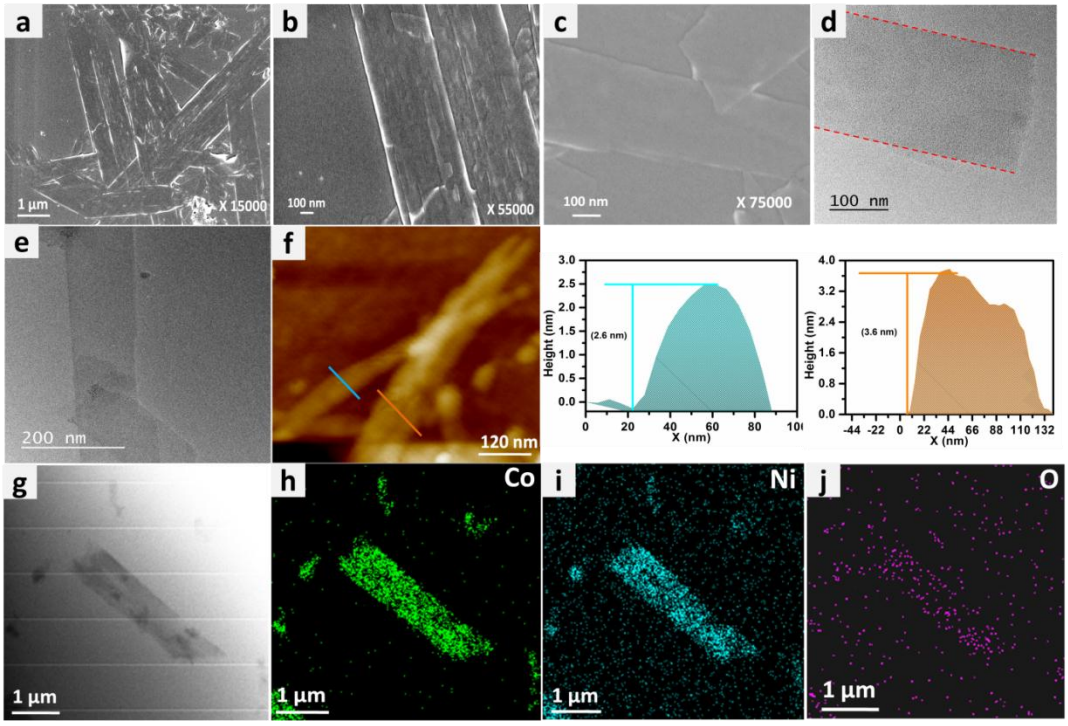

Figure 6.6. *FESEM images of NiCo-NR with different magnifications (a) 1µm (b) 100 nm (c) 100nm. TEM images of NiCo-NR with different magnification (d) 100 nm (e) 200 nm (f) AFM images with the corresponding height profile of NiCo-NR (g) image used for the elemental mapping with the corresponding elements (h) Co (i) Ni and (j) O with the uniform distribution over the catalyst surface.*

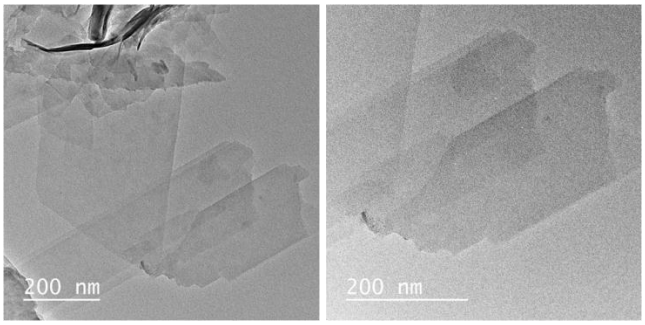

Figure 6.7*. TEM images of Co-NR at different magnification*

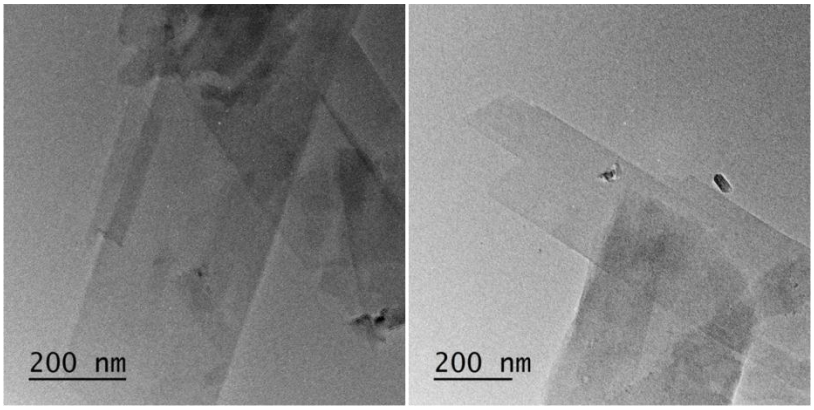

Figure 6.8 TEM images of Ni-NR at different magnification

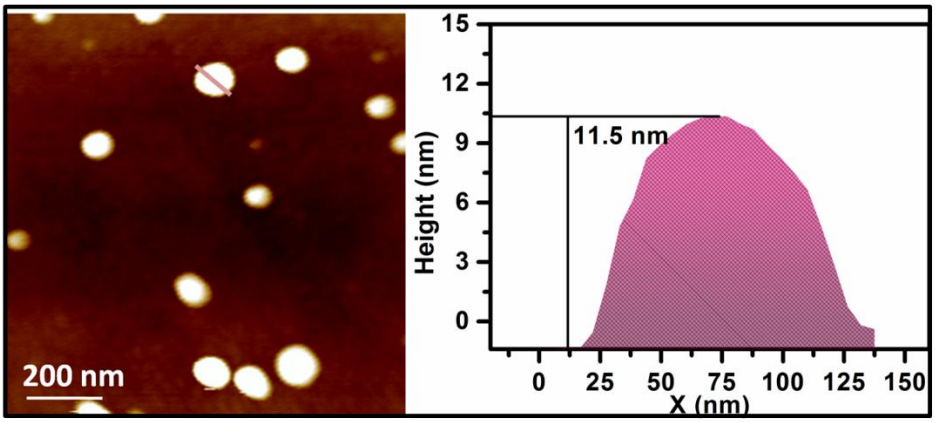

Figure 6.9 AFM image of $NiCo(OH)_2$ with the corresponding height profile

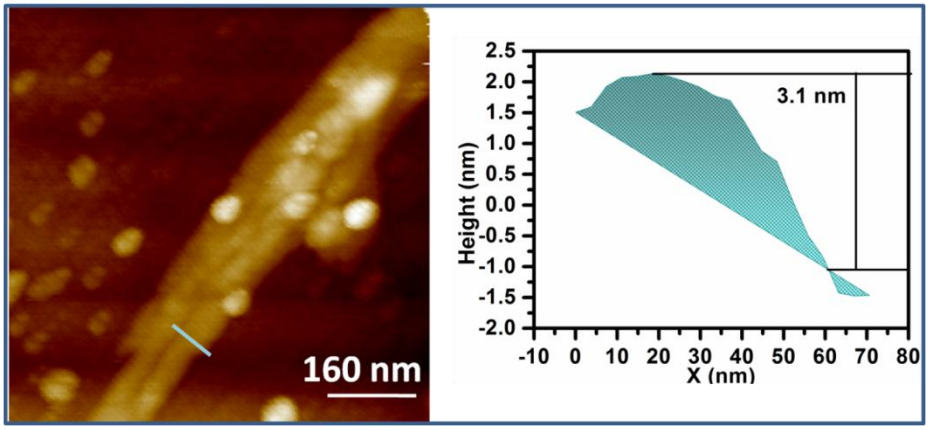

Figure 6.10. *AFM image of Ni-NR with the corresponding height profile*

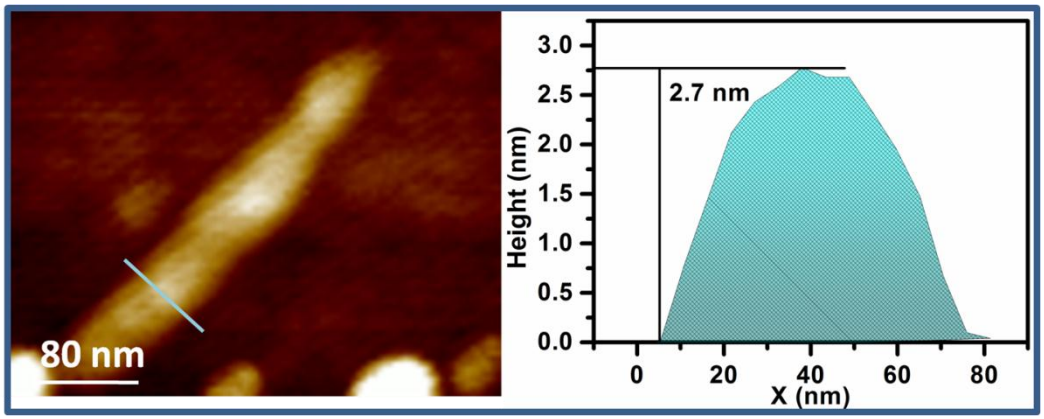

Figure 6.11. *AFM image of Co-NR with the corresponding height profile*

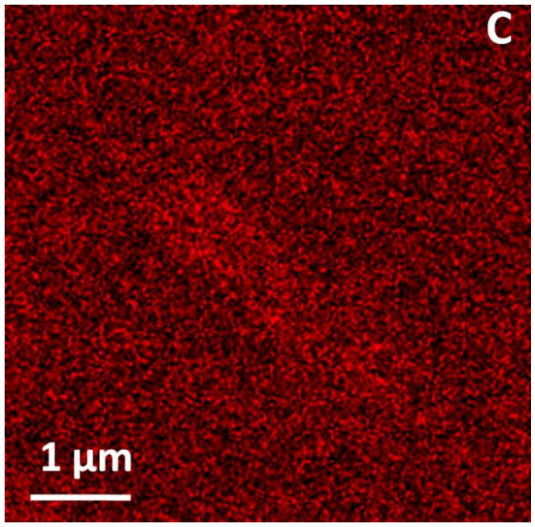

Figure 6.12. *elemental mapping for C present in NiCo-NR*

The OER performance of the as-prepared catalysts was subsequently studied in an aqueous electrolyte using a three electrode arrangement. All measurements were made at 25°C in 1M KOH. The polarisation curves of NiCo-NR, Ni-NR, Co-NR, and commercial RuO_2 catalysts towards the OER performances in alkaline conditions are shown in Figure 6.13(a). The overpotential of 244, 290, 308 and 284 mV was obtained respectively for NiCo-NR, Ni-NR, Co-NR and RuO_2 at a current density of 10 mA cm^{-2} .The NiCo-NR catalyst shows OER activity way better than the Co-NR, RuO_2 and bare graphitic sheet (GS).

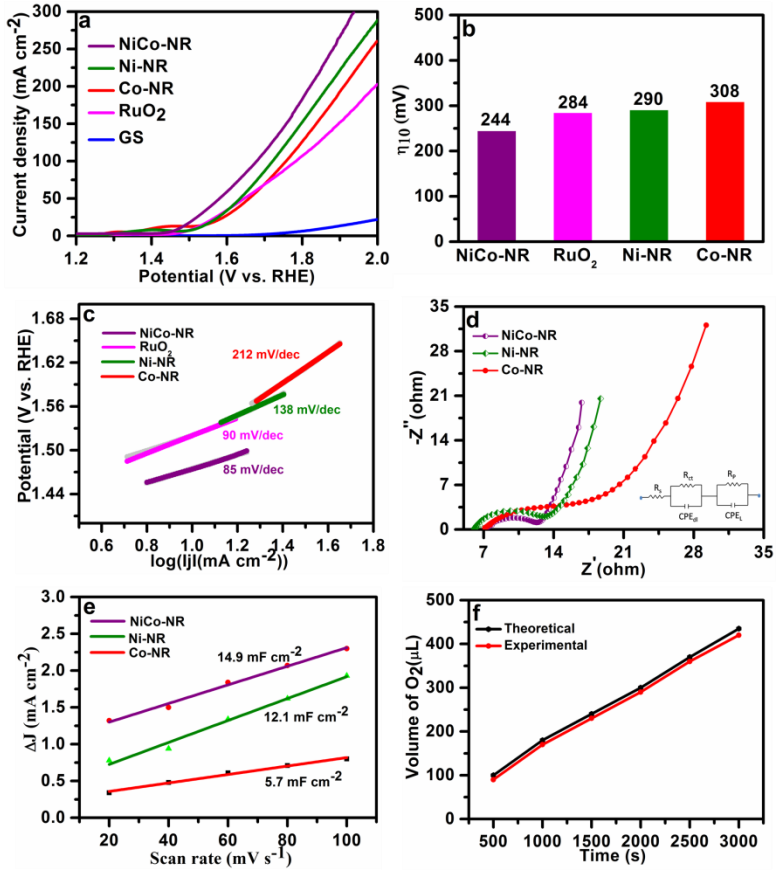

Figure 6.13. *(a) Polarization curve of all the supporting catalyst (b) overpotential of all the catalyst (c) Tafel slope of the corresponding catalysts obtained from the linear fitting of Tafel equation (d) The Nyquist plot for the calculation of charge transfer resistance (e) double-layer capacitance of all catalyst obtained from the CV curve in non-faradic region (f) faradaic efficiency of catalyst calculated by the water displacement method.*

The NiCo-NR catalyst outperforms RuO_2 at 10 mA cm^{-2} and at high current densities, demonstrating a high performance at all current densities. A comparison of the overpotential among all the catalysts at a current density of 10 mA cm^{-2} is shown in Figure 6.13(b). To investigate more about the reaction's kinetics, we derived the Tafel slope value by calculating the Tafel equation[34] as shown in figure 6.13(c). The obtained Tafel slope values are 85, 90, 138 and 212 mV/dec for NiCo-NR, RuO_2, Ni-NR and Co-NR respectively. The least Tafel slope value of NiCo-NR catalyst suggests an enhanced rate of reaction compared to the commercially available RuO_2. Figure 6.13d shows Nyquist plot acquired at an applied overpotential of 200 mV. In addition to the solution resistance, the fitted circuit contains two time-constant components, 'R_{ct}-CPE_{dL}' and 'Rp-

CPE_L'. A constant phase element (CPE) is an equivalent circuit constituent that simulates the behaviour of a double-layer non-ideal capacitor. The charge transfer resistance (Rct, 6.75Ω at 200 mV) was measured using an equivalent circuit, revealing strong interfacial contacts promoting fast electron passage through the electrode/electrolyte interface. 'Rp' can be correlated to the resistance due to the surface porosity of the catalyst. The Rct value for Ni-NR and Co-NR are slightly higher, indicating a slower charge transfer and poor OER activity than that of NiCo-NR. The value of Rs and Rct of all the catalysts is tabulated in ESI S7.2 Table S7. To determine the electrochemically active surface area (ECSA), double-layer capacitance (C_{dl}) of all the catalyst are determined by taking a cyclic voltammetry curve in a non-faradic region. The obtained Cdl value (Figure 6.13(e)) of NiCo-NR, Ni-NR and CoNR is 14.9, 12.1 and 5.7 mF cm^{-2} respectively. The higher value of C_{dl} indicates the presence of a higher number of active sites on the catalyst surface. The cyclic voltammetry curve used for the calculation of C_{dl} is given in Figure 6.14. A durability test was performed by means of chronoamperometry at an overpotential of 240 mV for 10 hours (Figure 6.15). Post-stability investigations such as TEM and XPS reveal that the metallic nodes present in the metal-organic frameworks are converted into the metal oxyhydroxide after the long- term durability test. The XPS data is provided in Figure 6.16 & 6.17. The post-stability TEM images of the catalyst (Figure 6.18)show that the morphology of the ribbons remains as it after the oxyhydroxide formation. The faradic efficiency (FE) was estimated using the water-gas displacement technique (figure 6.13(f)), in which the estimated faradic efficiency is the percentage of the overall ratio of the quantity of O_2 released to the quantity of O_2-release predicted theoretically. The FE value for NiCo-NR is 96.5%. The geometrical area normalised OER activity of NiCo-NR is also compared to the electrochemically active surface area (ECSA) normalised OER activity, and the results are available in the Figure 6.19.

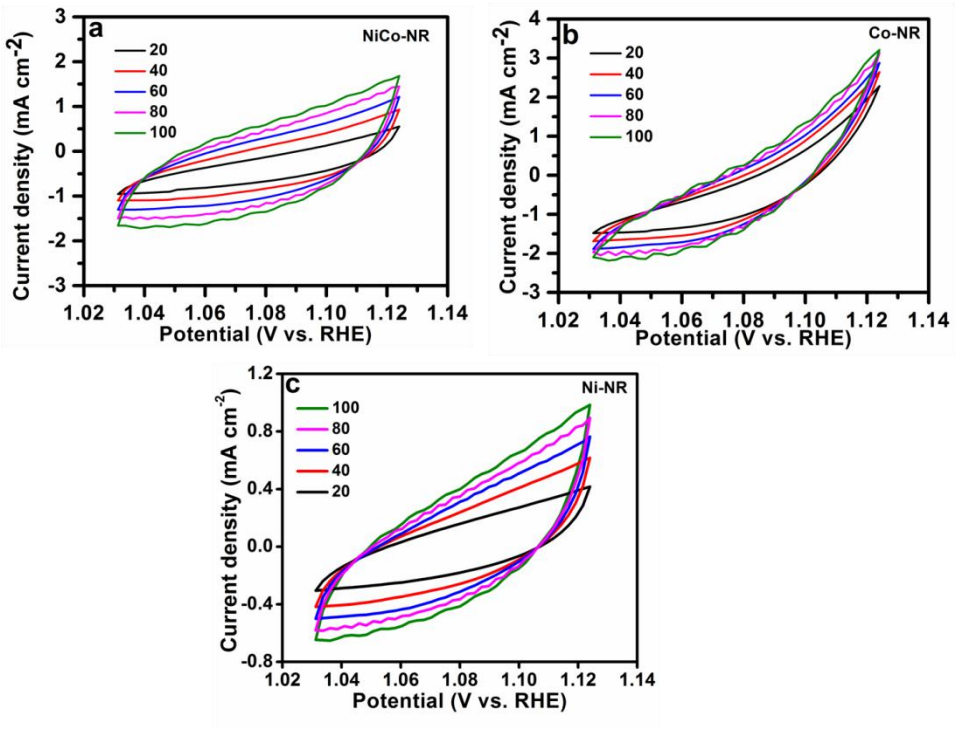

Figure 6.14. *Cyclic voltammetry curve of (a) NiCo-NR (b) Co-NR and (c) Ni-NR in non-faradic region*

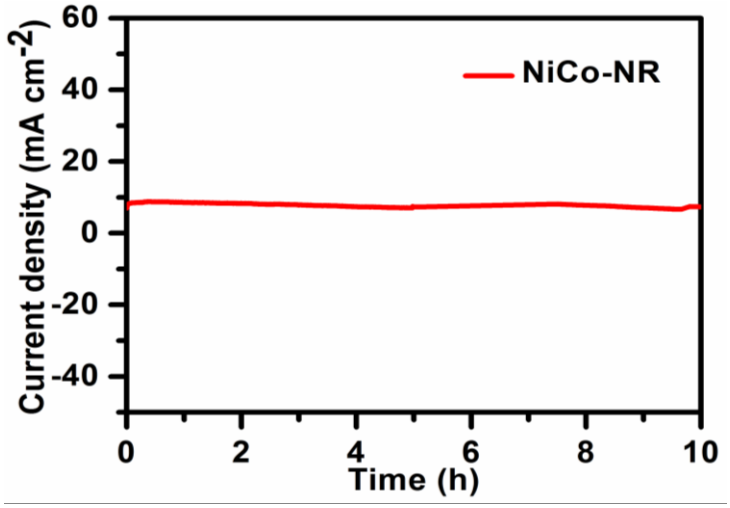

Figure 6.15.*Chronoamperometric study of the NiCo-NR at an overpotential of 240 mV. The catalyst is stable up to 10 hr.*

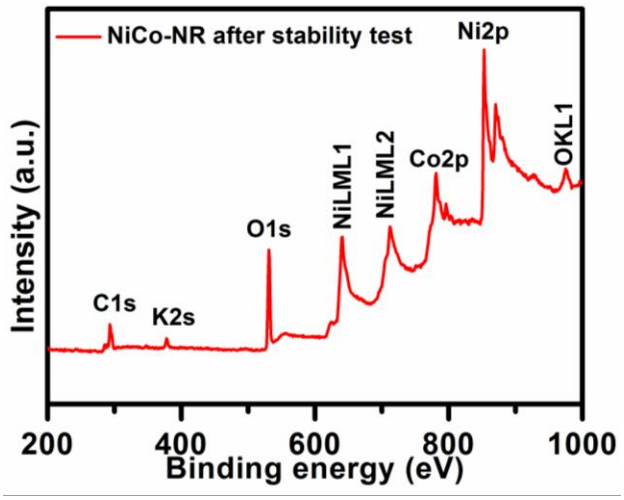

Figure 6.16. *wide scan spectra of NiCo-NR after durability test*

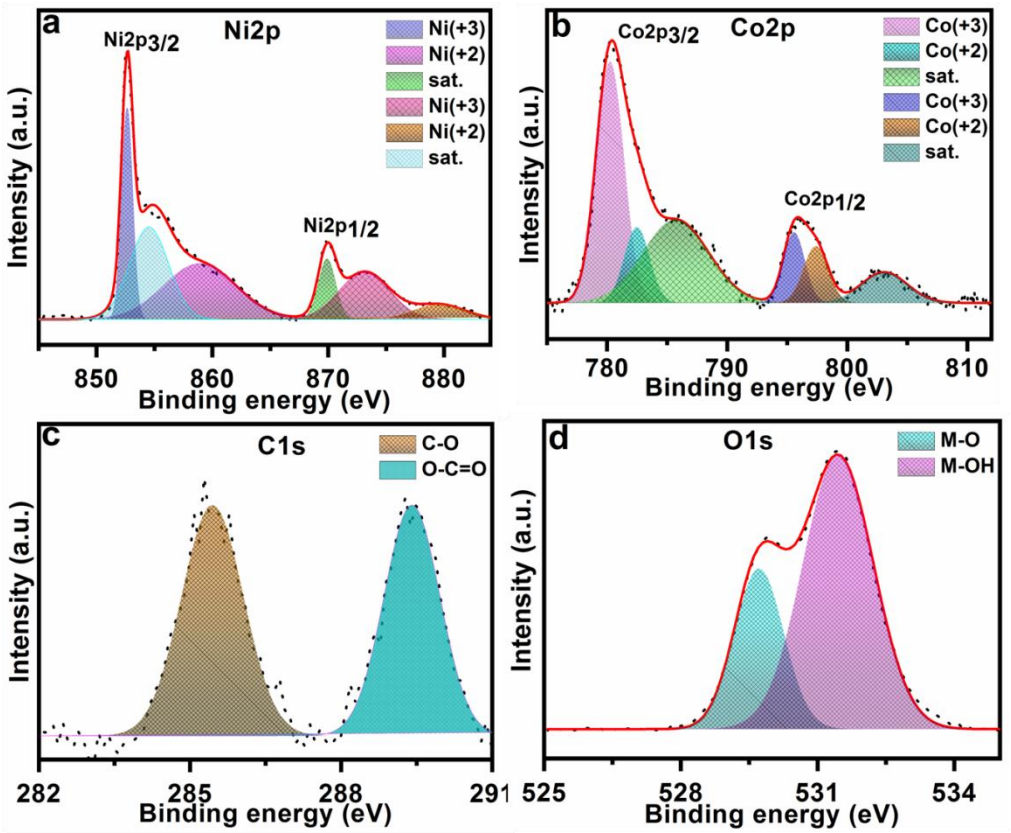

Figure 6.17. *XPS narrow scan spectra of (a) Ni2p (b) Co2p (c) C1s and (d) O1s present in NiCo-NR after durability test*

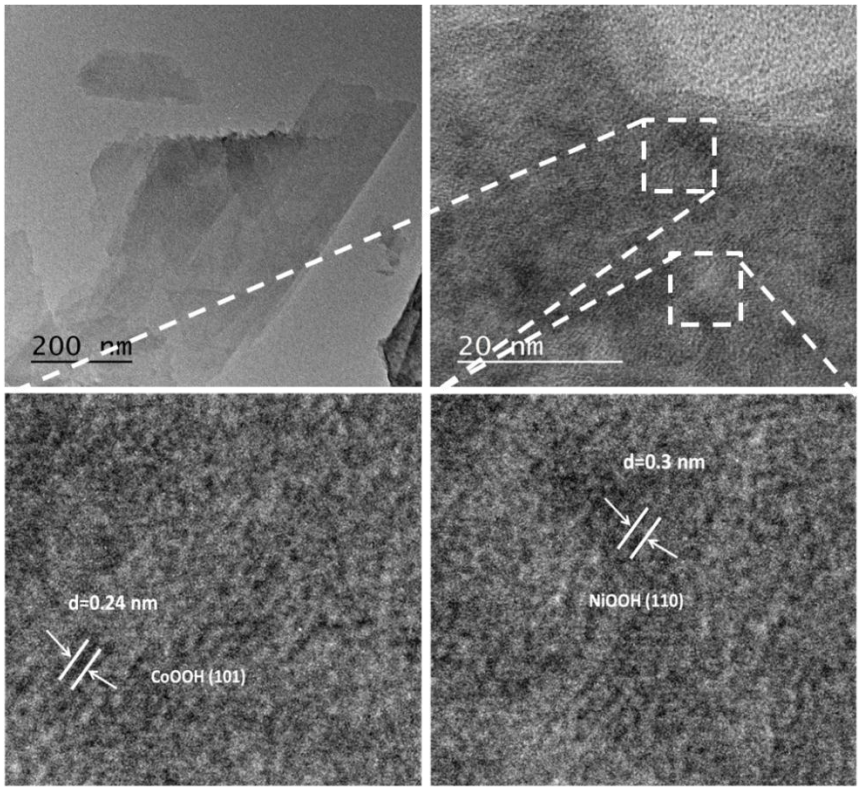

Figure 6.18. *TEM and HRTEM images of NiCo-NR after stability showing the formation of CoOOH and NiOOH species on the metal nodes.*

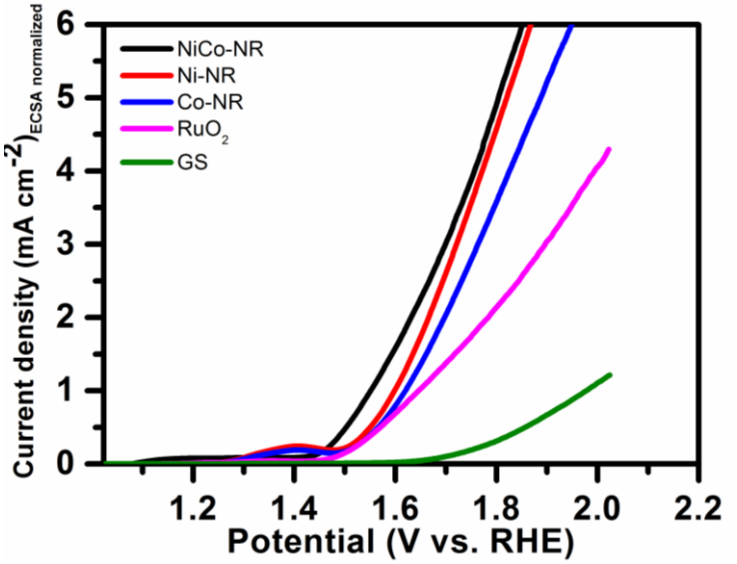

Figure 6.19. *ECSA normalized OER activity of NiCo-NR and other supporting catalyst*

To understand, the disparity in the OER activity of NiCo-NR with respect to Ni-NR and Co-NR, we dug deeper and focussed our study on the uniformly distributed alternative Ni and Co metal centres, which are coordinatively unsaturated. X-ray absorption spectroscopy (XAS) and high-resolution XPS of NiCoNR, Ni-NR, and Co-NR were carried out to investigate the impact of coupling between the metal sites in NiCo-NR. The synchrotron radiation-based X-ray absorption near-edge structure (XANES) spectra of NiCo-NR, Ni-NR, NiO and Ni-foil are given in Figure 6.20(a). The absorption edge line position of NiCo-NR is located at higher energy (Figure 6.20(b)) when compared to Ni-NR confirming the electron transfer from Ni to Co. The Fourier transform (FT) k^3-weighted EXAFS spectrum for Ni-K edge of the NiCo-NR (Figure 6.20(c)) catalytic shows that the most prominent peak is at 1.6 and 2.7 Å corresponds to the Ni-O coordination. Similarly for Co-K edge spectra (Figure 6.20(d)) the absorption edge position of NiCo-NR is located at lower energy (Figure 6.20(e)) than that of Co-NR confirming that Co is gaining electrons form Ni. The Fourier transform k^3 - weighted extended EXAFS spectrum for Co-K edge of the NiCo-NR (Figure 6.20(f)) catalytic shows that the most prominent peak is at 1.51 Å corresponds to the Co-O coordination. The parameters used for fitting along with the fitted figures of Ni-Kedge and Co-Kedge is given in Figure 6.21 & Table 6.22. The same background line setting was used for all the catalysts to rule out the probable influence of the background line setting in order to achieve reliable XPS findings. When compared, the peak of Ni 2p in NiCo-NR emerged at higher binding energy than in Ni-NR (Figure 6.20(g)). The peak of Co2p in NiCo-NR, on the other hand, emerged at a lower binding energy (Figure 6.20(h)) than the corresponding Co-NR MOF. This indicates that additional electrons are move from Ni sites to Co sites via the Ni-O-Co bonding, resulting in a considerable increase in Ni's valence state. Additionally, their electronic configurations might shed some light on this charge transfer phenomenon. In the high spin state, the electronic configuration of Co^{2+} is $3d^7$, so the Π-symmetry t_{2g}-orbital is unsymmetrically filled with the unpaired electron. These unpaired electrons can interact with the bridging ligands (O^{2-}) through π-donation (Figure 6.20(i)). Similarly, the high spin state electronic configuration of Ni^{2+} is $3d^8$, where the π-symmetry t_{2g}-orbital is symmetrically filled with zero unpaired electrons. In this case, the electron-electron repulsion will take place between the fully filled (t_{2g})

orbital and the orbital of bridging ligands (O^{2-}). However, in the case of NiCo-NR, the coupling effect arises due to the Ni-O-Co linkage. The π-donation between Co^{2+} and O^{2-} is higher due to the repulsion between Ni^{2+} and O^{2-}. This situation actually drives the electron transfer from Ni^{2+} to Co^{2+} . Integrating the XPS results, it is inferred that the presence of Ni and Co in the 2D MOF stimulated the transfer of electrons from Ni to Co metal centers, leading to an enhancement in the OER performance.

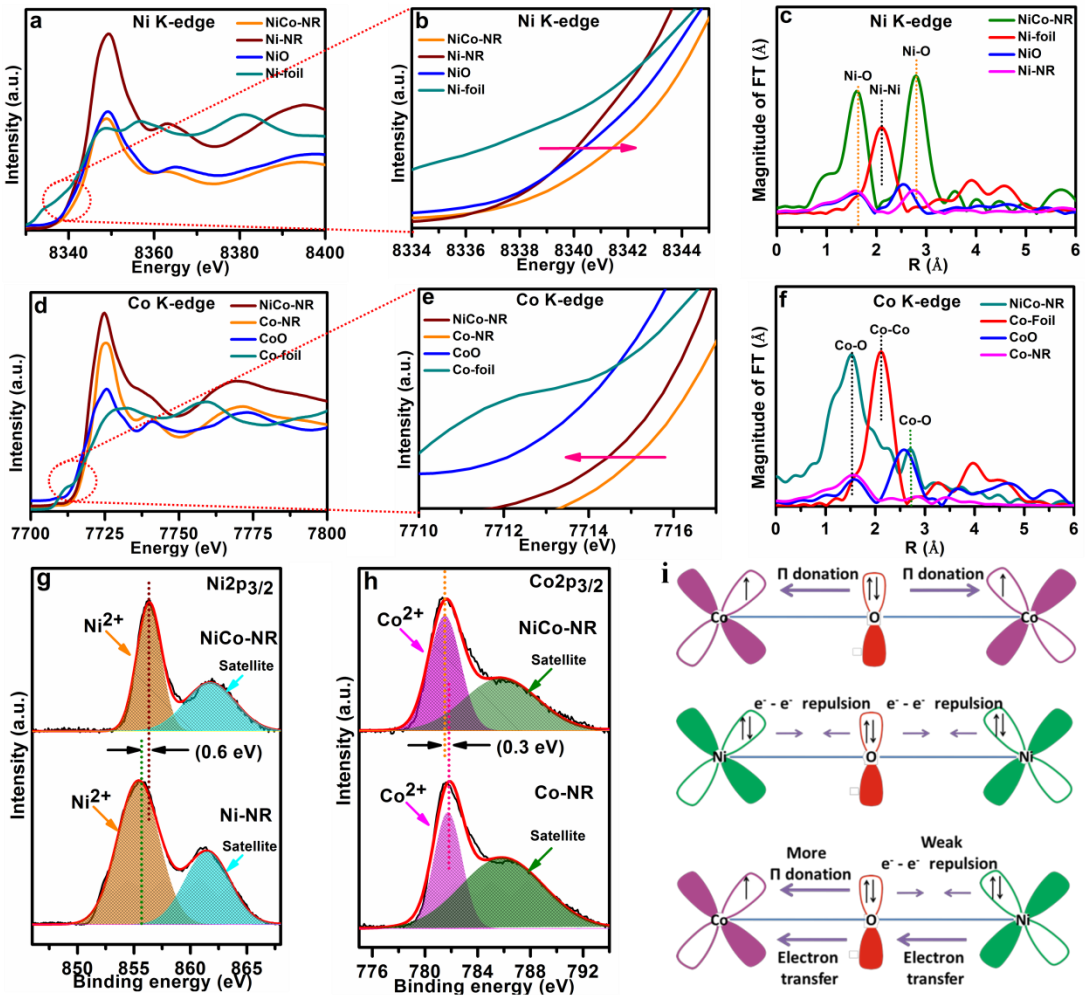

Figure 6.20. *Structural characterizations of NiCo-NR, Co-NR and Ni-NR using XAS spectrocopy. The normalized XANES spectra and the Fourier transform of EXAFS spectra at the Ni K-edge (a-c) and Co K-edge (d-f). shift in the binding energy obtained from the XPS analysis of NiCo-NR and Ni-NR (g) Ni2p3/2 (h) Co2p3/2 and (i) the scheme showing the electron transfer from Ni to Co via O.*

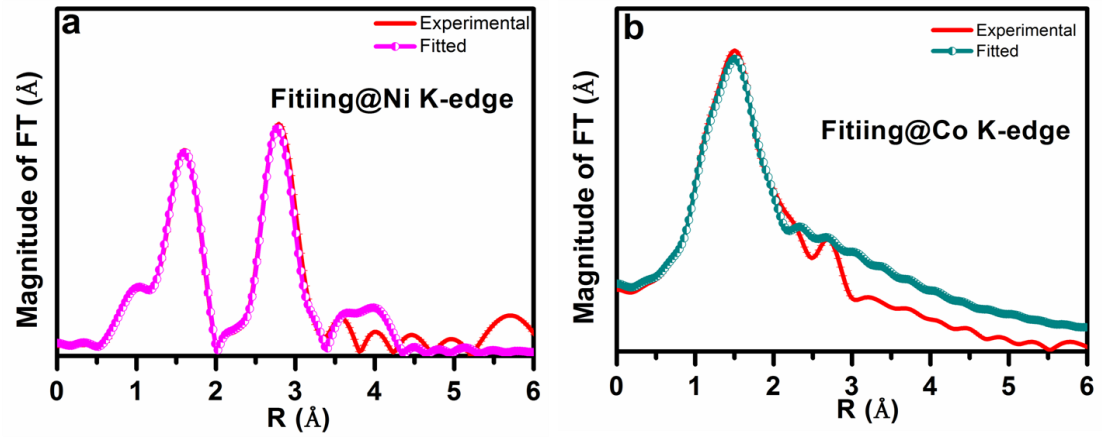

Figure 6.21. *Fitting of Ni-Kedge and Co-K edge using artemis*

Sample	Path	R(Å)	N	$\sigma^2(10^{-3}Å^2)$
NiCo-NR	Co-O	1.98±0.2	6	0.009
NiCo-NR	Ni-O	1.97±0.3	6	0.0089

Figure 6.22. *Fitting parameters of Ni-Kedge and Co-Kedge EXAFS using NiCo-NR*

6.4 Conclusion

In summary, we have shown a 2D bimetallic metal-organic framework nanoribbons (NiCo-NR), which performs OER excellently well with an overpotential of 244 mV at a current density of 10 mA cm^{-2} , and exhibits a Tafel slope value of 85 mV/dec. The reason for significantly low overpotential is the process of electron transfer from the metal centers via ligands occurring in the nanoribbon MOF. The inter-atomic electron transfer from the eg orbital of Ni to the eg orbital of Co through an oxygen atom, results in the attainment of a partially positive charge on the Ni atom, making it more active for the adsorption of the intermediate involved in the OER. The charge transfer process is

explicitly explained using X-ray absorption spectroscopy (XAS) including synchrotron radiation-based X-ray absorption near-edge structure (XANES), extended Xray absorption finestructure (EXAFS) and X-ray photoelectron spectroscopy.

Gaur, Ashish, , Vikas Pundir, Rajdeep Kaur, and Vivek Bagchi. " *Curtailing the excess e_g-orbital filling of Ni-atom by enhanced inter-atomic charge transfer within bimetallic 2-D MOF nanoribbons for electrocatalytic oxygen evolution reaction*" *Under revision in Journal of Materils Chemistry A.*

References

1. G. Ceballos, P. R. Ehrlich and R. Dirzo, *Proceedings of the National Academy of Sciences*, 2017, **114**, E6089-E6096.

2. M. A. Destek and A. Aslan, *Renewable Energy*, 2020, **151**, 1298-1306.

3. T. Li, T. Lu, X. Li, L. Xu, Y. Zhang, Z. Tian, J. Yang, H. Pang, Y. Tang and J. Xue, *ACS Nano*, 2021, **15**, 20032-20041.

4. M. G. Lee, C. W. Moon, H. Park, W. Sohn, S. B. Kang, S. Lee, K. J. Choi and H. W. Jang, *Small*, 2017, **13**, 1701644.

5. B. Zhang, X. Zheng, O. Voznyy, R. Comin, M. Bajdich, M. García-Melchor, L. Han, J. Xu, M. Liu, L. Zheng, F. P. García de Arquer, T. Dinh Cao, F. Fan, M. Yuan, E. Yassitepe, N. Chen, T. Regier, P. Liu, Y. Li, P. De Luna, A. Janmohamed, L. Xin Huolin, H. Yang, A. Vojvodic and H. Sargent Edward, *Science*, 2016, **352**, 333-337.

6. P. Zhai, Y. Zhang, Y. Wu, J. Gao, B. Zhang, S. Cao, Y. Zhang, Z. Li, L. Sun and J. Hou, *Nature Communications*, 2020, **11**, 5462.

7. T. Li, J. Yin, D. Sun, M. Zhang, H. Pang, L. Xu, Y. Zhang, J. Yang, Y. Tang and J. Xue, *Small*, 2022, **18**, 2106592.

8. M. Zhao, Y. Huang, Y. Peng, Z. Huang, Q. Ma and H. Zhang, *Chemical Society Reviews*, 2018, **47**, 6267-6295.

9. Z. Zhang, Y. Zhu, H. Asakura, B. Zhang, J. Zhang, M. Zhou, Y. Han, T. Tanaka, A. Wang, T. Zhang and N. Yan, *Nature Communications*, 2017, **8**, 16100.

10. S. Zhao, C. Tan, C.-T. He, P. An, F. Xie, S. Jiang, Y. Zhu, K.-H. Wu, B. Zhang, H. Li, J. Zhang, Y. Chen, S. Liu, J. Dong and Z. Tang, *Nature Energy*, 2020, **5**, 881-890.

11. L. Zhuang, L. Ge, H. Liu, Z. Jiang, Y. Jia, Z. Li, D. Yang, R. K. Hocking, M. Li, L. Zhang, X. Wang, X. Yao and Z. Zhu, *Angewandte Chemie International Edition*, 2019, **58**, 13565-13572.

12. N. Liu, Q. Zhang and J. Guan, *Chemical Communications*, 2021, **57**, 5016-5019.

13. J. Liang, X. Gao, B. Guo, Y. Ding, J. Yan, Z. Guo, E. C. M. Tse and J. Liu, *Angewandte Chemie International Edition*, 2021, **60**, 12770-12774.

14. S. Zhao, Y. Wang, J. Dong, C.-T. He, H. Yin, P. An, K. Zhao, X. Zhang, C. Gao, L. Zhang, J. Lv, J. Wang, J. Zhang, A. M. Khattak, N. A. Khan, Z. Wei, J. Zhang, S. Liu, H. Zhao and Z. Tang, *Nature Energy*, 2016, **1**, 16184.

15. C. Freire, D. M. Fernandes, M. Nunes and V. K. Abdelkader, *ChemCatChem*, 2018, **10**, 1703-1730.

16. V. K. Abdelkader-Fernández, D. M. Fernandes, S. S. Balula, L. Cunha-Silva and C. Freire, *Journal of Materials Chemistry A*, 2020, **8**, 13509-13521.

17. B. Standley, W. Bao, H. Zhang, J. Bruck, C. N. Lau and M. Bockrath, *Nano Letters*, 2008, **8**, 3345-3349.

18. X. Zhang and Y. Xie, *Chemical Society Reviews*, 2013, **42**, 8187-8199.

19. Y. Sun, S. Gao and Y. Xie, *Chemical Society Reviews*, 2014, **43**, 530-546.

20. J.-Q. Shen, P.-Q. Liao, D.-D. Zhou, C.-T. He, J.-X. Wu, W.-X. Zhang, J.-P. Zhang and X.-M. Chen, *Journal of the American Chemical Society*, 2017, **139**, 1778-1781.

21. C. S. Letko, J. A. Panetier, M. Head-Gordon and T. D. Tilley, *Journal of the American Chemical Society*, 2014, **136**, 9364-9376.

22. Y. Li, S. Wang, Y. Hu, X. Zhou, M. Zhang, X. Jia, Y. Yang, B.-L. Lin and G. Chen, *Journal of Materials Chemistry A*, 2022, **10**, 5273-5279.

23. Y. Xu, B. Li, S. Zheng, P. Wu, J. Zhan, H. Xue, Q. Xu and H. Pang, *Journal of Materials Chemistry A*, 2018, **6**, 22070-22076.

24. H. Liu, X. Ma, Y. Rao, Y. Liu, J. Liu, L. Wang and M. Wu, *ACS Applied Materials & Interfaces*, 2018, **10**, 10890-10897.

25. X. Li, M. Fan, D. Wei, M. Li and Y. Wang, *Electrochimica Acta*, 2020, **354**, 136682.

26. W.-D. Zhang, Q.-T. Hu, L.-L. Wang, J. Gao, H.-Y. Zhu, X. Yan and Z.-G. Gu, *Applied Catalysis B: Environmental*, 2021, **286**, 119906.

27. P. He, Y. Xie, Y. Dou, J. Zhou, A. Zhou, X. Wei and J.-R. Li, *ACS Applied Materials & Interfaces*, 2019, **11**, 41595-41601.

28. K. Fan, H. Chen, Y. Ji, H. Huang, P. M. Claesson, Q. Daniel, B. Philippe, H. Rensmo, F. Li, Y. Luo and L. Sun, *Nature Communications*, 2016, **7**, 11981.

29. A. Mesbah, P. Rabu, R. Sibille, S. Lebègue, T. Mazet, B. Malaman and M. François, *Inorganic Chemistry*, 2014, **53**, 872-881.

30. D. Y. Lee, I. Lim, C. Y. Shin, S. A. Patil, W. Lee, N. K. Shrestha, J. K. Lee and S.-H. Han, *Journal of Materials Chemistry A*, 2015, **3**, 22669-22676.

31. Q. Qian, Y. Li, Y. Liu, L. Yu and G. Zhang, *Advanced Materials*, 2019, **31**, 1901139.

32. Z. Chen, L. Cai, X. Yang, C. Kronawitter, L. Guo, S. Shen and B. E. Koel, *ACS Catalysis*, 2018, **8**, 1238-1247.

33. X. Zhang, N. Qu, S. Yang, Q. Fan, D. Lei, A. Liu and X. Chen, *Journal of Colloid and Interface Science*, 2020, **575**, 347-355.

34. J. Zhang, H. B. Tao, M. Kuang, H. B. Yang, W. Cai, Q. Yan, Q. Mao and B. Liu, *ACS Catalysis*, 2020, **10**, 8597-8610.

Chapter 7

Conclusion

The many types of material that were synthesised for the purpose of electrocatalytic oxygen and hydrogen generation using electrocatalysts produced from earth-abundant transition metal based heterostructures are the subject of the thesis. The first section of the thesis explains how energy is one of the most essential requirements of the globe as well as a fundamental social necessity that is necessary in order to drive economic expansion and civilise the development of human beings. It is common knowledge that the services related to energy have a direct influence on our social and physical success in terms of health care, educational opportunities, access to clean water, and effective communication. In the current day and age, the most significant energy-using industries, such as electricity, agriculture, and the contemporary culinary technology and transportation systems, etc., are all dependent on energy to function. When it comes to the amount of energy that is consumed, there is a significant discrepancy between wealthy countries and developing ones. This is an unfortunate reality. In the first portion of the thesis, a brief discussion is had regarding how it impacts, as well as how its impact could be reduced. In addition, the thesis investigates additional elements, such as how the distribution of energy, generation of energy, and supply of energy to the final users influence people's means of subsistence in the context of local, regional, and worldwide human development prospects. It discusses the ways in which each one of the primary causes can have an effect on the evolution of humankind as a whole. Once more, if we speak about the present day, the entire world is eager to look for an energy source that is more effective, favourable to the environment, and long-lasting. There are many various energy sources accessible, but we are primarily reliant on fossil fuels, which bring with them the concomitant problem of climate change brought on by the release of greenhouse gases. Several various energy sources are available. The chapter 2 of this thesis explain the formation of heterointerface between Metal organic framework derived N-doped carbon wrapped cobalt nanospheres. The catalyst Co@NC@MoS_2 have a low overpotential of 297 mV vs RHE at 10 mA cm^{-2} current density. The catalysthas long term stability with a Tafel slope value of 70 mV dec^{-1}. A chronoamperometric study for more than 10 hours does not show any significant change in the current density of the catalyst. Moving forward in chapter 3 we discussed the synergistic effect arrises from the formation of heterointerfaces between transition metal-

oxide based compounds. This chapter was devided into three parts with different heterostructures namely CuO-NiO, Co_3O_4-NiO and $NiWO_4$-NiO. The catalyst CuO-NiO/NF shows a low overpotential of 231 mV in driving a current density of 10 mA cm-2 and exhibits a Tafel slope value of 100 mV/dec. The catalyst's durability was measured up to 20 hr using chronoamperometry technique. DFT calculations indicate the existence of strong interfacial interactions which is further manifested in the XPS analysis. The results obtained from DFT are also in line with the experimental data. Similarly, the fine nanosheets of the Co2-BDC$(OH)_2$ was first uniformly grown oven the honeycomb-like structure of nickel foam (NF). After controlled calcination of these nanosheets/NF composite, a uniformly decorated, binder-free Co_3O_4-NiO/NF electrocatalyst was synthesized. The transformation of Co_2-BDC$(OH)_2$/NF into Co_3O_4-NiO/NF is characterized by employing several techniques such as powder X-ray diffraction (PXRD), X-ray photoelectron spectroscopy and Transmission electron microscopy, etc. The catalyst exhibits a low overpotential of 311 mV vs. RHE at 10 mA cm-2 current density. The catalyst also displays long term stability (24 h) with a Tafel slope value of 90 mV dec^{-1}. The obtained experimental results are also in-line with the theoretical data acquired from the model systems. $NiWO_4$-NiO has superior HER activity in alkaline (1M KOH) electrolyte with modest overpotential of 71 mV at 10 mA cm^{-2} current density. The catalyst is highly stable in an alkaline medium and negligible change was observed in the overpotential after 10,000 cycles upto 100 hrs. This study explores a unique method for high-performance hydrogen generation by constructing transition metal-oxides heterojunction. The XPS studie sreveal an electronic redistribution driven by charge transfer through the $NiWO_4$-NiO interface. The density functional theory (DFT) calculations show that the $NiWO_4$-NiO exhibits a Pt-like activity with the hydrogen Gibbs free energy (ΔG_H*) value of 0.06 eV compared to the Pt(ΔG_H*=-0.02eV). Moving forward we formed the heterostructure between metal nitride and metal fluoride in chapter 4 which shows an extremely low overpotential of 180 mV at a current density of 10 mA cm^{-2} for OER application. The Co-Ni_3N/CeF_3 catalyst also shows strong interfacial interaction causing significant electronic redistribution between Co-Ni_3N and CeF_3 phases. XPS studies reveal the charge transfer from Co-Ni_3N to the CeF_3 phase resulting in the augmentation in the valence states of Co and Ni making them highly

active sites for the adsorption of intermediates (O*, OH*, HOO*). This phenomenon is possibly driven by the high polarity of CeF3 due to the presence of highly electronegative F atoms. The stability study of the catalyst was performed for 120 h at large current densities of 110 and 200 mA cm^{-2}. The detailed analysis of the surface reconstruction of Co-Ni_3N/CeF_3 is also carried out after a long-term stability test. This work offers a fresh look at the possibilities of the design and fabrication of an efficient and low-cost catalyst. In this thesis we also worked on the heterostructure of transition metal oxide with transition metal nitride. The $MnCo_2O4$-Ni_3N heterostructure shows excellent OER activity with the overpotential of 224 mV at 10 mA cm^{-2} of current density. The durability of the catalyst is also excellent with no change in current density (100 mA cm^{-2}) even after 100 hr of stability. Whereas $MnCo_2O_4$@Co-Ni_3N is active for overall water splitting with the cell volatage of 1.45V. In last we worked on pristine metal-organic framework for oxygen evolution reaction. It is proposed that in the ultrathin MOF nanoribbons, the surface atoms (Co,Ni) are coordinatively unsaturated, due to which, the inter-atomic electron transfer within the MOF makes more active adsorption sites on the surface. Our findings showed that the coordinatively unsaturated transition metal atoms are the dominant active sites and the electrocatalytic activity can be tuned by the coupling interactions of Ni and Co metals. The excess eg-orbital filling of Ni-atom which limits the electrocatalytic performance can be reduced by π-donation from Ni to Co through the oxygen atom.

Appendix 1

List of Publication

1. **Ashish Gaur,** Parrydeep K sachdeva, Rajinder Kumar, Takahiro Maruyama, Chandan Bera and Vivek Bagchi* **"Ultrathin MoS_2 wrapped N-doped carbon coated cobalt nanospheres for OER application"** **Sustainable Energy and Fuels, 2021, 5, 801-807**

2. **Ashish Gaur,** Krishankant, Vikas Pundir, Ashwinder Singh, Takahiro Maruyama, Chandan Bera and Vivek Bagchi* "**Intense nano-interfacial interactivity stimulates OER in MOF derived superhydrophilic CuO-NiO heterostructure**" **Sustainable Energy and Fuels 5 (21), 5505-5512**

3. **Ashish Gaur,** Vikas Pundir, Krishankant, Baljeet Kaur, Takahiro Maruyama, Chandan Bera and Vivek Bagchi* "**Interfacial interaction induced OER activity of MOF derived superhydrophilic Co_3O_4-NiO hybrid nanostructures**" **Dalton Transactions**

4. **Arti joshi,‡ Ashish gaur,** ‡ Parul Sood and Monika Singh *"**One-Pot Crystallization of 2D and 3D Cobalt-Based Metal-Organic Frameworks and Their High-Performance Electrocatalytic Oxygen Evolution"** **Inorganic Chemistry DOI 10. 1021 /ac sin org chem. 1c01665**

5. Rajinder Kumar, **Ashish Gaur,** Takahiro Maruyama, Chandan Bera and Vivek Bagchi* **"Strong Interaction between the Nanointerfaces of Silica-supported Mo_2C/MoP Heterojunction Promote Hydrogen Evolution Reaction"** **ACS applied materials & Interfaces 2020, 12, 57898-57906**

6. Arti Joshi, Parul sood, **Ashish Gaur**, Deepika Rani, Venika Madan and Monika singh * "**Improved OER performance of an Anderson-supported Cobalt Coordination Polymer by Assembling with Acetylene Black"** **Journal of Material Chemistry A , 2022**

7. Rajinder Kumar, Zubair Ahmed, Ritu Rai, **Ashish Gaur,** Shilpa Kumari, Takahiro Maruyama, and Vivek Bagchi *, **"Uniformly Decorated Molybdenum Carbide/Nitride Nanostructures on Biomass Templates for Hydrogen Evolution Reaction Applications"** **ACS omega 2019,4,14155-14161**

8. Krishankant, Ashi Chauhan, Zubair Ahmed, Srinivasan A, **Ashish Gaur**, Rajdeep Kaur and Vivek Bagchi **" Nano-interfaced tingston oxide inwrought with layered double hydroxides for oxygen evolution reaction"** **Sustainable energy and fuels , 2022**

Under Revesion:

1. **Ashish Gaur,** Krishankant, Vikas Pundir, Chandan Bera and Vivek Bagchi * "**Electronic Redistribution Over the Active Sites of $NiWO_4$-NiO Induces Collegial Enhancement in Hydrogen Evolution Reactio" Under major revision in Journal of Colloid and Interface Science**

2. **Ashish Gaur,** Vikas Pundir, Rajdeep Kaur and Vivek Bagchi * **" Curtailing the excess e_g-orbital filling of Ni-atom by enhanced inter-atomic charge transfer within bimetallic 2-D MOF nanoribbons for electrocatalytic oxygen evolution reaction " Under revision in Journal of Material Chemistry A**

3. **Ashish Gaur,** Vikas Pundir, Rajdeep Kaur and Vivek Bagchi * **"An electronegativity induced valence states augmentation of Ni and Co through electronic redistribution in Co-Ni_3N/CeF_3 for oxygen evolution reaction " Under minor revision in ACS Applied Energy Materials**

4. **Vikas Pundir,$ Ashish Gaur,$** Rajdeep Kaur, Aashi and VivekBagchi* **"Nano-interfacial interactions in 2-D Ni_3S_2-Ni_3N nanosheets for hydrogen evolution reaction in alkaline medium" Under minor revision in Energy Advances**

5. **Rajdeep Kaur,$ Ashish Gaur,$** Vikas Pundir and VivekBagchi* **"Electronegativity Governed Reallocation of Electrons through Strong Coupling Effect in CeF_3-Ni_3N for Enhanced Oxygen Evolution Reaction" Under major revision in Inorganic Chemistry**

List of Conferences attended

1. Kolkata, India (March 2020), *International Conference on Nanoscience and technology 2020* by S. N. Bose National Centre for Basic Sciences: **Ashish Gaur,** Vivek Bagchi **Poster presentation:** Strong Interaction between the Nanointerfaces of Silica-supported Mo_2C/MoP Heterojunction Promote Hydrogen Evolution Reaction

2. Roorkee, India (September 2018), *Conference on Enabling Transition towards sustainable future* by IIT, Roorkee; **Ashish Gaur**, Vivek Bagchi **Poster presentation: Deciphering the synergy between superhydrophilic $NiWO_4$-NiO interfaces for hydrogen evolution reaction**

Vtae

Ashish Gaur
Ph.D. Research Scholar
Institute of Nanoscience and Technology
&
Indian Institute of Science Education and Research,
Mohali (Punjab), India

Ashish Gaur completed his bachelor's degree in Science from Himalayan Rajkiya Snatkottar Mahavidhyalaya Kotdwar affiliated to Hemwati Nandan Bahuguna Garhwal University, Srinagar in 2015 and completed his Master Degree in Industrial Chemistry from Department of Chemistry, Gurukul Kangri Vishwavidhyalaya Haridwar Uttarakahnd in 2017. In July 2018 he joined Institute of Nanoscience and Technology as a Ph.D. research scholar under the guidance of Dr. Vivek Bagchi. He published a number of articles based on his research and presented his findings at a number of conferences on both a national and international level. His research interest includes the synthesis of metal-organic framework, transition metal oxides, nitride, and sulphides electrocatalyst in hydrogen evolution reaction (HER) and oxygen evolution reaction (OER)

Gmail CAMPUS COPY CENTER Panjab University <campuscopycenter14@gmail.com>

Fwd: Request for use of paper in thesis

1 message

ashish gaur <kandari101@gmail.com> Mon, May 15, 2023 at 10:27 AM
To: "campuscopycenter14@gmail.com" <campuscopycenter14@gmail.com>

---------- Forwarded message ---------
From: **Ashish Gaur** <ashish.ph18212@inst.ac.in>
Date: Mon, May 15, 2023, 02:05
Subject: Fwd: Request for use of paper in thesis
To: Ashish Gaur <kandari101@gmail.com>

---------- Forwarded message ---------
From: **CONTRACTS-COPYRIGHT (shared)** <Contracts-Copyright@rsc.org>
Date: Tue, Dec 20, 2022 at 3:34 PM
Subject: RE: Request for use of paper in thesis
To: Ashish Gaur <ashish.ph18212@inst.ac.in>

Dear Ashish Gaur

The Royal Society of Chemistry (RSC) hereby grants permission for the use of your paper(s) specified below in the printed and microfilm version of your thesis. You may also make available the PDF version of your paper(s) that the RSC sent to the corresponding author(s) of your paper(s) upon publication of the paper(s) in the following ways: in your thesis via any website that your university may have for the deposition of theses, via your university's Intranet or via your own personal website. We are however unable to grant you permission to include the PDF version of the paper(s) on its own in your institutional repository. The Royal Society of Chemistry is a signatory to the STM Guidelines on Permissions (available on request).

Please note that if the material specified below or any part of it appears with credit or acknowledgement to a third party then you must also secure permission from that third party before reproducing that material.

Please ensure that the thesis includes the correct acknowledgement (see http://rsc.li/permissions for details) and a link is included to the paper on the Royal Society of Chemistry's website.

Please also ensure that your co-authors are aware that you are including the paper in your thesis.

Best wishes

Becky

Becky Roberts
Contracts & Copyright Executive, Sales Operations

Royal Society of Chemistry

T: +44 (0) 1223 432304 | www.rsc.org

From: Ashish Gaur <ashish.ph18212@inst.ac.in>
Sent: 19 December 2022 12:20
To: CONTRACTS-COPYRIGHT (shared) <Contracts-Copyright@rsc.org>
Subject: Request for use of paper in thesis

Dear Sir/Madam,

I, Ashish gaur, a Ph.D. student with Dr. Vivek Bagchi wish to use my publication, Published in the following journals in my thesis. The details of the papers are following

1. Ultrathin MoS2 wrapped N-doped carbon-coated cobalt nanospheres for OER applications DOI:

DOI

https://doi.org/10.1039/D0SE01543A

2. Intense nano interfacial interactivity stimulates the OER in a MOF-derived CuO-NiO heterostructure DOI: **https://doi.org/10.1039/D1SE01235E**

3. Interfacial interactions induced OER activity of MOF-derived superhydrophilic Co3O4-NiO hybrid nanostructures DOI: **https://doi.org/10.1039/D1DT03810A**

Please allow me to do the same

With regards

ASHISH GAUR

PhD student